Geophysical Monograph Series

Including

IUGG Volumes
Maurice Ewing Volumes
Mineral Physics Volumes

Remote Sensing in Northern Hydrology:
Measuring Environmental Change

Claude R. Duguay
Alain Pietroniro
Editors

Published under the aegis of the AGU Books Board

Covers: (Front) North-central portion of Old Crow Flats, Yukon Territory, Canada, showing a very shallow thaw lake (average depth 1.5 m) in the foreground. Under certain weather conditions in the early summer, the lake attracts large numbers (50+) of moose. (Back) King Edward Lake, Old Crow Flats, Yukon Territory, Canada.This thaw lake, one of the most turbid in this area, has coalesced on its east side with a smaller, shallower lake at a slightly higher elevation. The smaller lake has partially drained, resulting in a lush growth of emergent and submergent aquatic vegetation. Both photos courtesy of Jim Hawkins, Canadian Wildlife Service.

CONTENTS

PREFACE

The North, with its vast and varied landscapes, sparse population, and cold climate has always challenged its explorers: physically, mentally, logistically, and technically. The scientific community in particular has known such challenges in the past and does so today, especially in light of the projected intensification of climate change at high latitudes. Indeed, there are clear signs that change is already ongoing in many environmental variables: Air temperature and annual precipitation (including snowfall) are increasing in many regions; spring snow cover extent is decreasing; lake and river ice freeze-up dates are occurring later and breakup dates earlier; glaciers are retreating rapidly; permafrost temperatures are increasing and, in many cases, the permafrost is thawing; and sea-ice extent is at record minimums and thinning.

Although some of the documented change has occurred over long periods of time, it appears that the process has accelerated since the mid-1970s. Field measurements have provided some of the evidence for the observed changes. A steady decline in several in situ measurement sites over the last two or three decades, however, has left important geographical gaps in observational networks. Remote sensing observations, together with numerical models and traditional measurement techniques, have thus become an invaluable tool for studying hydrosphere and cryosphere changes in remote areas of the North.

As a result, we have focused this volume on remote sensing observations and interpretations of components of the hydrological cycle that are germane to northern environments, such as glaciers and ice sheets, snow cover, lake and river ice, permafrost, and seasonally frozen ground. The volume also covers determinations of soil moisture, surface water, and evaporation/evapotranspiration from satellite remote sensing. For these parameters, a particular effort was made to provide references and summarize work conducted at high latitudes.

With new sensors and methods constantly being developed, remote sensing in northern (and global) hydrology has become a quickly evolving field. This book thus provides readers a foundation from which to build on as developments occur. Over this and the coming decade Canada, Europe, Japan, and the United States will place into orbit highly capable sensor packages that will foster new advances, especially in northern hydrology.

Scientists, researchers, and students with a direct interest in the application of remote sensing in northern hydrology will find this volume of immediate interest. Scientists,

researchers, and students in the biophysical sciences who wish to learn about the research now being conducted will also benefit from this volume.

The volume derives from a task force on "Remote Sensing in Northern Hydrology," initially proposed by international delegates of the Northern Research Basins (NRB) working group. The NRB working group was established in 1975 as part of the International Hydrological Programme (IHP) to promote research on river basins at northern latitudes. In contrast to other snow and ice conferences, NRB is intended specifically for Arctic environments. Full membership, therefore, is limited to countries with territory north of the Arctic Circle. Founding members included Canada, Denmark (Greenland), Finland, Norway, Sweden, the USA, and the former USSR. Iceland joined in 1992 and Russia has since taken over the role of the former USSR. Countries with polar research programs are also eligible for associate membership; current associate members are Germany, Switzerland, the UK, and Japan.

A particular objective of the NRB Working Group, which meets every 2 years in either Europe or North America, is to set up task forces to promote research initiatives on topics of special interest to northern research basins. The objective of an NRB Task Force is to continue liaison among member countries between NRB meetings through investigation of an area of mutual interest. One such task force was formed to review the state of the art on the use of remote sensing in northern hydrology.

This volume specifically derives from the work of the original members of the task force—Duguay (Chair), Pietroniro, Scherer, and Winther—and other international contributors (Jeffries and Granger as lead authors, and many collaborators) who enthusiastically agreed to contribute material on subjects for which significant gaps were identified. The completion of this volume would not have been possible without their help and commitment to the project.

As editors, we are very grateful to all authors, who worked hard to make this project a success. We are indebted to the many reviewers who devoted so much of their time and effort to improve the various chapters of this volume. We extend our sincere thanks to Jan Mydynski who provided valuable editorial assistance. Finally, we appreciate the help, patience, and expertise of AGU staff who worked diligently to publish the book.

Claude R. Duguay
University of Alaska, Fairbanks, Alaska

Alain Pietroniro
National Water Research Institute, Canada

Introduction

Claude R. Duguay

Geophysical Institute, University of Alaska, Fairbanks, Alaska

Alain Pietroniro

National Water Research Institute, Saskatoon, Saskatchewan, Canada

At northern latitudes, instrumented sites are often sparse and poorly distributed, and their number has been steadily declining over the last two to three decades. This has been a major impediment to advancing our knowledge of northern hydrology. Satellite remote sensing is ideally suited to complement field measurements. In this chapter, summaries of the main topics covered in this book (i.e., snow cover, glaciers and ice sheets, lake and river ice, permafrost and seasonally frozen ground, surface water and soil moisture, evaporation and evapotranspiration) as well as current and upcoming contributions of satellite remote sensing in northern hydrology are provided.

The North is loosely defined as the geographical area of the Northern Hemisphere that encompasses the tundra and taiga ecosystems. The North also is identified as the region most susceptible to the effects of global warming. Since it is the various water components of the cryosphere (glaciers and ice sheets, snow cover, sea ice, lake and river ice, and frozen ground) that are considered the principal expressions and instruments of climate change, northern hydrologists have become a logical scientific body to pursue research on the prediction and evaluation of climate-change impacts.

Nonetheless there remain

...many hurdles to advancing our knowledge of northern hydrology (all cast in a time of changing climate). Foremost is the need for better measurements of various components of the hydrological cycle (this is globally true)—a need expressed at numerous workshops throughout my career, now of 30 years. Potential improvement, of course, is possible through improved technology; for example, the use of solid-state electronics in extremely cold environments can improve conti-

nuity of data collected. However, our greatest need lies elsewhere, and concerns access to larger instrumented research watersheds where numerous complementary hydrological measurements are made at a scale that can be coupled with atmospheric processes that drive the hydrological cycle. In fact, we need several such watersheds located in circumpolar basins with different environmental settings (permafrost distribution and thickness, vegetation, topography, glaciers, etc.) [Kane, 2005].

Notwithstanding this need for more data at larger scales, instrumented sites are sparse and poorly distributed in the North, and their number has been steadily declining in the last 20–30 years. As a result, the defining characteristics of remote sensing technology render it ideally suited to complement, if not supercede, many of the classical hydrological field techniques used in northern hydrology. Remote sensing can fill the geographical gaps that field measurements alone cannot. It is in this context, and with a view of remote sensing as an invaluable tool for northern hydrological researchers, that the idea for this book was conceived.

There has been significant progress in the application of remote sensing in hydrology since the 1970s. Further substantive developments are forthcoming over the next decade as

next-generation spacecrafts are launched by Canada, Europe, Japan, and the United States. At the time of this writing, many recently launched satellite platforms are providing important information on the state of the cryosphere and the hydrosphere, and new satellites will soon follow that will significantly contribute to the field of northern hydrology.

Earlier books on remote sensing in hydrology have tended to provide a broad overview of the use of remote sensing in hydrology and water management [e.g., *Engman and Gurney*, 1991; *Schultz and Engman*, 2000] or have focused primarily on well-defined parameters such as snow cover [e.g., *Seidel and Matinec*, 2004]. This monograph builds on these previous works by providing a review of the progress and prospects of remote sensing in hydrology focused on the North, a region where hydrology is dominated by snow, ice, and frozen ground.

OVERVIEW OF CONTENTS

This monograph is organized into seven chapters, ordered to reflect the relative importance of each topic to the recent primary literature. Clearly, remote sensing of the cryosphere is of primary importance in northern landscapes (for the purpose of this publication, the definition of cryosphere includes snow, frozen ground, glaciers and ice sheets, and lake and river ice) and is the focus of Chapters 2 through 5. The two succeeding chapters center on water in the liquid and vapor phases and demonstrate some of the challenges to characterizing surface waters and evaporative processes, as well as in the application of remote sensing techniques in these areas. All of the chapters provide discussions of the potential for future remote sensing applications in the North.

Chapter 2 presents a thorough review of snow cover and the subsequent application of remote sensing to the determination of snow cover properties. Scherer and colleagues provide a comprehensive synopsis of the reflective and thermal properties of snow. These are described within the context of existing remote sensing systems and provide the fundamental background for understanding the development of remote sensing algorithms in snow-covered regions. A detailed description of sensors and systems is also given, which highlights the history of remote sensing systems along with their uses in snow algorithm development. The satellites described include visible and infrared-based sensors such as the familiar AVHRR radiometer aboard the NOAA polar-orbiting satellites and the more recent ASTER platform aboard the Terra platform. Microwave sensors and the electromagnetic interaction between microwaves and snow surfaces are described in detail. Active systems described include the RADARSAT, ERS, and ENVISAT satellite systems. Passive sensors such as the SSM/I radi-

ometer and the more advanced AMSR-E system aboard the Aqua platform are also described. Subsequent discussion in this chapter presents applications and algorithms for deriving snow properties from the previously defined systems. The authors illustrate the development of remote sensing applications with specific examples relevant to the determination of snow-covered area, snow water equivalent (SWE), depth and temperature, wet snow, and snow reflectance. The chapter concludes with a proposal for future applications and future sensors for continued monitoring of snow properties by remote sensing. These include (1) the improvement of SWE retrieval algorithms and SWE determination at higher spatial resolutions; (2) the exploitation of data fusion techniques for snow research; (3) a greater use of land cover data sets and digital elevation models for the retrieval of snow cover properties, particularly in mountainous and forested areas; and (4) the development of physically based and spatially distributed snow models to overcome some of the limitations of current empirical and conceptual models.

In Chapter 3, Winther and colleagues describe remote sensing as a useful tool for the study of glaciers and large ice masses, which, due to harsh climate and insufficiency of daylight, in combination with extensive geographical coverage, are largely inaccessible. Satellites provide one of the few methods for the study of these types of landscapes at large spatial scales. The authors note that glaciers have long been recognized as sensitive indicators for climate change, since they contain a considerable fraction of the world's freshwater. Because of the nature of these targets, remote sensing studies are focused on change detection and monitoring of glacial features. Moreover, due to the essential similarities of glaciers and ice sheets to frozen rivers and lakes, much of the theoretical background on the optical, thermal, and microwave properties of snow and ice contained in Chapter 2 provides the essential background for information in Chapter 3. Winther and colleagues focus on the remote sensing applications used in mapping glacier extent, glacier faces, equilibrium lines, and glacier velocity. They identify a key role for interferometric synthetic aperture radar (InSAR) in monitoring glacier velocity. The process for determining glacier velocity is described in detail. The use of radar altimetry in the measurement of glacier elevation is also described in detail, with emphasis on its use in change detection. Other topics of interest include methods for estimating glacier properties such as surface temperature, albedo/grain size, and snow accumulation for use in mass and energy balance estimates.

Chapter 4 provides a comprehensive overview of ice characteristics and processes in northern rivers and lakes focusing on initial ice formation in autumn and ice-melt in spring. Jeffries and colleagues concentrate primarily on

SAR systems (ERS-1, ERS-2, JERS-1, RADARSAT-1), supplemented by aerial photographs, passive-microwave sensors, and Landsat images as a means of characterizing lake and river ice covers. Because of the nature of these targets (both in terms of size and dynamic temporal characteristics), systems with high temporal and spatial resolution are the most practicable. The authors focus on remote sensing applications that assist in determining seasonal ice characteristics such as autumn freeze-up, ice growth, thickening and grounding; fracturing and motion; and spring thaw and breakup. They point out that most northern freshwater ice is seasonal in nature and that characterizing ice variability and change, particularly in remote locations, underscores the importance of frequent data acquisition and the value of time series of images to follow the course of events and processes. This chapter's extensive and holistic approach to the remote sensing of lake and river ice provides a major contribution to the literature in this area. It affords easy access to an inclusive examination of the field that until now has been conspicuously lacking.

The remote sensing of permafrost (perennially frozen ground) and seasonally frozen ground is the focus of Chapter 5. Unlike most of the other terrestrial components covered in this book, permafrost is a subsurface phenomenon. After providing a description of the factors that control permafrost distribution and the surface features indicative of permafrost presence (e.g., thaw lakes, polygonal ground), Duguay and colleagues review the application of remote sensing to map permafrost extent, active layer depth (i.e., the layer of soil above permafrost that thaws and freezes annually), and surface features indicative of permafrost presence. The authors then describe some of the most recent advances on the use of active and passive microwave imagery to map the seasonal freeze/thaw status of the landscape from the regional to the continental and pan-Arctic scales. In the final section of this chapter, Duguay and colleagues identify areas in which research is likely to take place in the future: (1) mapping the evolution of permafrost-related features (e.g., thaw lakes, patterned ground) by using archived imagery or aerial photographs and more recent high-resolution satellite imagery; (2) increasing the use of (and the development of new) land surface temperature data products from thermal infrared and passive microwave sensors to examine the impact of climate variability and change on permafrost terrain; (3) increasing the use of (and the development of new) land surface freeze/thaw products from active and passive microwave satellite sensors to examine variability and trends in the onset of freezing and thawing in relation to climate; and (4) integrating the land surface products derived from remote sensing data (e.g., surface temperature, vegetation, snow cover variables) in spatially distributed permafrost models.

Chapter 6 centers on surface water and soil moisture remote sensing. These two important aspects of the hydrological cycle were combined because they both represent storage of the liquid phase of water within the northern hydrological cycle. Surface water storages (lakes and wetlands) are easily discriminated by using conventional visible and infrared sensors such as those flown on Landsat or SPOT. The utilization of active microwave sensors, such as RADARSAT-1 or ERS-1/2, has lead to improvements in the interpretation and classification of open-water bodies. Pietroniro and colleagues discuss open-water extent, and to a lesser degree water surface elevation, with particular emphasis on applications within the microwave frequencies. The methods discussed are well established and easily operationalized for regular monitoring of these important hydrological features. In contrast, because of the notoriously ubiquitous nature of soil moisture, the detection and mapping of water storage in the vadose zone or soil profile are much less straightforward. Of the very few soil moisture experiments that have been carried out in northern regimes, the chapter summarizes soil moisture experiments in areas with seasonally frozen mineral soils. Theoretically, one should be able to extract soil moisture from the 1–10-cm depths; however, reliable and consistent systematic observations of soil moisture derived from microwave satellites are still difficult to ascertain.

Chapter 7 describes recent advances in the remote sensing of evaporation and transpiration. Relatively few studies have been directed specifically towards the determination of evaporation or evapotranspiration in northern environments. However, because the evaporative components of the energy and water balances can be as high as 50% and 65%, respectively, it is essential that the evapotranspirative phase of the hydrological cycle be understood. Methods of estimating evapotranspiration developed in temperate climates are described. Granger and Bussières note that these methods may not be directly transferable to northern areas because of the different characteristics of the vegetation and other physiographic conditions such as permafrost or surface ice that dominate the northern landscape. Suggestions for incorporating remotely sensed ice-cover information in order to estimate large lake evaporation by reformulating the parameterization of canopy controls on evapotranspiration are included. The authors clearly identify current defects and provide direction for future improvements.

WHERE NEXT FOR REMOTE SENSING IN NORTHERN HYDROLOGY?

Each chapter in this volume includes a concluding section that contains a discussion on future directions for

remote sensing in northern hydrology. Several operational or research products derived from satellite sensors currently in orbit are available to northern hydrologists (e.g., snow-covered area, SWE, surface albedo, soil moisture). Data acquired by sensors onboard NASA's Terra and Aqua platforms, as well as by those on other U.S. satellites (e.g., QuikSCAT) and satellites from the Canadian (e.g., RADARSAT) and the European (e.g., ENVISAT) space agencies, are already providing some valuable products. The number and the quality of the products can only increase as new sensors are flown and new algorithms are being developed.

During this decade alone, several missions have been confirmed and others are planned that will further advance the contribution of remote sensing to northern hydrology. Planned satellite missions such as the Advanced Land Observing Satellite (ALOS) of the Japan Aerospace Exploration Agency (JAXA), due for launch in 2005, and RADARSAT-2 of the Canadian Space Agency (CSA), scheduled for launch in 2006, though not exclusively designed for hydrological applications, will provide important information to northern hydrologists (e.g., snow and ice, surface water, and soil moisture).

Other missions, more specifically designed for hydrological applications, will also take place. For example, the European Space Agency (ESA) launched the CryoSat platform on 8 October 2005. Unfortunately, the satellite was lost due to launch failure. CryoSat carried a sophisticated radar altimeter called SIRAL (Synthetic Aperture Radar Interferometric Radar Altimeter) to monitor precise changes in the thickness of the polar ice sheets and floating sea ice. The observations to be made over the 3-year lifetime of the mission were expected to provide conclusive evidence of rates at which ice cover may be diminishing. CryoSat was meant to be the first Earth Explorer mission of ESA's Living Planet Programme. ESA has initiated an assessment of ways to recover from the CryoSat satellite loss and will be exploring the range of options that may be available such as rebuilding the satellite for a future launch.

The second Earth Explorer mission of ESA, the Soil Moisture and Ocean Salinity (SMOS) mission, will provide global observations of soil moisture and ocean salinity, which are needed to advance our knowledge of the water cycle and to contribute to better forecasting of weather, extreme events, and seasonal climates. Soil moisture data are urgently required for hydrological studies. Due for launch in early 2007, SMOS will also provide observations over regions of snow and ice, contributing to studies of the cryosphere and thus of the hydrological cycle at northern latitudes. A novel instrument has been developed that is capable of observing both soil moisture and ocean salinity by capturing images of emitted microwave radiation around the frequency of 1.4 GHz (L-band). SMOS will carry the first-ever, polar-orbiting, space-borne, 2-D interferometric radiometer. The satellite will achieve global coverage every 3 days with more frequent coverage at northern latitudes.

In December 2009, NASA plans to launch the Hydrosphere State Mission (Hydros) satellite, specifically designed for soil moisture retrieval (10-km resolution with revisits of 2 to 3 days) and freeze/thaw mapping (3-km resolution with 1- to 2-day revisits). A combined radar and radiometer system, Hydros will operate at 1.26 GHz and 1.4 GHz, respectively [*Entekhabi et al.*, 2004]. Hydros will provide the first global view of the Earth's changing soil moisture and surface freeze/thaw conditions, thus enabling new scientific studies of global change and atmospheric predictability and making new hydrological applications possible.

Recently, the U.S. National Academy of Sciences has been asked by NASA to form a community assessment and strategy for the future of earth science and applications from space. This is referred to as the National Research Council (NRC) Decadal Survey. The panel requested submissions from the community regarding potential future satellite missions that addressed the NRC science themes. Several (close to 100) future mission concepts have been proposed, a few of direct relevance to hydrology: the Cold-Land Processes Pathfinder (CLPP) mission [*Cline et al.*, 2005], the Water Elevation Recovery (WatER) satellite mission [*Alsdorf et al.*, 2005], the Global Water Resources mission [*Hildebrand et al.*, 2005], the Global Hydrosphere Mapper mission [*Fu and Rodriguez*, 2005], and the Glaciers and Ice Sheets Mapping Orbiter (GISMO) mission [*Jezek et al.*, 2005]. Documents describing each satellite mission concept can be found at http://qp.nas.edu/decadalsurvey. Ultimately, perhaps only one or a combination of the proposed mission concepts will make it to orbit.

In the meantime, current and upcoming satellite missions will provide technologies that will permit the routine monitoring of many hydrological state variables over northern latitudes. These new developments will encourage greater integration (assimilation) of remote sensing–derived products into climate, weather forecasting, and hydrological models.

REFERENCES

Alsdorf, D., E. Rodriguez, D. Lettenmaier, and J. Famiglietti, *WatER: The Water Elevation Recovery Satellite Mission*, http://qp.nas.edu/decadalsurvey, 2005.

Cline, D., R.E. Davis, and S. Yueh, *Cold-Land Processes Pathfinder Mission Concept*, http://qp.nas.edu/decadalsurvey, 2005.

Engman, E.T., and R.J. Gurney, *Remote Sensing in Hydrology*, Chapman and Hall, London, 1991.

Entekhabi, D., and 20 others, The Hydrosphere State (Hydros) satellite mission: An earth system pathfinder for global mapping of soil moisture and land freeze/thaw, *IEEE Trans. Geosci. Remote Sens., 42*, 2184–2195, 2004.

Fu, L.-L., and E. Rodriguez, *The Global Hydrosphere Mapper*, http://qp.nas.edu/decadalsurvey, 2005.

Hildebrand, P.H., R. Adler, R. Kelly, C. Parkinson, C. Peters-Lidard, D. Rind, M. Rodell, and J. Susskind, *Global Water Resources Mission*, http://qp.nas.edu/decadalsurvey, 2005.

Jezek, K., E. Rodriguez, P. Gogineni, A. Freeman, and J. Curlander, *Glaciers and Ice Sheets Mapping Orbiter*, http://qp.nas.edu/decadalsurvey, 2005.

Kane, D.L., High-latitude hydrology:, What do we know?, *Hydrol. Proc., 19*, 2453–2454, 2005.

Schultz, G.A., and E.T. Engman (editors), *Remote Sensing in Hydrology and Water Management*, Springer-Verlag, Berlin, 2000.

Seidel, K., and J. Matinec, *Remote Sensing in Snow Hydrology: Runoff Modeling, Effect of Climate Change*, Springer-Praxis, 2004.

C. R. Duguay, Geophysical Institute, University of Alaska Fairbanks, 903 Koyukuk Drive P.O. Box 757320, Fairbanks, Alaska 99775-7320, USA. (claude.duguay@gi.alaska.edu)

A. Pietroniro, National Water Research Institute, 11 Innovation Boulevard, Saskatoon, Saskatchewan S7N 3H5, Canada.

Remote Sensing of Snow Cover

Dieter Scherer[1], Dorothy K. Hall[2], Volker Hochschild[3], Max König[4],
Jan-Gunnar Winther[4], Claude R. Duguay[5], Frédérique Pivot[6], Christian Mätzler[7],
Frank Rau[8], Klaus Seidel[9], Rune Solberg[10], and Anne E. Walker[11]

This chapter is dedicated to remote sensing of snow as one of the most important cryospheric components to be considered in Northern Hydrology. After a short introduction, general approaches in optical, thermal infrared, active and passive microwave, and airborne gamma remote sensing, including the most important systems, are presented and discussed. Then, specific applications of remote sensing of snow cover are shown, grouped by the respective snow properties, i.e., snow-covered area, liquid water content, snow water equivalent, snow reflectance, snow grain size, snow depth, and snow temperature. Finally, conclusions are drawn with respect to unresolved issues and future research needs.

1. INTRODUCTION

Snow cover, which is a characteristic element of alpine and high-latitude regions, strongly alters land–atmosphere interactions and radiation fluxes. Furthermore, snow is a significant component of the hydrological cycle. Over one billion people depend on water resources originating from snowmelt runoff [Goodison et al., 1999]. At high latitudes, snow accumulates during each winter, and most of the snow melts during a single, intense period in late spring. At lower latitudes, snowfall is frequently followed by snowmelt a few days later, making snow cover an episodic phenomenon of variable seasonal frequency.

Most of the Earth's snow-covered area (SCA), showing a mean annual maximum of approximately 47×10^6 km^2, is located in the Northern Hemisphere [Robinson et al., 1993], mainly at high latitudes. Plate 1 shows an example of a daily snow cover map derived from multisensor satellite data as part of the Interactive Multisensor Snow and Ice Mapping System (IMS) [Ramsay, 1998], demonstrating typical SCA distribution during a northern hemispheric winter. Groisman et al. [1994] observed that snow cover exhibits the greatest influence on Earth's radiation budget in April and May, since most of the incoming solar radiation, which shows highest values at northern latitudes during that period, is reflected at the snow surface, hence strongly reducing net radiation over snow-covered regions.

On time scales of 1 year or less, monitoring of snow cover, particularly by remote sensing systems, is of interest for both basic and applied research. In addition, it has reached

---

[1]Department of Climatology, Institute of Ecology, Berlin University of Technology, Berlin, Germany.
[2]NASA/Goddard Space Flight Center, Greenbelt, Maryland.
[3]Geographisches Institut, Universität Tübingen, Tübingen, Germany.
[4]Norwegian Polar Institute, Polar Environmental Centre, Tromsø, Norway.

[5]Geophysical Institute, University of Alaska at Fairbanks, Fairbanks, Alaska.
[6]Department of Geography, York University, Toronto, Canada.
[7]Institute of Applied Physics, University of Bern, Bern, Switzerland.
[8]Department of Physical Geography, University of Freiburg, Freiburg, Germany.
[9]Swiss Federal Institute of Technology, ETH Zürich, Zürich, Switzerland.
[10]Norwegian Computing Center, Oslo, Norway.
[11]Climate Research Branch, Meteorological Service of Canada, Downsview, Ontario, Canada.

an operational status in different fields of applications. Snow data are useful in numerical weather prediction, for estimates of snowpack water storage, as well as for flood and reservoir recharge forecasts. Snow structure and (volumetric) liquid water content influence the stability of the snowpack and, hence, the formation of avalanches or slushflows. Detection of critical snow conditions can be used in early-warning systems for snow-related natural hazards. Remotely sensed snow data are used as input to drive or validate meteorological and hydrological numerical models. The strong tendency towards physically based and spatially distributed models is setting new requirements on snow data sets with respect to spatial and temporal resolution and particularly to higher accuracy.

Looking on longer time scales, the role of snow as an important component of the climate system has to be considered. Snow carries information on other components of the climate system. For this reason, snow monitoring by remote sensing is highly relevant to climate research, a fact also stressed by the Earth Observing System (EOS) Science Plan [NASA, 1999]. For example, glacier facies [see Winther et al., this volume] delimited by the physical properties of the overlying snow cover exhibit remarkable interannual variations caused by the prevailing meteorological conditions. Therefore, shifts in climatic conditions are expected to manifest in positional shifts in the boundaries [Bindschadler, 1998]. Not only spatial but also temporal changes of snow-cover properties may be used as indicators of climate change, such as Foster [1989] has discussed for the date of snow disappearance on the arctic tundra in North America. Consequently, monitoring long-term temporal evolution of the snow cover offers a valuable tool for detecting regional or even global climate variability.

Snow cover is not only the result of the climatic conditions of a certain region, it is also a strong climatic control. It plays an important role in several global and regional feedback mechanisms of the climate system, as the well-known example of the positive snow-albedo feedback demonstrates. Again, snow monitoring by remote sensing provides us with information on forcing and feedback mechanisms related to the presence of snow. In particular, snow data may be used for initialization, calibration, and validation of global or regional climate models. Such models not only allow studying the (still insufficiently known) present climate, they also can answer questions or, at least, give additional information concerning past and future climates. In any case, comprehensive data on present snow conditions are essential to create a baseline for a quantitative determination of future changes.

Spatially distributed snow data are often required for large areas. In addition, these data sets have to be acquired frequently to ensure data homogeneity and to allow (near)

real-time applications and high repetition rates, which are of particular importance for operational purposes. Therefore, remote sensing has received increased attention over the last two decades, since it is the only feasible way for acquisition of such data sets. This holds particularly true for the remote northern research basins.

The physical similarities of snow processes all over the world, in combination with the general nature of the methodological problems of remote sensing of snow, are the reasons this review is not restricted to northern latitudes. Studies carried out for alpine regions in different parts of the world and in Antarctica are also considered here, as long as they are of relevance to northern research basins. A discussion on remote sensing of snow on glaciers is given in Winther et al. [this volume]. Comprehensive reviews on this topic were also presented by Bindschadler [1998] and by König et al. [2001], to mention two other recent publications.

2. GENERAL APPROACHES

2.1. Overview

As early as in 1982, a Plan of Research for Snowpack Properties Remote Sensing (PRS)[2] was prepared to identify critical research topics and to outline a research strategy for developing the scientific understanding, models, and techniques required to make remote sensing of snow cover a useful operational tool [NASA, 1982]. Despite the huge technological and scientific improvements achieved since that time, the description of general approaches for remote sensing of snow as well as many of the recommendations are still valid, particularly the necessity for micro- to macroscale field studies and improved numerical modeling approaches for a better utilization of remotely sensed snow data. More recently, the EOS Science Plan [NASA, 1999] comprehensively described the state of knowledge, the unresolved problems, and the new possibilities and strategies of snow research offered by remote sensing systems in the context of Earth observation.

Generally, there is a trade-off between the spatial and the temporal resolution in remote sensing. However, this serious drawback does not affect northern research basins as much since polar-orbiting satellites, which are most relevant for remote sensing of high-latitude regions, are on converging orbits, hence drastically reducing the time needed to cover the same area repeatedly. For example, it is possible to obtain daytime Landsat images of Svalbard (75° to 81°N) each second or third day, while the repeat rate is 16 days for low latitudes. Shorter repeat cycles at higher latitudes are of particular interest for optical remote sensing systems, which provide useful snow data only under clear-sky conditions.
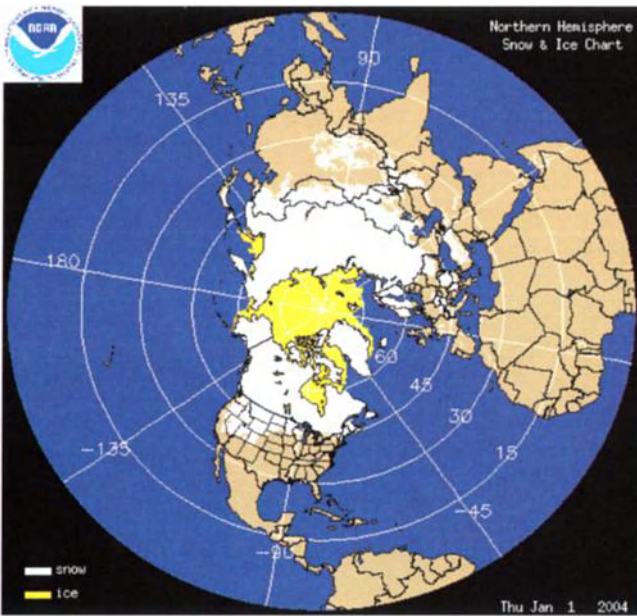
Plate 1. Northern hemisphere snow and ice chart for January 1, 2004 (source: NOAA, http://www.ssd.noaa.gov/PS/SNOW/index.html).
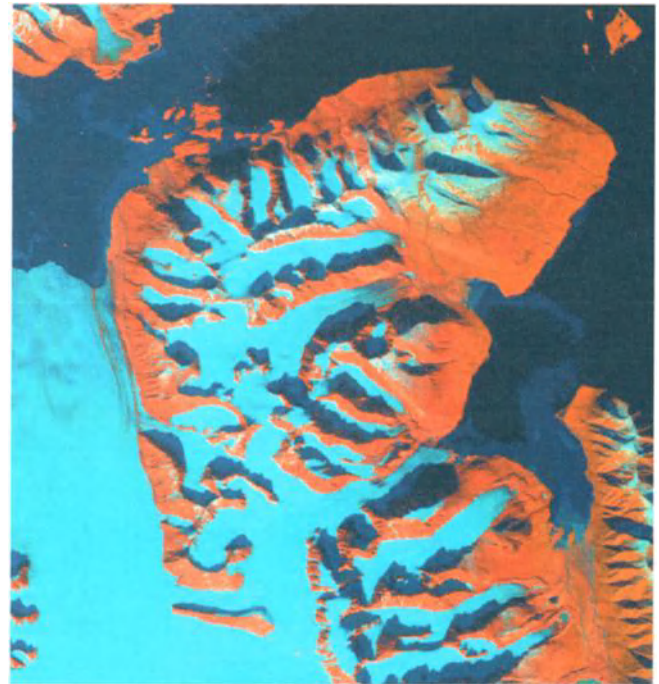
Plate 2. Landsat-5 TM false-color composite (band 5: red, 4: green, 2: blue) of northwestern Spitsbergen, Svalbard (data acquisition on August 19, 1990, 11:32 UTC). The influence of topography on satellite imagery is clearly visible, especially in shadow areas.
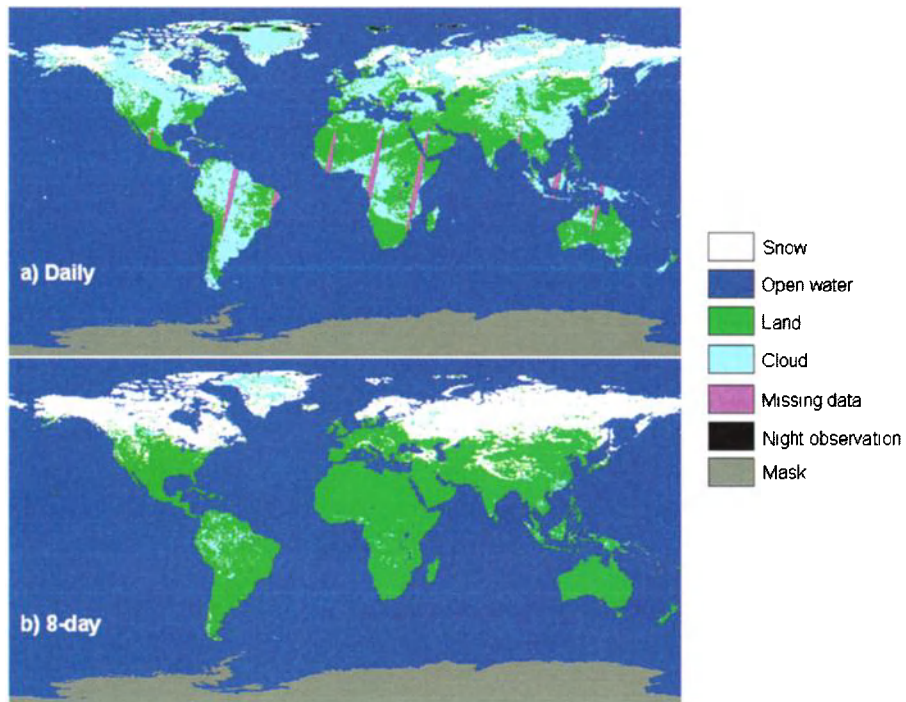
Plate 3. MODIS/Terra Snow Cover L3 Global 0.05Deg CMG data products available from National Snow and Ice Data Center (NSIDC): (a) Daily product (April 3, 2003); (b) 8-day composite product (March 30–April 6, 2003) (source: NSIDC, http://nsidc.org/data/modis/).

The advantage of converging orbits frequently overcompensates for the drawback of high cloud coverage typical of northern regions.

Terrain-induced effects cause strong impacts on remote sensing of snow cover and therefore need to be considered. This holds true for most types of sensors and for different spatial resolutions. During the last decade, a large number of global and regional digital elevation models (DEM) have been generated and are routinely utilized for correcting geometric and radiometric effects induced by topography. For instance, such effects include foreshortening or varying local incidence angles of the radar pulse in active microwave imagery, changing sun illumination conditions affecting optical remote sensing systems (as shown in Plate 2), or different atmospheric conditions caused by altitude variations, which must be taken into account by radiative-transfer models used for correcting optical, thermal infrared, and passive microwave data. Atmospheric correction not only is based on a DEM of the study area but also requires ancillary meteorological data (mainly atmospheric profiles of temperature, water vapor, trace gases, and aerosols). Inclusion of DEM and meteorological data as well as physically based numerical models in remote sensing analyses of snow is essential, particularly for mountainous regions at northern latitudes. Increasingly, DEM generation is based on remote sensing data themselves, such as from interferometric products. In addition, some of the existing and forthcoming remote sensing platforms are designed to provide supplemental data that could be used directly for atmospheric correction.

2.2. Optical and Thermal Infrared Remote Sensing

Satellite remote sensing of snow at visible (VIS) and infrared (IR) wavelengths has been important for research and operational applications since the late 1970s. Parts of this region of the electromagnetic spectrum were covered early on by remote sensing satellite sensors such as the NOAA Advanced Very High Resolution Radiometer (AVHRR) and the Landsat Multispectral Scanner (MSS). The VIS part of the electromagnetic spectrum is located between 0.4 and 0.7 μm. The IR is subdivided into the Near IR (NIR) from 0.7 to 1.1 μm, the Short-Wave IR (SWIR) from 1.1 to 3 μm, and the Thermal IR (TIR) from 3 to 100 μm. Bands located between 0.4 and 1.1 μm are commonly called VNIR bands, whereas the VIS + NIR + SWIR range is also called the solar spectrum used in optical remote sensing.

Optical and thermal remote sensing quickly led to the application of snow monitoring [Rango et al., 1977; Andersen, 1982]. The most important snow information that can be derived at optical and TIR wavelengths is SCA, surface reflectance, surface temperature, liquid water content,

and snow grain size [NASA, 1982, 1999; Kuittinen, 1997; Solberg et al., 1997, 1998]. Snow depth and snow water equivalent (SWE) may be retrieved at these wavelengths if the snow cover is very shallow, as shown for NOAA VHRR [McGinnis et al., 1975] and for the Geostationary Operational Environmental Satellite (GOES) [Donald et al., 1991]. The first two variables are of great importance for weather and climate models. For water management and hydropower applications, SCA is an important substitute to SWE, which is, in general, more difficult to derive by remote sensing techniques.

2.3. Reflective Properties of Snow

Optical remote sensing is based on measurement of the reflective properties of snow with airborne or spaceborne sensors and is therefore dependent on the sun as the primary source of energy. Solar radiation passing through the atmosphere is partly reflected at the surface and, after passing through the atmosphere again, reaches the sensor, where the upwelling radiance is measured. However, a fraction of the at-satellite radiance is not originating from the target surface but is caused by atmospheric scattering. In addition, scattering is also the reason that not all radiation reflected at the surface reaches the sensor. Radiative-transfer models are necessary to estimate the influence of atmosphere–radiation interactions disturbing the signal (radiance or reflectance) from the surface to be measured. However, not only the atmosphere but also complex terrain cause additional effects, e.g., by shadowed areas or counter-reflected radiation from adjacent surfaces (see Plate 2), a problem that is very important for snow-covered regions, particularly at northern latitudes, where solar elevations are low. Some authors [e.g., Obled and Harder, 1979; Parlow, 1996a; Sandmeier and Itten, 1997; Duguay and LeDrew, 1991, 1992; Duguay, 1993a,b, 1995; Scherer and Brun, 1997; Scherer, 1998] have addressed this problem, but a general solution is not yet available and remains one of most important tasks in the future.

Bidirectional reflectance, defined as the ratio of reflected and incident radiance for a specific illumination/viewing geometry, is a vectorial property, whereas albedo, defined as the ratio of the flux density of reflected radiation and the corresponding irradiance, is a hemispheric, and thus scalar, variable. Albedo as hemispheric reflectance is often just called "reflectance" or "reflectivity" (the latter term being used especially in the microwave range). Remote sensing systems can measure only bidirectional reflectance, hence albedo has to be computed—e.g., by hemispherically integrating reflectance measurements taken from different combinations of illumination and viewing angles—or has to be modeled by assuming characteristic bidirectional

reflectance distribution functions (BRDF) for each pixel. Lambertian surfaces show isotropic reflectance, making albedo computation a trivial job.

Reflective properties can be defined spectrally or as integrals over larger parts of the electromagnetic spectrum, which can be sampled either continuously or at discontinuous bands. Solar albedo, one of the important surface properties for many climatological and hydrological applications, is often just called "albedo", although it is the integral of the spectral albedo over the solar part of the electromagnetic spectrum (*Duguay*, 1993a). Multispectral optical sensors such as the Landsat Thematic Mapper (TM), the Système Probatoire d'Observation de la Terre (SPOT) High Resolution Visible (HRV), or the Moderate Resolution Imaging Spectroradiometer (MODIS) have a number of discontinuous bands of variable widths, whereas hyperspectral sensors such as the Airborne Visible Infrared Imaging Spectrometer (AVIRIS) or the HYPERION onboard the Earth Observing-1 (EO-1) satellite deliver reflectance spectra for more than 200 continuous narrow bands of less than 20 nm in width. Reflectance integrated over the solar part of the electromagnetic spectrum can be computed by using reflectance values from discrete parts of the spectrum (e.g., from TM measurements) along with published information on solar energy input and numerical integration schemes adapted to snow [e.g., *Brest and Goward*, 1987; *Duguay and LeDrew*, 1991, 1992] to establish band-specific weights. In this respect, hyperspectral sensors make any spectral interpolation unnecessary and therefore provide a major improvement over multispectral systems.

Important studies on reflective properties of snow have been carried out by *Wiscombe and Warren* [1980], *Warren and Wiscombe* [1980], *Warren* [1982], and *Zeng et al.* [1984], and a summary of the factors influencing reflectance can be found in *Foster et al.* [1987] and *Winther and Hall* [1999]. Typical snow spectra for various snow grain sizes are presented by *Dozier* [1989]. The ASTER Spectral Library (cf. http://speclib.jpl.nasa.gov/) provides spectral reflectance data for a variety of surface materials, including snow.

Snow is characterized by high reflectance at visible wavelengths (Figure 1). Reflectance falls rapidly in the NIR and SWIR. The SWIR spectrum is characterized by very low reflectance in general but shows peaks around 1.8 and 2.2 μm. The reflectance of snow can vary substantially, depending mainly on impurities, snow grain size, liquid water content, snow depth, and illumination geometry [e.g., *Hall and Martinec*, 1985; *Dozier*, 1989]. Fresh snow has high reflectance at visible wavelengths, whereas old metamorphosed snow (with larger grain size) shows somewhat lower reflectance in the VIS and a significant decrease in the NIR and SWIR. Satellite bands in this region have therefore been
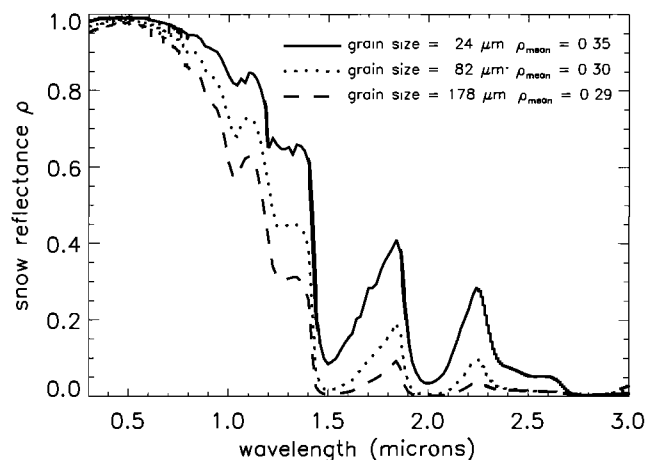
Figure 1. Reflectance of snow in the solar part of the spectrum for three different grain sizes. Solid line: fine snow; dotted line: medium granular snow; dashed line: coarse granular snow. (Reproduced from the ASTER Spectral Library through the courtesy of the Jet Propulsion Laboratory, California Institute of Technology, Pasadena, California. Copyright © 1999, California Institute of Technology. All rights reserved.)

used for the determination of snow grain size [e.g., *Dozier et al.*, 1981; *Bourdelles and Fily*, 1993; *Fily et al.*, 1997, 1999]. Liquid water in the snow pack has the effect of increasing effective grain size and thus lowers the albedo. Model work by *Choudhury and Chang* [1979], *Wiscombe and Warren* [1980], and *Warren* [1982] furthermore concludes that snow reflectance is independent of snow density. Observed snow density dependence may therefore actually be a dependence on snow grain size [*Warren*, 1982]. Impurities in the snow cover such as carbon soot, volcanic ash, or continental dust decrease reflectance the most at visible wavelengths.

Reflectance of snow is anisotropic (non-Lambertian), and thus albedo is dependent on BRDF. *Knap and Reijmer* [1998], for example, have examined the BRDF for wavelengths equivalent to Landsat TM bands 2 and 4 and find errors of several percent for snow albedo when BRDF is neglected. The effect of anisotropic reflection increases as snow metamorphoses, e.g., with increasing snow grain size and surface melt–freeze processes that sometimes produce a highly specular surface. Generally, old snow results in strong forward scattering. During the last few years, BRDF has been gaining more attention, as evident in the growing number of publications [e.g., *Leroux et al.*, 1998a, 1998b; *Sergent et al.*, 1998; *Mondet and Fily*, 1999; *Painter and Dozier*, 2004]. However, most studies dealing with satellite-derived albedo do not explicitly consider the anisotropic reflectance behavior of snow.

Even if very few surface materials show such brightness at visible wavelengths as snow does, retrieval of snow variables

by remote sensing is not trivial due to changing reflectance characteristics, especially in mountainous terrain. Snow research in areas with significant vegetation is even more difficult, and the common need for subpixel analysis due to the low spatial resolution of the satellites with high temporal resolution also increases the problems.

2.4. Thermal Properties of Snow

Sensors operating in the TIR measure upwelling thermal radiation originating from surfaces of a given temperature. However, observed brightness temperatures are not equal to kinetic surface temperatures because emissivity is generally below 100%. Fortunately, snow exhibits values of 99% and higher in the TIR, particularly for the wavelengths between 10.5 and 12.5 μm [e.g., *Dozier and Warren*, 1982; *Warren*, 1982; *Salisbury et al.*, 1994]. Hence, surface-temperature retrieval of snow is less complicated compared with that for other land surfaces, and snow is commonly treated as a blackbody radiator. However, *Dozier and Warren* [1982] show that emissivity is dependent on viewing angle, and that neglecting to account for this fact can lead to errors of up to 3 K. *Orheim and Lucchitta* [1988] observed surface patterns in Antarctic snow in Landsat TM bands 5 and 7 due to variations in snow grain size that do not appear in band 6. This suggests that emissivity is insensitive to snowpack parameters in the TIR, which has also been shown through numerical modeling [*Wiscombe and Warren*, 1980]. However, *Salisbury et al.* [1994] find that emissivity varies due to snow grain size, snow density, and liquid water content in this spectral region. This departure from blackbody behavior can lead to errors.

2.5. Optical and TIR Systems

Optical sensors are of two main types: scanners and pushbrooms. Scanners scan either normal to the satellite's direction of movement (in one or two directions: forward or two-way scanning) or in a circular pattern that gives the same spatial resolution all along the scan (conical scanners). Pushbroom sensors measure all pixels along one line simultaneously. Beam splitters, filters, prisms or gratings, or a combination of these are applied for splitting the spectrum. For a detailed presentation of the principles of optical imaging sensors, see (e.g.) *Norwood and Lansing* [1983] or *Massom* [1995], who focuses his discussion on remote sensing of polar snow and ice.

The low temporal resolutions of sensors like Landsat TM and SPOT HRV, and the comparably high prices for imagery with high spatial resolution, have limited such data sets mainly to experimental applications. NOAA AVHRR, with

repetition rates of at least two overpasses per day and limited costs for data acquisition has, on the other hand, has led to operational applications. The coarse resolution data from AVHRR is used at various scales, from global SCA down to relatively small basins (from a few 100 km^2). At the global scale, various geostationary satellites like GOES have been and still are important. However, they are of limited use for northern research basins because of the limitations of their viewing geometry, which does not allow data acquisition at polar latitudes and, further, results in coarser spatial resolutions with increasing distance from the nadir, which is located at the equator.

The number of satellites and types of sensors suitable for snow research at northern latitudes has increased rapidly in the last years and is expected to do so at an even greater pace in the future. Many sensors are interesting for experimental purposes where frequent coverage is not a constraint. Only few spectral features related to snow require very high spectral resolution to be measured, so broadband sensors do well for most operational applications. However, as demonstrated in Figure 2 for MODIS, ASTER, and Landsat-5 TM, it is particularly useful to cover the spectral range from 1.2 to 1.4 μm, where sensitivity of reflectance to grain size is strong. Unfortunately, only MODIS, but none of the sensors of higher spatial resolution, has bands in that part of the solar spectrum.

All optical sensors with spectral bands in both VNIR and SWIR are relevant for measuring SCA, reflectance, and snow
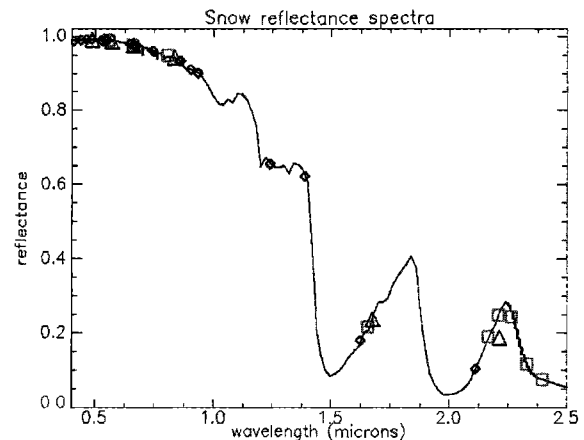
Figure 2. Reflectance of fine snow (grain size 24 μm) as measured by different optical sensors. Black line: fine snow reflectance spectrum (reproduced from the ASTER Spectral Library through the courtesy of the Jet Propulsion Laboratory, California Institute of Technology, Pasadena, California. Copyright © 1999, California Institute of Technology. All rights reserved). Diamonds: MODIS; squares: ASTER; triangles: Landsat-5 TM. Spectral resampling was done by sensor-specific convolution of the original spectrum.

grain size. TM, Enhanced Thematic Mapper Plus (ETM+), AVHRR, Along Track Scanning Radiometer-2 (ATSR-2), Advanced Along Track Scanning Radiometer (AATSR), Advanced Spaceborne Thermal Emission and Reflection Radiometer (ASTER), and MODIS all have bands in the TIR and, hence, are suitable for snow temperature measurements. The Medium Resolution Imaging Spectrometer (MERIS), ASTER, and MODIS are of some interest for retrieval of liquid water content. Measurements of the rather subtle spectral changes attributable to the presence of liquid water at the snow surface require two or more narrow bands at the right locations in the 0.9–1.4 µm spectral range [*Green and Dozier*, 1996]. None of the current sensors are optimal for this application, but MERIS and MODIS may have some potential.

For subpixel analysis of SCAs, a high number of bands is of great interest for the use of algorithms such as linear spectral unmixing [e.g., *Nolin et al.*, 1993; *Rosenthal and Dozier*, 1996], that is, for decomposing the effective spectrum of a single pixel into its primary spectra related to the different ground classes present (spectral end members). Therefore, sensors such as ASTER, MODIS, and MERIS (and partly ETM+) are of significant interest. Unfortunately, none of the existing hyperspectral systems delivers operational data. Most sensors like AVIRIS or the Digital Airborne Imaging Spectrometer (DAIS) are airborne systems used during special flight campaigns. The spaceborne HYPERION is also working merely on an experimental basis.

A large number of bands and better spectral coverage are also increasing the accuracy of albedo estimates [e.g., *Jin et al.*, 2002; *Klein and Stroeve*, 2002; *Zhang et al.*, 2003; *Stroeve et al.*, 2005], even for snow in forested areas [e.g., *Vikhamar and Solberg*, 2003a]. In any case a spectral reflectance model for snow has to be used [e.g., *Melloh et al.*, 2002; *Jin et al.*, 2003a,b]. The sensors carried by SPOT 4/5 and Terra are of particular interest for subpixel studies, since multisensor analyses of High Resolution Visible Infra-Red (HRVIR)/High Resolution Geometric (HRG), and VEGETATION or ASTER, MODIS, and Multi-angle Imaging SpectroRadiometer (MISR), respectively, data enable multiscale approaches.

The ability for snow-cloud discrimination varies between the sensors. TM, ETM+, HRVIR, HRG, AVHRR, ATSR-2, AATSR, VEGETATION, ASTER, and MODIS all have SWIR bands suitable for cloud detection. Multiangle systems such as ATSR-2, AATSR, and MISR make it possible to apply atmospheric correction by using an atmospheric model directly derived from remote sensing data. The quality of the atmospheric correction depends, however, on a suitable treatment of the BRDF of the surfaces. MISR provides detailed information on anisotropic reflectance, in that nine different viewing angles are concurrently used in four VNIR bands. In general, if relative measurements are sufficient, all multi-angle sensors or such with pointing capabilities are of interest for measuring anisotropic reflectance of snow.

NOAA AVHRR is still the most important system for operational monitoring of snow. The satellite provides coverage at least daily, and there are usually two satellites in orbit (morning and afternoon orbits). Spectral features have been found that discriminate most clouds from snow and ground-cover types. However, there are problems with discrimination between cirrus clouds and snow, although *Hutchinson and Locke* [1997] have developed a technique based on AVHRR band 3. The new version of AVHRR (NOAA 15 and later) has an additional band suitable for snow–cirrus discrimination, covering the spectral range from 1580 to 1640 nm. This band alternates with band 3, which is used during the night.

Since 1984, the TM sensor has been in orbit on the Landsat-5 platform. The ETM+ sensor on-board Landsat-7, launched in 1999, is an advanced version of the TM. Both TM and ETM+ have six bands with 30-m spatial resolution covering the VNIR and the SWIR part of the solar spectrum, complemented by one thermal band, numbered as band 6, of 120-m (TM) or 60-m (ETM+) spatial resolution. In addition, ETM+ is able to acquire panchromatic data (520 to 900 nm) at a spatial resolution of 15 m. Saturation of TM bands 1 and 3 is a problem over snow surfaces, but bands 2, 4, and 5 have been used successfully in various fields of snow research. Onboard calibration was not available for TM, thus causing serious drawbacks for scientific applications, but ETM+ data are thoroughly calibrated. However, the failure of the Scan Line Corrector (SLC) in 2003 has seriously affected data quality of ETM+. The U.S. Geological Survey (USGS) now provides gap-filled ETM+ data sets, obtained by using a histogram-matching technique for merging SLC off data with older, undisturbed image data to overcome the problem with the SLC failure.

The ATSR is one of the sensors onboard the European Remote Sensing (ERS) satellites. The two versions of the sensor, ATSR-1 and ATSR-2, have been carried on ERS-1 (operation completed in 1999) and ERS-2, respectively. The ATSR sensors have not been used very much for snow research. ATSR-1 is an IR sensor with bands located at 1600, 3700, 10,800, and 12,000 nm. Only three bands have been operational at the same time (bands 1, 3, and 4 or bands 2, 3, and 4). The ATSR is a dual-angle system composed of two conical scanners. One sensor is pointing towards nadir and the other one in the forward along-track direction (47° or 900 km ahead). Spatial resolution is 1×1 km^2 in the nadir direction and 1.5×2 km^2 for the forward scene. The ATSR-2 system is an enhanced version with additional VNIR bands

located at 555, 665, and 870 nm, added with land applications in mind. ATSR-2 could be regarded as a spectrally improved version of the AVHRR with better potential for landcover and snow–cloud discrimination. An advanced version (AATSR) is now available on the European Environment Satellite (ENVISAT) launched in 2002.

OrbView-2 (also known as SeaStar) carries the Sea-viewing Wide Field-of-view Sensor (SeaWiFS). Although it was originally developed for oceanic applications, it is also suitable for land applications. SeaWiFS has eight VNIR bands, located at 412, 443, 490, 510, 555, 670, 765, and 865 nm. Bands 1 to 6 have a bandwidth of 20 nm, whereas the bandwidth of bands 7 and 8 is 40 nm. A new feature to avoid band saturation is a bilinear representation of the detector response. The dynamic range is divided into two parts, each having different linear response functions. This is interesting for snow applications, since band saturation is a frequent problem of various sensors. However, SeaWiFS's spectral features are not very good for snow–cloud discrimination, which is a serious drawback. On completely clear days (e.g., determined by NOAA AVHRR), the sensor is suitable for very good subpixel class discrimination.

The Terra satellite, previously called EOS AM-1, launched in 1999, carries five sensors, of which ASTER, MODIS, and the MISR are of great interest for snow research.

ASTER is divided in three subsystems operating in the VNIR (three bands from 520 to 860 nm plus one backward-viewing band providing stereoscopic observations, 15-m spatial resolution), SWIR (six bands from 1600 to 2430 nm, 30-m spatial resolution), and TIR (five bands from 8125 to 11,650 nm, 90-m spatial resolution). Besides its stereo capability, which is restricted to the NIR band, it also provides cross-track pointing capability for all bands.

MODIS has 36 bands covering the spectral range from 405 to 14,385 nm. Spatial resolutions are 250 m for bands 1 and 2, 500 m for bands 3 to 7, and 1000 m for bands 8 to 36. The spectral coverage of MODIS makes it a very suitable instrument for snow monitoring. Snow–cloud discrimination in polar regions is much better than with AVHRR [Liu et al., 2004]. For snow cover, 500-m spatial resolution products are produced on an operational basis even if cloud masks have only 1-km resolution [Hall et al., 2002; Maurer et al., 2003]. MODIS is also part of the payload of the Aqua satellite (formerly called EOS PM-1). Unfortunately, the high number of defect sensors in MODIS band 6 is a serious drawback for snow monitoring by Aqua.

MISR has four VNIR bands, located at 443, 555, 670 and 865 nm. Spectral bandwidths are less than 30 nm in the blue band, less than 20 nm in the green and red bands and below 60 nm in the NIR band. The unique multiangle view-ing geometry of this instrument, provided by nine cameras pointing from 70.5° in forward and 70.5° in backward direction, enables rigorous use of radiative transfer models for atmospheric correction. In addition, BRDF measurements are possible at a quality level not reached so far [e.g., Stroeve and Nolin, 2002].

Multisensor analysis of ASTER, MODIS, and MISR will be of great interest for snow research. These sensors provide complementary data sets, e.g., atmospheric correction may be based on MISR, while MODIS or ASTER data are used for SCA mapping. In addition, multiscale imagery enables developing, improving, and testing of subpixel analysis methods.

The HRV sensor is part of the payload of the SPOT 1-3 satellites. It provides data in three VNIR bands at 20-m spatial resolution in the multispectral (XS) mode. A panchromatic (P) mode (510 to 730 nm) allows even 10-m spatial resolution. One SWIR band (1580 to 1750 nm) was added in the HRVIR sensor onboard SPOT 4 and the HRG sensor onboard SPOT 5, respectively. The stereo capability of the SPOT HRV/HRVIR/HRG systems enables high-resolution DEM and orthophoto generation.

SPOT 4/5's sensor VEGETATION is of potential interest to operational remote sensing of snow [e.g., Xiao et al., 2001, 2002; Dankers and De Jong, 2004]. An unusual new feature of the sensor is a compensator for across-track variable instantaneous field-of-view (IFOV) size. Each detector images what would be an equal area on the ground if Earth's surface were flat. Thus, this feature compensates for most of the panoramic effect. The VEGETATION sensor has four spectral bands, of which only the first one (430 to 470 nm) is not identical to the those of the HRVIR/HRG sensors. The SWIR band is suitable for cloud detection. SPOT VEGETATION is an interesting alternative to NOAA AVHRR. Simultaneous multiscale image acquisition by HRVIR and VEGETATION are of interest for snow research the same way as mentioned before for the Terra systems. The three identical spectral bands of HRVIR and VEGETATION are further simplifying subpixel analyses.

MERIS is one of the key sensors of ESA's satellite ENVISAT [Rast, 1996]. Primarily designed for oceanographic applications, MERIS is also receiving some attention for land applications. Since band positions are programmable, 15 spectral bands between 390 and 1040 nm can be selected, and spectral resolution can be set equal to, or in multiples of, 1.25 nm. A drawback for snow applications is the lack of bands in the SWIR, which would be useful not only for analysis of snow reflectance but also for cloud detection. However, the high spectral resolution in the NIR makes the sensor promising for measurements of liquid water content in the topmost snow layer.

2.6. Active Microwave Remote Sensing

Active microwave instruments operate at wavelengths of several millimeters up to several tenths of centimeters arranged in different frequency bands listed in Table 1. Sensors using frequencies at C and X bands are of most relevance for snow research, although there is some demonstrated potential also from Ku to Ka bands [e.g., *Papa et al.*, 2002; *Kimball et al.*, 2004].

Large-scale and year-round monitoring of snowcover dynamics in high-latitude regions has become feasible over the last few years through the all-weather operating capabilities of orbital Synthetic Aperture Radar (SAR) satellites. The first successful SAR data for snow studies were collected during the European SAR-580 Campaign in 1981 [e.g., *Mätzler and Schanda*, 1984; *Rott and Mätzler*, 1987]. Starting with the launch of the first spaceborne SAR instrument onboard of the SEASAT satellite in 1978, active microwave remote sensing from space has proved to be a valuable tool for snow research. The recent generation of active microwave remote sensing satellites provides high temporal and spatial resolution unhampered by high cloud coverage or limited daylight during the winter season. In addition, unlike optical sensors, microwaves penetrate the snow surface, which provides scientists with a tool capable of sensing internal snowpack properties.

Considerable work on remote sensing of snow by active microwave systems has been presented by several different authors [e.g., *Ulaby et al.*, 1982, 1986; *Shi and Dozier*, 1993, 1995; *Shi et al.* 1994; *Parlow*, 1996b; *Wunderle*, 1996; *Nagler and Rott*, 1997, 2000; *Rau et al.*, 2000; *Rees and Steel*, 2001]. *Mätzler* [1987], *NASA* [1986, 1989], *Henderson and Lewis* [1998], and *König et al.* [2001] provide a large number of further references on this topic. More details on glacier facies are given by *Winther et al.* [this volume].

Table 1. Radar Band Designations.

Band designation	Frequency range (in GHz)	Wavelength range (in cm)
L	1 to 2	30 to 15
S	2 to 4	15 to 7.5
C	4 to 8	7.5 to 3.75
X	8 to 12	3.75 to 2.5
Ku	12 to 18	2.5 to 1.67
K	18 to 27	1.67 to 1.11
Ka	27 to 40	1.11 to 0.75
V	40 to 75	0.75 to 0.4
W	75 to 110	0.4 to 0.27

2.7. Backscattering Properties of Snow

Interactions between the emitted radar pulse and the snow cover are affected by two sets of parameters: (a) sensor parameters, including frequency, polarization, and viewing geometry; and b) snowpack parameters, including snow density, liquid water content, snow grain size and shape, stratification, and surface roughness. These snowpack parameters determine the dielectric properties and therefore influence backscattering characteristics.

In contrast to optical data, active microwave imagery not only shows the surface structure but also reveals information on subsurface layers within the snow cover. The backscatter coefficient, σ^0, is determined by reflection at the snow surface, scattering within the snowpack, and reflection at the snow–soil or snow–ice boundary; thus, the measured backscatter is a combination of surface and volume scattering [*Ulaby et al.*, 1986]. The atmospheric influence on active microwave imagery can be neglected in most cases.

Figure 3 displays an ERS-1 SAR image of northwestern Spitsbergen, demonstrating the effects of surface and subsurface properties as well as topography on the resulting C-band SAR signal, which will be explained in the following paragraphs.

Because of the large difference between the dielectric constants of water ($\varepsilon \approx 80$) and ice ($\varepsilon \approx 3.15$), even small variations

Figure 3. ERS-1 (C-VV) SAR image of northwestern Spitsbergen showing the effects of surface and subsurface properties as well as topography on the resulting radar return.

of liquid water content of the snow cover significantly influence the resulting microwave backscattering at C-band. Dry snow has a dielectric constant between 1.2 and 2.0 when snow densities range from 0.1 to 0.5 g·cm^{-3} [*Hallikainen and Ulaby*, 1986]. Surface scattering depends mainly on dielectric contrasts at the layer interfaces, surface roughness, and local incidence angle. Due to the high dielectric constant of water compared with that of ice, increasing liquid water content causes a significant increase in reflection and, in turn, a decrease of transmission at the snow–air interface. Hence, surface roughness has a great impact on the backscattered signal for wet snow conditions: A smooth surface leads to specular reflection of the emitted radar pulse and therefore a low backscatter coefficient, whereas increasing surface roughness results in an increasing diffuse component of the scattered radar signal and therefore higher backscattering. Surface scattering at the snow–atmosphere interface is negligible for dry snow.

The part of backscatter resulting from volume scattering is influenced by snow properties such as liquid water content and snow density, grain size, and stratification. Penetration depth for a given frequency therefore depends mainly on liquid water content and snow density. The effect of liquid water is caused by its high absorption coefficient due to dielectric loss. Thus, backscatter resulting from volume scattering is inversely correlated to liquid water content. *Rott and Nagler* [1993] find a penetration depth of 13.8 cm for 1% liquid water content and 4.9 cm for 3%, whereas *Schneider et al.* [1997] reported a penetration depth of 22 cm for 2% liquid water content. The differences in penetration depth are, most probably, due to differences in further snowpack properties influencing σ^0. Under dry snow conditions, snow density, grain size, and stratification are the dominant factors determining the backscatter coefficient, which is inversely correlated with snow density and increases with snow grain size.

The above-mentioned effects are frequency-dependent. *Ulaby and Stiles* [1980, 1981] reported an inverse relationship of σ^0 and liquid water content between 35.6 and 4.6 GHz and little or no sensitivity at 1.2 GHz. Maximum penetration depth varies with frequency, ranging between a few meters in the X-band, about 20 m at the C-band, and several hundreds of meters at the P-band [e.g., *Wunderle*, 1996]. Thus, separation of dry snow and bare ground is hardly possible, at least with single-polarization, single-frequency SAR [*Rott and Nagler*, 1994; *Koskinen et al.*, 1997].

In general, wet snow appears darker than dry snow in C-band SAR imagery. For instance, *Braun et al.* [2000] report σ^0 values for dry snow in Antarctica between –14 and –20 db whereas σ^0 of wet snow areas ranged between –18 and –25 db. On the basis of snow-profile measurements, *Schneider et al.* [1997] computed with a multiple snow layer model that total backscatter of a snowpack in King George Island

changed from –6 db to –10 db when liquid water content changed from 0 to 0.5%, and stayed constant at –20 db for liquid water contents of 2% and higher. *Partington* [1998] retrieved σ^0 values for dry snow in Greenland between –5 and –14 db, whereas *Smith et al.* [1997] observed dry snow values between –3 and –7 db and wet snow values between –11 and –22 db for an alpine icefield in British Columbia. Lower values are typical for deep snowpacks on top of glaciers and ice sheets; as soon as snow depth is equal to or less than the penetration depth of the radar beam, then σ^0 is largely controlled by the underground conditions. On glaciers, the percolation facies in between zones of dry and wet snow usually shows higher σ^0 values attributable to development of large snow grains, ice lenses, and ice layers within the snow cover, causing significant increase of the backscatter coefficient as long as liquid water content is very low. This has been reported from Alaska [*Way et al.*, 1990], Greenland [*Fahnestock et al.*, 1993], and Antarctica [e.g., *Braun et al.*, 2000], where σ^0 values ranged between 0 and –8 db in the percolation zone. There are strong contrasts in X-band signals from wet snow (relatively low return) and those from snow-free ground (high return), indicating the potential for mapping the progression of snowmelt [*Mätzler and Schanda*, 1984].

Because of the side-looking imaging geometry of SAR sensors, active microwave data are subject to geometric distortions. These terrain-induced distortions include foreshortening, layover, and shadow effects. Geometric distortions other than shadowing effects decrease with increasing incidence angle. Since σ^0 is strongly influenced by topography, either local incidence-angle corrections have to be applied in mountainous areas [e.g., *Saurer et al.*, 1998; *Rau et al.*, 2000] or the dependency of backscattering on local incidence angles has to analyzed and modeled explicitly [e.g., *Nagler and Rott*, 2000]. Both approaches are based on the existence of DEM data of suitable spatial resolution and accuracy. However, standardized and generally accepted correction procedures are still lacking. In this respect, polarimetric SAR data were found to be more effective than single-polarized imagery for studying wet snow or ice surfaces since topographic information is not required [*Shi et al.*, 1991, 1994]. A further possibility to overcome the problems induced by alpine terrain is to use multitemporal SAR data as discussed by *Rott and Nagler* [1994] or by *Shi et al.* [1997] and *Strozzi et al.* [1999], who used interferometric techniques based on repeat-pass coherence measurements.

2.8. Active Microwave Systems

The following section focuses on SAR systems, although other studies [e.g., *Wismann*, 2000; *Nghiem and Tsai*, 2001;

Papa et al., 2002] have demonstrated the potential of scatterometer/altimeter instruments for global and regional snow monitoring. Although the sole instrument of ICESat (successfully launched in 2003), the Geoscience Laser Altimeter System (GLAS) is not an active microwave system. ICESat will definitely foster this kind of snow research and application. This would also hold true for CryoSat, an ESA Earth Explorer Opportunity Mission lost in 2005, if it is rebuilt.

Single-frequency C-band data from ERS-1 and ERS-2 and from RADARSAT-1 have been widely used for snow cover investigations in the recent years. These satellites have provided invaluable data sets to establish the scientific exploitation of SAR imagery for snow research. SAR sensors onboard the ERS satellites and the Canadian RADARSAT-1 operate at C-band (5.3 GHz, 5.66 cm), but show different polarization characteristics (ERS-1/2: VV; RADARSAT-1: HH). The Japanese JERS-1 SAR (terminated in 1998) operated at L-band (1.275 GHz, 23.5 cm; HH-polarized), which is not suitable for snow research because of the relatively long wavelength. All of these Earth-observing satellites are in polar, sun-synchronous orbits. The SAR sensors onboard SEASAT and JERS-1 provided a limited amount of L-band data. The Space-Shuttle SIR-C/X-SAR missions provided multifrequency (L-, C-, and X-band) and multipolarimetric data sets, thus demonstrating extended capabilities for snow research. The SAR onboard RADARSAT-1 is the first active microwave system that has reached an operational status with respect to snow monitoring; it covers the Arctic daily and most of Canada every 3 days utilizing different beam modes, of which the ScanSAR Wide mode supports swaths of 500 km at a spatial resolution of 100 m.

The Advanced SAR (ASAR) onboard the ENVISAT platform as well as the SAR system onboard the RADARSAT-2 (launch scheduled for 2006) will be very interesting for active microwave snow research because both systems are, on the one hand, advanced versions of C-band SAR sensors that have been successfully operating in space for long years and hence are able to continue the high-resolution SAR tradition achieved by those systems. On the other hand, both systems operate in different polarization modes: co-polarization and cross-polarization modes (ASAR has three so-called alternating polarization modes; RADARSAT-2 will operate in a polarimetric mode, providing four differently polarized images). A major advantage of ASAR for SCA mapping is its capability (like RADARSAT-1) to use incidence angles larger than ERS-1/2 SAR used to reduce specular returns, to increase the contrast between snow-free ground and wet snow, and to reduce layover and geometric distortions induced by the topography. For instance, *Guneriussen* [1998] showed that snow and bare ground on Kongsfjellet, Norway, could be better discriminated at high incidence

angles. ASAR and RADARSAT-2 operate in different beam modes, including the ScanSAR technology already used by RADARSAT-1. Different beam modes of variable spatial resolution, swath widths, and incidence-angle ranges allow flexible data acquisition needed for operational purposes. Finally, RADARSAT-2 will have an Ultra-Fine mode providing a spatial resolution of 3 m. How far this mode will be useful for snow research will mainly depend on the resulting data accuracy.

2.9. Passive Microwave Remote Sensing

Passive microwave remote sensing techniques involve the measurement of naturally emitted microwave radiation from the Earth's surface by an instrument called a microwave radiometer. The amount of radiation measured by the radiometer is commonly expressed as microwave brightness temperature in degrees Kelvin. The major advantages of microwave remote sensing are the ability of microwave radiation to penetrate through clouds and to sense conditions at any time of day or night. In northern latitudes, where cloud cover is prevalent and the period of darkness during winter lasts many months, passive microwave remote sensing is an ideal tool for monitoring snow cover in support of northern hydrological applications.

Passive microwave signatures of snowpacks have been observed during ground-based studies [e.g., *Kennedy and Sakomoto*, 1966; *Hofer and Schanda*, 1978; *Ulaby and Stiles*, 1980; *Mätzler*, 1987, 1994] and satellite observations [e.g., *Josberger et al.*, 1993]. An early review of the potential and limitations for microwave remote sensing of snow was published by *Bernier* [1987]. A number of studies have been conducted [e.g., *Hofer and Schanda*, 1978; *Stogryn*, 1986; *Mätzler*, 1987, 1998a; *Tsang*, 1987; *Surdyk and Fily*, 1995; *Tsang et al.*, 1995; *Mätzler et al.*, 1997; *Strozzi et al.*, 1997], including studies of microwave radiative transfer [*Chandrasekar*, 1960; *Chang et al.*, 1976; *Tsang and Kong*, 1977], to understand the influence of snowpack microstructure on the microwave signal and to explain snow signatures [cf. *Mätzler*, 1998b]. Mean and standard deviations of empirical emissivity spectra from 5 to 100 GHz of winter landscapes are presented in *Mätzler* [1994].

Several researchers have developed algorithms based on spectral features to retrieve SWE from satellite radiometer data [e.g., *Hallikainen and Jolma*, 1986; *Chang et al.*, 1987; *Wang et al.*, 1992; *Goodison and Walker*, 1995; *Tait and Armstrong*, 1996; *De Sève et al.*, 1997; *Goïta et al.*, 2003; *Koenig and Forster*, 2004; *Foster et al.*, 2005]. Although snow depth can be retrieved successfully under special conditions, the usefulness of the underlying empirical models has, with a few exceptions [e.g., *Kelly and Chang*, 2003; *Kelly et al.*, 2003], been limited to spe-

cific geographic regions and special snowpack histories [*Rango et al.*, 1979; *Foster et al.*, 1980; *Künzi et al.*, 1982; *Tait and Armstrong*, 1996]. *Rott and Nagler* [1995] showed that different snow types (wet snow, snow with crusts, dry snow) could be successfully delineated but that a universal algorithm for SWE does not exist. *Mätzler* [1994] as well as *Surdyk and Fily* [1995] found from surface-based experiments that snow structure and layering of dry snow could strongly influence the signal through shifts in spectral emissivity. *Tait and Armstrong* [1996], being aware of special snowpack signatures, tried to optimize snow depth algorithms by excluding certain data (types of snowpacks, special regions, and weather conditions).

The above experiments have revealed that a physical approach including all snow parameters would be more adequate than empirical algorithms for single parameters, although semiempirical models have been shown to be quite useful [e.g. *Pulliainen et al.*, 1999]. Information gain by physical analysis is manifold, because all snow properties, not just SWE alone, can give valuable geophysical information. Parameters to be derived from snow structure are solar albedo and diffusivity for mass and heat transfer within the snowpack. Furthermore, it is possible to include terrain-induced effects [*Mätzler and Standley*, 2000] as well as background radiation in a physical treatment of snow. Recent experiments showed that even background radiation can be measured through dry, alpine snowpacks, and that such data sets are useful for permafrost mapping by microwave radiometry at frequencies near 10 GHz [*Gubler and Hauck*, 1998].

There are many advantages of combining snow physical models (i.e., models describing the detailed state of the snow cover from meteorological data) with radiative transfer models. In particular, this strategy enables one to include surface effects in numerical weather prediction and data assimilation procedures. Three recent cases of combining microwave and snow physical models are mentioned here. First, *Shih et al.* [1997] published a model to calculate backscattering of layered snow, based on dense-medium radiative transfer in combination with SNTHERM, a one-dimensional mass and energy balance model of snow physics that was developed at the U.S. Army Cold Regions Research and Engineering Laboratory (CRREL) for predicting temperature profiles within snow and frozen soil [*Jordan*, 1991]. Second, *Galantowicz and England* [1997] published a passive microwave model utilizing radiative transfer combined with a soil–vegetation–atmosphere scheme based on the physical snow model of *Anderson* [1975]. Finally, the Microwave Emission Model of Layered Snowpacks (MEMLS) [*Mätzler and Wiesmann*, 1998, 1999; *Wiesmann and Mätzler*, 1999; *Wiesmann et al.*, 2000] was developed and applied to layered snowpacks simulated by snow pro-

files obtained from the physical snow models CROCUS and SNTHERM [*Wiesmann et al.*, 2000]. CROCUS is a one-dimensional numerical energy and mass evolution model of snow cover developed at Meteo France [*Brun et al.*, 1989]. Its main objective is operational avalanche forecasting. Project 1, Development of Radiative-Transfer Models, of the COST (European Cooperation in the Field of Scientific and Technical Research) action 712, Application of Microwave Radiometry to Atmospheric Research and Monitoring, addresses the problem of microwave emissions from snowpacks, the influence of terrain on microwave remote sensing, and radiation–atmosphere interactions in the microwave region [*Strozzi et al.*, 1999; *Mätzler*, 2000].

Despite the promising results achieved by physically based models, empirical approaches are still important, particularly for operational purposes. One of the reasons for this is the difficulty so far to validate the results of physically based models because the snow structure cannot be quantified easily.

2.10. Passive Microwave Systems

Although microwave radiometers have been flown on satellite platforms since the late 1960s [see *Njoku*, 1982], it was not until the launch of the Scanning Multichannel Microwave Radiometer (SMMR) on the Nimbus-7 satellite in 1978 that algorithms began to be developed to retrieve information on SCA, snow depth, SWE, and snow state (wet/dry) from satellite passive microwave data [e.g., *Künzi et al.*, 1982; *Goodison et al.*, 1986; *Hallikainen and Jolma*, 1986; *Chang et al.*, 1987].

The Special Sensor Microwave Imager (SSM/I), one of the current satellite-based microwave radiometers, operates at 19.35, 22.235, 37, and 85 GHz frequencies. A complete description of the SSM/I instrument can be found in *Hollinger et al.* [1990]. The first SSM/I was launched in June 1987 on the U.S. Defense Meteorological Satellite Program (DMSP) F-8 satellite. Since that time, additional SSM/I's have been launched on DMSP F-10, F-11, F-13, F-14, and F-15 to provide continual coverage. With an orbital swath of 1,400 km and 14 orbits per day, multiple orbits of SSM/I cover most northern areas on a daily basis. A major advantage of the SSM/I for hydrological applications is the capability to access the data in near real-time (e.g., a few hours after a satellite overpass), even via the Internet (e.g., NOAA National Environmental Satellite Data and Information Services). As a result, SSM/I-derived snow cover products have been developed by several agencies to provide routine information for hydrological applications.

The development of snowpack algorithms using SSM/I data for northern areas in Canada has been and continues

to be a major goal of the Canadian multidisciplinary project Cryospheric System for Monitoring Global Change in Canada (CRYSYS). This Canadian interdisciplinary science investigation operates within NASA's Earth Observing System program [NASA, 1999]. Some investigations have been carried out in the prairie region [e.g., Goodison et al., 1986, 1990], the boreal forest [e.g., Goïta et al., 2003], the taiga region of Quebec [De Sève et al., 1997], the boreal forest–tundra ecotone of northern Manitoba [Pivot et al., 2002; Derksen and Walker, 2004], and the tundra areas of the Arctic islands [Woo et al., 1995]. Similar efforts have been undertaken in Europe in a research project called SNOWTOOLS [Solberg et al., 1997, 1998; Guneriussen et al., 2000a].

The Advanced Microwave Scanning Radiometer (AMSR-E) is the passive microwave radiometer onboard the NASA Aqua platform. Originally, AMSR was also planned for the Japanese ADEOS-II mission, which unfortunately failed in 2003. AMSR-E measures microwave radiance at 6.925, 10.65, 18.7, 23.8, 36.5, and 89 GHz at both vertical and horizontal polarizations. AMSR-E provides advances over the current SSM/I through use of the additional lower frequencies (6.925 and 10.65 GHz) and higher spatial resolutions (e.g., 12 km at 36.5 GHz, compared with 25 km for SSM/I 37 GHz). The higher spatial resolutions extend passive microwave capabilities for monitoring snow cover characteristics, especially for SWE, to smaller watersheds and mountainous areas. The algorithm developed for AMSR snow cover products is described in Chang and Rango [2000] and Kelly et al. [2003].

The Advanced Microwave Sounding Unit-B (AMSU-B) onboard the new NOAA operational satellites has some potential for high-frequency passive microwave remote sensing of snow cover. Frequencies beyond 89 GHz may be used to determine snow cover at higher resolution than the traditional microwave frequencies of 19 and 37 GHz. Preliminary studies using the Millimeter-wave Imaging Radiometer (MIR) onboard the NASA ER-2 aircraft have shown that high-frequency microwave data are well related to snow and vegetation cover of New England and the Great Lakes region [Tait et al., 1999].

2.11. Airborne Gamma Remote Sensing

Airborne gamma surveys have been used in many northern countries for retrieval of SWE information in support of operational hydrological monitoring. The method is applicable to all sizes of basins, and surveys can generally be conducted during a single day (depending on the size of the basin) to provide information on the spatial distribution of SWE and an estimate of total snow volume contained in the basin.

Terrestrial gamma radiation is emitted by potassium, uranium, and thorium radioisotopes in the soil, the majority of the emission coming from the top 20 cm. Because gamma radiation is attenuated by water in any phase, derivation of SWE from gamma measurements is possible as the result of attenuation by the mass of water in the overlying snow cover. Intensity of terrestrial gamma emission is measured with a gamma radiation spectrometer, which is typically flown on an aircraft for basin snow surveys. Flights are usually conducted at low altitudes to minimize attenuation by water in the atmosphere. Offenbacher and Colbeck [1991] review the application of the gamma technique for snow research, including the physical principles and methods used.

Airborne gamma snow surveys are generally conducted along an established network of flight lines in a basin, thus providing information on spatial variation of SWE. A background (no-snow) flight is usually conducted in the fall before snow accumulation, and then the same lines are flown during winter when snow-covered. If soil moisture conditions are the same for both surveys, mean SWE for the line can be derived as a function of the ratio between gamma emission from bare ground and that from snow-covered ground. If soil moisture conditions change after the background flight (e.g., with additional rainfall), ground-based soil moisture measurements acquired along the flight line can be used to derive a more accurate SWE [Carroll et al., 1983]. Errors in SWE associated with this method are on the order of 4% to 10% for agricultural environments [Carroll, 1987]. In forested environments, errors can be much higher because of the effects of the vegetation biomass, which can attenuate the terrestrial gamma signal and contribute its own emission. Glynn et al. [1988] and Carroll and Carroll [1989] describe potential correction methods for forest biomass effects. In areas containing swamps, bogs, and wetlands, the airborne gamma technique for snow surveying is generally not reliable since water layers absorb gamma radiation.

3. CURRENT APPLICATIONS

This section presents current applications of remote sensing data relevant to snow research with respect to northern research basins. Due to the large number of publications dealing with this topic, it is almost impossible and thus is not intended to give a complete review of the relevant literature. The general overview of remote sensing of snow cover presented in the previous section is illustrated with more specific examples in this section.

3.1. Snow-Covered Area

Already in the 1930s, panoramic terrestrial photographs were used for seasonal runoff forecasts by mapping SCA [Potts, 1937]. Later, more realistic SCA mapping was con-

ducted by periodical expeditions in experimental basins with terrestrial observations [*Garstka et al.*, 1958]. The continuous decline of SCA was obtained by interpolation between the measured points, resulting in so-called SCA depletion curves [*Leaf*, 1967]. The expediency of SCA mapping was improved by aerial photography [*Martinec*, 1973], which, however, necessitated an extensive evaluation of orthophotos.

A significant improvement in SCA mapping was achieved after the advent of remote sensing [*Haefner and Seidel*, 1974; *Rango and Itten*, 1976; *Seidel and Martinec*, 1992]. Comparison of SCA derived from a Landsat-MSS classified image of the Dischma basin in the Swiss Alps and a simultaneous orthophoto demonstrated the capability of optical sensors for snow monitoring in mountainous regions [*Hall and Martinec*, 1985]. SCA was evaluated by counting the 80×80 m^2 snow-covered, snow-free, and mixed pixels. SCA mapping by Landsat MSS, covering periodical acquisitions for a complete runoff season, were carried out for the Alpine basin of the Rhine at Felsberg [*Seidel and Martinec*, 1992]. For computations of snowmelt runoff, it is advisable to evaluate SCA for different elevation zones into which the basin is subdivided. This was demonstrated by depletion curves of five different zones of the Rhine at Felsberg and by a study performed in a small drainage basin in NW-Spitsbergen [*Scherer*, 1996]. SCA mapping using Landsat MSS and TM as well as SPOT HRV was further presented by a large number of authors [e.g., *Bowley and Barnes*, 1979; *Dozier and Marks*, 1987; *Martinec and Rango*, 1987; *Dozier*, 1989; *Gangkofner*, 1989; *Rott and Markl*, 1989; *Hall et al.*, 1995; *Steinmeier*, 1995; *Rosenthal and Dozier*, 1996; *Scherer*, 1996; *Schneider et al.*, 1996, *Seidel et al.*, 1996; *Winther and Hall*, 1999]. A data processing method has been developed that enables SCA mapping with acceptable accuracy from Landsat TM images partially obscured by clouds [*Ehrler et al.*, 1997]. Thus, the number of satellite images available for snow monitoring could be increased.

For more than 30 years, the National Environmental Satellite Data and Information Service (NESDIS) of the U.S. National Oceanic and Atmospheric Administration (NOAA) has been providing weekly maps of SCA in the Northern Hemisphere [*Robinson et al.*, 1993]. In 1999, after a short period of concurrent data acquisition, the weekly maps were replaced by daily maps (available online at www.ssd.noaa. gov; cf. Plate 1) derived by a robust multisensor approach that uses both geostationary and polar-orbiting satellite systems, including SSM/I data [cf. *Ramsay*, 1998].

The National Operational Hydrologic Remote Sensing Center (NOHRSC) publishes weekly snow charts for North America at 1.1-km spatial resolution, which are also available online (at www.nohrsc.nws.gov) [cf. *Maxson et al.* 1996; *Cline and Carroll*, 1998].

In Norway, Norges Vassdragsog Energiverk (NVE) produces snow maps from AVHRR by using an algorithm developed by *Andersen* [1982]. AVHRR bands 3, 4, and 5 are used for snow–cloud discrimination, whereas AVHRR band 2 is used for snow mapping. The value distribution is viewed in a histogram, in which an upper limit for 100% snow cover is set from glacier- or snow-covered areas and the lower limit of 0% snow cover is set from water or land areas. Then, the snow coverage is interpolated linearly [*Schjødt-Osmo and Engeset*, 1997]. The Tromsø Satellite Station provides SCA maps of Norway based on *Andersen*'s [1982] algorithm. This is a simple and robust algorithm, which can be easily applied to the satellite images. However, accuracy determination is poor.

A fully automated algorithm has been developed [*Hall et al.*, 1995, 2002; *Klein et al.*, 1998; *Maurer et al.*, 2003] to map global SCA on a daily basis by using MODIS data. The snow-cover products are available at 500-m and 0.05° (climate-modeling grid; CMG) resolutions as daily and 8-day composite products. Examples of global daily and 8-day composite CMG products are shown in Plate 3. The MODIS snow-cover algorithm uses the normalized difference snow index (NDSI) to discriminate snow-covered from snow-free areas; additional threshold tests are used to distinguish snow from open water and to map SCA in forested areas. This is also the MODIS at-launch algorithm used to generate the MODIS snow-cover products. Validation of the MODIS snow-cover algorithms has been conducted for many different landcover types in Alaska [*Hall et al.*, 1998a,b] and Canada [*Klein et al.*, 1998]. Results show that the at-launch algorithm can map snow with nearly 100% accuracy in all landcover types except forests. *Hall et al.* [2001] determined SCA errors from field measurements for seven different land-cover types. When the results were extrapolated to the entire Northern Hemisphere, maximum monthly snow-mapping errors obtained when using MODIS snow products ranged from 5% to 10%. The larger errors are found to occur in the boreal forest during the winter months.

Binary or multiple end-member classifiers, band ratio thresholds, or normalized difference ratios are used for SCA mapping based on optical sensors, as well as spectral mixture analysis (SMA), thereby resulting in subpixel SCA data to overcome the problem of mixed pixels [e.g., *Romanov et al.*, 2003; *Vikhamar and Solberg*, 2003b; *Salomonson and Appel*, 2004]. Although studies have been conducted for multispectral sensors such as Landsat TM [*Rosenthal and Dozier*, 1996], SMA is particularly useful for the analysis of hyperspectral sensor data like that of AVIRIS, which were successfully used for SCA determination [*Nolin et al.*, 1993].

Generally suitable methods for SCA mapping by active microwave systems do not exist, particularly for dry snow, but promising results were achieved with SIR-C/X-SAR

data, which successfully classified five different types of snow surfaces, including dry snow in mountainous terrain [*Albright et al.*, 1998].

Based on the passive microwave sensors SMMR and SSM/I, weekly hemispheric and global SCA maps with a spatial resolution of 25 km have been available since 1978 [cf. *Chang et al.*, 1987; *Grody*, 1991; *Grody and Basist*, 1996; *Goodison et al.*, 1999]. Together with SCA maps derived from NOAA AVHRR, it has been possible to analyze variations in the Northern Hemisphere's SCA, which shows an annual mean of 25.3×10^6 km^2, with 14.7×10^6 km^2 over Eurasia and 10.6×10^6 km^2 over North America. Between 1972 and 1985, annual values of SCA fluctuated around a mean of 25.9×10^6 km^2. Since then, mean annual SCA has been 24.2×10^6 km^2.

Since both optical- and microwave-based methods for estimating SCA have specific drawbacks, an approach that combines the benefits of both data sources is regarded as optimal. The NOAA Satellite Analysis Branch performs an operational multispectral SCA analysis [*Ramsay*, 1998], and the Hydrological Sciences Branch of the NASA Goddard Space Flight Center is currently developing a North American SCA data set based on optical, passive microwave, and surface data. *Haefner and Piesbergen* [1997] and *Koskinen et al.* [1999] developed methods on the synergistic use of optical and microwave data for snow-cover monitoring in mountainous areas. The Multitemporal Optimal Resolution Approach (MORA) system [*Haefner and Piesbergen*, 1997] uses ERS SAR data to cover the periods between cloud-free Landsat TM acquisitions. To overcome the strong terrain effects in SAR data, they integrate ascending and descending orbits. Merging optical and microwave data turns out to be a practical solution for exploiting the specific advantages of each sensor type. However, it is not always possible to obtain nearly simultaneous data, a situation that makes data fusion more complicated.

3.2. Wet-Snow Mapping and Liquid Water Content

Nagler and Rott [1997, 2000] as well as *Shi et al.* [1997] developed different methods for the derivation of areas of wet snow from ERS SAR data for high-mountain regions in the central Alps. The results have been compared with results from optical remote sensing data and correspond well with those data. Snow maps derived by this method were used as input for snowmelt-runoff models, producing good correlation between measured and simulated runoff. Similar approaches for monitoring wet snow by multitemporal analysis of ERS and RADARSAT SAR data have been applied successfully in other regions of the world [e.g., *Baghdadi et al.*, 1997; *Koskinen et al.*, 1997; *Magagi and*

Bernier, 2003]. Multitemporal active microwave data can therefore be used to detect the onset and progression of snowmelt [e.g., *Haefner et al.*, 1993; *Rott and Nagler*, 1993; *Winebrenner et al.*, 1994; *Wunderle et al.*, 1994; *Wunderle and Saurer*, 1995; *Koskinen et al.*, 1997; *Smith et al.*, 1997; *Ramage and Isacks*, 1998; *Saurer et al.*, 1998; *Braun et al.*, 2000; *Rau et al.*, 2000; *Wismann*, 2000]. For example, time series of Seawinds (Ku-band) images from the QuikSCAT satellite have been utilized to map summer melt extent over Greenland (Plate 4).

It is difficult, however, to measure liquid water content of deep snowpacks by spaceborne SAR data because of the large number of parameters influencing backscatter coefficients, although polarimetric SAR appears to have some potential for this task. For instance, SIR-C data were used to infer liquid water content from polarimetric SAR imagery [*Shi and Dozier*, 1995]. Qualitative estimates of this variable could be successfully derived from ERS SAR [*Saurer et al.*, 1998], enabling determination of mean annual temperature (temperature in a 10-m-deep bore-hole). Quantitative data on liquid water content at the snow surface can be retrieved from passive microwave data [e.g., *Mätzler*, 1994].

3.3. Snow Water Equivalent

SWE mapping is one of the most important but insufficiently resolved tasks in remote sensing of snow cover. Most of the current applications are based on passive microwave data.

In Canada, a federal government program (Climate Research Branch, Meteorological Service of Canada) has been ongoing since the early 1980s. focusing on the development, validation, and application of passive microwave satellite data to derive information on SCA, SWE, and snowpack state (wet/dry) for Canadian regions in support of hydrological and climatological applications. *Goodison and Walker* [1995] provide a summary of the program, including a description of algorithm research and future thrusts. Algorithm development for SWE retrieval is focused on the major landscape regions within Canada, specifically the prairies, boreal forest, tundra, and high Arctic [*Walker and Goodison*, 1993; *Woo et al.*, 1995; *Goïta et al.*, 2003]. For example, weekly SWE maps for the prairie region in Canada are produced by utilizing SSM/I data [*Goodison and Walker*, 1995].

Since 1989, SWE maps for the prairie region of western Canada have been generated on a weekly basis from DMSP SSM/I data acquired in near real-time, using an algorithm that was empirically derived from airborne microwave radiometer data [*Goodison et al.*, 1986]. The prairie maps have been disseminated by fax machine and, more recently, by
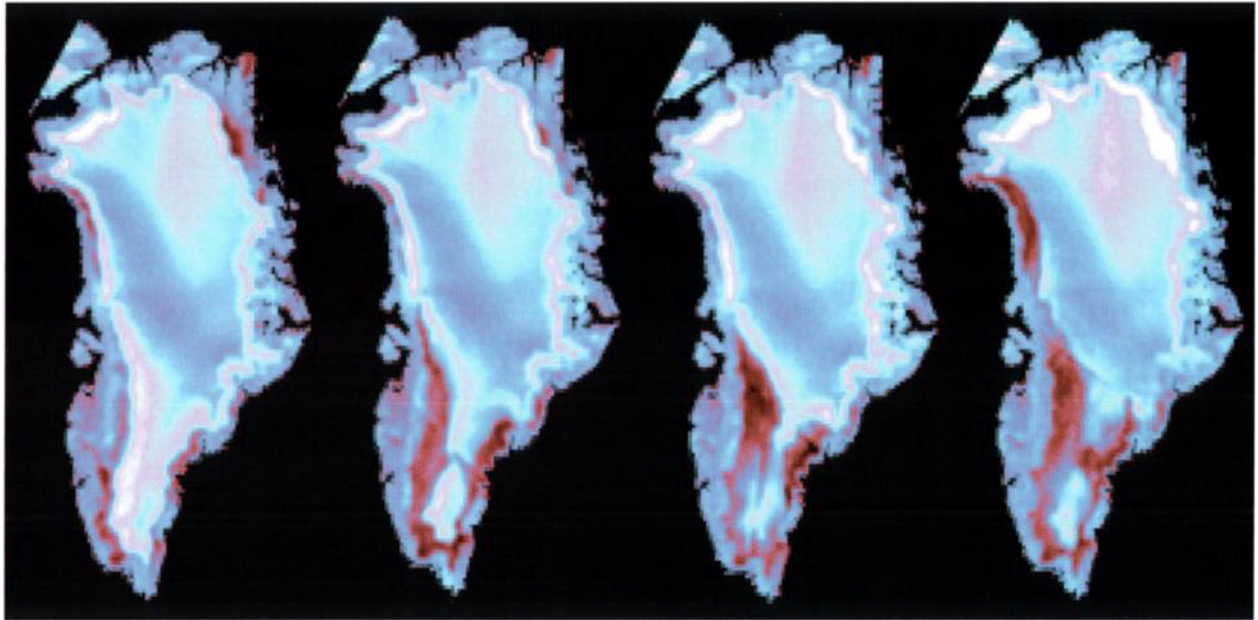
Plate 4. QuikSCAT backscatter images over Greenland for days 203, 208, 213, and 218 in 1999 (left to right). Blue and white colors indicate dry surfaces; red and black indicate wet snow surfaces experiencing melt (source: NASA/JPL 2003).
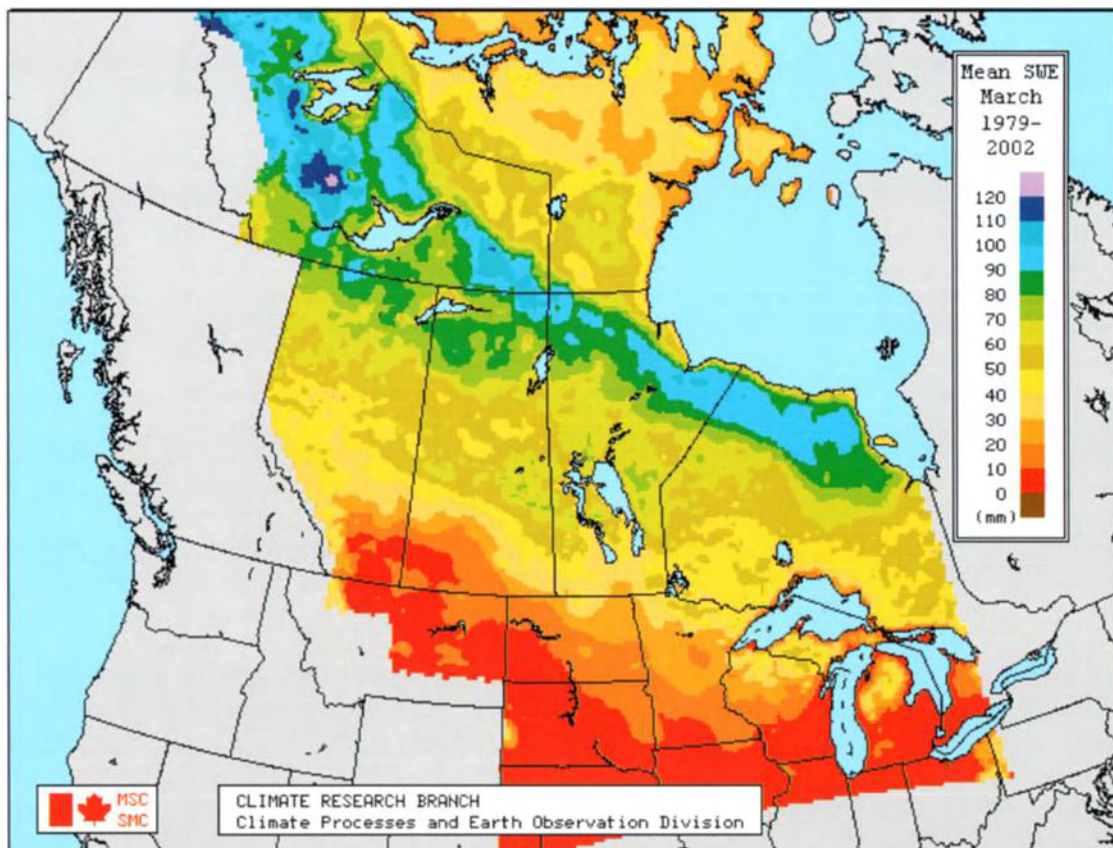
Plate 5. Distribution of snow water equivalent (March mean, 1979–2002) over a section of western Canada and the United States as derived from SMMR and SSM/I data using the retrieval algorithm suite of the Meteorological Service of Canada. Original provided by C. Derksen, Meteorological Service of Canada. Reproduced with the permission of the Minister of Public Works and Government Services Canada, 2005.

e-mail and internet to water-resource agencies and meteorological offices throughout the prairie region, where they are used to monitor snow-cover conditions, plan field surveys, and forecast spring water supply, including the potential for flooding or drought. The development of a wet-snow indicator [*Walker and Goodison*, 1993] overcomes a major limitation of the passive microwave technique by providing the capability to discriminate wet-snow areas from snow-free areas, hence enabling a more accurate retrieval of SCA during snowmelt conditions.

The presence of vegetation complicates the retrieval of snow-cover information with passive microwave techniques by attenuating the microwave emission from the underlying snow cover and contributing its own emission [e.g., *Hall et al.*, 1982; *Hallikainen*, 1984]. Algorithms developed for prairie environments generally underestimate SWE and snow depth when applied in forested regions. A series of algorithms for the boreal forest region of western Canada were recently derived from airborne microwave data acquired during the Boreal Ecosystem Atmosphere Study (BOREAS) winter field campaign in February 1994 [*Goita et al.*, 2003]. *Derksen et al.* [2003] present the operational SWE retrieval algorithm suite developed by the Meteorological Service of Canada for western Canada. In this approach, separate algorithms are used to retrieve SWE for open environments and for deciduous, coniferous, and sparse forest cover. Plate 5 shows a map of the mean (1979–2002) SWE for the month of March produced from the application of the algorithm suite to a time series of SMMR and SSM/I images.

Testing and validation of the passive microwave algorithms is in progress at several sites in western and northern Canada, including the Mackenzie River basin, where the spatial and temporal variability of snow cover is being investigated as part of the Mackenzie GEWEX Study (MAGS) [e.g., *Derksen et al.*, 2003]. *Chang et al.* [1997] used passive microwave data to infer SCA and SWE over forested areas in southern Saskatchewan during the BOREAS winter experiment. Aircraft data at 18, 37, and 92 GHz were used to reconfirm the relationship between SWE and brightness temperature. However, aircraft and satellite data did not correspond, probably due to a difference in footprint averaging. Aircraft results match the results of radiative-transfer calculations.

The development of snow-cover algorithms using active and passive microwave data for Canadian regions is one of the science objectives of CRYSYS. *Goodison et al.* [1999] provide an overview of the CRYSYS project, which involves researchers from 15 universities, 4 federal government institutions, and 1 nonprofit organization. Research at the Université du Québec (INRS-ETE) has resulted in a SWE algorithm for the Taiga region of Quebec using SSM/I data [*De Sève et al.*,

1997]; this region is characterized by deep snowpacks (SWE higher than 200 mm). The development of methods to estimate SWE from active microwave data, including ERS-1/2 and RADARSAT-1 SAR, is another research thrust at INRS-ETE. Despite the fact that dry snow is generally transparent at SAR frequencies, *Bernier and Fortin* [1998] describe a method of estimating SWE in a dry, shallow snow cover using SAR-derived estimates of thermal resistance. This method is also being tested on RADARSAT-1 SAR data for monitoring the spatial distribution of SWE in the La Grande River watershed in Northern Quebec, with the goal of operational implementation of RADARSAT-1 data in hydrological forecasting for hydroelectric applications [*Bernier et al.*, 1997]. Passive microwave studies of SWE have also been conducted in Norway as part of the SNOWTOOLS project [cf. *Standley*, 1997], and the data obtained were used as input in snowmelt-runoff modeling [*Engeset and Schjødt-Osmo*, 1997]. The development of improved global and regional SWE retrieval algorithms from passive microwave sensors continues to be an area of active research. Recent papers include, to name a few, *Tedesco et al.* [2004], *Koenig and Forster* [2004], and *Foster et al.* [2005].

Guneriussen [1997] has given an overview of the theoretical physical background of snowpack microwave backscattering. The author utilized ERS-1 SAR data for the determination of SWE in mountainous regions. *Mätzler et al.* [1997] used SIR-C/X-SAR data for the same purpose. Active microwave sensors offer the possibility to measure SWE directly, as demonstrated by *Guneriussen et al.* [2000b], even for dry snow in the Heimdalen area, Norway. Since snow refracts the radar wave, the phase of the radar signal changes in relation to SWE. However, these findings are preliminary and need more testing. Thus, operational methods are still under development. With passive microwaves, the spatial resolution has been a limiting factor [*Rango et al.*, 1989], particularly in mountainous regions. SCA mapping at high spatial resolutions may also be used to evaluate average SWE for whole drainage basins. As explained by *Martinec* [1985], SCA depletion curves can be converted to so-called modified depletion curves. To this effect, cumulative daily snowmelt depths replace the time axis on the *x*-axis. If SCA is plotted as a ratio of the whole area, the result is the average SWE. Intermittent summer snowfalls complicate derivation of modified depletion curves, because new snow is incorporated into the seasonal snow cover. To obtain the initial SWE, snowmelt depths for new snow must be eliminated from the cumulative snowmelt depths, resulting in a version of the modified depletion curve that excludes new snow.

The result is thus obtained after the end of the snowmelt season, which is a disadvantage for real-time runoff forecasts. However, a set of curves can be derived from different

years, and a proper curve for the current year can be identified by SCA monitoring as the snowmelt season progresses. In addition, results from modified curves can be compared with point measurements, which can help to select a suitable curve at the beginning of the snowmelt season. The derivation of modified depletion curves has been included in the computer program of the Snowmelt Runoff Model [*Martinec et al.*, 1998], enabling the evaluation of SWE in areas with adequate SCA mapping.

Although modified depletion curves that exclude new snow are used to evaluate SWE for current years, modified curves that include new snow (directly derived from conventional depletion curves) can serve to predict future snow conditions for various climate scenarios. If, for example, a modified curve indicates that SCA is reduced to 40% by a cumulative snowmelt depth of 50 cm, one can compute at which earlier date this situation would occur in a warmer climate. From conventional depletion curves shifted in time accordingly, modified depletion curves and future SWE can be evaluated, as demonstrated by *Seidel et al.* [1998] for the Rhine–Felsberg basin, and also by changed SWE values for various hypothetical combinations of increased temperatures and precipitation.

The aerial gamma method of SWE surveying was developed in the USSR in the 1960s and has been used operationally in the USSR [*Vershinina*, 1985], Sweden [*Bergstrom and Brandt*, 1985], Norway [*Tollan*, 1979], Finland [*Kuittinen*, 1986], Canada [*Carroll et al.*, 1983], and the United States [*Carroll*, 1987; *Peck et al.*, 1980]. Radioactive pollution from the Chernobyl disaster in 1986 negatively influenced operational airborne gamma snow survey programs in Scandinavian countries, such as Norway [*Killingtveit*, 1994]. The U.S. National Weather Service (NWS) operates one of the largest airborne gamma snow survey programs in support of operational hydrological monitoring. Over 1,500 flight lines have been established in the United States and Canada, and each winter SWE measurements are collected along many of these lines [*Carroll*, 1990]. After each airborne gamma survey, data are transmitted to NOHRSC for processing, archiving, and distribution to forecast offices and other government agencies. The NOHRSC website (www. nohrsc.nws.gov) provides a description of the NWS airborne gamma snow survey program, locations of flight lines, and access to data products.

3.4. Snow Reflectance

SCA mapping by optical remote sensing systems is based on the particular spectral reflectance characteristics of snow. However, many of the methods used for this task are not based on quantitative spectral reflectance data. Band saturation, not a serious problem in SCA mapping, is a significant drawback for spectral reflectance measurements of snow by remote sensing instruments.

Landsat-5 TM data have been used by several authors to derive spectral reflectance of snow [e.g., *Dozier*, 1984, 1989; *Hall et al.*, 1989, 1992; *Duguay and LeDrew*, 1991, 1992; *Winther*, 1992, 1993, 1994; *Parlow*, 1996a; *Scherer and Brun*, 1997; *Scherer*, 1998, *Winther et al.*, 1999, 2001]. Studies were carried out both in polar and alpine regions. Some of these and other studies [e.g., *Winther*, 1994; *Greuell and de Ruyter de Wildt*, 1999] also deal with bidirectional reflectance and anisotropic reflectance characteristics of snow, a topic that has been gaining attention in recent years.

In a study on the estimation of albedo of snow and glacier ice in the Wrangell Mountains of Alaska from Landsat TM data and field spectrometer measurements, *Hall et al.* [1989] showed that reflectance integrated over the full solar spectrum is considerably lower (0.788) than reflectance integrated over the visible part of the spectrum (0.951). A similar study was undertaken by *Winther et al.* [1999] in Svalbard. They found that the relationship between narrow-band albedo in the VIS and the solar albedo varied considerably through the melt season, due to changing spectral characteristics of the snowpack. This is significant because some climate models use only albedo from the visible part of the spectrum as input, thus overestimating solar albedo [*Winther et al.*, 2001]. *Winther* [1993] presents a comprehensive study on solar albedo retrieval from Landsat TM imagery. Besides his results obtained from Landsat-5 TM data, he reviews the general approaches used in determining reflectance from space as well as dependencies of reflective properties on other snow variables such as grain size and depth. Several authors [e.g., *Duguay and LeDrew*, 1992; *Duguay*, 1993b, 1995; *Scherer and Brun*, 1997; *Sandmeier and Itten*, 1997; *Scherer*, 1998] have demonstrated the necessity of utilizing DEM data for physically based modeling of topographic effects in optical satellite data analysis for SCA. The contribution of incoming solar radiation from adjacent pixels may be as large as 250 W·m^{-2} for highly reflective surfaces in complex terrain [*Scherer*, 1998], which causes serious problems in shadow regions where reflectance values, e.g., those measured by Landsat TM, are showing large errors.

NOAA AVHRR has also been used for determining snow albedo. Use of the AVHRR, with its 1100-m resolution, is acceptable for large ice sheets like Greenland, where large areas of similar snow conditions exist. On smaller ice masses and over seasonally snow-covered ground, mixed pixels occur frequently, containing several surface types within one pixel, which makes interpretation difficult.

Haefliger et al. [1993], *Knap and Oerlemans* [1996], and *Stroeve et al.* [1996] present approaches to calculate narrow-

band ground reflectance on the Greenland ice sheet with AVHRR. Differences with ground measurements (over- or underestimation) are generally between 2% and 14%. *Knap and Oerlemans* [1996] as well as *Stroeve et al.* [1996] find that errors due to atmospheric correction or anisotropic reflection are too small to account for this deviation; all three studies assume sensor drift and inaccurate calibration constants to be the main cause of error. More recently, *Greuell and Oerlemans* [2004] have proposed a suite of equations for narrow-to-broad-band (NTB) albedo conversion for glacier ice and snow for four types of satellite sensors: TM, AVHRR, MODIS, and MISR. They show that the calculated albedo values correspond well to albedo measurements made over Greenland and Iceland (root-mean-square differences of about 0.016). *Stroeve et al.* [2005], assessing the accuracy of the MODIS 16-day albedo product (MOD43) for snow, report that this MODIS product retrieves snow albedo with an average root-mean-square-error (RMSE) of ±0.07 compared with ground-based albedo measurements taken on the Greenland ice sheet. A surface albedo image of Greenland from the MODIS/Terra Snow Cover Daily L3 Global 500m Grid data product (used to produce the 16-day composite product) is presented in Plate 6.

3.5. Snow Grain Size

A snowpack is composed of layers of different types of snow. Each layer is more or less homogeneous, having been formed from a single snowfall, occurring under different meteorological conditions. Typically, these layers consist of snow crystals that metamorphose over time [cf. *LaChapelle*, 1969]. *Sommerfeld and LaChapelle* [1970] presented a snow classification that distinguishes two basic types of metamorphism: temperature-gradient (TG) metamorphism and equitemperature (ET) metamorphism. In the case of ET metamorphism, melt–freeze processes cause the crystals to become more rounded. As soon as liquid water is present, snow metamorphism leads to rapid changes of the snow crystals and to the formation of wet grain clusters [cf. *Colbeck*, 1986]. This is associated with an increasing density of the snowpack. However, when the temperature gradient in the snowpack is large, depth-hoar crystals are formed. Depth hoar is the most coarse-grained type of snow that can form without the presence of the liquid phase. Snowpack layers containing depth hoar may have a density of 200 to 300 kg·m^{-3}. Fully developed depth-hoar crystals at the base of a snowpack are often 1 cm in diameter; small snow crystals may have grain radii of about 50 μm.

Basic research on optical remote sensing of snow reflectance and grain size was performed by *Wiscombe and Warren* [1980] and *Dozier et al.* [1981]. Since then, Landsat-5 TM and hyperspectral AVIRIS data have been used for measuring

snow grain size [e.g., *Nolin and Dozier*, 1993, 2000; *Fily et al.*, 1997; *Painter et al.*, 1998, 2003; *Dozier and Painter*, 2004] (Plate 7). However, only the top-most snow layers are sensed by VNIR sensors, whereas microwave systems can also provide information on deeper snow layers, since grain size directly affects microwave brightness temperatures [*Hall et al.*, 1986; *Armstrong et al.*, 1993; *Josberger et al.*, 1995]. For example, using a two-layer radiative-transfer model, *Hall et al.* [1986] showed that depth-hoar crystals at the base of the snowpack in the Alaskan Arctic are not as effective at scattering the microwave signal (in this case at 37 GHz) as are comparable-sized spherical crystals. However, the large depth-hoar crystals cause more microwave scattering than the smaller crystals typically found at and near the surface of a snowpack. *Hall et al.* [1986] and *Sturm et al.* [1993] also showed that as the thickness of the depth-hoar layer increases from the coastal to the inland areas in northern Alaska, the microwave brightness temperature decreases in response to the greater scattering that results from the thicker layers containing depth-hoar crystals.

3.6. Snow Depth

Passive microwave data have been used to derive snow depth from space [e.g., *Rango et al.*, 1979; *Schanda et al.*, 1983; *Foster et al.*, 1984, 1991; *Chang et al.*, 1987; *Goodison et al.*, 1990]. In general, increasing snow depth results in decreasing brightness temperature due to enhanced scattering. The scattering information comes largely from the 37 GHz frequency. Both SMMR and SSM/I data have been utilized for snow-depth retrieval on regional and global scales. Airborne passive microwave systems appropriate for validating the retrieval algorithms were flown, e.g., in Alaska [*Hall et al.*, 1991], in order to compare the microwave results with field data.

Only a few studies have compared field data with satellite-based snow depth estimates [e.g., *Tait and Armstrong*, 1996; *Papa et al.*, 2002; *Kelly and Chang*, 2003; *Kelly et al.*, 2003; *Grippa et al.*, 2004]. It is generally acknowledged that forest cover and snow pack physical properties (e.g., snow crystal size) are the two main sources of errors in passive microwave snow depth retrievals. Algorithms that consider fractional forest cover information or the time-evolving nature of snow cover (i.e., dynamic algorithms) have shown to improve estimates of snow depth and SWE from SMMR, SSM/I, and AMSR-E [e.g., *Kelly and Chang*, 2003; *Kelly et al.*, 2003; *Grippa et al.*, 2004; Foster *et al.*, 2005] (Plate 8).

3.7. Snow Temperature

TIR sensors have been used to measure snow surface temperature as well as emitted long-wave radiation, an important
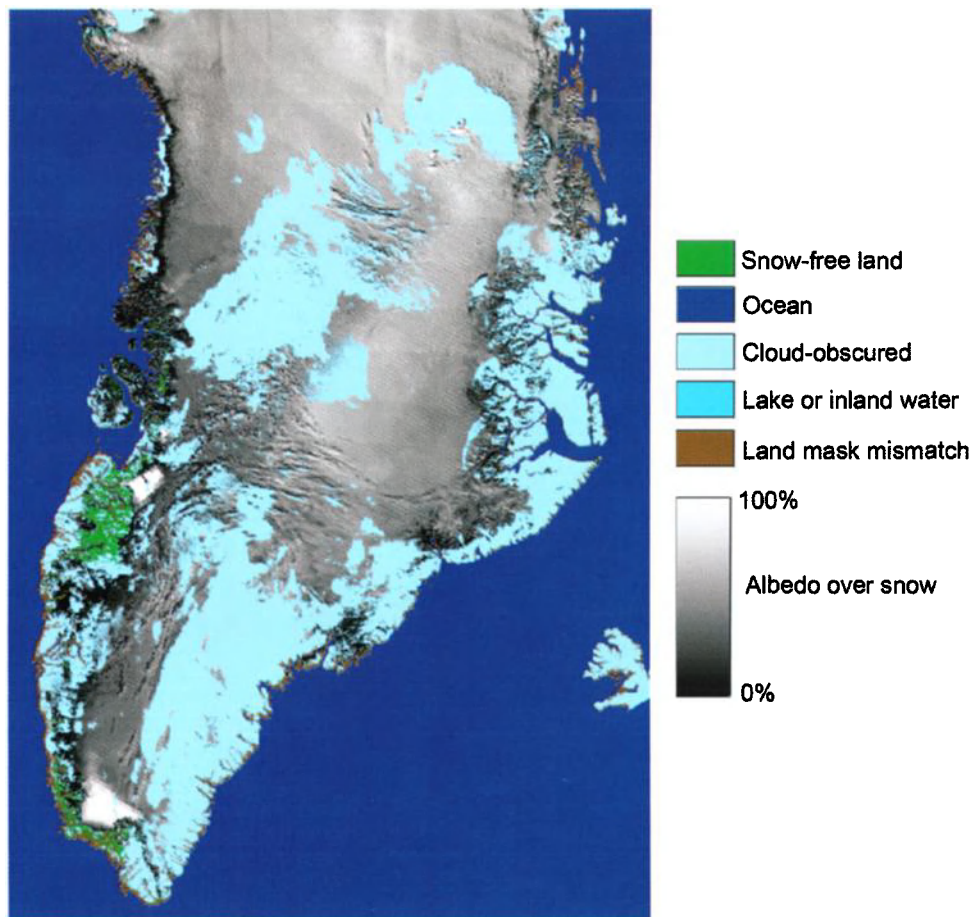
Plate 6. Surface albedo image of Greenland created from a mosaic of eight input tiles of the "Day_ Tile_Snow_Albedo" field of the MODIS/Terra Snow Cover Daily L3 Global 500m Grid data set from May 15, 2004 (source: NSIDC, http://nsidc.org/data/modis/gallery/index.html).

April 5, 1994

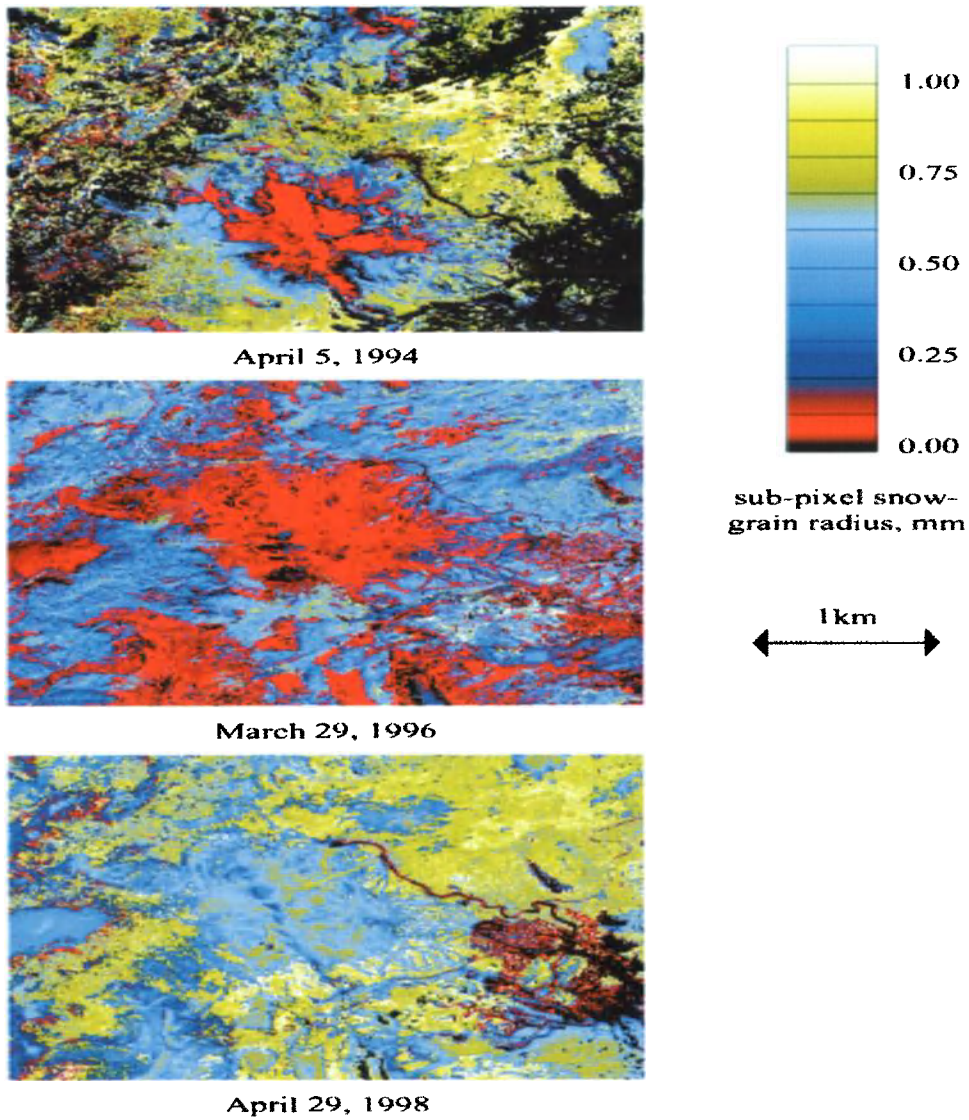March 29, 1996

April 29, 1998

Plate 7. Snow mean grain radii estimated for three AVIRIS acquisitions near Mammoth Mountain, Sierra Nevada, for a wide range of snow conditions. An accuracy of 0.048 mm was achieved when comparing AVIRIS grain-size estimates with stereological analysis of snow samples. After *Dozier and Painter* [2004].
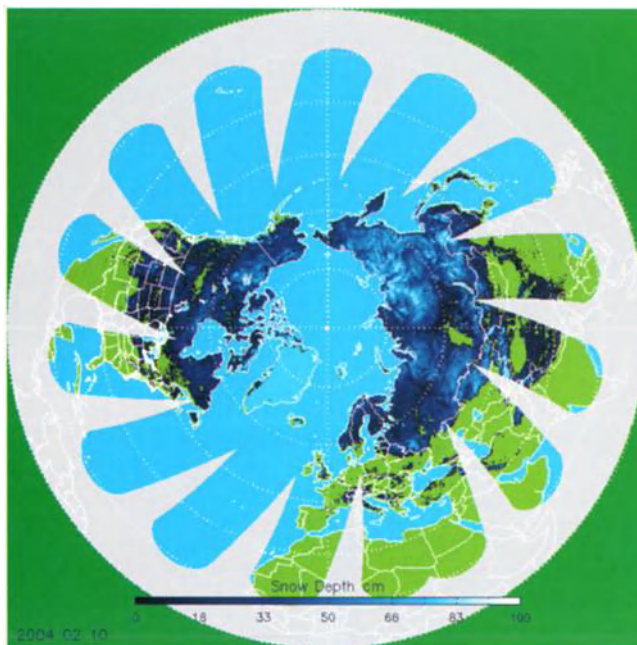
Plate 8. Snow depth derived from AMSR-E on February 10, 2004. Original provided by R. Kelly, NASA, Goddard Space Flight Center, Greenbelt, Maryland, and reprinted with his kind permission.
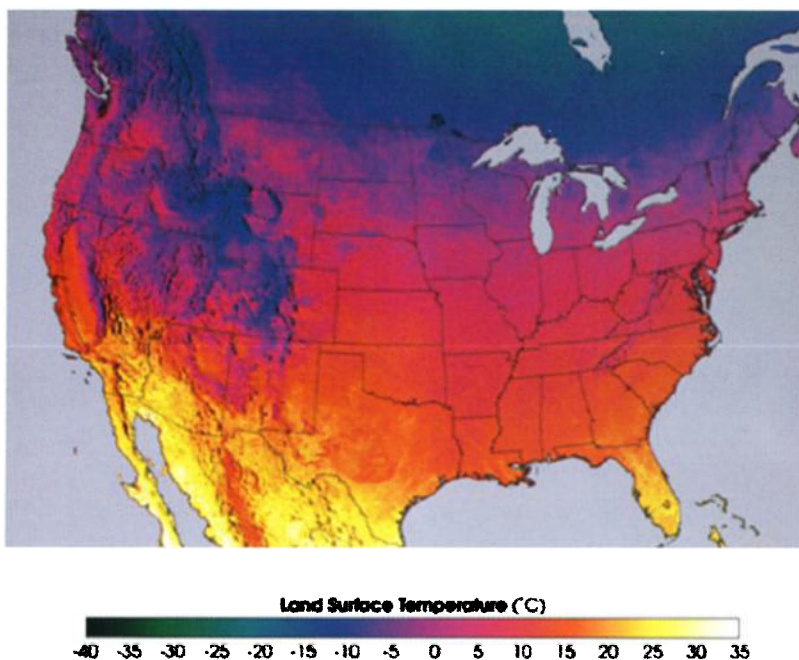

Plate 9. Average winter land surface temperature (December 2001 to February 2002) derived from MODIS/Terra Land Surface Temperature/Emissivity Level 3 image products over the continental U.S. and parts of Canada and Mexico. Lower land surface temperatures correspond to snow-covered areas of the mountainous and northernmost regions.

component of the surface radiation budget. Atmospheric correction procedures in the TIR region of the spectrum as well as detailed calibration data are important for accurate measurements of snow surface temperature. Night-time TIR data are often subject to errors from the presence of clouds since cloud masks are usually derived from SWIR bands. Although passive microwave systems are also able to measure snow surface temperature, the resulting temperature error is generally larger (2 to 4 K) than for accurate TIR data (0.5 to 1.5 K).

Landsat TM band 6 has been used for surface temperature retrieval by a number of authors, e.g., *Orheim and Lucchitta* [1988] and *Pattyn and Decleir* [1993]. Comparison to ground measurements show quite large deviations, usually an over- or underestimation of up to 10 K. Both *Orheim and Lucchitta* [1988] and *Pattyn and Decleir* [1993] conclude that Landsat TM band 6 "faithfully" reproduces relative temperature variations, but not absolute temperature. High-resolution surface temperature data from Landsat-5 TM band 6 is of particular interest for small drainage basins or in mountainous regions. For example, *Parlow* [1996a] used multitemporal Landsat-5 TM TIR data to compute terrestrial long-wave emission, which was then used to derive spatially distributed data on net radiation for a small drainage basin in NW-Spitsbergen.

NOAA AVHRR TIR data are widely used for surface temperature retrieval including snow on a regional scale. *Key and Haefliger* [1992] developed an algorithm for surface temperature retrieval, which relates brightness temperature from AVHRR bands 4 and 5 to surface temperature. The accuracy has been determined to be between 1 and 4 K [*Key et al.*, 1997]. A refined version, presented in *Key et al.* [1997] for AVHRR and the ATSR, finds an agreement with ground measurements between 0.3 and 2.1 K, where the larger errors are attributed to spatial variation within the low-resolution pixel. *Bamber and Harris* [1994] and *Stroeve et al.* [1996], using the dual-angle view of ATSR for surface temperature retrieval for the Greenland Ice Sheet, report an accuracy of better than 0.2 K for their algorithms. ATSR looks at the surface in both vertically and inclined forward directions, which allows much improved atmospheric correction with increased accuracy. The authors state that this method is less sensitive to changing atmospheric constituents than split-window techniques used, e.g., for AVHRR TIR data, which may be of particular interest for polar regions where ancillary atmosphere data sets are rare and atmospheric conditions may vary largely. Land surface temperature (LST) is also one of the standard products from MODIS/Terra and Aqua. In Plate 9, MODIS LST data for the period between December 1, 2001, and February 28, 2002, were combined to create a 3-month winter composite product over an area encompassing the continental United States as well as northern Mexico and southern Canada. Based on a comparison with in situ LSTs for a variety of cover types, including one snow-covered site, *Wan et al.* [2002] conclude that MODIS-derived LSTs have an accuracy of ±1 K in the 263–322 K range.

Given that the upper boundary of the wet-snow facies [cf. *Winther et al.*, this volume] is roughly coincident with the 0°C isotherm, SAR-images are as well effective for estimating the spatial air-temperature distribution in remote areas. In addition, as SAR data facilitate direct mapping of wet snow, the spatial extent of areas where snow temperature is near the freezing point can be derived [e.g., *Rau et al.*, 2000]. This is of special interest for energy balance studies, snowmelt runoff modeling, calibration of meteorological models and climate monitoring purposes.

4. UNRESOLVED ISSUES AND FUTURE RESEARCH NEEDS

Remote sensing is an important tool for many different scientific and practical applications related to snow cover. Thus, user requirements on snow data and accuracy are rather diverse. Unfortunately, not all of the snow variables can be retrieved with sufficient accuracy at the spatial and temporal scales provided by current spaceborne systems. This holds true particularly for SWE, which is one of the most important snow variables in hydrology. Future research and technological developments with respect to remote sensing of snow cover from space should set emphasis on SWE determination at higher spatial resolutions without decreasing temporal resolution. Multiscale approaches by different sensors on the same satellite platform will be highly interesting, since downscaling approaches for different snow properties may be tested on optimally suited data sets.

The next generation of satellites will provide a large variety of new remote sensing techniques concerning wavelengths, bandwidths, total number of bands, polarization modes, pointing modes, multiangle views, and other features of optical, thermal, and microwave sensors. Demonstration studies will be necessary to show how these new features could be utilized for snow research, particularly through data fusion techniques. Rigorous validation and error analysis of satellite-derived snow data with high-accuracy field measurements is a prerequisite of such investigations, an aspect that was not given as much attention as necessary for sensors with low spatial resolution. Accurate field measurements of snow variables, which should be carried out contemporaneously with image acquisition, partly require new or improved instruments and data analysis techniques.

More and more DEM data sets are becoming available for integrative remote sensing analysis. However, standard

approaches (e.g., for correcting topographic influences on satellite data) are not available for SCAs. Although numerical models like MODTRAN or 6S have become widely used tools for atmospheric correction of optical data, this is not the case for DEM processing. Unfortunately, topographic and atmospheric processes are nonlinearly coupled (e.g., multiple scattering of radiation from adjacent pixels), thus drastically complicating retrieval of snow variables in mountainous regions, since the effects cannot be corrected separately.

Not only topography but also different land-cover types strongly affect retrieval of snow variables by remote sensing. Studies focusing on this aspect are important to achieve a better understanding of the complex radiation interactions between snow and ground or vegetation. In particular, forested areas need to be investigated more thoroughly, since forests show the most pronounced effects, and are one of the most important landcover types of northern regions. Digital landcover data sets of appropriate spatial scales and accuracy should be included in remote sensing analyses in the same way as DEM data sets.

Development of physically based, spatially distributed snow models for local- and regional-scale studies should be enforced in the future to overcome the limitations of empirical or conceptual models widely used today. On the one hand, such models should be able to utilize remote sensing data as input to drive or validate the models. For instance, a physically based snowmelt runoff model could be initialized by spatially distributed SWE derived from remote sensing data. On the other hand, analysis of remote sensing data has to be assisted by such models by providing the parameters needed for the retrieval of snow variables. An example is a fully distributed radiative-transfer model that includes BRDF and adjacency effects to be used for atmospheric correction of optical satellite data, particularly for areas of complex terrain.

REFERENCES

Albright, T., T. H. Painter, D.A. Roberts, J. Shi, J. Dozier, and E. Fielding, Classification of surface types using SIR-C/X-SAR, Mount Everest area, Tibet, *J. Geophys. Res.*, *103*, 25823–25837, 1998.

Andersen, T., Operational snow mapping by satellites, hydrological aspects of alpine and high-mountain areas, in *Hydrological Aspects of Alpine and High Mountain Areas*, edited by J.W. Glen, pp. 149–154, IAHS Publ. 138, 1982.

Anderson, E. A., A point energy mass balance model of snow cover, Ph.D. thesis, Stanford University, U.S.A., 1975.

Armstrong, R., A. Chang, A. Rango, and E. Josberger, Snow depths and grain size relationships with relevance for passive microwave studies, *Ann. Glaciol.*, *17*, 171–176, 1993.

Baghdadi, N., Y. Gauthier, and M. Bernier, Capability of multi-temporal ERS-1 SAR data for wet-snow mapping, *Remote Sens. Environ.*, *60*, 174–189, 1997.

Bamber, J.L., and A. R. Harris, The atmospheric correction for satellite infrared radiometer data in Polar Regions, *Geophys. Res. Lett.*, *21*, 2111–2114, 1994.

Bergstrom, S., and M. Brandt, Snow mapping and hydrological forecasting by airborne gamma-ray spectrometry in northern Sweden, in *Hydrological Application of Remote Sensing and Remote Data Transmission*, pp. 421–428, IAHS Publ. 145, 1985.

Bernier, M., and J.-P. Fortin, The potential of time series of C-Band SAR data to monitor dry and shallow snow cover, *IEEE Trans. Geosci. Remote Sens.*, *36*, 229–243, 1998.

Bernier, M., J.P. Fortin, Y. Gauthier, N. Baghdadi, R. Gauthier, D. Tremblay, and P. Vincent, Suivi du couvert nival à l'aide des donnés de RADARSAT, in *Proc. GER '97 (International Symposium: Geomatics in the Era of Radarsat)*, Ottawa, Canada, 1997.

Bernier, P. Y., Microwave remote sensing of snowpack properties: potential and limitations, *Nordic Hydrol.*, *18*, 1–20, 1987.

Bindschadler, R., Monitoring ice sheet behaviour from space, *Rev. Geophys.*, *36*, 79–104, 1998.

Bourdelles, B., and M. Fily, Snow grain-size determination from Landsat imagery over Terre Adélie, Antarctica, *Ann. Glaciol.*, *17*, 86–92, 1993.

Bowley, C. J., and J. C. Barnes, Satellite snow mapping techniques with emphasis on the use of Landsat, in *Satellite Hydrology*, pp. 158–164, American Water Resources Association, 1979.

Braun, M., F. Rau, H. Saurer, and H. Gossmann, Development of radar glacier zones on the King George Island ice cap, Antarctica, during the austral summer 1996/97 as observed in ERS-2 SAR-data, *Ann. Glaciol.*, *31*, 357–363, 2000.

Brest, C. L., and S. N. Goward, Deriving surface albedo measurements from narrow band satellite data, *Int. J. Remote Sens.*, *8*, 351–367, 1987.

Brun, E., E. Martin, V. Simon, C. Gendre, and C. Coleou, An energy and mass model of snow cover suitable for operational avalanche forecasting, *J. Glaciol.*, *35*, 333–342, 1989.

Carroll, S. S., and T. R. Carroll, Effect of forest biomass on airborne snow water equivalent estimates obtained by measuring terrestrial gamma radiation, *Remote Sens. Environ.*, *27*, 313–320, 1989.

Carroll, T. R., Operational remote sensing of snow water equivalent and soil moisture in the United States using natural terrestrial gamma radiation, in *Large Scale Effects of Seasonal Snow Cover*, pp. 213–223, IAHS Publ. 166, 1987.

Carroll, T. R., Airborne and satellite data used to map snow cover operationally in the U.S. and Canada, in *Proc. Int. Symposium on Remote Sensing and Water Resources*, pp. 147–155, Enschede, The Netherlands, 1990.

Carroll, T. R., J. E. Glynn, and B. E. Goodison, A comparison of U.S. and Canadian airborne gamma radiation snow water

equivalent measurements, in *Proc 51st Annual Western Snow Conference*, pp. 27–37, Vancouver, Washington USA, 1983.

Chandrasekar, S., *Radiative transfer*, Dover, New York, 1960.

Chang, A. T. C., J. L. Foster, and D.K. Hall, Nimbus-7 SMMR derived global snow cover parameters, *Ann. Glaciol.*, *9*, 39–44, 1987.

Chang, A. T. C., J. L. Foster, D. K. Hall, B. E. Goodison, A. E. Walker, J. R. Metcalfe, and A. Harby, Snow parameters derived from microwave measurements during the BOREAS winter field campaign, *J. Geophys. Res.*, *102*, 29,663–29,671, 1997.

Chang, A. T. C., P. Gloersen, and T. Schmugge, Microwave emission from snow and glacier ice, *J. Glaciol.*, *16*, 23–39, 1976.

Chang, A. T. C., and A. Rango, *Algorithm theoretical basis document (ATBD) for the AMSR snow water equivalent algorithm*, NASA EOS Project Science Office Document (http://eospso.gsfc.nasa.gov/ftp_ATBD/REVIEW/AMSR/atbd-amsr-snow.pdf), 2000.

Choudhury, B. J., and A. T. C. Chang, Two-stream theory of reflectance of snow, *IEEE Trans. Geosci. Remote Sens.*, *17*, 63–68, 1979.

Cline, D., and T. Caroll, *Operational automated production of daily, high-resolution, cloud-free snow cover maps of the continental U.S.*, U.S. NWS NOHRSC Report (www.nohrsc.nws.gov/html/papers/gcip98/gcip98.htm), 1998.

Colbeck, S. C., Classification of seasonal snow cover crystals, *Water Resour. Res.*, *22*, 59–70, 1986.

Dankers, R., and S. M. De Jong, Monitoring snow-cover dynamics in northern Fennoscandia with SPOT VEGETATION images, *Int. J. Remote Sens.*, *25*, 2933–2949, 2004.

Derksen, C., and A. Walker, Evaluating spaceborne passive microwave snow water equivalent retrievals across the Canadian northern boreal – tundra ecotone, in *Proc. of the Int. Geoscience and Remote Sensing Symposium*, 2004.

Derksen, C., A. Walker, and B. Goodison, A comparison of 18 winter seasons of in situ and passive microwave-derived snow water equivalent estimates in Western Canada, *Remote Sens. Environ.*, *88*, 271–282, 2003.

De Sève, D., M. Bernier, J.-P. Fortin, and A. Walker, Preliminary analysis of snow microwave radiometry using the SSM/I passive-microwave data: the case of La Grande River watershed (Quebec), *Ann. Glaciol.*, *25*, 353–361, 1997.

Donald, J. R.; E. D. Soulis; F. Seglenieks, and N. Kouwen, Snow depth estimates for shallow snowpacks from GOES visible imagery, in *Proc. Eastern Snow Conference, 48th Annual Meeting*, pp. 149–161, 1991.

Dozier, J., Snow reflectance from Landsat-4 Thematic Mapper, *IEEE Trans. Geosci. Remote Sens.*, *22*, 323–328, 1984.

Dozier, J., Remote sensing of snow in visible and near-infrared wavelengths, in *Theory and Applications of Optical Remote Sensing*, edited by G. Asrar, pp. 527–547, John Wiley & Sons, 1989.

Dozier, J., and D. Marks, Snow mapping and classification from Landsat TM data, *Ann. Glaciol.*, *9*, 97–103, 1987.

Dozier, J., and T. H. Painter, Multispectral and hyperspectral remote sensing of alpine snow properties, *Annu. Rev. Earth Planet. Sci.*, *32*, 465–494, 2004.

Dozier, J., S. R. Schneider, and D.F. McGinnis, Effect of grain size and snowpack water equivalence on visible and near-

infrared satellite observations of snow, *Water Resour. Res.*, *17*, 1213–1221, 1981.

Dozier, J., and S. G. Warren, Effect of viewing angle on the infrared brightness temperature of snow, *Water Resour. Res*, *18*, 1424–1434, 1982.

Duguay, C. R., Radiation modelling in mountainous terrain: review and status. *Mountain Res. Develop.*, *13(4)*, 339–357, 1993a.

Duguay, C. R., Modelling the radiation budget of alpine snowfields with remotely sensed data: model formulation and validation. *Ann. Glaciol*, *17*, 288–294, 1993b

Duguay, C. R., An approach to the estimation of surface net radiation in mountain areas using remotely sensed and digital terrain data. *Theor. and Appl. Clim.*, *52(1-2)*, 55–68, 1995.

Duguay, C. R., and E. F. LeDrew, Mapping surface albedo in the east slope of the Colorado Front Range with Landsat-5 Thematic Mapper, *Arct Alp. Res.*, *23(2)*, 213–223, 1991.

Duguay, C. R., and E. F. LeDrew, Estimating surface reflectance and albedo over rugged terrain from Landsat-5 Thematic Mapper, *Photogram. Engin. Rem. Sens.*, *58(5)*, 551–558, 1992.

Ehrler, C., K. Seidel, and J. Martinec, Advanced analysis of the snow cover based on satellite remote sensing for the assessment of water resources, in *5th Scientific Assembly of the International Association of Hydrological Sciences IAHS*, edited by M.F. Baumgartner, G.A. Schultz, and A.I. Johnson, pp. 93–101, Rabat, Morocco, 1997.

Engeset, R., and O. Schjødt-Osmo, Retrieval of snow information using passive microwave data in Norway, in *Proc. Remote Sensing of Land Ice and Snow*, Freiburg, Germany, 1997.

Fahnestock, M. A., R. A. Bindschadler, R. Kwok, and K. C. Jezek, Greenland ice sheet surface properties and ice flow from ERS-1 SAR imagery, *Science*, *262*, 1530–1534, 1993.

Fily, M., B. Bourdelles, J. P. Dedieu, and C. Sergent, Comparison of in situ and Landsat Thematic Mapper derived snow grain characteristics in the Alps, *Remote Sens. Environ.*, *59*, 452–460, 1997.

Fily, M., J. P. Dedieu, and Y. Durand, Comparison between the results of a snow metamorphism model and remote sensing derived snow parameters in the Alps, *Remote Sens. Environ.*, *68*, 254–263, 1999.

Foster, J. L., The significance of the date of snow disappearance on the Arctic tundra as a possible indicator of climate change, *Arct. Alp. Res.*, *23*, 60–70, 1989.

Foster, J. L., A. T. C. Chang, D. K. Hall, and A. Rango, Derivation of snow water equivalent in boreal forests using microwave radiometry, *Arctic*, *44*, 147–152, 1991.

Foster, J. L., D. K. Hall, and A. T. C. Chang, Remote sensing of snow, *EOS*, *68*, 682–684, 1987.

Foster, J. L., D. K. Hall, A. T. C. Chang, and A. Rango, An overview of passive microwave snow research and results, *Rev. Geophys.*, *22*, 195–208, 1984.

Foster, J. L., A. Rango, D. K. Hall, A. T. C. Chang, L. J. Allison, and B.C. Diesen, Snowpack monitoring in North America and Eurasia using passive microwave satellite data., *Remote Sens. Environ.*, *10*, 285–298, 1980.

Foster, J. L., C. Sun, J. P., Walker, R. Kelly, A. Chang, J. Dong, and H. Powell, Quantifying the uncertainty in passive microwave

snow water equivalent observations, *Remote Sens. Environ.*, *94*, 187–203, 2005.

Galantowicz, J. F., and A. W. England, Seasonal snowpack radio-brightness interpretation using a SVAT-linked emission model, *J. Geophys. Res.*, *102*(D18), 21933–21946, 1997.

Gangkofner, U., Multitemporal snow classification with TM data, in *Proc. Workshop on Earthnet Pilot Project on Landsat Thematic Mapper Applications*, pp. 13–21, Italy, 1989.

Garstka, W. U., L. D. Love, B. C. Goodell, and F.A. Bertle, Factors affecting snowmelt and streamflow, *Frazer Experimental Forest*, *51*, 1958.

Glynn, J. E., T. R. Carroll, P. B. Holmann, and R. L. Grasty, An airborne gamma ray snow survey of a forest covered area with a deep snowpack, *Remote Sens. Environ.*, *26*, 149–160, 1988.

Goita K., A. E. Walker, and B. E. Goodison, Algorithm development for the estimation of snow water equivalent in the boreal forest using passive microwave data. *Int. J. Remote Sens* , *24*, 1097–1102, 2003.

Goodison, B. E., R. D. Brown, and R. G. Crane, Cryospheric systems, in *Earth Observing System (EOS) Science Plan, Chapter 6*, NASA, 1999.

Goodison, B. E., I. Rubinstein, F. W. Thirkettle, and E. J. Langham, Determination of snow water equivalent on the Canadian prairies using microwave radiometry, in *Modelling Snowmelt Induced Processes*, pp. 163–173, 1986.

Goodison, B. E., and A. E. Walker, Canadian development and use of snow cover information from passive microwave satellite data, in *Passive Microwave Remote Sensing of Land-Atmosphere Interactions*, edited by B.J. Choudhury, Y.H. Kerr, E.G. Njoku, and P. Pampaloni, pp. 245–262, Utrecht, 1995.

Goodison, B., A. E. Walker, and F. W. Thirkettle, Determination of snow cover on the Canadian prairies using microwave data, in *Proc. Int. Symposium on Remote Sensing and Water Resources*, pp. 127–136, Enschede, The Netherlands, 1990.

Green, R. O., and J. Dozier, Retrieval of surface snow grain size and melt water from AVIRIS spectra, in *Summaries of the Sixth Annual JPL Airborne Earth Science Workshop*, pp. 127–133, JPL Publ., 1996.

Greuell, W. and M. de Ruyter de Wildt, Anisotropic reflection by melting glacier ice: measurements and parameterizations in Landsat TM bands 2 and 4, *Remote Sens. Environ.*, *70*, 265–277, 1999.

Greuell, W., and J. Oerlemans, Narrow-to-broadband albedo conversion for glacier ice and snow: equations based on modeling and ranges of validity of the equations, *Remote Sens. Environ.*, *89*, 95–105, 2004.

Grippa, M., N. Mognard, T. Le Toan, and E. G. Josberger, Siberia snow depth climatology derived from SSM/I data using a combined dynamic and static algorithm, *Remote Sens. Environ.*, *93*, 30–41, 2004.

Grody, N., Classification of snow cover and precipitation using the special sensor microwave imager, *J. Geophys. Res.*, *94*, 7423–7435, 1991.

Grody, N. C., and A. N. Basist, Global identification of snow cover using SSM/I measurements, *IEEE Trans. Geosci. Remote Sens.*, *34*, 237–249, 1996.

Groisman, P. Y., T. R. Karl, and R. W. Knight, Observed impact of snow cover on the heat balance and the rise of continental spring temperatures, *Science*, *263*, 198-200, 1994.

Gubler, H., and C. Hauck, *Preliminary measurements of BTS using a microwave radiometer*, PACE Project WP 2, 1998.

Guneriussen, T., Backscattering properties of wet snow cover derived from DEM corrected ERS-1 SAR data, *Int. J. Remote Sens.*, *18*, 375–392, 1997.

Guneriussen, T., Snow characteristics in mountainous areas as observed with synthetic aperture radar (SAR) instruments, Ph.D. thesis, Univ. of Tromsø, 1998.

Guneriussen, T., P. L. Bjerke, M. Hallikainen, D. Hiltbrunner, H. Johnson, V. Jääskeläinen, S. A. Kolberg, J. Koskinen, C. Mätzler, J. Pulliainen, K. Sand, R. Solberg, A. Standley, and A. Wiesmann, *Snowtools — Research and development of remote sensing methods for snow hydrology*, Final report, EC Contract ENV4-CT96-0304, ISBN 82-7747-107-6, NORUT, Tromsø, 2000a.

Guneriussen, T., K. A. Høgda, H. Johnson, and I. Lauknes, InSAR for estimation of changes in snow water equivalent of dry snow, in *Proc. of the Int. Geoscience and Remote Sensing Symposium*, 2000b.

Haefliger, M., K. Steffen, and C. Fowler, AVHRR surface temperature and narrow-band albedo comparison with ground measurements for the Greenland ice sheet, *Ann. Glaciol.*, *17*, 49–54, 1993.

Haefner, H., F. Holecz, E. Meier, and D. Nüesch, Monitoring of snow cover in high mountain terrain with ERS-1 SAR, *ESA SP*, *1102*, 583–588, Cannes, France, 1993.

Haefner, H., and J. Piesbergen, High alpine snow cover monitoring using ERS-1 SAR and Landsat TM data, in *Proc. 5th Scientific Assembly of the International Association of Hydrological Sciences, IAHS*, pp. 113–118, Rabat, Morocco, 1997.

Haefner, H., and K. Seidel, Methodological aspects and regional examples of snow cover mapping from ERTS-1 and EREP imagery of Swiss Alps, *ESA SP*, *100*, 155–165, 1974.

Hall, D. K., A. T. C. Chang, C. S. Benson, and W. M. Kovalick, Comparison of in-situ and Landsat derived reflectance of Alaskan glaciers, *Remote Sens. Environ.*, *28*, 23–31, 1989.

Hall, D. K., A. T. C. Chang, and J. L. Foster, Detection of the depth hoar layer in the snowpack of the Arctic Coastal Plain of Alaska using satellite data, *J. Glaciol.*, *32*, 87–94, 1986.

Hall, D. K., J. L. Foster, and A. T. C. Chang, Measurements and modeling of microwave emission from forested snowfields in Michigan, *Nordic Hydrol.*, *13*, 129–138, 1982.

Hall, D. K., J. L. Foster, and A. T. C. Chang, Reflectance of snow as measured in-situ and from space in sub-Arctic areas in Canada and Alaska, *IEEE Trans. Geosci. Remote Sens.*, *30*, 634–637, 1992.

Hall, D. K., J. L. Foster, A. T. C. Chang, C. S. Benson, and J. Y. L. Chien, Determination of snow covered area in different land covers in central Alaska from aircraft data, April 1995, *Ann. Glaciol.*, *26*, 149–155, 1998a.

Hall, D. K., J. L. Foster, V.V. Salomonson, A. G. Klein, and J. Y. L. Chien, Development of a technique to assess snow-cover mapping error from space, *IEEE Trans. Geosci. Remote Sens.*, *39*, 432–438, 2001.

Hall, D. K., J. L. Foster, D. L. Verbyla, A. G. Klein, and C. S. Benson, Assessment of snow cover mapping accuracy in a variety of vegetation cover densities in central Alaska, *Remote Sens. Environ.*, *66*, 129–137, 1998b.

Hall, D. K., and J. Martinec, *Remote sensing of ice and snow*, Chapman & Hall, London, 1985.

Hall, D. K., G. A. Riggs, and V. V. Salomonson, Development of methods for mapping global snow cover using Moderate Resolution Imaging Spectroradiometer (MODIS) data, *Remote Sens. Environ.*, *54*, 127–140, 1995.

Hall, D. K, G. A. Riggs, V. V. Salomonson, N. E. DiGirolamo, and K. J. Bayr, MODIS snow-cover products. *Remote Sens. Environ.*, *83*, 181–194, 2002.

Hall, D. K., M. Sturm, C. S. Benson, A. T. C. Chang, J. L. Foster, H. Garbeil, and E. Chaco, Passive microwave remote and in situ measurements of Arctic and Subarctic snow covers in Alaska, *Remote Sens. Environ.*, *38*, 161–172, 1991.

Hallikainen, M. T., Retrieval of snow water equivalent from Nimbus-7 SMMR data: effect of land-cover categories and weather conditions, *IEEE J. Ocean. Eng.*, *9*, 372–376, 1984.

Hallikainen, M. T., and P. A. Jolma, Retrieval of the water equivalent of snow cover in Finland by satellite microwave radiometry, *IEEE Trans. Geosci. Remote Sens.*, *24*, 855–862, 1986.

Hallikainen, M., and F. T. Ulaby, Dielectric scattering behaviour of snow at microwave frequencies, in *Proc. Int. Geoscience and Remote Sensing Symposium*, pp. 87–91, Zürich, Switzerland, 1986.

Henderson, F. M., and A. J. Lewis, *Principles and applications of imaging radar*, John Wiley & Sons, New York, 1998.

Hofer, R., and E. Schanda, Signatures of snow in the 5-94 GHz range, *Radio Science*, *13*, 365–369, 1978.

Hollinger, J. P., J. L. Peirce, and G. A. Poe, SSM/I Instrument evaluation, *IEEE Trans. Geosci. Remote Sens.*, *28*, 781–790, 1990.

Hutchison, K. D., and J. K. Locke, Snow cover identification through cirrus-cloudy atmospheres using daytime AVHRR imagery, *Geophys. Res. Lett.*, *24*, 1797–1794, 1997.

Jin, Y., C. Schaaf, F. Gao, X. W. Li, A. H. Strahler, and X. B. Zeng, How does snow impact the albedo of vegetated land surfaces as analyzed with MODIS data? *Geophys. Res. Let.*, *29*, 2002.

Jin, Y., C. Schaaf, F. Gao, X. Li, A. H. Strahler, W. Lucht, and S. Liang, Consistency of MODIS surface BRDF/Albedo retrievals 1. Algorithm performance, *J. Geophys. Res. - Atmosphere*, *108*, 2003a.

Jin, Y., C. Schaaf, C. Woodcock, F. Gao, X. Li, A. Strahler, W. Lucht and S. Liang, Consistency of MODIS surface BRDF/Albedo retrievals 2. Validation, *J. Geophys. Res. - Atmosphere*, *108*, 2003b.

Jordan, R., *A One Dimensional Temperature Model for Snow Cover: Technical Documentation for SNTHERM.89*, CRREL Report, 91–16, U.S. Army Corps of Engineers, Cold Regions Research and Engineering Laboratory, 1991.

Josberger, E. G., W. J. Campbell, P. Gloersen, A. T. C. Chang, and A. Rango, Snow conditions and hydrology of the upper Colorado river basin from satellite passive microwave observations, *Ann. Glaciol.*, *17*, 322–326, 1993.

Josberger, E., P. Gloersen, A. Chang, and A. Rango, The effect of snow grain size on passive microwave signature for the upper Colorado River basin snowpack, *J. Geophys. Res.*, *101*, 6679–6688, 1995.

Kelly, R. E. J., and A. T. C. Chang, Development of a passive microwave global snow depth retrieval algorithm for Special Sensor Microwave Imager (SSM/I) and Advanced Microwave Scanning Radiometer-EOS (AMSR-E) data, *Radio Sci.*, *38(4)*, 8076, doi: 10.1029/2002RS002648, 2003.

Kelly, R. E., A. T. C. Chang, L. Tsang, and J. L. Foster, A prototype AMSR-E global snow area and snow depth algorithm, *IEEE Trans. Geosci. Remote Sens.*, *41*, 230–242, 2003.

Kennedy, J. M., and R. T. Sakomoto, Passive microwave determination of snow wetness factors, in *Proc. 4th Int. Symposium on Remote Sensing of Environment*, pp. 161–171, Ann Arbor, Michigan USA, 1966.

Key, J., and M. Haefliger, Arctic ice surface-temperature retrieval from AVHRR thermal channels, *J. Geophys. Res.*, *97*, 5885–5893, 1992.

Key, J. R., J. B. Collins, C. Fowler, and R. S. Stone, High-latitude surface temperature estimates from thermal satellite data, *Remote Sens. Environ.*, *61*, 302–309, 1997.

Killingtveit, A., Northern hydrology in Norway, in *Northern Hydrology: International Perspectives, NHRI Science Report*, pp. 81–107, National Hydrology Research Institute, 1994.

Kimball, J. S., K. C. McDonald, S. W. Running, and S. E. Frolking, Satellite radar remote sensing of seasonal growing seasons for boreal and subalpine evergreen forests, *Remote Sens. Environ.*, *90*, 243–258, 2004.

Klein, A. G., D. K. Hall, and G. A. Riggs, Improving snow-cover mapping in forests through the use of a canopy reflectance model, *Hydrol. Process.*, *12*, 1723–1744, 1998.

Klein, A. G., and J. Stroeve. Development and validation of a snow albedo algorithm for the MODIS instrument, *Ann. Glaciol.*, *34*, 45–52, 2002.

Knap, W. H., and J. Oerlemans, The surface albedo of the Greenland ice sheet: Satellite-derived and in situ measurements in the Sondre Stromfjord area during the 1991 melt season, *J. Glaciol.*, *42*, 364–374, 1996.

Knap, W. H., and C. H. Rejmer, Anisotropy of the reflected radiation field over melting glacier ice: Measurements in Landsat TM Bands 2 and 4, *Remote Sens. Environ.*, *65*, 93–104, 1998.

Koenig, L. S., and R. R. Forster, Evaluation of passive microwave snow water equivalent algorithms in the depth-hoar dominated snowpack of the Kuparuk River Watershed, Alaska, USA, *Remote Sens. Environ.*, *93*, 511–527, 2004.

König, M., J.-G. Winther, and E. Isaksson, Measuring snow and glacier ice properties from satellite, *Rev. Geophys.*, *39*, 1–27, 2001.

Koskinen, J. T., J. T. Pulliainen, and M. T. Hallikainen, The use of ERS-1 SAR data in snow melt monitoring, *IEEE Trans. Geosci. Remote Sens.*, *35*, 601–610, 1997.

Koskinen, J., S. Metsämäki, J. Grandell, S. Jänne, L. Matikainen, and M. Hallikainen, Snow monitoring using radar and optical satellite data, *Remote Sens. Environ.*, *69*, 16–29, 1999.

Künzi, K. F., S. Patil, and H. Rott, Snow-cover parameters retrieval from Nimbus-7 scanning multichannel microwave radiometer

(SMMR) data, *IEEE Trans. Geosci. Remote Sens.*, *20*, 452–467, 1982.

Kuittinen, R., Determination of areal snow-water equivalent values using satellite imagery and aircraft gamma-ray spectrometry, in *Hydrologic Applications of Space Technology*, pp. 181–189, IAHS Publ. 160, 1986.

Kuittinen, R., Optical and thermal sensors in snow cover monitoring, in *Proc. EARSeL Workshop on Remote Sensing of Land Ice and Snow*, pp. 7–20, Freiburg, Germany, 1997.

LaChapelle, E. R., *Properties of snow*, University of Washington, Seattle, 1969.

Leaf, C. F., Areal extent of snow cover in relation to streamflow in Central Colorado, in *Proc. Int. Hydrology Symposium*, pp. 157–164, Fort Collins, Colorado USA, 1967.

Leroux C., J. Lenoble, G. Brogniez, J. W. Hovenier, and J. F. De Haan, A model for the bidirectional polarized reflectance of snow, *J. Quant. Spectro. Radiat. Transfer*, *61*, 273–285, 1998a.

Leroux C., J. L. Deuze, P. Goloub, C. Sergent, and M. Fily, Ground measurements of the polarized bidirectional reflectance of snow in the middle infrared spectral domain: Comparisons with model results, *J. Geophys. Res.*, *103*, 19721–19731, 1998b.

Liu, Y., J. R. Key, R. A. Frey, S. A. Ackerman, and W. P. Menzel, Nighttime polar cloud detection with MODIS, *Remote Sens. Environ.*, *92*, 181–194, 2004.

Magagi, R., and M. Bernier, Optimal conditions for wet snow detection using RADARSAT SAR data, *Remote Sens. Environ.*, *84*, 221–233, 2003.

Martinec, J., Evaluation of air photos for snowmelt-runoff forecasts, in *Proc. UNESCO-WMO-IAHS Symposia on the Role of Snow and Ice in Hydrology*, pp. 915–926, Banff, Canada, 1973.

Martinec, J., Snowmelt runoff models for operational forecasts, *Nordic Hydrol.*, *16*, 129–136, 1985.

Martinec, J., and A. Rango, Interpretation and utilization of areal snow-cover data from satellites, *Ann. Glaciol.*, *9*, 153–161, 1987.

Martinec, J., A. Rango, and R. Roberts, Snowmelt runoff model (SRM) user's manual, Geographica Bernesia, 1998.

Massom, R., Satellite remote sensing of polar snow and ice: Present status and future directions, *Polar Record*, *31*, 99–114, 1995.

Mätzler, C., Applications of the interaction of microwave with the natural snow cover, *Remote Sens. Rev.*, *2*, 259–387, 1987.

Mätzler, C., Passive microwave signatures of landscapes in winter, *Meteorol. Atmos. Phys.*, *54*, 241–260, 1994.

Mätzler, C., Improved born approximation for scattering in a granular medium, *J. Appl. Phys.*, *83*, 6111–6117, 1998a.

Mätzler, C., Microwave properties of ice and snow, in *Solar System Ices*, edited by B. Schmitt, pp. 241–257, Kluwer Academic Publ., Dordrecht, 1998b.

Mätzler, C., *Cost Action 712 "Application of microwave radiometry to atmospheric research and monitoring", Meteorology*, Final Report of Project 1, ISBN 92-828-9842-3, European Commission, Directorate General for Research, EUR 19543, 2000.

Mätzler, C., and E. Schanda, Snow mapping with active microwave sensors, *Int. J. Remote Sens.*, *5*, 409–422, 1984.

Mätzler, C., and A. Standley, Relief effects for passive microwave remote sensing, *Int. J. Remote Sens.*, *21*, 2403–2412, 2000.

Mätzler, C., T. Strozzi, and T. Weise, Microwave snowpack studies made in Austrian Alps during the SIR-C/X-SAR experiment, *Int. J. Remote Sens.*, *18*, 2505–2530, 1997.

Mätzler, C., and A. Wiesmann, *Extension of the microwave emission model of layered snowpacks to coarse-grained snow*, IAP-Report 97-14, Institute of Applied Physics, University of Berne, 1998.

Mätzler, C., and A. Wiesmann, Extension of the Microwave Emission Model of Layered Snowpacks to coarse-grained snow, *Remote Sens. Environ.*, *70*, 317–325, 1999.

Maurer, E. P., J. D. Rhoads, R. O. Dubayah, and D. P. Lettenmaier. Evaluation of the snow-covered area data product from MODIS. *Hydrol. Process.*, *17*, 59–71, 2003.

Maxson, R. W., M. W. Allen, and T. L. Szeliga, *Theta-image classification by comparison of angles created between multi-channel vectors and an empirically selected reference vector*, U.S. NWS NOHRSC Report (www.nohrsc.nws.gov/html/papers/theta/theta.htm), 1996.

McGinnis, D. F., J. A. Pritchard, D. R. Wiesnet, et al, Determination of snow depth and snow extent from NOAA 2 satellite very high resolution radiometer data, *Water Resour. Res.*, *11*, 897–902, 1975.

Melloh, R. A., J. P. Hardy, R. N. Bailey, and T. J. Hall, An efficient snow albedo model for the open and sub-canopy, *Hydrol. Process.*, *16*, 3571–3584, 2002.

Mondet J., and M. Fily, The reflectance of rough snow surfaces in Antarctica from POLDER/ADEOS remote sensing data, *Geophys. Res. Lett.*, *26*, 3477–3480, 1999.

Nagler, T., and H. Rott, Backscattering signatures and techniques for snow and glacier monitoring using ERS-SAR and X-SAR data, in *Proc. EARSeL Workshop on Remote Sensing of Land Ice and Snow*, pp. 121–122, Freiburg, Germany, 1997.

Nagler, T., and H. Rott, Retrieval of wet snow by means of multitemporal SAR data, *IEEE Trans. Geosci. Remote Sens.*, *38*, 754–765, 2000.

NASA, *Plan of research for snowpack properties remote sensing-(PRS)²*, Goddard Space Flight Center, Greenbelt, Maryland, 1982.

NASA, *Shuttle Imaging Radar - C science plan*, California Institute of Technology, Pasadena, 1986.

NASA, *Instrumental panel report. SAR: Synthetic Aperture Radar (Earth Observing System)*, Earth Science and Applications Division, Washington D.C., 1989.

NASA, *EOS science plan*, Earth Science and Applications Division, Washington D.C., 1999.

Nghiem, S. V. and W.-Y. Tsai, Global snow cover monitoring with spaceborne K{u}-band scatterometer, *IEEE Trans. Geosci. Remote Sens.*, *39*, 2118–2134, 2001.

Njoku, E.G., Passive microwave remote sensing of the earth form space — a review, *Proc. IEEE*, *70*(7), 728–750, 1982.

Nolin, A., J. Dozier, and L. A. K. Mertes, Mapping alpine snow using a spectral mixture modeling technique, *Ann. Glaciol.*, *17*, 121–124, 1993.

Nolin, A. W., and J. Dozier, Estimating snow grain size using AVIRIS data, *Remote Sens. Environ.*, *44*, 231–238, 1993.

Nolin, A. W., and J. Dozier, A hyperspectral method for remotely sensing grain size of snow, *Remote Sens. Environ.*, *74*, 207–216, 2000.

Norwood, V. T., and J. C. Lansing, Electro-optical imaging sensors, in *Manual of Remote Sensing*, edited by R.N. Colwell, pp. 335–367, Falls Church, 1983.

Obled, C., and H. Harder, A review of snowmelt in the mountain environment, in *Proc. Modeling of Snow Cover Runoff*, pp. 179–204, Hanover, New Hampshire USA, 1979.

Offenbacher, E. L., and S. C. Colbeck, *Remote sensing of snow covers using the gamma-ray technique*, CRREL Report, 91–9, U.S. Army Corps of Engineers, Cold Regions Research and Engineering Laboratory, 1991.

Orheim, O., and B. K. Lucchitta, Numerical analysis of Landsat Thematic Mapper images of Antarctica: Surface temperatures and physical properties, *Ann. Glaciol.*, *11*, 109–120, 1988.

Painter, T. H., and J. Dozier, The effect of anisotropic reflectance on imaging spectroscopy of snow properties, *Remote Sens. Environ.*, *89*, 409–422, 2004.

Painter, T. H., D. A. Roberts, R. O. Green, and J. Dozier, The effect of grain size on spectral mixture analysis of snow-covered area from AVIRIS data, *Remote Sens. Environ.*, *65*, 320–322, 1998.

Painter T. H., J. Dozier, D. A. Roberts, R. E. Davis, and R. O. Green, Retrieval of subpixel snow-covered area and grain size from imaging spectrometer data, *Remote Sens. Environ.*, *85*, 64–77, 2003.

Papa, F., B. Legresy, N. M. Mognard, E. G. Josberger, and F. Remy, Estimating terrestrial snow depth with the Topex-Poseidon altimeter and radiometer, *IEEE Trans. Geosci. Remote Sens.*, *40*, 2162–2169, 2002.

Parlow, E., Determination and intercomparison of radiation fluxes and net radiation using Landsat-TM data of Liefdefjorden, NW-Spitsbergen, in *Proc. Fourth Symposium on Remote Sensing of the Polar Environments*, pp. 27–32, Lyngby, Denmark, 1996a.

Parlow, E. (ed.), *Progress in environmental research and applications*, Balkema, Rotterdam, 1996b.

Partington, K. C., Discrimination of glacier facies using multi-temporal SAR data, *J. Glaciol.*, *44*, 480–488, 1998.

Pattyn, F., and H. Decleir, Satellite monitoring of ice and snow conditions in the Sør Rondane Mountains, Antarctica, *Ann. Glaciol.*, *17*, 41–48, 1993.

Peck, E. L., T. R. Carroll, and S. C. Van Denmark, Operational areal snow surveying in the United States, *Hydrol. Sci. Bull.*, *25*, 51–62, 1980.

Pivot, F., C. Kergomard, and C.R. Duguay, On the use of passive microwave data to monitor spatial and temporal variations of snowcover near Churchill, Manitoba, Ann. Glaciol., *34*, 58–64, 2002.

Potts, H.L., Snow surveys and runoff forecasting from photographs, in *Proc. Transactions Amer. Geophys. Union, South Continental Divide Snow-Survey Conference*, pp. 658–660, , 1937.

Pulliainen, J., J. Grandell, and M. Hallikainen, HUT snow emission model and its applicability to snow water equivalent retrieval, *IEEE Trans. Geosci. Remote Sens.*, *37*, 1378–1390, 1999.

Ramage, J. M., and B. L. Isacks, Seasonal changes in Alaskan radar glacier zones, in *Proc. Final ADRO Symposium*, Montreal, Canada, 1998.

Ramsay, B., The interactive multisensor snow and ice mapping system, *Hydrol. Process.*, *12*, 1537–1546, 1998.

Rango, A., A. T. C. Chang, and J. L. Foster, The utilization of spaceborne microwave radiometers for monitoring snowpack properties, *Nordic Hydrol.*, *10*, 25–40, 1979.

Rango, A., and K. I. Itten, Satellite potentials in snow cover monitoring and runoff prediction, *Nordic Hydrol.*, *7*, 209–230, 1976.

Rango, A., J. Martinec, A. T. C. Chang, J. L. Foster, and V. Van Katwıjk, Average areal water equivalent of snow in a mountain basin using microwave and visible satellite data, *IEEE Trans. Geosci. Remote Sens.*, *27*, 740–745, 1989.

Rango, A., V. V. Salomonson, and J. L. Foster, Seasonal streamflow estimation in the Himalayan region employing meteorological satellite snow cover observation, *Water Resour. Res.*, *13*, 109–112, 1977.

Rast, M. (ed.), *MERIS - The Medium Resolution Imaging Spectrometer*, ESA SP, 1184, 1996.

Rau, F., M. Braun, H. Saurer, H. Gossmann, G. Kothe, F. Weber, M. Ebel, and D. Beppler, Monitoring multi-year snow cover dynamics on the Antarctic Peninsula using SAR imagery, *Polarforschung*, *67*, 27–40, 2000.

Rees, W. G., and A.M. Steel, Radar backscatter coefficients and snow detectability for upland terrain in Scotland, *Int. J. Remote Sens.*, *22*, 3015–3026, 2001.

Robinson, D. A., K. F. Dewey, and R. P. Heim, Global snow cover monitoring: an update, *Bull. Amer. Meteorol. Soc.*, *74*, 1689–1696, 1993.

Romanov, P., D. Tarpley, G. Gutman, and T. Carroll, Mapping and monitoring of the snow cover fraction over North America, *J. Geophys. Res.*, *108(D16)*, 8619, doi:10.1029/2002JD003142, 2003.

Rosenthal, W., and J. Dozier, Automated mapping of montane snow cover at subpixel resolution from the Landsat Thematic Mapper, *Water Resour. Res.*, *32*, 115–130, 1996.

Rott, H., and G. Markl, Improved snow and glacier monitoring by the Landsat Thematic Mapper, *ESA SP, 1102*, 3–12, 1989.

Rott, H., and C. Mätzler, Possibilities and limits of SAR for snow and glacier surveying, *Ann. Glaciol.*, *9*, 195–199, 1987.

Rott, H., and T. Nagler, Snow and glacier investigations by ERS-1 SAR — first results, *ESA SP, 359*, 577–582, 1993.

Rott, H., and T. Nagler, Capabilities of ERS-1 SAR for snow and glacier monitoring in alpine areas, *ESA SP, 359*, 965–970, 1994.

Rott, H., and T. Nagler, Intercomparison of snow retrieval algorithms by means of spaceborne microwave radiometry, in *Passive Microwave Remote Sensing of Land-Atmosphere Interactions*, edited by B.J. Choudhury, and Y.H. Kerr, pp. 245–262, Utrecht, 1995.

Salisbury, J. W., D. M. D'Aria, and A. Wald, Measurements of thermal infrared spectral reflectance of frost, snow and ice, *J. Geophys. Res.*, *99*, 24235–24240, 1994.

Salomonson, V. V., and I. Appel, Estimating fractional snow cover from MODIS using the normalized difference snow index, *Remote Sens. Environ.*, *89*, 351–360, 2004.

Sandmeier, S., and K. I. Itten, A physically-based model to correct atmospheric and illumination effects in optical satellite data of rugged terrain., *IEEE Trans. Geosci. Remote Sens.*, *35*, 708–717, 1997.

Saurer, H., S. Wunderle, and H. Gossmann, Radarfernerkundung der Antarktischen Halbinsel, *Geogr. Rundschau, 50*, 71–77, 1998.

Schanda, E., C. Mätzler, and K. Künzi, Microwave remote sensing, *Int. J. Remote Sens.*, *4*, 149–158, 1983.

Scherer, D., Significance of satellite data for studying atmospheric and hydrological processes in the High Arctic, in *Progress in Environmental Remote Sensing Research and Applications*, edited by E. Parlow, pp. 361–367, Balkema, Rotterdam, 1996.

Scherer, D., Regionale Geosystemanalyse - Theorie und Beispiele, Habilitation thesis, Univ. Basel, Switzerland, 1998.

Scherer, D., and M. Brun, Determination of the solar albedo of snow-covered regions in complex terrain, in *Proc. EARSeL Workshop on Remote Sensing of Land Ice and Snow*, pp. 21–29, Freiburg, Germany, 1997.

Schjødt-Osmo, O., and R. Engeset, Remote sensing and snow monitoring: Application to flood forecasting, in *Proc. European Water Resources Association Conference*, Copenhagen, Denmark, 1997.

Schneider, C., E. Parlow, and D. Scherer, GIS-based modelling of the energy balance of Tarfala Valley, Sweden using Landsat-TM data, in *Progress in Environmental Remote Sensing Research and Applications*, edited by E. Parlow, pp. 401–408, Balkema, Rotterdam, 1996.

Schneider, C., S. Wunderle, and M. Friedrich, Snow cover investigations by means of ERS-SAR imagery on the Antarctic Peninsula, *EARSeL Adv. Remote Sens.*, *5*, 71–81, 1997.

Seidel, K., C. Ehrler, and J. Martinec, Multisensor analysis of satellite images for regional snow distribution, in *Progress in Environmental Remote Sensing Research and Applications*, edited by E. Parlow, pp. 213–220, Balkema, Rotterdam, 1996.

Seidel, K., C. Ehrler, and J. Martinec, Effects of climate change on water resources and runoff in an alpine basin, *Hydrol. Process.*, *12*, 1659–1669, 1998.

Seidel, K., and J. Martinec, Operational snow cover mapping by satellites and real time runoff forecasts, in *Proc. Proc. ISSGH 92*, pp. 123–132, Kathmandu, Nepal, 1992.

Sergent C., C. Leroux, E. Pougatch, and F. Guirado, Hemispherical-directional reflectance measurements of natural snows in the 0.9–1.45 μm spectral range. Comparison with adding-doubling modelling, *Ann. Glaciol.*, *26*, 59–63, 1998.

Shi, J., and J. Dozier, Measurements of snow- and glacier-covered areas with single-polarization SAR, *Ann. Glaciol.*, *17*, 72–76, 1993.

Shi, J., and J. Dozier, Inferring snow wetness using C-band data from SIR-C's polarimetric synthetic aperture radar, *IEEE Trans. Geosci. Remote Sens.*, *33*, 905–914, 1995.

Shi, J., J. Dozier, and H. Rott, Snow mapping in alpine regions with Synthetic Aperture Radar, *IEEE Trans. Geosci. Remote Sens.*, *32*, 152–158, 1994.

Shi, J., J. Dozier, H. Rott, and R. E. Davis, Snow and glacier mapping in alpine regions with polarimetric SAR, in *Proc.*

Int. Geoscience and Remote Sensing Symposium (IGARSS'91), Houston, USA, 1991.

Shi, J., S. Hensley, and J. Dozier, Mapping snow cover with repeat pass synthetic aperture radar, in *Proc. Int. Geoscience and Remote Sensing Symposium (IGARSS'97)*, pp. 628–630, 1997.

Shih, S.-E., K.-H. Ding, J. A. Kong, and Y. E. Yang, Modeling of millimeter wave backscatter of timevarying snow cover, *PIER*, *16*, 305–330, 1997.

Smith, L. C., R. R. Forster, B. L. Isacks, and D. K. Hall, Seasonal climatic forcing of alpine glaciers revealed with orbital synthetic aperture radar, *J. Glaciol.*, *43*, 480–488, 1997.

Solberg, R., D. Hiltbrunner, J. Koskinen, T. Guneriussen, K. Rautiainen, and M. Hallikainen, Snow algorithms and products - Review and recommendations for research and development. *Project SNOWTOOLS WP 410*, NR Report No. 924, Norwegian Computing Center, Oslo, 1997.

Solberg, R., D. Hiltbrunner, J. Koskinen, T. Guneriussen, K. Rautiainen, and M. Hallikainen, SNOWTOOLS: Research and development of methods supporting new snow products, in *Proc. XX Nordic Hydrological Conference (NHK-98)*, Helsinki, Finland, 1998.

Sommerfeld, R. A., and E. R. LaChapelle, The classification of snow metamorphism, *J. Glaciol.*, *9*, 3–17, 1970.

Standley, A., The use of passive microwave and optical data in the snow-tools project, in *Proc EARSeL Workshop on Remote Sensing of Land Ice and Snow*, pp. 61–68, Freiburg, Germany, 1997.

Steinmeier, C., Model-based snow cover mapping from remote sensing data for operational snowmelt forecasts, Ph.D. thesis, ETH Zürich, Switzerland, 1995.

Stogryn, A., A study of the microwave brightness temperature of snow from the point of view of strong fluctuation theory, *IEEE Trans. Geosci. Remote Sens.*, *24*, 220–231, 1986.

Stroeve J. C., and A. W. Nolin, New methods to infer snow albedo from the MISR instrument with applications to the Greenland ice sheet, *IEEE Trans. Geosci. Remote Sens.*, *40*, 1616–1625, 2002.

Stroeve, J., M. Haefliger, and K. Steffen, Surface temperature from ERS-1 ATSR infrared thermal satellite data in polar regions, *J. Appl. Meteorol.*, *35*, 1231–1239, 1996.

Stroeve, J., J. E. Box, F. Gao, S. Liang, A. Nolin, and C. Schaaf, Accuracy assessment of the MODIS 16-day albedo product for snow: comparisons with Greenland in situ measurements, *Remote Sens. Environ.*, *94*, 46–60, 2005.

Strozzi, T., U. Wegmüller, and C. Mätzler, Mapping wet snow-covers with SAR interferometry, *Int. J. Remote Sens.*, *20*, 2395–2403, 1999.

Strozzi, T., A. Wiesmann, and C. Mätzler, Active microwave signature of snow covers at 5.3 and 35 GHz, *Radio Science, 32*, 479–495, 1997.

Sturm, M., T. C. Grenfell, and D. K. Perovich, Passive microwave measurements of tundra and taiga snow covers in Alaska, U.S.A, *Ann. Glaciol.*, *17*, 125–129, 1993.

Surdyk, S., and M. Fily, Results of stratified emissivity model based on the wave approach: Application on the Antarctic Ice Sheet, *J. Geophys. Res.*, *100*, 8837–8848, 1995.

Tait, A., and R. Armstrong, Evaluation of SMMR satellite-derived snow depth using ground-based measurements, *Int. J. Remote Sens.*, *17*, 657–665, 1996.

Tait, A.B., D. K. Hall, J. L. Foster, and A. T. C. Chang, High frequency passive microwave radiometry over a snow-covered surface in Alaska, *Photogramm. Eng. Remote Sens.*, *65*, 689–695, 1999.

Tedesco, M., J. Pulliainen, M. Takala, M. Hallikainen, and P. Pampaloni, Artificial neural network-based techniques for the retrieval of SWE and snow depth from SSM/I data, *Remote Sens. Environ.*, *90*, 76–85, 2004.

Tollan, O., Weather effects on aerial snow measurement, in *Proc. Workshop on Remote Sensing of Snow and Soil Moisture by Nuclear Techniques*, pp. 113–118, Voss, Norway, 1979.

Tsang, L., Passive remote sensing of dense nontenuous media, *J. Electr. Waves Appl.*, *1*, 159–173, 1987.

Tsang, L., D. T. Davis, R. West, Z. Chen, J.-H. Hwang, and D. P. Winebrenner, Passive microwave remote sensing of snow: Volume scattering in snow and parametric inversion of snow parameters with an artificial neural network, in *Passive Microwave Remote Sensing of Land-Atmosphere Interactions*, edited by B. J. Choudhury, Y. H. Kerr, E. G. Njoku, and P. Pampaloni, pp. 245–262, Utrecht, 1995.

Tsang, L., and J. A. Kong, Theory for thermal microwave emission from a bounded medium containing spherical scatterers, *J. Appl. Phys.*, *48*, 3593–3599, 1977.

Ulaby, F. T., R. K. Moore, and A. K. Fung, Surface scattering and emission theory, *Microwave Remote Sensing*, *2*, 457–1064, 1982.

Ulaby, F. T., R. K. Moore, and A. K. Fung, From theory to applications, *Microwave Remote Sensing*, *3*, 1065–2162, 1986.

Ulaby, F. T., and W. H. Stiles, The active and passive microwave response to snow parameters, *J. Geophys. Res.*, *85*, 1045–1049, 1980.

Ulaby, F. T., and W. H. Stiles, Microwave response of snow, *Adv. Space Res.*, *1*, 131–149, 1981.

Vershinina, L. K., The use of aerial gamma surveys of snowpack for spring snowmelt runoff forecasts, in *Hydrological Applications of Remote Sensing and Remote Data Transmission*, pp. 411–420, 1985.

Vikhamar, D., and R. Solberg, Subpixel mapping of snow cover in forests by optical remote sensing, *Remote Sens. Environ.*, *84*, 69–82, 2003a.

Vikhamar, D., and R. Solberg, Snow cover mapping in forests by constrained linear spectral unmixing of MODIS data, *Remote Sens. Environ.*, *88*, 309–323, 2003b.

Walker, A. E., and B. E. Goodison, Discrimination of a wet snow cover using passive microwave satellite data, *Ann. Glaciol.*, *17*, 307–311, 1993.

Wan, Z., Y. Zhang, Q. Zhang, and Z. Li, Validation of the land-surface temperature products retrieved from Terra Moderate Resolution Imaging Spectroradiometer data, *Remote Sens. Environ.*, *83*, 163–180, 2002.

Wang, J. R., A. T. C. Chang, and A. K. Sharma, On the estimation of snow depth from microwave radiometric instruments, *IEEE Trans. Geosci. Remote Sens.*, *30*, 785–792, 1992.

Warren, S. G., Optical properties of snow, *Rev. Geophys. Space Phys.*, *20*, 67–89, 1982.

Warren, S. G., and W.J. Wiscombe, A model for the spectral albedo of snow. II: Snow containing atmospheric aerosols, *Atmos. Sci.*, *37*, 2734–2745, 1980.

Way, J., J. Paris, E. Slaughter, L. Viereck, N. Christensen, and M. Dobson, The effect of changing environmental conditions on microwave signatures of forest ecosystems: Preliminary results of the March 1988 Alaskan aircraft SAR experiment, *Int. J. Remote Sens.*, *11*, 1119–1144, 1990.

Wiesmann, A., and C. Mätzler, Microwave Emission Model of Layered Snowpacks, *Remote Sens. Environ.*, *70*, 307–316, 1999.

Wiesmann, A., C. Fierz, and C. Mätzler, Simulation of microwave emission from physically modeled snowpacks, *Ann. Glaciol.*, *31*, 397–405, 2000.

Winebrenner, D. P., E. D. Nelson, R. Colony, and R. D. West, Observation of melt onset on multiyear Arctic sea ice using the ERS-1 synthetic aperture radar, *J. Geophys. Res.*, *99*, 22425–22441, 1994.

Winther, J.-G., Landsat Thematic Mapper (TM) derived reflectance from a mountainous watershed during the snow melt season, *Nordic Hydrol.*, *23*, 273–290, 1992.

Winther, J.-G., Snow and glacier ice characteristics measured using Landsat TM data, Ph.D. thesis, Univ. Trondheim, Norway, 1993.

Winther, J.-G., Spectral bi-directional reflectance of snow and glacier ice measured in Dronning Maud Land, Antarctica, *Ann. Glaciol.*, *20*, 1–5, 1994.

Winther, J.-G., S. Gerland, J. B. Ørbæk, B. Ivanov, A. Blanco, and J. Boike, Spectral reflectance of melting snow in a high Arctic watershed on Svalbard: some implications for optical satellite remote sensing studies, *Hydrol. Process.*, *13*, 2033–2049, 1999.

Winther, J.-G., S. Gerland, J. B. Ørbæk, B. Ivanov, A. S. Zachek, and A. M. Bezgreshnov, Effects on spectral reflectance from snow ageing, *Mem. Natl. Inst. Polar Res., Spec. Issue*, *54*, 2001.

Winther, J.-G., and D. K. Hall, Satellite-derived snow coverage related to hydropower production in Norway — present and future, *Int. J. Remote Sens.*, *20*, 2991–3008, 1999.

Wiscombe, W. J., and S. G. Warren, A model for the spectral albedo of snow. I: Pure snow, *J. Atmos. Sci.*, *37*, 2712–2733, 1980.

Wismann, V., Monitoring of seasonal snowmelt on Greenland with ERS scatterometer data, *IEEE Trans. Geosci. Remote Sens.*, *38*, 1821–1826, 2000.

Woo, M. K., A. Walker, D. Yang, and B. E. Goodison, Pixel-scale ground snow survey for passive microwave study of the Arctic snow cover, in *Proc. 52nd Annual Meeting of the Eastern Snow Conference*, pp. 51–57, Toronto, Canada, 1995.

Wunderle, S., Die Schneedeckendynamik in der Antarktischen Halbinsel und ihre Erfassung mit aktiven und passiven Fernerkundungsverfahren, Ph.D. thesis, Univ. Freiburg, Germany, 1996.

Wunderle, S., H. Gossman, and H. Saurer, Snow cover development as a component of the local geosystem on Potter Peninsula, King George Island, Antarctica, in *Proc. 2nd ERS-1 Symposium,*

Space at the Service of our Environment, pp. 987–991, Noord-wijk, The Netherlands, 1994.

Wunderle, S., and H. Saurer, Snow properties of the Antarctic Peninsula derived from ERS-1 SAR images, in *Proc. 21st Annual Conference of the Remote Sensing Society*, pp. 1231–1237, Southampton, UK, 1995.

Xiao, X., Z. Shen, and X. Qin, Assessing the potential of VEGETA-TION sensor data for mapping snow and ice cover: a Normalized Difference Snow and Ice Index, *Int. J. Remote Sens.*, *22*, 2479–2487, 2001.

Xiao, X., B. Moore III, X. Qin, Z. Shen, and S. Boles, Large-scale observations of alpine snow and ice cover in Asia: Using multi-temporal VEGETATION sensor data, *Int. J. Remote Sens.*, *23*, 2213–2228, 2002.

Zeng, Q., M. Cao, X. Feng, F. Liang, X. Chen, and W. Sheng, A study of spectral reflection characteristics for snow, ice and water in the north of China, in *Proc. Hydrological Applications of Remote Sensing and Remote Data Transmission, IAHS Publ. 145*, pp. 451–462, Hamburg, Germany, 1984

Zhang, T., T. Scambos, T. Haran, L.D. Hinzman, R.G. Barry, and D.L. Kane. Ground-based and satellite-derived measurements of surface albedo on the North slope of Alaska, *J. Hydrometeorol.*, *4*, 77–91, 2003.

C. R. Duguay, Geophysical Institute, University of Alaska Fairbanks, 903 Koyukuk Drive, P.O. Box 757320, Fairbanks, Alaska 99775-7320, USA. (claude.duguay@gi.alaska.edu)

D. K. Hall, Oceans and Ice Branch, Code 971, NASA/Goddard Space Flight Center, Greenbelt, Maryland 20771, USA. (dorothy.k.hall@nasa.gov)

V. Hochschild, Geographisches Institut, Universität Tübingen, Hölderlinstraße 12, 72074 Tübingen, Germany. (volker.hochschild@uni-tuebingen.de)

M. König and J.-G. Winther, Norwegian Polar Institute, Polar Environmental Centre, N-9296 Tromsø, Norway. (max.koenig@npolar.no; winther@npolar.no)

C. Mätzler, Institute of Applied Physics, University of Bern, Sidlerstrasse 5, CH-3012 Bern, Switzerland. (matzler@iap.unibe.ch)

F. Pivot, Department of Geography, York University, 4700 Keele Street, Toronto, Ontario, M3J 1P3 Canada. (fpivot@yorku.ca)

F. Rau, Department of Physical Geography, University of Freiburg, Werderring 4, Freiburg, D-79085, Germany. (frank.rau@ipg.uni-freiburg.de)

D. Scherer, Department of Climatology, Institute of Ecology, Berlin University of Technology, Rothenburgstr. 12, D-12165 Berlin, Germany. (Dieter.Scherer@TU-Berlin.DE)

K. Seidel, Computer Vision Laboratory, Swiss Federal Institute of Technology ETHZ, Gloriastrasse 35, CH-8092 Zürich, Switzerland. (seidel@vision.ee.ethz.ch)

R. Solberg, Norwegian Computing Center, P.O. Box 114 Blindern, N-0314 Oslo, Norway. (Rune.Solberg@nr.no)

A. E. Walker, Climate Processes and Earth Observation Division, Climate Research Branch, Meteorological Service of Canada, 4905 Dufferin Street, Downsview, Ontario, M3H 5T4, Canada. (anne.walker@ec.gc.ca)

Remote Sensing of Glaciers and Ice Sheets

Jan-Gunnar Winther[1], Robert Bindschadler[2], Max König[1], and Dieter Scherer[3]

This chapter summarizes research on satellite remote sensing of glaciers and ice sheets. It covers a number of topics, including studies of the equilibrium line; characteristic glacier surface zones or glacier facies; glacier velocity; glacier mapping; change detection; surface features; and snow pack characteristics. Finally, we briefly outline new opportunities for northern hydrology with the utilization of recent and planned spaceborne sensors such as MODIS, ENVISAT MERIS and ASAR, ICESat, and CryoSat.

1. INTRODUCTION

In the field of glaciology, satellite remote sensing has proven to be a particularly useful tool since the areas of interest often are inaccessible. Furthermore, in many regions at high latitudes like the Greenland and Antarctic ice sheets, only during parts of the year can effective ground-based research be carried out due to the harsh climate and the lack of daylight. Satellite remote sensing often permits real-time, year-round, and long-term studies. Also, the extensive spatial coverage of satellite remotely sensed data enables monitoring and process-studies over enormous areas. In this way satellite data help in understanding processes and tele-connections on regional, continental, and even global scales. In recent years, such data have become particularly important since they assist interpretation and analyses concerning changes in the hydrological cycle due to global change. However, it has been already 40 years since work started on glacier and ice sheet reconnaissance using artificial satellites [*Lachapelle*, 1962; *Meier and Post*, 1962].

Glaciers have long been recognised as sensitive indicators for climate change. Their importance for climate research is especially significant since they contain a considerable fraction of the world's freshwater and therefore changes in glacier volume change sea level. The most obvious indicator for a glacier's response to changing climatic conditions is the advance or retreat of its front position, which is caused by changes in glacier mass balance. Changes in glacier mass balance have a direct effect on runoff volumes from northern basins. Further, changes in runoff influence a wide variety of processes in the hydrological regime including erosion, sediment transport, groundwater levels, and input of freshwater and nutrients to the ocean. The response time to such changes, however, is highly variable depending on both direct climate forcing and physical conditions of individual glaciers [*Paterson*, 1994]. The equilibrium line position is affected by annual perturbations of climate and is therefore also an important part of glacier studies.

In addition to direct observations of glacier front positions, other aspects of glaciers also provide insight into our understanding of their dynamics. For example, information about glacier size, ice velocity, ice thickness, ice temperature, surface and bedrock topography, accumulation rate, and surface conditions are all valuable additions in order to understand past dynamics and eventually model future behaviour of these ice masses. For small-scale studies, satellite remote sensing can be a vital tool both for obtaining a basic understanding of processes (e.g., glacier velocities from interferometry) or for monitoring programs (e.g., glacier retreat for water balance calculations).

Previous reviews on remote sensing of snow, glaciers, and ice sheets have been made by *Hall and Martinec* [1985], *Foster et al.* [1987], *Rott* [1987], *Bernier* [1987], *Massom* [1991], *Bindschadler* [1998], and *König et al.* [2001a]. Many of the issues described in *Scherer et al.* [this volume] are

[1]Norwegian Polar Institute, Polar Environmental Centre, N-9296 Tromsø, Norway.
[2]NASA Goddard Space Flight Center, Greenbelt, Maryland.
[3]Climatology Section, Institute of Ecology, Berlin University of Technology, Berlin, Germany

also directly relevant for glacier research since ice sheets and large portions of glaciers normally have snow exposed at the surface (Figure 1). This chapter describes various topics and study areas in glacier research where satellite remote sensing techniques are used. Our emphasis is on the principles and theory of various methods. We exclude ground studies and most studies using airborne remote sensing. Tables 1 and 2 present an overview of the sensors most commonly used in snow and glacier ice studies. An extensive list of references allows the reader to delve into specific topics.

2. EQUILIBRIUM LINE AND GLACIER FACIES

2.1. Equilibrium Line and Glacier Facies—General

In simple terms, a glacier can be divided into an area that annually gains mass—the accumulation area—and an area that annually loses mass—the ablation area. The equilibrium line, where net mass balance is zero, separates accumulation and ablation areas. Changes in the equilibrium line's position give important information on the glacier's status. Accumulation and ablation areas can be further divided into glacier facies, being distinct zones with specific characteristics in surface layers. These were first described by *Benson* [1962] and later modified slightly by *Williams et al.* [1991].

Figure 1. Spectral reflectance curves for snow and ice in different stages [modified from *Zeng et al.,* 1984]. Reprinted with permission from the International Association of Hydrological Sciences.

Information on glacier facies can also be found in *Paterson* [1994] and *Benson* [1996].

Glacer facies are formed by melt and diagenetic processes, related to specific patterns of accumulation and ablation. Briefly, facies types are (i) *dry-snow facies*, where practically no melt occurs; (ii) *percolation facies*, where some surface melt occurs, leading to percolation of melt water that refreezes in the snow pack; (iii) *wet-snow facies*, where the entire year's accumulation is raised to the melting point; (iv) *superimposed-ice facies*, where meltwater refreezes, forming an ice layer on the glacier surface in the accumulation area; and (v) *bare-ice facies*, which represent the ablation area of a glacier (Figure 2). First, we present some overall controlling factors for remote sensing of glacier facies. Later in this chapter, the various glacier facies are described in more detail.

Satellite imagery can identify several distinct zones on a glacier. However, these zones develop and change location with time and therefore are not always identical with glacier facies. The term radar glacier zone has been suggested for these variable zones on synthetic aperture radar (SAR) imagery [*Forster et al.,* 1996; *Smith et al.,* 1997; *Ramage et al.,* 2000; *Rau et al.,* 2000]. Comparable problems in correlating snow zones with glacier facies exist for visible imagery. In most studies, insufficient ground data make interpretation of the observed zones difficult and the question remains how much these zones match actual glacier facies.

Visible imagery taken at the end of the ablation season may allow determination of accumulation and ablation areas [e.g., *Hall et al.,* 1987; *Rott and Markl,* 1989; *Williams et al.,* 1991; *Parrot et al.,* 1993]. *Williams et al.* [1991] identify three distinguishable zones on Landsat images of Icelandic glaciers, which they name snow facies, ice facies, and slush zone. The slush zone is more a transition zone of wet snow, while snow and ice facies appear as distinct peaks in the distribution of reflectance values. *Hall et al.* [1987] found the same three zones on glaciers in the Grossglockner glacier group and believe that the slush zone represents some or all of the wet-snow facies. *Parrot et al.* [1993] studied a glacier on Svalbard with SPOT images. Correcting albedo for topographic effects and adjusting for pixels in shadowed areas with the help of a digital elevation model, they found the snow line, which they assumed was within 40 m of altitude to the equilibrium line due to the superimposed-ice facies separating these two lines. Studying the same glacier, *Winther* [1993a] also found these two areas to have distinct reflectance values.

Fresh snowfall may obscure the facies and produce erroneous results [*Hall et al.,* 1987]. *Williams et al.* [1991] cite an example where early snowfall down to lower elevations masked the real late-summer snow line. Debris may increase snow-line detection by enhancing the contrast between accu-
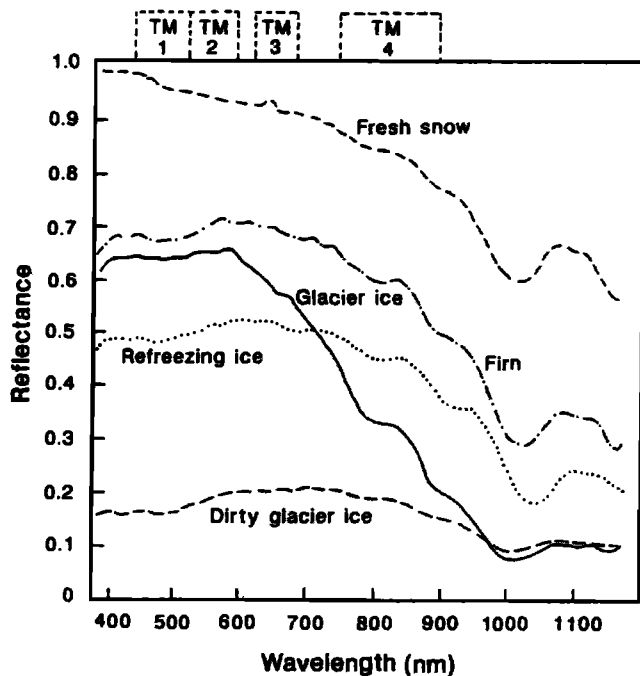
Table 1. Comparison of Sensors in the Visible and Infrared Spectrum.

Name of sensor	MERIS	MODIS	MOS	TM	ETM+	MSS	HRV	ASTER	AVHRR 1–3	AATSR	ATSR-2 (I)
Platform	Envisat	Terra	IRS/(PRIR)	Landsat 4–5	Landsat 7	Landsat 1–7	SPOT 1-5	Terra	NOAA 9–15	Envisat	ERS-1/2
Type	CCD pushbroom scanner	CCD whisk broom scanner	CCD pushbroom scanner	Opto-mechanical scanner	Opto-mechanical scanner	Opto-mechanical scanner	CCD push-broom scanner	Opto-mechanical scanner	Opto-mechanical scanner	Opto-mechanical scanner	Opto-mechanical scanner
Pixel size, m (bands)	300 (1–15) 1200 (1–15)	250 (1,2) 500 (3–7) 1000 (8–36)	520	30/120 (6)	30/60 (6) (15 PAN)	79	10 (Pan) 20 (1–3)	15 (1–3) 30 (4–9) 90 (10–14)	1100 (1–5) 4000 (1–5)	1000	1000
Spectral range, nm	390–1040	405–14,385	403–1650	450–12,500	450–12,500	500–1100	500–890 (1750)	520–11,650	580–12,400	550–12,000	500 (1600)–12,000
Numbers of bands	15	36	18	7	7 + Pan	4	3 (4 on Spot 4) + PAN	14	4/5/6	7	7 (4)
Temporal resolution, days	<3	<3	<5	<16	<16	<16/18	<3	<16	0.5	3	3
Revisit, days	35	16	5	16	16	16/18	26	16	1	35	35
Size of image, km	296 × 296 575 × 575 low res.; 1150 × 1150	2330 × 2020	200 × 200	185 × 172	185 × 170	185 × 185	60 × 60	60 × 60	2800 × various	512 × 512	512 × 512
Swath, km	1150	2330	200	185	185	185	60	60	2800	512	512
Ground coverage	up to 86.6°	up to 90°	Europe, India, North America (east)	up to 81°	up to 81°	up to 81°	up to 80°	up to 85° (1–9) up to 83° (10–14)	up to 90°	up to 83.9°	up to 83.9°
Mission Date	March 2002	Dec. 1999	March 1996	July 1982 to July 1987; March 1985	April 1999	since 1972	Feb. 1986; Jan. 1990; Sept. 1993; March 1998; 2002	Dec. 1999	since 1978	March 2002	July 1991; April 1995
Altitude, km	799.8	705	817	705	705	910/705	830	705	833	799.8	785
Inclination	98.55°	98.3°	98.7°	98.2°	98.2°	99.2°/98.2°	98.8°	98.3°	98.8°	98.55°	97.5°

Table 2. Comparison of SAR and Passive Microwave Sensors.

Sensor	ASAR	AMISAR	SAR	SAR	SIR-C	X-SAR	SSM/I	SMMR
Satellite	Envisat	ERS-1/ERS-2	RADARSAT	JERS 1	Space shuttle	Space shuttle	DMSP F8, F10, F11–14	Nimbus-7
Band	C	C	C	L	C,L	X	-	-
Frequency, GHz	5.3	5.3	5.3	1.275	5.3/1.275	9.6	19.35, 22.235, 37.0, 85.5	6.6, 10.7, 18.0, 21.0, 37.0
Polarization	HH/VV	VV	HH	HH	HH, VV, HV, VH	VV	V (all), H (not 22.2)	V, H
Resolution, m	<30/150/1000	<30	8–100	18	25	10–25	>25,000	>25,000
Repeat, days	35	35	24	44	N/A	N/A	<1	<6
Incidence angle	14°–45°	20°–26°	10°–60°	37°–43°	20°–55°	15°–55°	53.1°	50.3°
Image size, km	100 × 100 400 × 400	100 × 100	50 × 50 to 500 × 500	75 × 80	100 × 62.5	100 × 62.5 50 × 31.2	-	-
Swath, km	60–100 400	100	45–500	75	10–100	50/100	1400	780
Coverage	up to 87.5°N, 79.8°S	up to 84.5°	up to 90°	up to 85.5°	up to 60° (selected areas)	up to 60° (selected areas)	up to 90°	up to 85°
Mission	since March 1, 2002	since July 17, 1991; since April 20, 1995	since Nov. 4, 1995	since Feb. 11, 1992	April and Oct. 1994; Sept. 1999	April and Oct. 1994; Sept. 1999	since July 1987	Oct. 1978 to Aug. 1987
Altitude, km	799.8	785	798	568	222	222	830	955
Inclination	98.55°	97.5°	98.7°	97.7°	57°	57°	98.8°	99.1°

mulation and ablation areas, but it also can make it impossible to distinguish glacier ice from moraine. Both *Williams et al.* [1991] and *Hall et al.* [1987] found TM Band 4 (800–1110 nm) most useful for such studies, since it is more sensitive to grain size than the shorter-wavelength bands are. They used the TM4/TM5 ratio for their studies, which also improves the contrast between glacier and terrain.

Visible imagery cannot separate the percolation facies from the wet-snow facies [*Williams et al.*, 1991]. This transition is defined by water percolating into previous year's layers and, as such, having no surface manifestation. The dry-snow facies may be discernible from the wet-snow facies, but actually depends also on observations below the snow surface, i.e., the presence or absence of slightly wet snow in deeper layers.

SAR data offer the possibility to discriminate the actual zones of wet and dry snow on glaciers by means of backscatter intensity data. The capability of multitemporal SAR data for discrimination of radar glacier zones has been demonstrated by several authors [e.g., *Bindschadler and Vornberger*, 1992; *Shi and Dozier*, 1993; *Brown and Johansson*, 1998; *Ramage and Isacks*, 1998; *Rau and Saurer*, 1998; *Engeset and Ødegard*, 1999; *Matsuoka and Shiraiwa*, 1999]. A concise overview of glacier facies as seen with SAR imagery is given by *Fahnestock et al.*

[1993]. The ability of radar to penetrate the surface snow allows SAR imagery to discriminate facies based on important subsurface differences in structure. Thus, glacier facies are best identified in winter images, when no melting snow overlies the characteristic backscatter of a particular zone. *Partington* [1998] uses multitemporal images, acquired at different seasons, to define signatures for each facies for Greenland and Alaskan glaciers. *Jezek et al.* [1993] and *König et al.* [2001b] have done studies with airborne, multifrequency, multipolarisation SAR of Greenland and Norway. Temporal evolution of backscatter zones during summer was examined by *Rees et al.* [1995] for the Austfonna ice cap in Svalbard and by *Smith et al.* [1997] for the Stikine Icefield in British Columbia.

Relatively few studies have compared SAR with ground observations [e.g., *Demuth and Pietroniro*, 1999]. *Engeset and Weydahl* [1998] found absolute agreement for equilibrium line location with SAR and in situ stake measurements on Kongsvegen, Svalbard (Plate 1). They also presumed to see the previous year's snow line, which had been much lower than that of the present year. Similarly, without ground truth, *Hall et al.* [1995a] assumed to see the previous year's snow line on Brúarjökull, Iceland, which had been much higher, through the present year's firn. The boundary between the bare-ice facies and the wet-snow facies is distinct, which
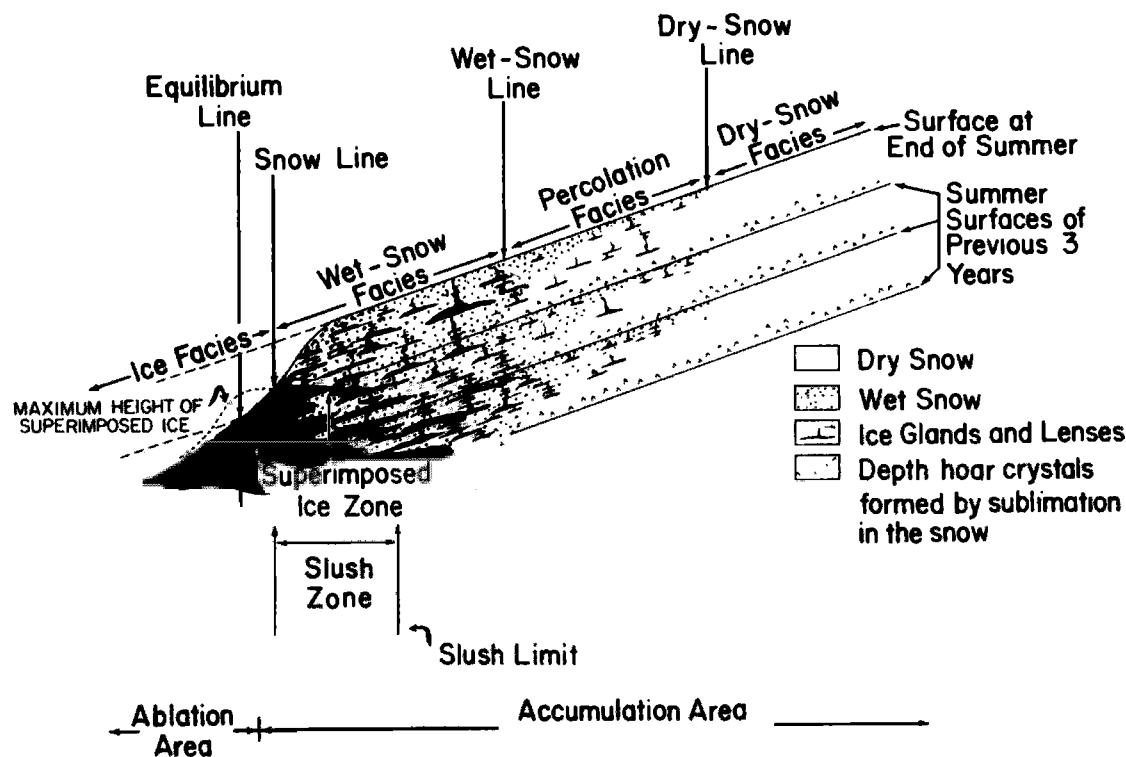
Figure 2. Generalized cross-section of glacier facies [from *Benson*, 1996]. Negligible melt occurs in the dry-snow facies. Some melting occurs in the percolation facies, forming ice lenses when it refreezes. The entire year's accumulation is raised to the melting point and wetted in the wet-snow facies, and some meltwater may percolate into previous year's layers. Extensive melting occurs in the superimposed-ice facies and a continuous mass of ice is formed. The bare-ice facies represents the ablation area. Reprinted with permission from the Cold Region Research and Engineering Laboratory (CRREL).

allows the determination of the snow line [*Bindschadler and Vornberger*, 1992; *Fahnestock et al.*, 1993; *Hall et al.*, 1995a; *Engeset and Weydahl*, 1998]. Overall, if water is present in the snow pack, it represents the primary effect on backscatter variations, while grain size is a secondary effect.

2.2. C-Band SAR Observations

Observations made with C-band SAR have been interpreted as follows for the different facies:

2.2.1. Dry-snow facies. Dry-snow facies are found only in Greenland and Antarctica (and on some glaciers in Alaska and Svalbard at high elevations, where the air temperature never rises above 0°C). In general, dry snow appears dark in SAR images because the absence of any surface melt and the consequently small snow grain size cause little volume scattering and thus give a relative low backscatter value [*Fahnestock et al.*, 1993]. σ^0, the backscatter coefficient, ranges between −14 and −20 dB, and does not show any

seasonal variation due to the absence of snowmelt events [*Partington*, 1998].

2.2.2. Percolation facies. At lower elevations, backscatter rises dramatically due to enhanced volume scattering from the network of subsurface ice bodies and larger snow grain sizes. Ice lenses in the snow cover due to occasional melt cause very high backscatter [*Bindschadler and Vornberger*, 1992; *Fahnestock et al.*, 1993] during the winter months, where σ^0 values range between −2 and −6 dB. However, the surface of the percolation facies becomes wet during the melt season, since superficial melting occurs regularly or occasionally, and then the backscatter drops to low values. Because the frequency of melting events generally decreases with increasing altitude, average grain size and number of ice layers decrease with altitude. Consequently, the dry snow line is a transition zone stretching over several kilometres, in which backscatter intensities gradually change. Several authors [e.g., *Smith et al.*, 1997; *Ramage and Isacks*, 1998] designated this zone on glaciers in Alaska as the dry zone.

In order to avoid ambiguities, for instance, with studies of the Greenland Ice Sheet, we stress that a consistent nomenclature is lacking but urgently required.

2.2.3. Wet-snow facies.

2.2.3. Wet-snow facies. The actual location of the upper transition depends on the recent meteorological conditions and is approximately coincident with the 0°C isotherm. In this zone, snow properties are dominated by metamorphism of wet snow leading to enhanced recrystallisation. This results in large snow grain size, further densification, and the production of high amounts of meltwater. Typical σ^0 values range between −11 and −23 dB.

The eroded and roughened surface that appear in the wet-snow zone causes an increasing diffuse component of surface scattering and therefore leads to higher backscatter values [*Braun et al.*, 2000]. *Smith et al.* [1997] designated this zone as the phase 2 melt zone (P2), which is characterised by σ^0 values between −3 and −8 dB [*Ramage and Isacks*, 1998]. Especially at lower elevations, slush accumulates at the snow–ice interface and can reach the surface in supraglacial depressions, where it creates slush lagoons and meltwater lakes. These cause dark patches in a SAR image. *Bindschadler and Vornberger* [1992], also studying Greenland, observed a distinct boundary at the percolation facies, the wet-snow facies being a bright area with dark patches (slush around surface lakes). However, the term slush zone for the wet-snow radar zone should be avoided, since even a liquid water content of only 1% in the snowpack results in a dramatic decrease of σ^0.

Fahnestock et al. [1993] observed a narrow zone of intermediate brightness due to snowmelt in Greenland. *Partington* [1998] identified three zones within the percolation and wet-snow facies. At high elevations, high backscatter is found in all seasons, since hardly any melt is present. At middle elevations, backscatter is high in winter and spring, but low in late summer due to surface melt. At low elevations, backscatter is high in winter, but low in spring and summer due to surface melt.

2.2.4. Superimposed-ice facies.

2.2.4. Superimposed-ice facies. On temperate glaciers, the late-summer snow line is nearly coincident with the equilibrium line. On some glaciers, however, a zone of superimposed ice separates the equilibrium line from the snow line. *Bindschadler and Vornberger* [1992] consider it very difficult to detect these facies, since both bare-ice facies and superimposed-ice facies consist of bare ice. *Marshall et al.* [1995], however, reported to have detected the superimposed-ice facies on Ayerbreen, Svalbard, on the basis of marked differences in surface roughness variability of bare and superimposed ice. *König et al.* [2002] successfully separated superimposed ice from glacier ice and firn on

Kongsvegen, Svalbard, using winter ERS SAR images from several years. Ground truth data, i.e., shallow ice cores, were used to confirm the satellite-derived surface classification.

2.2.5. Bare-ice facies.

2.2.5. Bare-ice facies. The lowest part of glaciers and ice sheets consists of the ablation area. Here, the total year's accumulation (and more) is lost by melting and subsequent runoff, and bare ice is exposed towards the end of the ablation season. According to *Bindschadler and Vornberger* [1992] and *Fahnestock et al.* [1993], the smooth ice surface, being a specular reflector, causes a lower backscatter than the wet-snow facies in winter. Typical backscatter values vary between −10 and −15 dB. In summer, however, backscatter of the bare-ice facies appears higher due to the presence of melt and low backscatter in the wet-snow facies. *Partington* [1998] similarly finds a higher backscatter in September than in June and December from the bare ice facies. In contrast to the above, *Partington* [1998] finds ice a strong scatterer, for which the high backscatter is attenuated in winter by overlying snow. Crevasses in the bare-ice facies appear as bright areas [*Fahnestock et al.*, 1993; *Engeset and Weydahl*, 1998].

2.2.6. Glacier mapping.

2.2.6. Glacier mapping. It is often difficult to discriminate glacier ice from the surrounding moraine by SAR data due to similar backscatter characteristics [e.g., *Shi and Dozier*, 1993]. *Engeset and Weydahl* [1998] distinguished non-glaciated ground from glacier ice in all seasons but did best in spring. Ice-margin lakes, if present, provide a way to detect the edge of a glacier using SAR and even Landsat data [*Hall et al.*, 1995a].

2.2.7. Equilibrium line.

2.2.7. Equilibrium line. The transient snow line on a glacier is extremely sensitive to the prevailing meteorological conditions. At the end of the ablation period, which corresponds to the end of the mass balance year, the transient snow line may be regarded as an approximation of the equilibrium line altitude (ELA), which is directly related to glacier mass balance. Due to backscatter differences of the radar zones, SAR data offer the possibility to identify the location of the transient snow line [e.g., *Ahlnäs et al.*, 1992; *Dowdeswell et al.*, 1994; *Marshall et al.*, 1995; *Adam et al.*, 1997; *Bingham and Rees*, 1997; *Kelly et al.*, 1997]. The highest position of the transient snow line can also be detected under a thick, dry, winter snow cover, which appears to be transparent for microwaves. This offers the possibility to locate the ELA during winter conditions, when liquid water is absent. However, if superimposed-ice facies occur, the ELA may be located inside this zone of refrozen melt water and thus make it impossible to use SAR for mass balance determination. *König et al.* [2001b] were able to localize the firn line, i.e., the lower

boundary of snow layers from several previous years, but not the snow line using airborne multipolarisation SAR data from a single year. Later, *König et al.* [2002] identify the firn line on a series of winter SAR images from Kongsvegen, Svalbard. They suggest that the firn line altitude (FLA) could be used as a long-term indication of mass balance changes. For the same study area, *Engeset et al.* [2002] report that the minimum and maximum altitude of the equilibrium line and perennial firn accumulation areas on timescales of a couple of years could be mapped but that the altitude of the annual equilibrium line could not be resolved through the analysis of 8 years of wintertime ERS SAR data.

3. GLACIER VELOCITY

3.1. Glacier Velocity With Feature Tracking

Glacier velocity can be determined with sequential satellite imagery by observing the movement of surface features, such as crevasses, over time [*Bindschadler and Scambos*, 1991]. This can be done simply by visual registration [*Lefauconnier et al.*, 1994]. *Lucchitta et al.* [1993] coregister sequential images, one in the red channel, one in the green channel. Features that have moved will appear as tones of green or red. Moving one image over the other until a moved feature matches results in a yellow tone for this feature and the moved distance can be determined.

Scambos et al. [1992] developed an automated method, which was successfully applied in many studies in Antarctica [*Bindschadler and Scambos*, 1991; *Scambos and Bindschadler*, 1993; *Bindschadler et al.*, 1994; *Lucchitta et al.*, 1995; *Bindschadler et al.*, 1996; *Rosanova et al.*, 1998] (see Figure 3). A comparable method was used by *Rolstad et al.* [1997] for a surging glacier in Svalbard. Sequential images taken at the same time are used so as to have similar illumination. Additionally, a principal component image is used, which enhances topography. The images are then split into a long-wavelength image and a short-wavelength image by using high- and low-pass filters, respectively. The long-wavelength image contains topographic effects only, which have a low spatial frequency, and is used to coregister images. This approach is necessary on ice sheets, where nonglaciated terrain often is not available for coregistering images. The short-wavelength image is used to track small,
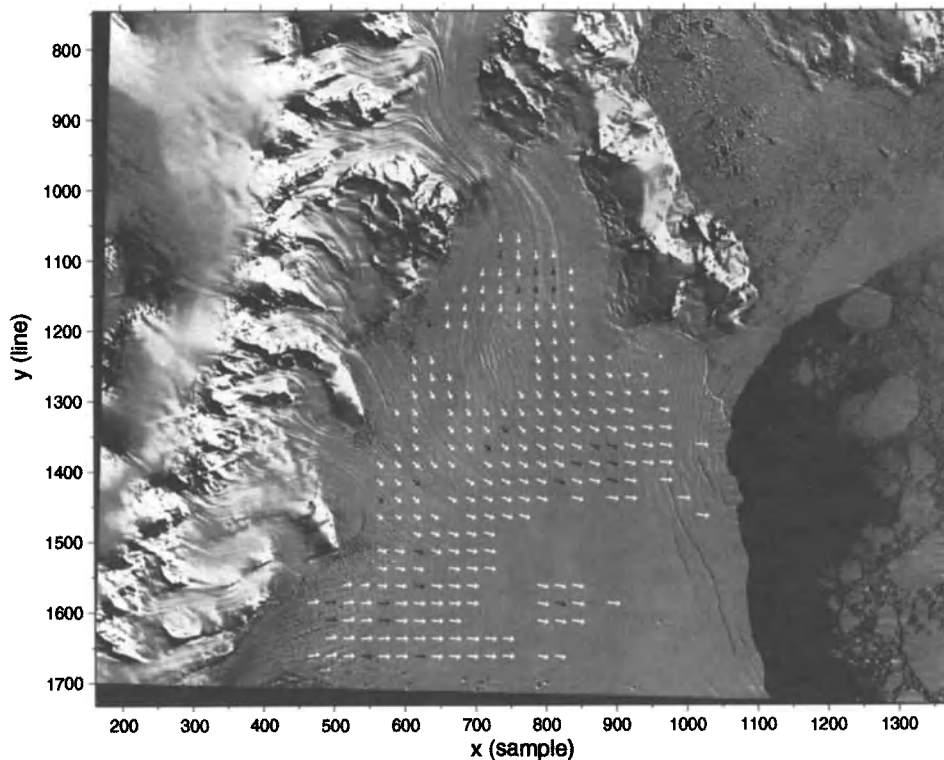
Figure 3. Landsat-TM image collected on 5 November 1989. The plotted velocity field is derived from a MSS-TM image pair using cross-correlation to track features by *Scambos et al.* [1992]. Vector lengths correspond to actual displacements over the 3.68-year interval. Vector grid spacing is 25 pixels (1425 m) [from *Bindschadler et al.*, 1994]. Reprinted from the *Annals of Glaciology* with permission of the International Glaciological Society.

sharp features. A chip (16 pixels × 16 pixels or 32 pixels × 32 pixels) from the first image, containing a feature, is moved over the second image. The correlation field is calculated and the position is determined where the correlation is highest. Since a whole chip is matched rather than a single pixel, the position of the correlation maximum will be more accurate than the pixel size. *Scambos and Bindschadler* [1993] give an accuracy of about 0.2 pixels, which can be further improved in areas with many measurements. *Lucchitta et al.* [1993] find an error of as little as 20 m yr^{-1} when older Landsat MSS images, with 80-m-resolution pixels separated by more than 10 years, are used. *Frezzotti et al.* [1998] compared velocities derived by feature tracking with global positioning system (GPS)-inferred velocity measurements. They found good agreement, with maximum differences of 15–20 m yr^{-1}. *Bindschadler et al.* [1996] calculated the surface strain rate fields from velocities of Ice Stream D and E in Antarctica as determined by feature tracking. By combining the velocity measurements with transverse depth profiles collected by airborne radar, they also calculated discharge fluxes. By comparing Scambos' method to visual tracking of features with repeat photogrammetry, *Whillans and Tseng* [1995] concluded that the "machine beats the human". The large number of tracked features that an automated method is able to process results in a much more detailed velocity field.

All the feature-tracking studies above, as well as the most recent investigation of *Scambos et al.* [2004] on glacier acceleration and thinning after the collapse of an ice shelf in Antarctica, used Landsat imagery. More recently, *Berthier et al.* [2005] successfully completed a detailed map of the ice-velocity field in the French Alps by cross-correlating SPOT-5 optical images. *Fahnestock et al.* [1993] and *Lucchitta et al.* [1995] successfully used this method on SAR imagery. An additional use of this method is tracking the motion of "speckle" in SAR imagery. Speckle gives SAR images the grainy appearance and is the result of constructive or destructive interference of the coherent integration used to form the image. This speckle pattern is the result of the arrangement of scatters in a region and has been used successfully to track the motion of the surface between images collected at different times [*Gray et al.*, 2001].

3.2. Glacier Velocity Using SAR Interferometry

The possible use of SAR interferometry (InSAR) to determine glacier velocity even more accurately than by feature tracking was developed by R. M. Goldstein after the launch of ERS-1 [*Goldstein et al.*, 1993]. A detailed description of the theory of InSAR can be found in *Fatland and Lingle* [1998]. Recent results on the use of InSAR to determine

glacier velocity can be found in *Joughin et al.* [2003] and *Rignot et al.* [2004a,b; 2005].

The amplitude of the returned radar signal is influenced by the target properties. The time delay of the signal gives the distance between radar and target. The distance between sensor and target is called the range. With a SAR sensor, identical signals are transmitted, frequently making it difficult to determine the absolute time delay, but the phase of the reflected wave is the key information used in interferometry. While the phase information of a single SAR image is random and of no use, two SAR images taken from approximately the same location will have nearly identical reflection characteristics but slightly varying phases. Any slight differences in range of the same pixel in the two images are measurable as a phase difference between the two reflected waves in each image. An image of these phase differences is called an interferogram and usually contains fringes of constant phase that represent a coherent spatial pattern of path length differences resulting from either surface topographic variation and/or movement of the surface (Plate 2). Phase noise is commonly 15°, which translates into roughly 4% of the wavelength. This is a very small distance, e.g., 3 mm for C-band, illustrating the path length precision possible with this technique.

Assuming no movement of a target, the phase in an interferogram is influenced by geometric effects and the topography. Once geometric effects are removed, it is possible to calculate the elevation of a target and create a digital elevation model (DEM). For this the range and the baseline (i.e., the distance between the two satellite orbits) need to be known. Since satellite orbits are not known well enough to determine the baseline, the baseline is determined iteratively. This results in an effective baseline, which compensates for errors. Inaccuracy due to baseline errors is discussed by *Joughin et al.* [1996a].

Phase differences contain a 2π ambiguity, since the phase values do not continue beyond 2π but start again with zero (Figure 4). In other words, a path difference of 1.5 wavelengths has the same phase difference as a path difference of 0.5 wavelength. Resolving this 2π ambiguity is called "unwrapping the phase", e.g., by adding or subtracting 2π to eliminate discontinuities across fringe boundaries (Figure 4).

For a moving target, the phase difference is additionally influenced by the translation of the target. The phase difference due to topography has to be extracted to determine the velocity. If a precise DEM and accurate orbit data are available from the study area, then a synthetic interferogram containing only the topographic phase can be made [*Joughin et al.*, 1996a, 1998; *Mattar et al.*, 1998]. The synthetic interferogram is then subtracted from the real interferogram,
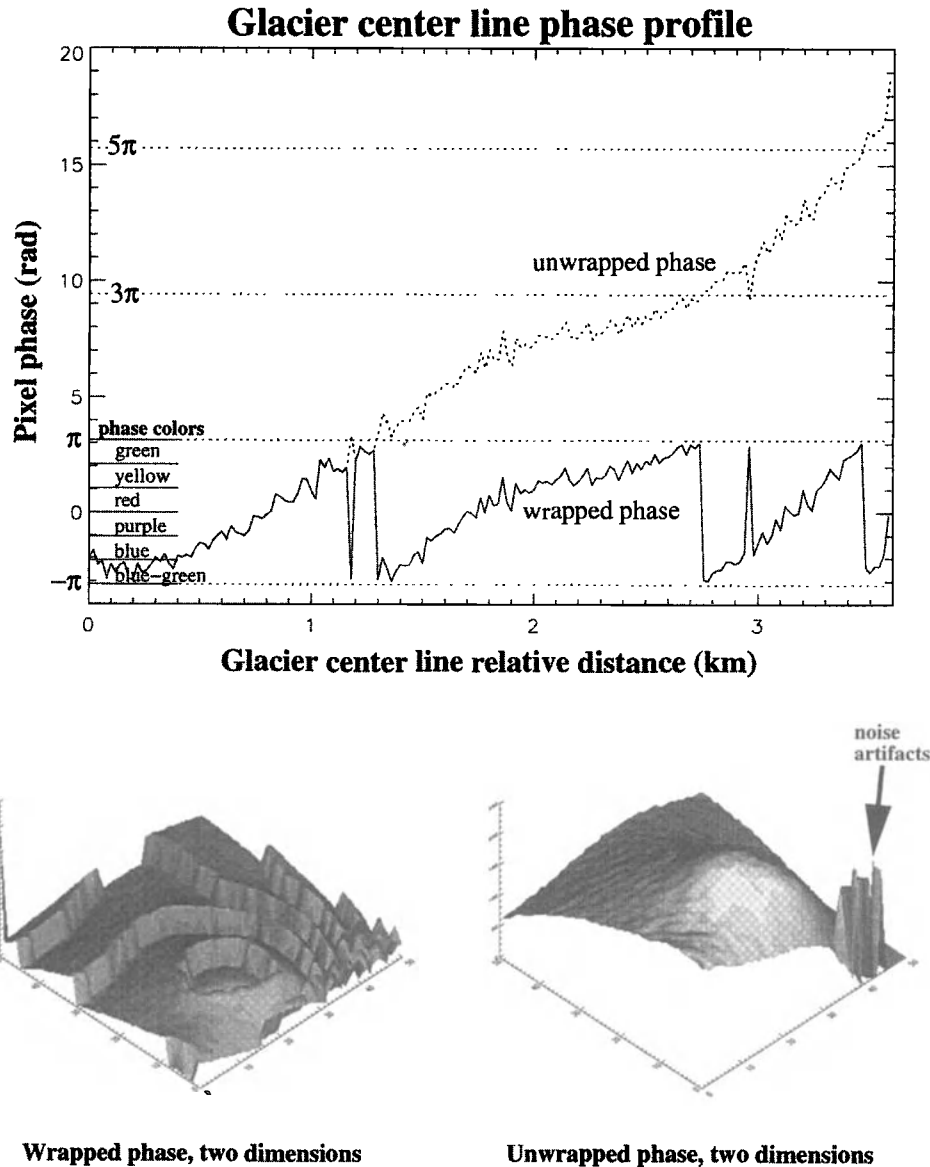
Glacier center line phase profile

Figure 4. Phase unwrapping in one and two dimensions [from *Fatland and Lingle,* 1998]. Jagged nature of the center-line plot is indicative of data noise rather than variations in velocity. Reprinted from the *Journal of Glaciology* with permission of the International Glaciological Society.

resulting in an interferogram that contains only the phase term due to translation.

If surface topography is unknown, two interferograms are needed to extract the translation phase term. This approach was used by (e.g.) *Joughin et al.* [1998] and *Fatland and Lingle* [1998]: Images 1 and 2 result in interferogram A. Images 3 and 4 result in interferogram B of the same site some time later. Assuming that the target, e.g., the glacier, moves with constant velocity, then it moved Δx between the acquisition of images 1 and 2 and the same distance Δx

between the acquisition of images 3 and 4, assuming the time interval is constant. Subtracting interferogram B from interferogram A cancels the phase-difference term due to translation, leaving only the topographic phase difference in the differential interferogram C. Subtracting C from A again gives an interferogram containing only the translation phase-difference term. Thus, this method of velocity determination is referred to as "double-differencing".

The velocity determined by this method is, however, only the component along the line-of-sight from sensor to target.

Therefore, having only one interferogram requires two further assumptions to obtain the complete three-dimensional velocity vector. Having two interferograms from two look directions, i.e., an ascending and a descending pass, only one additional information is needed. Having three look directions is theoretically possible with a sensor that can look both right and left (using ascending and descending orbits), but has not yet been demonstrated. Instead, most studies assume ice flow parallel to the glacier surface [*Joughin et al.*, 1996a, 1998; *Rignot et al.*, 1996; *Fatland and Lingle*, 1998; *Mattar et al.*, 1998] as the first assumption and either flow along the steepest slope [*Joughin et al.*, 1996a; *Mattar et al.*, 1998] or parallel to the valley walls [*Fatland and Lingle*, 1998] as the second assumption. *Mattar et al.* [1998] and *Eldhuset et al.* [2003] find good agreement with in situ measurements. Having two look directions, *Mattar et al.* [1998] examined the three possible cases for the one needed assumption. The first assumption, flow along steepest slope, failed in a glacier bend; the second assumption, flow along the centreline, failed in some places of complex flow; and the third assumption, flow parallel surface, failed in areas of high vertical velocity (accumulation/ablation area). Generally, however, *Mattar et al.* [1998] found good agreement with in situ measurements.

We refer to *Mattar et al.* [1998] for further discussion on accuracy and comparison with in situ measurements. The major limitation is the ability to correlate the phase information. Poor correlation is most often due to a large baseline that alters the radar return, or to a temporal change in the target's radar properties. *Rignot et al.* [1996] found that interferometry-derived velocity and velocities by feature tracking complement each other and overlap. Feature tracking with optical imagery requires surface features. Speckle tracking can extend the mapped regions devoid of visible surface features. The planned RADARSAT-2 satellite is expected to make the speckle tracking technique suitable for monitoring glacier surface motion [*Short and Gray*, 2004]. Interferometry, by virtue of its greater precision, can be utilised anywhere that images correlate. Temporal decorrelation usually dictates a shorter temporal separation for interferometric measurements than for feature tracking.

4. GLACIER AND ICE SHEET TOPOGRAPHY

4.1. Glacier/Ice Sheet Topography With Radar Altimetry

Radar altimetry does not provide satellite images but is a direct measurement of elevation. Figure 5 shows this method for a flat surface. A radar pulse is emitted towards the ground and the distance between satellite and ground (i.e., the range) is determined from the time delay of the return signal. As the pulse's energy first returns to the satellite, the leading edge of the return waveform is formed. As time proceeds, the "pulse-limited footprint", the area simultaneously illuminated by the finite-length pulse, spreads out away from the surface point nearest the satellite. The elevation, calculated from the range and the known orbit position, is the average elevation within the initial pulse-limited footprint, typically having a diameter of about 2 km. An example is shown in Figure 6.

Retracking algorithms are used to detect the leading edge in the return signal. *Davis* [1996] compares two such commonly used algorithms. A correction also needs to be applied for sloped surfaces. Unlike in Figure 5, the first return from sloped surfaces does not come from directly below the satellite but is displaced upslope, often on a local topographic rise. The effectively measured footprint is thus displaced by up to several kilometers, and the set of measurements can be biased toward higher elevations. We refer to *Bamber* [1994a] and *Brenner et al.* [1983] for discussions on retracking and slope correction.

Altimetry-derived elevation has been compared to ice-shelf elevation inverted from Antarctic ice thickness data [*Bamber and Bentley*, 1994], airborne altimetry data in Greenland [*Ekholm et al.*, 1995], GPS-derived elevation in Antarctica [*Phillips et al.*, 1998], and airborne laser altimetry in Greenland [*Bamber et al.*, 1998]. Agreement is usually within a few metres (<3 m) for flat surfaces, but increases for larger slopes to mean differences of around 10 m for $0.7°$ slopes [*Ekholm et al.*, 1995; *Bamber et al.*, 1998]. Slopes greater than $0.7°$ are difficult to measure because the nearest surface receives so little transmitted energy. In general, errors can be caused by inhomogeneous terrain, uncertainties in satellite-orbit position, and penetration of the radar pulse into the surface layer. The latter can be up to 3.3 m [*Ridley and Partington*, 1988].

Altimetry has been used to create elevation maps of Antarctica [*McIntyre*, 1991; *Bamber*, 1994b; *Legrésy and Rémy*, 1997; *Herzfeld and Matassa*, 1999] and Greenland [*Bindschadler et al.*, 1989]. It has also been used for detecting elevation changes over time in these areas [*Zwally et al.*, 1989; *Herzfeld et al.*, 1997; *Lingle and Covey*, 1998; *Davis et al.*, 2001; *Paterson and Reeh*, 2001]. Snowpack characteristics can also be mapped due to different penetration of the radar signal [*Partington et al.*, 1989; *Legrésy and Rémy*, 1998].

4.2. Glacier/Ice Sheet Topography From Visible Imagery

When the snow surface within a visible wavelength image is of sufficiently homogeneous reflectivity, the brightness of
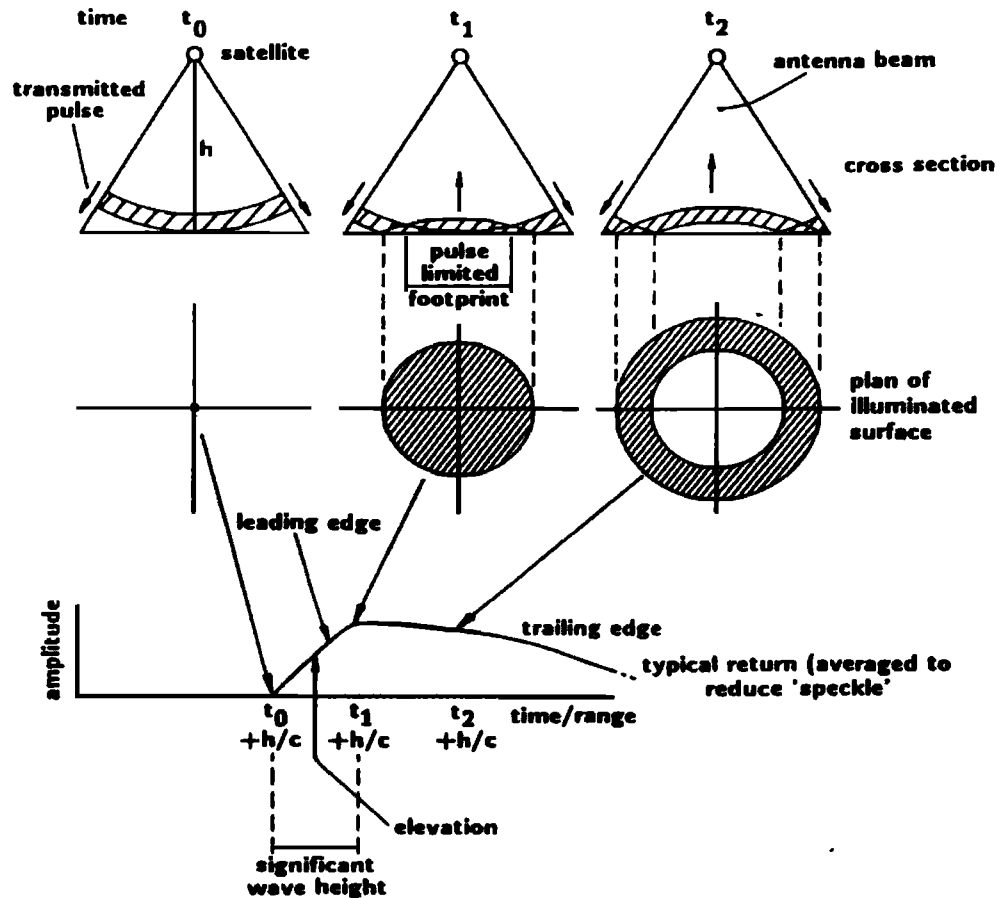
Figure 5. The interaction of an altimeter radar pulse with a horizontal and planar surface, from its initial intersection (t_0), through the intersection of the back of the pulse shell with the surface (t_1), to the stage where the pulse begins to be attenuated by the antenna beam (t_2). The return is from the surface only [from *Ridley and Partington*, 1988].

each pixel can be converted to a surface slope [*Bindschadler and Vornberger*, 1994]. Integration of these slopes along the direction of solar illumination produce profiles of relative elevation that can be combined and converted to a field of absolute elevation with control elevations. Alternatively, two images with different illumination directions can provide the complete surface slope, decreasing the required number of control elevations [*Scambos and Fahnestock*, 1998]. Control elevations also help in determining the average surface reflectivity and the contribution of atmospheric scattering to the image brightness.

4.3. Glacier/Ice Sheet Topography With SAR Interferometry

InSAR, as discussed earlier, can be used to generate DEMs. As seen in Figure 6, interferometric DEMs show more detail than topography from radar altimetry [*Joughin et al.*, 1996b], but control points are needed for accurate

elevation. *Joughin et al.* [1996b] determine topography in Greenland with an absolute elevation accuracy of about 4 m. Similarly, *Unwin and Wingham* [1997] studied the topography of the Austfonna ice cap in Svalbard.

Rignot [1996; 1998] has also used interferometry to locate the hinge line of floating ice stream tongues in Greenland and Antarctica. Vertical displacement of the floating ice caused by tides generates a tight band of phase-difference fringes at the boundary between floating ice and grounded ice. The migration of this boundary has been followed through time by *Rignot* [1996; 1998]. *Muskett et al.* [2003] more recently used DEMs of the Bagley Ice Valley and Malaspina Glacier, Alaska, produced from airborne and spaceborne InSAR data to estimate elevation changes between 1972/1973 (aerial photographs) and 2000 (InSAR). The Bagley Ice Valley was estimated to have thickened by 10 ± 7 m (average) in its accumulation area, and glaciers of the Malaspina complex to have thinned by 47 ± 5 m, mostly in the ablation area.
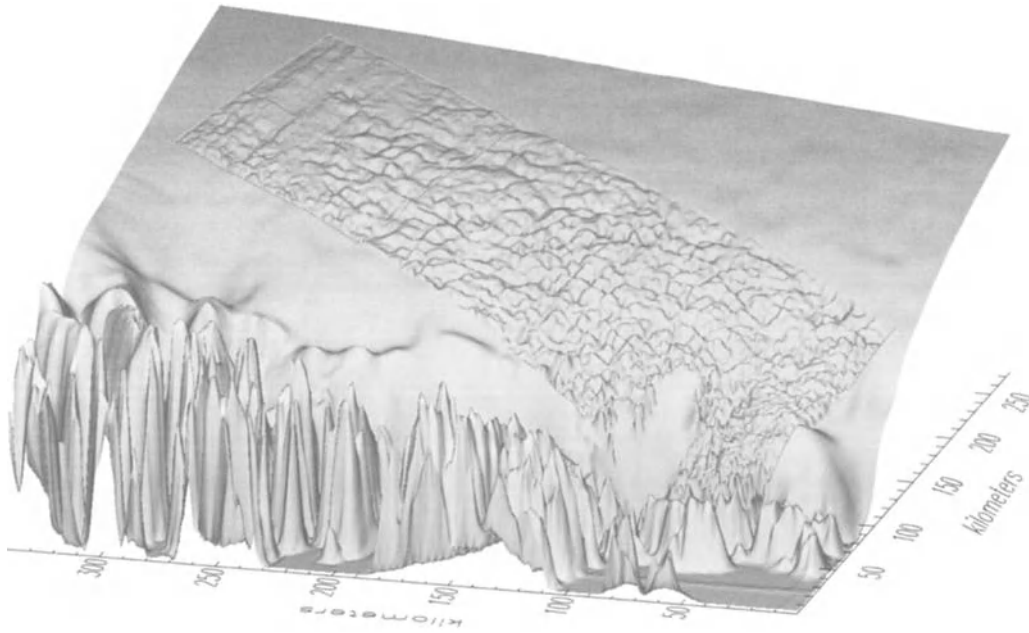
Figure 6. Shaded surface of the combination of radar-altimetry-derived DEM and the smoother interferometry-derived DEM [from *Joughin et al.*, 1996b]. Reprinted from the *Journal of Glaciology* with permission of the International Glaciological Society.

5. MAPPING GLACIERS, GLACIER CHANGE, AND CHARACTERISTICS

Remote sensing allows mapping of glacier extent and surface features on large scales not feasible with ground observations. Many studies have been conducted, mostly by visual interpretation of satellite images, i.e., with little or no image processing, e.g., *Østrem* [1975], *Cogley and Adams* [2000], *Bindschadler et al.* [2001], and *Williams and Dowdeswell* [2001]. *Dowdeswell and Williams* [1997] identified surge-type glaciers from surface features such as looped moraines and crevasses. *Dowdeswell et al.* [1995] identified ice divides and drainage basins from visible as well as SAR imagery. *Hambrey and Dowdeswell* [1994] derived the flow directions of an Antarctic ice shelf from surface features (foliation, crevasses, and moraines), but *Casassa and Turner* [1991] demonstrated that some features can be distorted by time-variable flow fields, and *Fahnestock et al.* [2000] have used flow features to interpret a variable flow history of the Ross Ice Shelf.

The visible bands are more suitable than infrared bands for studying topographic features. A principal component analysis on multispectral images supports this observation. The first principal component image, PC1, contains most of the image variance attributable to topography and is dominated by the visible bands [*Winther*, 1993b; *Orheim and Lucchitta*, 1988]. A PC1 image thus enhances topographic effects and is therefore often superior to the visible bands themselves. The PC2 image is mostly related to the infrared bands (e.g., Landsat TM Bands 5 and 7) and enhances surface characteristics not seen in the visible, such as patterns due to surface grain-size variations [*Orheim and Lucchitta*, 1987; *Winther*, 1993b]. Band ratioing (e.g., Landsat TM Bands 4/5, 2/5, 4/2) reveals subtle features like dry watercourses and frozen lakes [*Winther*, 1993b; *Winther et al.*, 1996].

Efforts are underway to create coastal-change and glaciological maps of the entire perimeter of Antarctica using Landsat data from the 1970s until today [*Williams et al.*, 1995; *Swithinbank et al.*, 1997; *Ferrigno et al.*, 1998]. Also, Landsat TM image maps, mosaiced from many cloud-free, enhanced images, are produced for some areas [*Ferrigno et al.*, 1994]. Many other studies analysed glacier changes and fluctuations in Antarctica by using SAR and visible satellite imagery from different years [*Pattyn and Decleir*, 1993; *Skvarca*, 1994; *Skvarca et al.*, 1995; *Wendler et al.*, 1996]. *Hall et al.* [1992] did the same for glaciers in Iceland and Austria, *Hall et al.* [1995b] for Alaskan glaciers, *Jacobs et al.* [1997] for Canadian glaciers, and *Paul et al.* [2004] for Swiss glaciers. Starting with declassified imagery from the 1960s, *Sohn et al.* [1998] compared a time series of images to study fluctuations of Jacobshavn glacier in Greenland. *Skvarca et al.* [1999] summarised the retreat of ice shelves at the Antarctic Peninsula, presenting a 30-year-long time series from various satellite sensors (Figure 7). The recent ice shelf

collapses at the Antarctic Peninsula have been discussed by *De Angelis and Skvarca* [2003] and *Rott et al.* [2002].

A cloud-free AVHRR map of Antarctica has been published by the USGS [*Ferrigno et al.,* 1996]. This map was mosaiced from 38 images collected between 1980 and 1994. Details on the processing and geometric corrections can be found in *Merson* [1989]. *Winther et al.* [2001] used the AVHRR mosaic to map blue ice areas and found them to occupy about 1% of Antarctica.

The whole Antarctic continent has also been mapped with SAR images during the RADARSAT Antarctic Mapping Mission in fall 1997 [*Choi,* 1999; *Jezek,* 2002]. RADARSAT was rotated from the normally right-looking mode into left-looking mode to allow complete coverage of Antarctica, col-

lecting more than 8000 images in an 18-day period. A second Antarctic mapping with RADARSAT in fall 2000 collected three full cycles of images (each lasting 24 days) north of 79°S for interferometric analysis. Complete Antarctic coverage to its southern limit of 82.6°S with the ETM+ imager on Landsat-7 has been accomplished during the 1999–2000 and 2000–2001 austral summers. In addition, the ETM+ is tasked to image all land ice areas at least once per year. A similar tasking for all glaciers and ice sheet margins has been assigned to the Advanced Spaceborne Thermal Emission and Reflection Radiometer (ASTER) imager on board the Terra spacecraft.

6. SURFACE FEATURES AND SNOW PACK CHARACTERISTICS

The earliest satellites took pictures from space using film. This means of investigating the polar regions remains useful today, although the sophistication of the imaging systems and their resolution has increased dramatically. Presently, spatial resolution varies over more than three orders of magnitude from the approximately 1-km resolution of the Advanced Very High Resolution Radiometer [AVHRR], to the 1-m resolution of the recent commercial imagery IKONOS. In between are the familiar series of Landsat and SPOT imagers. Each of these sensors is capable of collecting data within specific spectral bands, yet most snow and ice targets contain no significant spectral variations in the visible wavelength region. Equally important is the radiometric resolution of these sensors. The high surface reflectance of snow and ice can saturate some sensors, however, and if the dynamic range is large, the radiometric resolution suffers. This can result in a poor signal-to-noise ratio and make many detection of important surface features difficult. Despite these challenges, satellite imagery has been a powerful tool in the identification, location, and mapping of a variety of surface features.

Figure 7. Section of the Kosmos KATE-200 photograph taken on 3 October 1975, showing superimposed ice front positions (numbers in black boxes) from different years for Larsen Inlet and Larsen A ice shelf at the Antarctic Peninsula. 1: August 1963, 2: October 1975, 3: November 1978, 4: February 1979, 5: March 1986, 6: November 1989, 7: December 1992, 8: January 1993, 9: February 1993, 10: October 1994, 11: January 1995, 12: January, 1995, 13: January 1995, 14: March 1995, 15: March 1997, 16: July 1997. The front positions after 1992 were derived from ERS-SAR, except for position 10, which was surveyed with GPS. The positions prior to 1992 correspond to Landsat TM (5 and 6), Landsat MSS (3 and 4), Argon (1), and Kosmos KATE-200 (2) [from *Skvarca et al.,* 1999].

6.1. Crevasses and Flow Dynamics

The coarser resolution AVHRR data have been used to map the undulated surface of the large ice sheets and ice caps where the wide swath can cover these large areas with a limited set of passes [*Merson,* 1989]. Variations in image brightness reveal the surface topography. The first scientific discussion of ice sheet dynamics based on AVHRR imagery focused on the set of adjacent ice streams in West Antarctica [*Bindschadler and Vornberger,* 1990]. On fast-flowing ice, the undulations are stretched along the flow and have been used as passive tracers of the flow field. Normally the tracers are oriented parallel to the current flow direction; however,

deviations in this parallelism indicate temporal changes in the flow direction. *Fahnestock et al.* [2000] used imagery of the Ross Ice Shelf to infer large changes in ice-stream discharge. Very flat terrain usually indicates floating ice. A dramatic example is the large subglacial Lake Vostok underneath the Antarctic ice sheet [*Kapitsa et al.*, 1996]. This transition from an undulated surface to a smoother surface is also used to locate and monitor the grounding line of ice streams and outlet glaciers [*Bindschadler and Vornberger*, 1990].

Fields of intense crevassing can be seen on AVHRR imagery, but higher spatial resolution is required to see the orientations of individual crevasses. Landsat and SPOT have become very useful means for studying the pattern of crevassing and inferring the orientation of local stresses. Crevasses formed at a specific site are carried downstream by ice flow, being replaced at the formation site by subsequent crevasses. Changes in the character of the downstream trail of crevasses reveal much about the conditions downstream. Deformation of the crevasses indicates the tensile and compressive character and orientation of the stress field downstream. The burial rate of the open crevasses hints at accumulation rate, and any sudden change in crevasse character indicates a change in ice flow rate at a time that can be estimated by the distance travelled and the current ice speed.

Radar imagery can be used in many of the same ways as visible imagery. In addition, the radar's ability to penetrate the surface has demonstrated an ability to detect crevasses where no surface expression is seen. This can be useful in identifying the actual formation site. For monitoring studies, the radar's ability to penetrate clouds is a huge advantage in collecting a regular set of data. Most current satellite radars achieve a high resolution, comparable to Landsat and SPOT, using synthetic aperture technology. RADARSAT includes a coarser mode where spatial resolution is sacrificed to 100 m for a wider swath 500 km across. This mode has been very popular within the scientific community in general and is of great use in monitoring ice sheet behaviour.

Two ice sheet phenomena that require frequent monitoring are iceberg calving and ice-shelf disintegration. The most recent decade has seen numerous large calving events, resulting in the formation of the largest iceberg on record. Large icebergs last longer and can drift farther, increasing the likelihood of interfering with shipping or movements of Antarctic researchers. Coarse-resolution imagery is well suited to the identification of new icebergs and subsequent tracking of their locations. Higher resolution imagery is needed to study the processes of crack initiation and propagation. A similar combination of moderate- and high-resolution imagery has been brought to bear on the issue of ice-shelf disintegration [*Rott et al.*, 1996; *Scambos et al.*, 2000].

6.2. Albedo and Grain Size

Ice and snow are two of the most reflective natural surfaces. Albedo determines how much solar radiation is absorbed and is a critical quantity in the energy balance of glaciers and ice sheets. Because the albedo is so large, a small albedo change means a large change in the amount of absorbed energy [*Scherer et al.*, this volume]. For large-scale studies, AVHRR data have been employed most often because of the wide swath and frequent coverage this method provides. However, AVHRR only has one channel in the visible portion of the spectrum and one in the near infrared, its remaining channels being at wavelengths where ice is not particularly reflective. Extension of such limited spectral information to broadband characteristics is difficult. In addition, the calibration of the AVHRR sensors is known to change with time. A discussion of the challenges in using these data and practical solutions to determining the broadband albedo from narrow spectral information can be found in *Steffen et al.* [1993], *Haefliger et al.* [1993], *Nolin and Stroeve* [1997], and *Winther et al.* [1999].

Spectral reflectance varies with grain size [*Dozier*, 1989; *Gay et al.*, 2002]. The more quantitative approaches have used this fact by employing band ratios. *Bourdelles and Fily* [1993] applied this dependence to TM imagery; *Nolin and Stroeve* [1997] utilised AVHRR data. In the latter case, the grain-size analysis was conducted in combination with a snow-metamorphism model that derived independent estimates of snow-grain size driven by temperature data from the thermal band of AVHRR. *Klein and Stroeve* [2002] developed and validated a snow albedo algorithm for the Moderate Resolution Imaging Spectrometer (MODIS) instrument. *Greuell and Oerlemans* [2004] propose a set of equations for obtaining broadband albedos derived from narrowband albedos from TM, AVHRR, MODIS, and the Medium Resolution Imaging Spectrometer (MERIS) for glacier ice and snow. The narrowband-to-broadband albedo conversion equations developed in that study describe measurements with root-mean-square differences of about 0.016. Also, the accuracy of the MODIS 16-day albedo product (MOD43) for snow has been assessed using ground-based albedo observations of the Greenland Ice Sheet [*Stroeve et al.*, 2005]. Results indicate that the MOD43 product retrieves snow albedo with an average root-mean-square error between ±0.04 and ±0.07. A recent further improvement to the retrieval algorithm provides daily snow/ice albedo estimates with a mean biais of less than 0.02 and residual standard error of 0.04.

6.3. Surface Temperature

Not only does temperature drive the rate of snow metamorphism, it is also a critical parameter in the rate at which ice flows. Warm ice deforms much more readily than cold ice. The warmest temperatures (softest ice) occur nearest the bed closest to the source of geothermal heat and farthest from the cold polar atmosphere and the view of satellites. Nevertheless, the thermal properties of ice are well behaved, and surface temperature, along with an estimate of subglacial heat flux, can be used to model the vertical temperature profile and estimate the thermal condition at the ice–bed interface.

Temperatures on specific days can be extracted from the thermal-infrared channels of Landsat [*Orheim and Lucchitta*, 1988] or AVHRR [*Steffen et al.*, 1993], but the mean annual air temperature is more meaningful for ice temperature modelling. A compilation of surface temperatures in the polar regions using the Temperature Humidity Infrared Radiometer [THIR), the forerunner of the thermal channel of the AVHRR, showed a strong correlation of surface temperature with ice sheet elevation [*Comiso*, 1994]. These data agreed very well with surface station data and were gauged to be accurate within 2 K. *Haefliger et al.* [1993] have been able to achieve a 0.5-K agreement between surface measurements and AVHRR-derived surface temperatures.

A very important temperature for snow and ice studies is the melting temperature. When this threshold is reached, significant thermal and structural ramifications ensue within the underlying snowpack to form the various snow facies discussed earlier. The passive microwave instruments easily detect this thermal threshold. When snow becomes wet, its emission of energy increases dramatically. Passive microwave instruments measure this energy, expressed as "brightness temperature", the product of physical temperature and emissivity (Figure 8). Passive microwave emissions from the Earth have been monitored continuously at a number of frequencies since 1973. The data are collected at a much lower spatial resolution, typically 25 km, but the temporal resolution is near-global coverage every 2 days. As a sensitive indicator of melt onset, this data set has a uniquely useful role in monitoring the duration and extent of melting conditions over large ice masses over many years [*Zwally and Fiegles*, 1994] (Plate 3). More difficult to quantify is the amount of melting, i.e., the ablated volume.

In regions that do not experience melting, the relative stability of microwave emissivity affords passive microwave data a different use. By assuming the annual variation of emissivity, its effect on brightness temperature can be removed, leaving only the physical temperature. This temperature is that of the snowpack, rather than the air temperature, albeit it is a depth-weighted average dependent on the scattering properties of the snowpack. This technique has been applied to the temperature time-series at specific automated weather stations to fill gaps in the temperature series [*Shuman et al.*, 1996].
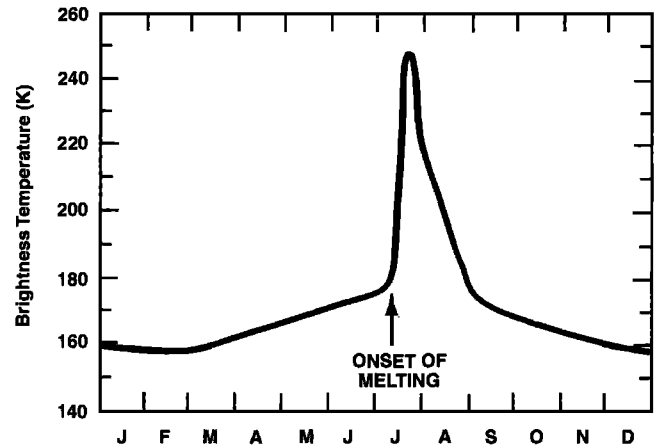
Figure 8. Smoothed time series of brightness temperature data of an ice sheet showing large increase when melting occurs [from *Thomas et al.*, 1985].

6.4. Accumulation Rate

The emissivity of a snowpack depends on the grain size, which, in turn, depends on the accumulation rate. With time, snow grains metamorphose to ever-larger grains until they eventually form pure ice. This rate is both time- and temperature-dependent. Because colder temperatures inhibit grain growth, low-accumulation regions have relatively older, and therefore relatively larger, grains nearer the surface than do the high-accumulation regions. Field measurements of density–depth profiles have confirmed this tendency. Scattering theories to relate the emissivity to accumulation rate by accounting for this temperature-dependent grain growth effect have been moderately successful, but the method has had to rely to a large degree on empirical fits [*Zwally*, 1977; *Zwally and Giovinetto*, 1995]. *Davis* [1995] has combined extinction coefficients from radar altimetry and passive microwave brightness temperatures to develop a semiempirical model to obtain accumulation rate estimates of dry snow. *Bingham and Drinkwater* [2000] have utilised scatterometer data and, by using a technique described by *Long and Drinkwater* [1994] that removes the azimuthal dependence while increasing the spatial resolution, have extracted qualitative information on temporal variations of accumulation rate. *Munk et al.* [2003] combined ERS-1 SAR and the mean annual temperature to produce an accumulation rate map within the Greenland dry-snow facies. The
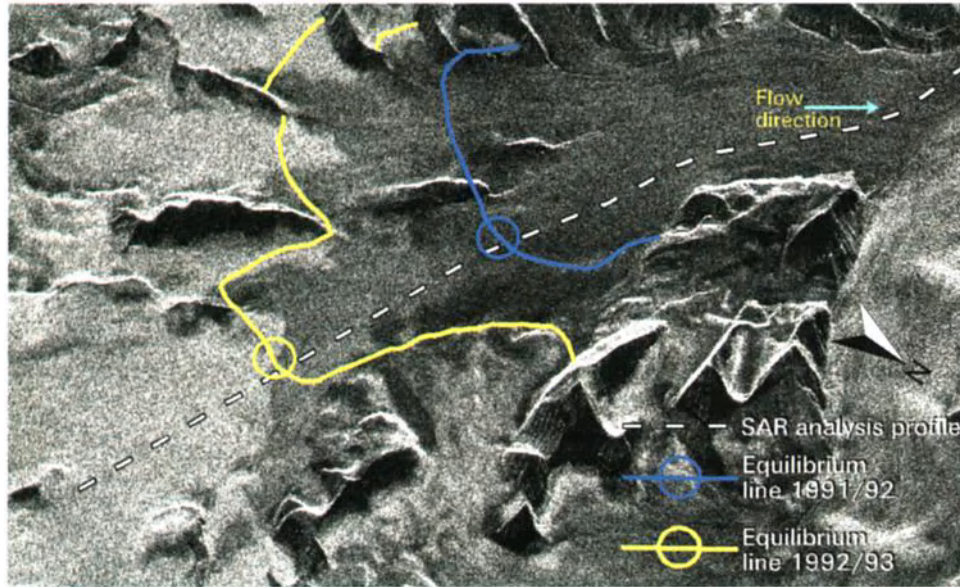
Plate 1. ERS-1 SAR image from 19 January 1994, covering Kongsvegen glacier [from *Engeset and Weydahl,* 1998]. The equilibrium lines estimated from stake measurements from 1991/1992 and 1992/1993 are superimposed and extrapolated along iso-elevation. The circles mark intersections with mass balance measurement profiles. SAR image data were provided by ESA (© 1998 IEEE).
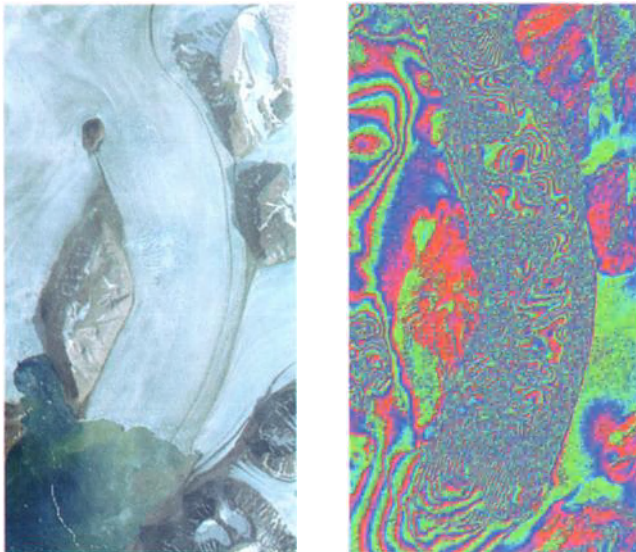
Plate 2. On the left a SPOT image of the fast-flowing Kronebreen, Svalbard, from August 1996 and an interferogram of the same area from February 1995. No fringes are seen on the terrain, since this effect has been removed. Note that the much slower flowing Kongsbreen to the right of Kronebreen has less fringes. Fringes on the ocean are due to the moving sea ice. The images are ~10 km across, and the lower left corner is at ~79°N, 12°20'E. Reprinted with permission from the Norwegian Defense Research Institute (FFI).
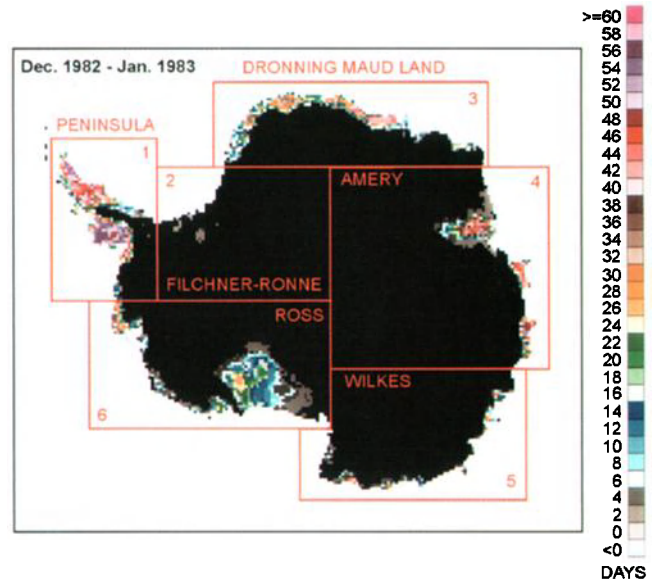
Plate 3. Map of Antarctica showing the duration and extent of melt determined by a time series of 1982–1983 passive micro-wave data [from *Zwally and Fiegles,* 1994]. Reprinted from the *Journal of Glaciology* with permission of the International Glaciological Society.

derived accumulation rates compared favorably (15% average difference) with those measured at 124 sites within the study area. *Zwally and Giovinetto* [1995] showed that melting destroys the accumulation-rate dependence on grain size, so estimates of the accumulation rate pattern by this technique apply only to dry snow found on ice sheets, large ice caps, and very high mountain glaciers. Hence, some researchers have recently exploited the effect of surface melt on microwave signals to map snowmelt extent and duration on small Arctic ice caps [*Smith et al.*, 2003] and the Greenland ice sheet [*Steffen et al.* 2004].

A related use of passive microwave data takes advantage of the fact that the emissions can be measured in different polarisations. Structures within the snowpack can alter the relative amplitudes of the two polarised components. In particular, periods in which large cup-shaped crystals, 1–2 cm in diameter, are formed can be identified [*Shuman and Alley*, 1993]. This is significant because the same crystals are easily identifiable as layers in snow pits and ice cores. The correlation with the satellite data enables these layers to be "time-tagged" (Figure 9) [*Shuman et al.*, 1995; *Alley et al.*, 1997]. The mass of snow between these dated layers then can be converted to a time-series of accumulation rates. No other remote detection scheme is as reliable in identifying the times when mass is delivered to the ice sheet except for very isolated views provided by automated weather stations or the infrequent measurements by field observers.

7. CONCLUSIONS AND OUTLOOK

Over the last few decades, the use of satellite remotely sensed data has revolutionised the field of glaciology. As described, remote sensing is used to acquire a wide variety of data such as surface albedo, snow grain size, surface temperature, accumulation rate, glacier facies, glacier velocities, glacier extent, and ice sheet topography. These measurements are used in studies on local to global scales, covering the full range from process-oriented research studies to monitoring and operational use. Remotely sensed products are often needed to accomplish a particular goal; however, complementary data are usually also required. Normally, ground truth data are still crucial for precise interpretation of remotely sensed data.
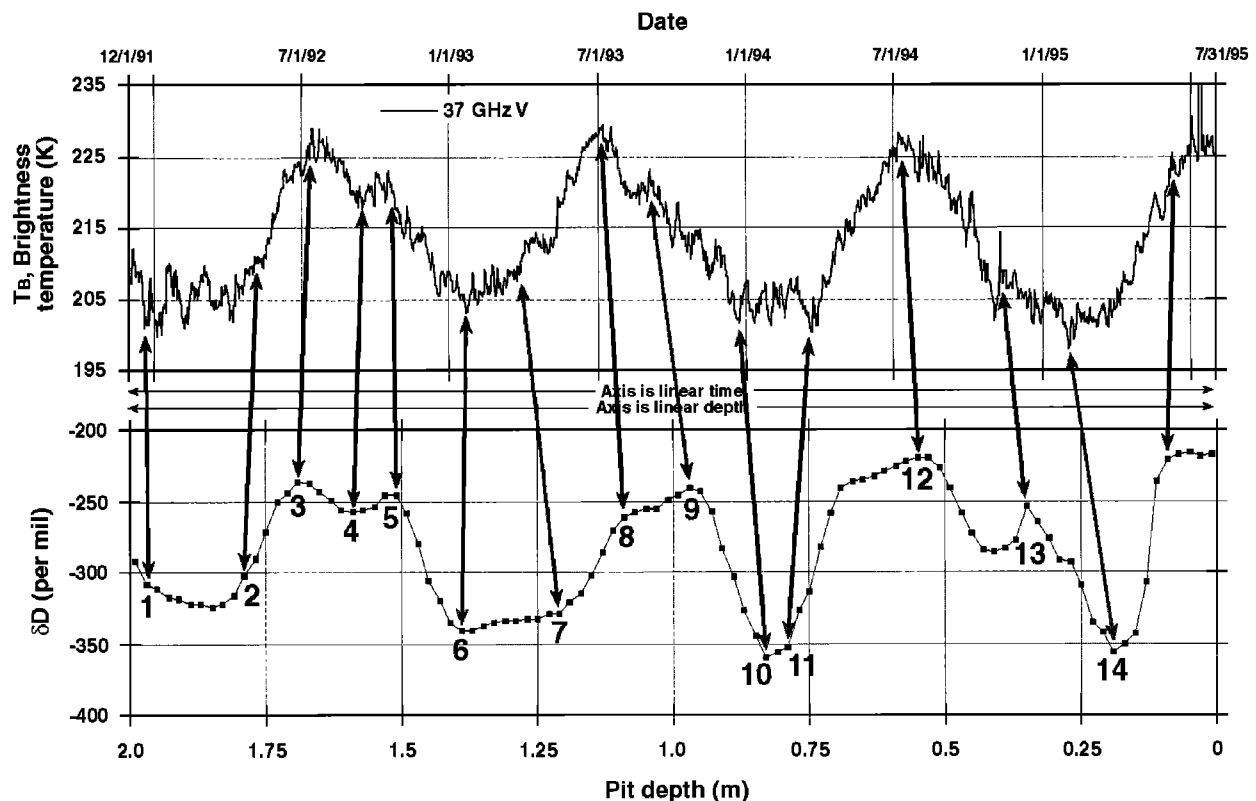
Figure 9. Example of how stratigraphic record of oxygen isotope ratio (bottom panel) can be "time tagged" on the basis of its similarity with the time series of passive microwave brightness temperatures [from *Shuman et al.,* 1995]. Data are from central Greenland.

Recently launched and future sensors will advance our possibilities for glacier studies from space. MODIS and MERIS, described in Table 1, belong to a new class of satellite sensors with greatly improved capabilities. Imaging spectrometers are able to record a continuous spectral range, in contrast to multispectral scanners, on Landsat for example, which record only distinct, selected bands within a spectral region. MERIS and MODIS have 15 and 36 bands selected in their spectral range, respectively, but the newest satellite sensors capable of providing continuous spectral coverage are being tested in orbit. The Earth Observer 1 (EO-1), launched in November 2000, has both an imaging spectrometer called Hyperion with 220 bands, giving continuous coverage between 400 nm and 2500 nm in 10-nm intervals and with 30-m spatial resolution, and an imager with a much improved radiometric sensitivity (Advanced Land Imager). EO-1 will, however, work only on an experimental basis. The ASTER, launched in December 1999 on board the EOS Terra spacecraft, has high spatial resolution and near-global coverage and is thus a vital tool for monitoring and mapping glaciers around the world. A project known as Global Land Ice Monitoring From Space (GLIMS) uses ASTER data to monitor the spatial extent, velocity fields, and other glaciological parameters [e.g., *Khromova et al.*, 2003; *Paul et al.*, 2004; *Kääb*, 2005].

SAR on European Remote Sensing Satellites ERS-1 and ERS-2 was followed by the Advanced Synthetic Aperture Radar (ASAR) on ENVISAT, launched in March 2002. ASAR has vertical as well as horizontal polarisation of the signal. Studies with airborne sensors and the Shuttle Imaging Radar (SIR)-C/X-SAR mission on the space shuttle suggest improved results, e.g., for glacier facies studies, when ASAR is used. The SIR-C/X-SAR is a multiple-frequency, multi-polarisation SAR, and studies suggest a strong potential for snow and ice studies.

The future use of laser altimetry from space is also very promising. While radar satellites like ASAR might measure glacier mass balance indirectly through monitoring the equilibrium line position, precise altimeters such as onboard NASA's ICESat [*Zwally et al.*, 2002] and ESA's CryoSat satellites will provide direct determination of subtle elevation changes (CryoSat was launched on 8 October 2005 but unfortunately the mission failed). Satellite laser altimetry elevation data from ICESat are starting to be used to examine glacier thinning in Antarctica [*Scambos et al.*, 2004; *Rignot et al.*, 2005]. Converting changes in ice sheet elevation to changes in ice volume requires knowledge of isostatic movement of the crust and possible systematic effects in the density structure of the upper layers (affecting surface elevation but not mass). Precise measurements of the Earth's gravity field from space by the GRACE satellite, combined with ground-based GPS measurements, provide much of these needed data. If future

brings altimeters with improved resolution in the x-, y-, and z-directions, and if the necessary corrections mentioned above can be made with the required precision, the glacier mass balance from space can be fully realised.

We also may expect that specially designed instrumentation with improved capabilities for snow and glacier studies will open up for new applications of remotely sensed data. Developments of new techniques and algorithms using such new sensors will become important in northern hydrology. Possibly, an even greater challenge in the coming years will be utilising the enormous amount of data available (also other than remotely sensed data) and synthesise these into high-quality products appropriate for specific tasks. In turn, this has implications for data-sharing policy, computer capacities, and the general understanding and knowledge of individual scientists. The latter calls for an increased use of interdisciplinary research teams, combining experience within such fields as hydrology, atmospheric sciences, sensor technology, and climatology, to mention some.

Finally, we conclude that in the early part of this new century the field of satellite remote sensing in northern hydrology will challenge this community immensely to achieve the full advantage of these powerful and quickly advancing tools.

REFERENCES

Adam, S., A. Pietroniro, and Brugman, M. M., Glacier snow line mapping using ERS-1 SAR imagery, *Rem. Sens. Env. 61(1)*, 46–54, 1997.

Ahlnäs, K., C. S. Lingle, W. D. Harrison, T. A. Heinrichs, and K. A. Echelmeyer, Identification of late-summer snow lines on glaciers in Alaska and the Yukon Territory with ERS-1 SAR imagery, *Eos Trans.*, p. 204, 1992.

Alley, R. B., C. A. Shuman, D. A. Meese, A. J. Gow, K. C. Taylor, K. M. Cuffey, J. J. Fitzpatrick, G. Spinelli, G. A. Zielinski, M. Ram, P. M. Grootes, and B. Elder, Visualstratigraphic dating of the Greenland Ice Sheet Project 2 (GISP2) ice core: Bais, reproducibility, and application, *J. Geophys. Res., 102*, 26,367–26,381, 1997.

Bamber, J. L., Ice sheet altimeter processing scheme, *Int. J. Remote Sens., 15(4)*, 925–938, 1994a.

Bamber, J. L., A digital elevation model of the Antarctic ice sheet derived from ERS-1 altimeter data and comparison with terrestrial measurements, *Ann. Glaciol., 20*, 48–54, 1994b.

Bamber, J. L., and C. R. Bentley, A comparison of satellite-altimetry and ice-thickness measurements of the Ross Ice Shelf, Antarctica, *Ann. Glaciol., 20*, 357–364, 1994.

Bamber, J. L., S. Ekholm, and W. Krabill, The accuracy of satellite radar altimeter data over the Greenland ice sheet determined from airborne laser data, *Geophys. Res. Lett., 25(16),* 3177–3180, 1998.

Benson, C. S., Stratigraphic studies in the snow and firn of the Greenland ice sheet, US Army Corps of Eng., 1962.

Benson, C. S., Stratigraphic studies in the snow and firn of the Greenland ice sheet, *SIPRE Res Rep. 70* (revised edition of the 1962 report), 1996.

Bernier, P. Y., Microwave remote sensing of snowpack properties: Potential and limitations, *Nordic Hydrol., 18,* 1–20, 1987.

Berthier, E., H. Vadon, D. Baratoux, Y. Arnaud, C. Vincent, K. L. Feigl, F. Rémy, and B. Legrésy, Surface motion of mountain glaciers derived from satellite optical imagery, *Rem. Sens. Env., 95,* 14–28, 2005.

Bindschadler, R., Monitoring ice sheet behavior from space, *Rev. Geophys., 36(1),* 79–104, 1998.

Bindschadler, R. A., and Scambos, T. A., Satellite-image-derived velocity field of an Antarctic ice stream, *Science, 252,* 242–246, 1991.

Bindschadler, R.A, and P. L. Vornberger, AVHRR imagery reveals Antarctic ice dynamics, *Eos Trans. AGU, 71(23),* 741–742, 1990.

Bindschadler, R., and P. L. Vornberger, Interpretation of SAR imagery of the Greenland ice-sheet using coregistered TM imagery, *Rem. Sens. Environ., 42(3),* 162–175, 1992.

Bindschadler, R.A, and P. L. Vornberger, Detailed elevation map of ice stream C using satellite imagery and airborne radar, *Ann. Glaciol., 20,* 327–335, 1994.

Bindschadler, R., H. J. Zwally, J. A. Major, and A. C. Brenner, Surface topography of the Greenland ice sheet from satellite radar altimetry, *NASA SP-503,* NSA Scientific and Technical Information Division, Washington, DC, 105 pp., 1989.

Bindschadler, R. A., M. A. Fahnestock, P. Skvarca, and T. A. Scambos, Surface-velocity field of the northern Larsen Ice Shelf, Antarctica, *Ann. Glaciol., 20,* 319–326, 1994.

Bindschadler, R., P. L. Vornberger, D. Blankenship, T. A. Scambos, and R. Jacobel, Surface velocity and mass balance of Ice Stream D and E, West Antarctica, *J. Glaciol. 42(142),* 461–475, 1996.

Bindschadler, R., J. Dowdeswell, D. K. Hall, and J-G. Winther, Glaciological applications with Landsat-7 imagery: early assessments, *Rem. Sens. Env., 78 (1–2),* 163–179, 2001.

Bingham, A. W., and M. R. Drinkwater, Recent changes in the microwave scattering properties of the Antarctic ice sheet, *IEEE Transactions on Geoscience and Remote Sensing, 38 (4),* 1810–1820, 2000.

Bingham, A. W., and W. G. Rees, Satellite data synergies for monitoring Arctic ice masses, in *3rd ERS Symposium on Space at the service of our environment,* 867–870, Florence, 1997.

Bourdelles, B., and M. Fily, Snow grain-size determination from Landsat imagery over Terre Adelie, Antarctica, *Ann. Glaciol., 17,* 86–92, 1993.

Braun, M., F. Rau, H. Saurer, and H. Gossmann, Development of radar glacier zones on the King George Island ice cap, Antarctica, during austral summer 1996/97 as observed in ERS-2 SAR data, *Ann. Glaciol., 31,* 357–363, 2000.

Brenner, A. C., R. A. Bindschadler, R. H. Thomas, and H. J. Zwally, Slope-induced errors in radar altimetry over continental ice sheets, *J. Geophys. Res., 88,* 1617–1623, 1983.

Brown, I. A., and A. M. Johansson, Arctic snowpack monitoring using SAR, in *49th Arctic science conference,* IARC Inauguration, Fairbanks, 1998.

Casassa, G. and J. Turner, Dynamics of the Ross Ice Shelf, *Eos Trans. AGU, 72 (44),* 473–481, 1991.

Choi, E. M., The Radarsat Antarctic Mapping Mission. *IEEE Aerospace and Electronic Systems Magazine, 14*(5), 3–5, 1999.

Cogley, J. G., and W. P. Adams, Remote-sensing resources for monitoring glacier fluctuations on Axel Heiberg Island, *Arctic 53(3),* 248–259, 2000.

Comiso, J. C., Surface temperatures in the polar regions from Nimbus-7 temperature humidity infrared radiometer, *J. Geophys Res., 99 (C3),* 5181–5200, 1994.

Davis, C. H., Synthesis of passive microwave and radar altimeter data for estimating accumulation rates of dry polar snow, *Int. J. Rem. Sens., 16,* 2055–2067, 1995.

Davis, C. H., Comparison of ice-sheet satellite altimeter retracking algorithms, *IEEE Trans. Geosci. Remote Sens., 34(1),* 229–236, 1996.

Davis, C. H., J. R. McConnell, J. Bolzan, J. L. Bamber, R. H. Thomas, and E. Mosley-Thomsen, Elevation change of the southern Greenland ice sheet from 1978 to 1988: Interpretation, *J. Geophys. Res., 106(D24),* 33,743–33,754, 2001.

De Angelis, H., and P. Skvarca, Glacier surge after ice shelf collapse, *Science 299(5612),* 1560–1562, 2003.

Demuth, M. N., and A. Pietroniro, Inferring glacier mass balance using RADARSAT – results from Peyto Glacier, Canada, *Geogr. Ann. 81A(4),* 521–540, 1999.

Dowdeswell, J. A., and M. Williams, Surge-type glaciers in the Russian high arctic identified from digital satellite imagery, *J. Glaciol., 43(145),* 489–494, 1997.

Dowdeswell, J. A., W. G. Rees, and A. D. Diament, ERS-1 SAR investigations of snow and ice facies on ice caps in the European high Arctic, in *2nd ERS-1 Symposium, ESA SP,* 1171–1176, 1994.

Dowdeswell, J. A., A. F. Glazovsky, and Y. Y. Macheret, Ice divides and drainage basins on the ice caps of Franz-Josef-Land, Russian High Arctic, defined from Landsat, KFA-1000, and ERS-1 SAR satellite imagery. *Arct. Alp. Res., 27*(3), 264–270, 1995.

Dozier, J., Spectral signature of alpine snow cover from the Landsat Thematic Mapper, *Rem. Sens. Environ., 28,* 9–22, 1989.

Ekholm, S., R. Forsberg, and J. M. Brozena, Accuracy of satellite altimeter elevations over the Greenland ice sheet, *J. Geophy. Res., 100 (C2),* 2687–2696, 1995.

Eldhuset, K., P. H. Andersen, S. Hauge, E. Isaksson, D. J. Weydahl, ERS tandem InSAR processing for DEM generation, glacier motion estimation and coherence analysis on Svalbard, *Int. J. Rem. Sens. 24(7),* 1415–1437, 2003.

Engeset, R. V., and R. S. Ødegard, Comparision of annual changes in winter ERS-1 SAR images and glacier mass balance of Slakbreen, Svalbrad, *Int. J. Rem. Sens., 20,* 259–271, 1999.

Engeset, R. V., and D. J. Weydahl, Analysis of glaciers and geomorphology on Svalbard using multitemporal ERS-1 SAR images, *IEEE Trans. Geosci. Rem. Sens., 36(6),* 1879–1887, 1998.

Engeset, R. V., J. Kohler, K. Melvold, and B. Lundén, Change detection and monitoring of glacier mass balance and facies

using ERS SAR winter images over Svalbard, *Int. J. Rem. Sens.,* *23(10),* 2023–2050, 2002.

Fahnestock, M., R. Bindschadler, R. Kwok, and K. Jezek, Greenland ice sheet surface properties and ice dynamics from ERS-1 SAR imagery, *Science, 262(5139),* 1530–1534, 1993.

Fahnestock, M. A., T. A. Scambos, R. A. Bindschadler, and G. Kvaran, A Millennium of Variable Ice Flow Recorded by the Ross Ice Shelf, Antarctica, *J. Glaciol., 46 (155),* 652–664, 2000.

Fatland, D. R., and C. S. Lingle, Analysis of the 1993–1995 Bering Glacier (Alaska) surge using differential SAR interferometry, *J. Glaciol., 44(148),* 532–546, 1998.

Ferrigno, J. G., J. L. Mullins, J. A. Stapleton, R. A. Bindschadler, T. A. Scambos, L. B. Bellisime, J-A. Bowell, and A. V. Acosta, Landsat TM image maps of the Shirase and Siple Coast ice streams, West Antarctica, *Ann. Glaciol., 20,* 407–412, 1994.

Ferrigno, J. G., J. L. Mullins, J. A. Stapleton, P. S. Chavez Jr., M. G. Velasco, R. S. Williams Jr., G. F. Delinski Jr., and D. Lear, Satellite image map of Antarctica, *USGS Miscellaneous Investigation Series Map I-2560,* 1996 (http://terraweb.wr.usgs.gov/TRS/projects/Antarctica/AVHRR.html).

Ferrigno, J. G., R. S. Williams, Jr., E. Rosanova, B. K. Lucchitta, and C. Swithinbanks, Analysis of coastal change in Marie Byrd Land and Ellsworth Land, West Antarctica, using Landsat imagery, *Ann. Glaciol., 27,* 33–40, 1998.

Forster, R. R., B. L. Isacks, and S. B. Das, Shuttle imaging Radar (SIR-C/X-SAR) reveals near-surface properties of the South Patagonian icefield, *J. Geophys. Res., 101(E10),* 23,169–23,180, 1996.

Foster, J. L., D. K. Hall, and A. T. C. Chang, Remote Sensing of Snow, *Eos Trans. AGU, 68(32),* 682–684, 1987.

Frezzotti, M., A. Capra, and L. Vittuari, Comparison between glacier ice velocities inferred from GPS and sequential satellite images. *Ann. Glaciol., 27,* 54–60, 1998.

Gay, M., Fily, M., Genthon, C., Frezzotti, M., Oerter, H., and Winther, J-G., Snow grain-size measurements in Antarctica, *J. Glaciol., 48(163),* 527–535, 2002.

Goldstein, R. M., H. Engelhart, B. Kamb, and R. M. Frolich, Satellite radar interferometry for monitoring ice sheet motion: application to an Antarctic ice stream, *Science, 262(5139),* 1525–1539, 1993.

Gray, A. L., N. Short, K. E. Mattar, and K. C. Jezek, Velocities and flux of the Filchner ice shelf and its tributaries determined from speckle tracking interferometry, *Can. J. Rem. Sens. 27(3),* 193–206, 2001.

Greuell, W., and J. Oerlemans, Narrow-to-broadband albedo conversion for glacier ice and snow: equations based on modeling and ranges of validity of the equations, *Rem. Sens. Environ., 89(1),* 95–105, 2004.

Haeflinger, M., K. Steffen, and C. Fowler, AVHRR surface temperature and narrow-band albedo comparison with ground measurements for the Grenland ice sheet, *Ann. Glaciol., 17,* 49–54, 1993.

Hall, D. K., and J. Martinec, *Remote Sensing of Ice and Snow,* 189 pp., Chapman and Hall, New York, 1985.

Hall, D. K., J. P. Ormsby, R. A. Bindschadler, and H. Siddalingaiah, Characterization of snow and ice reflectance zones on glaciers using Landsat Thematic Mapper data, *Ann. Glaciol., 9,* 1–5, 1987.

Hall, D. K., R. S. Williams Jr., and K. J. Bayr, Glacier recession in Iceland and Austria, *Eos Trans. AGU, 73(12),* 1992.

Hall, D. K., R. S. Williams Jr., and O. Sigurðsson, Glaciological observations of Brúarjökull, Iceland, using synthetic aperture radar and thematic mapper satellite data, *Ann. Glaciol., 21,* 271–276, 1995a.

Hall, D. K., C. S. Benson, and W. O. Field, Changes of glaciers in Glacier Bay, Alaska, using ground and satellite measurements, *Phys. Geogr., 16(1),* 27–41, 1995b.

Hambrey, M. J., and J. A. Dowdeswell, Flow regime of the Lambert Glacier-Amery Ice Shelf system, Antarctica: structural evidence from Landsat imagery, *Ann. Glaciol., 20,* 401–406, 1994.

Herzfeld, U. C., and M. S. Matassa, An atlas of Antarctica north of 72.1° S from GEOSAT radar altimeter data, *Int. J. Rem. Sens., 20(2),* 241–258, 1999.

Herzfeld, U. C., C. S. Lingle, C. Freeman, C. A. Higginson, M. P. Lambert, L-H. Lee, and V. A. Voronina, Monitoring changes of ice streams using time series of satellite-altimetry-based digital terrain models, *Math. Geol., 29(7),* 859–890, 1997.

Jacobs, J. D., E. L. Simms, and A. Simms, Recession of the southern part of Barnes Ice Cap, Baffin Island, Canada, between 1961 and 1993, determined from digital mapping of Landsat TM, *J. Glaciol., 43(143),* 98–102, 1997.

Jezek, K. C., RADARSAT-1 Antarctic mapping project: change-detection and surface velocity campaign, *Ann. Glaciol. 34,* 263–268, 2002.

Jezek, K. C., M. R. Drinkwater, J. P. Crawford, R. Bindschadler, and R. Kwok, Analysis of synthetic aperture radar collected over the southwestern Greenland ice sheet, *J. Glaciol., 39(131),* 119–132, 1993.

Joughin, I., R. Kwok, and M. Fahnestock, Estimation of ice-sheet motion using satellite radar interferometry: method and error analysis with application to Humboldt Glacier, Greenland. *J. Glaciol., 42(142),* 564–575, 1996a.

Joughin, I., D. Winebrenner, M. Fahnestock, R. Kwok, and W. Krabill, Measurement of ice-sheet topography using satellite-radar interferometry, *J. Glaciol., 42*(140), 10–22, 1996b.

Joughin, I. R., R. Kwok, and M. A. Fahnestock, Interferometric estimation of three-dimensional ice-flow using ascending and descending passes, *IEEE Trans. Geosci. Remote Sens. 36(1),* 25–37, 1998.

Joughin, I., E. Rignot, C. E. Rosanova, B. K. Lucchitta, and J. Bohlander, Timing of recent accelerations of Pine Island glacier, Antarctica, *Geophys. Res. Lett., 30(13),* 1706, doi:10.1029/2003GL017609, 2003.

Kääb, A., Combination of SRTM3 and repeat ASTER data fro deriving alpine glacier flow velocities in the Bhutan Himalaya, *Rem. Sens. Env., 94,* 463–474, 2005.

Kapitsa, A. P., J. K. Ridley, G. D. Robin, M. J. Siegert, and I. A. Zotikov, A large deep freshwater lake beneath the ice of central East Antarctica, *Nature, 381,* 684–686, 1996.

Kelly, R. E. J., R. Engeset, M. Kennett, E. C. Barrett, and W. Theakstone, Characteristic snow and ice properties of a Norwegian ice cap determined from complex ERS SAR, in *3rd*

ERS Symposium on Space at the Service of our Environment, 831–836, Florence, 1997.

Khromova, T. E., M. B. Dyurgerov, and R. G. Barry, Late-twentieth century changes in glacier extent in the Ak-shirak Range, Central Asia, determined from historical data and ASTER imagery, *Geophys. Res. Lett., 30(16),* 1863, doi:10.1029/2003GL017233, 2003.

Klein, A. G., and J. Stroeve, Development and validation of a snow albedo algorithm for the MODIS instrument, *Ann. Glaciol. 34,* 45–52, 2002.

König, M., J-G. Winther, and E. Isaksson, Measuring snow and glacier ice properties from satellite, *Rev. Geophys., 39(1),* 1–27, 2001a.

König, M., J-G. Winther, N. T. Knudsen, and T. Guneriussen, Firn-line detection on Austre Okstindbreen, Norway, with airborne multipolarisation SAR, *J. Glaciol., 47(157),* 251–257, 2001b.

König, M., Wadham, J., Winther, J-G., Kohler, J., and Nuttall, A-M., Detection of superimposed ice on the glaciers Kongsvegen and Midre Lovènbreen, Svalbard, using SAR satellite imagery, *Ann. Glaciol., 34,* 335–342, 2002.

Lachapelle, E. R., Assessing glacier mass budgets by reconnaissance aerial photography, *J. Glaciol., 4,* 290–297, 1962.

Lefauconnier, B., J. O. Hagen, and J. P. Rudant, Flow speed and calving rate of Kongsbreen glacier Svalbard, using Spot images, *Pol. Res., 13(1),* 59–65, 1994.

Legrésy, B., and F. Rémy, Altimetric observations of surface characteristics of the Antarctic ice sheet, *J. Glaciol., 43(144),* 265–275, 1997.

Legrésy, B., and F. Rémy, Using the temporal variability of satellite radar altimetric observations to map surface properties of the Antarctic ice sheet, *J. Glaciol., 44(147),* 197–206, 1998.

Liang, S., J. Stroeve, and J. E. Box, Mapping daily snow/ice shortwave broadband albedo from Moderate Resolution Imaging Spectroradiometer (MODIS): The improved direct retrieval algorithm and validation with Greenland in situ measurement, *J. Geophys. Res., 110,* D10109, doi:10.1029/2004JD005493, 2005.

Lingle, C. S., and D. N. Covey, Elevation changes on the East Antarctic ice sheet, 1978–1993, from satellite radar altimetry: A preliminary assessment, *Ann. Glaciol., 27,* 7–18, 1998.

Long, D. G., and M. R. Drinkwater, Greenland ice-sheet surface properties observed by the Seasat-A scatterometer at enhanced resolution, *J. Glaciol., 40 (135),* 213–230, 1994.

Lucchitta, B. K., K. F. Mullins, A. L. Allison, and J. G. Ferrigno, Antarctic glacier tongue velocities from Landsat images: first results, *Ann. Glaciol., 17,* 356–366, 1993.

Lucchitta, B. K., C. E. Rosanova, and K. F. Mullins, Velocities of Pine Island Glacier, West Antarctica, from ERS-1 SAR images, *Ann. Glaciol., 21,* 277–283, 1995.

Marshall, G. J., W. G. Rees, and J. A. Dowdeswell, The discrimination of glacier facies using multi-temporal ERS-1 SAR data, in *J. Askne (Ed.), Sensors and Environmental Applications of Remote Sensing,* Balkema, Rotterdam, 263–269, 1995.

Massom, R., *Satellite Remote Sensing of Polar Regions,* 307 pp., Lewis Publishers, London, Belhaven, Boca Raton, FL, 1991.

Matsuoka, T., and T. Shiraiwa, An analysis of L-band SAR images of Ushkovsky ice cap, Kamchatka, Russia. *Cryospheric Studies in Kamchatka II,* 43–50, Hokkaido, 1999.

Mattar, K. E., P. W. Vachon, D. Geudtner, A. L. Gray, I. G. Cumming, and M. Brugman, Validation of Alpine glacier velocity measurements using ERS tandem-mission SAR data, *IEEE Trans. on Geosci. Rem. Sens., 36(3),* 974–984, 1998.

McIntyre, N., Mapping ice sheets with the altimeter, *Int. J. Rem. Sens., 12(8),* 1775–1793, 1991.

Meier, M. F., and A. S. Post, Recent variations in mass net budgets of glaciers in western North America. Obergurgl Symposium on the variations of the regime of existing glaciers, *IAHS Publ. No. 58,* 63–77, 1962.

Merson, R. H., An AVHRR mosaic image of Antarctica, *Int. J. Rem. Sens., 10(4–5),* 669–674, 1989.

Munk, J., K. C. Jesek, R. R. Forster, and S. P. Gogineni, An accumulation map for the Greenland dry-snow facies derived from spaceborne radar, *J. Geophys. Res., 108(D9),* 4280, doi:10.1029/2002JD002481, 2003.

Muskett, R. R., C. S. Lingle, W. V. Tangborn, and B. T. Rabus, Multi-decadal elevation changes on Bagley Ice Valley and Malaspina Glacier, Alaska, *Geophys. Res. Lett., 30(16),* 1857, doi:10.1029/2003GL017707, 2003.

Nolin, A. W., and J. Stroeve, The changing albedo of the Greenland ice sheet: Implications for climate modelling, *Ann. Glaciol., 25,* 51–57, 1997.

Orheim, O., and B. K. Lucchitta, Snow and ice studies by Thematic Mapper and Multispectral Scanner images, *Ann. Glaciol., 9,* 109–118, 1987.

Orheim, O., and B. K. Lucchitta, Numerical analysis of Landsat Thematic Mapper images of Antarctica: Surface temperatures and physical properties, *Ann. Glaciol. 11,* 109–120, 1988.

Østrem, G., ERTS data in glaciology, an effort to monitor glacier mass balance from satellite imagery, *J. Glaciol. 15(72),* 403–415, 1975.

Parrot, J. F., N. Lyberis, B. Lefauconnier, and G. Manby, SPOT multispectral data and digital terrain model for the analysis of ice-snow fields on Antarctic Glaciers, *Int. J. Remote Sens., 14(3),* 425–440, 1993.

Partington, K. C., Discrimination of glacier facies using multitemporal SAR data, *J. Glaciol. 44(146),* 42–53, 1998.

Partington, K. C., J. K. Ridley, C. G. Rapley, and H. J. Zwally, Observations of the surface properties of the ice sheets by satellite radar altimetry, *J. Glaciol., 35(120),* 267–275, 1989.

Paterson, W. S. B. *The Physics of Glaciers,* 480 pp., Third Edition, Pergamon Press, Oxford, 1994.

Paterson, W. S. B., and N. Reeh, Thinning of the ice sheet in northwest Greenland over the past forty years, *Nature 414(6859),* 60–62, 2001.

Pattyn, F., and H. Decleir, Satellite monitoring of ice and snow conditions in the Sør Rondane Mountains, Antarctica, *Ann. Glaciol., 17,* 41–48, 1993.

Paul, F., C. Huggel, and A. Kääb, Combining satellite multispectral image data and a digital elevation model for mapping debris-covered glaciers, *Rem. Sens. Environ., 89(4),* 510–518, 2004.

Paul, F., A. Kääb, M. Maisch, T. Kellenberger, and W. Haeberli, Rapid disintegration of alpine glaciers observed with satellite data, *Geophys. Res. Lett., 31,* L21402, doi:10.1029/2004GL020816, 2004

Phillips, H. A., I. Allison, R. Coleman, G. Hyland, P. J. Morgan, and N. W. Young, Comparison of ERS satellite radar altimeter heights with GPS-derived heights on the Amery ice shelf, East Antarctica, *Ann. Glaciol., 27,* 19–24, 1998.

Ramage, J. M., and B. L. Isacks, Seasonal changes in Alaskan radar glacier zones, in *Final ADRO Symposium*, Montreal, 1998.

Ramage, J. M., B. L. Isacks, and M. M. Miller, Radar glacier zones in southeast Alaska, USA: field and satellite observations, *J. Glaciol., 46(153),* 287–296, 2000.

Rau, F., and H. Saurer, Investigations into snow cover dynamics on two glaciers in the central Marguerite Bay (Antarctic Peninsula) using ERS and RADARSAT SAR imagery, in *Final ADRO Symposium*, Montreal, 1998.

Rau, F., M. Braun, H. Saurer, H. Gossmann, G. Kothe, F. Weber, M. Ebel, and D. Beppler, Monitoring multi-year snow cover dynamics on the Antarctic Peninsula using SAR imagery, *Polarforschung 67 (1/2),* 27–40, 2000.

Rees, W. G., J. A. Dowdeswell, and A. D. Diament, Analysis of ERS-1 synthetic aperture radar from Nordaustlandet, Svalbard, *Int. J. Rem. Sens., 16(5),* 905– 924, 1995.

Ridley, J. K., and K. C. Partington, A model of satellite radar altimeter return from ice sheets, *Int. J. Rem. Sens., 9(4),* 601–624, 1988.

Rignot, E., Tidal motion, ice velocity and melt rate of Petermann Gletscher, Greenland, measured from radar interferometry, *J. Glaciol., 42(142),* 476–485, 1996.

Rignot, E., Radar interferometry detection of hinge-line migration on Ruthford Ice Stream and Carlson Inlet, Antarctica, *Ann. Glaciol., 27,* 25–32, 1998.

Rignot, E., R. Forster, and B. Isacks, Interferometric radar observations of Glaciar San Rafael, Chile, *J. Glaciol., 42(141),* 279–291, 1996.

Rignot, E., D. Braaten, S. P. Gogineni, W. B. Krabill, and J. R. McConnell, Rapid ice discharge from southeast Greenland glaciers, *Geophys. Res. Lett., 31,* L10401, doi:10.1029/2004GL019474, 2004a.

Rignot, E., G. Casassa, P. Gogineni, W. Krabill, A. Rivera, and R. Thomas, Accelerated ice discharge from the Antarctic Peninsula following the collapse of Larsen B ice shelf, *Geophys. Res. Lett., 31,* L18401, doi:10.1029/2004GL020697, 2004b.

Rignot, E., G. Casassa, S. P. Gogineni, P. Kanagaratnam, W. Krabill, H. Pritchard, A. Rivera, R. Thomas, J. Turner, and D. Vaughan, Recent ice loss from the Fleming and other glaciers, Wordie Bay, West Antarctic Peninsula, *Geophys. Res. Lett., 32,* L07502, doi:10.1029/2004GL021947, 2005.

Rolstad, C., J. Amlien, J. O. Hagen, and B. Lundén, Visible and near-infrared digital images for determination of ice velocities and surface elevation during a surge on Osbornebreen, a tidewater glacier in Svalbard, *Ann. Glaciol., 24,* 255–261, 1997.

Rosanova, C. E., B. K. Lucchitta, and J. G. Ferrigno, Velocities of Thwaites Glacier and smaller glaciers along the Marie Byrd Land coast, West Antarctica, *Ann. Glaciol., 27,* 47–53, 1998.

Rott, H., Remote sensing of snow, *Proceedings of the Vancouver Symposium Large Scale Effects of Seasonal Snow Cover, IAHS Publ. 166,* August 1987, 279–290, 1987.

Rott. H., and G. Markl, Improved snow and glacier monitoring by the Landsat Thematic Mapper, *Proceedings of a Workshop on Earthnet Pilot Project on Landsat TM Applications, ESA SP-1102,* Frascati, Italy, December 1987, 3–12, 1989.

Rott, H., P. Skvarca, and T. Nagler, Rapid collapse of northern Larsen Ice Shelf, Antarctica, *Science, 271,* 788–792, 1996.

Rott, H., W. Rack, P. Skvarca, and H. De Angelis, Northern Larsen ice shelf, Antarctica: further retreat after collapse, *Ann. Glaciol. 34,* 277–282, 2002.

Scambos, T. A., and R. Bindschadler, Complex ice stream flow revealed by sequential satellite imagery, *Ann. Glaciol., 17,* 177–182, 1993.

Scambos, T. A., and M. A. Fahnestock, Improving digital elevation models over ice sheets using AVHRR-based photoclinometry, *J. Glaciol., 44 (146),* 97–103, 1998.

Scambos, T. A., J. A. Bohlander, C. A. Shuman, and P. Skvarca, Glacier acceleration and thinning after ice shelf collapse in the Larsen B embayment, Antarctica, *Geophys. Res. Lett., 31,* L18402, doi:10.1029/2004GL020670, 2004.

Scambos, T. A., M. J. Dutkiewicz, J. C. Wilson, and R. A. Bindschadler, Application of image cross-correlation to the measurement of glacier velocity using satellite image data, *Rem. Sens. of Environ., 42(3),* 177–186, 1992.

Scambos, T. A., C. Hulbe, M. Fahnestock, and J. Bohlander, The link between climate warming and breakup of ice shelves in the Antarctic Peninsula, *J. Glaciol., 46 (154),* 516–530, 2000.

Scherer, D., D. K. Hall, V. Hochschild, M. König, J-G. Winther, C. R. Duguay, C. Mätzler, F. Rau, K. Seidel, R. Solberg, and A. Walker, Remote sensing of snow cover, *Remote Sensing in Northern Hydrology, AGU's Geophysical Monograph Series* (Eds.: C. R. Duguay and A. Pietroniro), this volume.

Shi, J., and J. Dozier, Measurements of snow and glacier-covered areas with single polarization SAR, *Ann. Glaciol., 17,* 72–76, 1993.

Short, N. H., and A. L. Gray, Potential for RADARSAT-2 interferometry: glacier monitoring using speckle tracking, *Can. J. Rem. Sens., 30(3),* 504–509, 2004.

Shuman, C. A., and R. B. Alley, Spatial and temporal characterization of hoar formation in central Greenland using SSM/I brightness temperatures, *Geophys. Res. Lett., 20,* 2643–2646, 1993.

Shuman, C. A., R. B. Alley, S. Anandakrishnan, J. W. C. White, P. M. Grootes, and C. R. Stearns, Temperature and accumulation at the Greenland summit: Comparison of high-resolution isotope profiles and satellite passive microwave brightness temperature trends, *J. Geophys. Res., 100,* 9165–9177, 1995.

Shuman, C. A., M. A. Fahnestock, R. A. Bindschadler, R. B. Alley, and C. R. Stearns, Composite temperature record from the Greenland Summitt, 1987–1994: Synthesis of multiple automatic weather station records and SSM/I brightness temperatures, *J. Climate, 9,* 1421–1428, 1996.

Skvarca, P., Changes and surface features of the Larsen Ice Shelf, Antarctica, derived from Landsat and Kosmos mosaics, *Ann. Glaciol., 20,* 6–12, 1994.

Skvarca, P., H. Rott, and T. Nagler, Satellite imagery, a base line for glacier variation study on James Ross Island, Antarctica, *Ann. Glaciol., 21,* 291–296, 1995.

Skvarca, P., W. Rack, H. Rott, and T. Ibarzábal y Donángelo, Climatic trend and the retreat and disintegration of ice shelves on the Antarctic Peninsula: an overview, *Pol. Res., 18(2),* 151–157, 1999.

Smith, L. C., R. R. Forster, B. L. Isacks, and D. K. Hall, Seasonal climatic forcings on alpine glaciers revealed using orbital synthetic aperture radar, *J. Glaciol. 43(145)*, 480–488, 1997.

Smith, L. C., Y. Sheng, R. R. Forster, K. Steffen, K. E. Frey, and D. E. Alsdorf, Melting of small Arctic ice caps from ERS scatterometer time series, *Geophys. Res. Lett., 30(20)*, 2034, doi:10.1029/2003GL017641, 2003.

Sohn, H.-G., K. C. Jezek, and C. J. van der Veen, Jakobshavn Glacier, West Greenland: 30 years of spaceborne observations, *Geophys. Res. Lett., 25(14)*, 2699–2702, 1998.

Steffen, K., R. Bindschadler, G. Casassa, J. Comiso, D. Eppler, F. Fetterer, J. Hawkins, J. Key, D. Rothrock, R. Thomas, R. Weaver, and R. Welch, Snow and ice applications of AVHRR in polar regions, Report of a workshop held in Boulder, Colorado, 20 May 1992, *Ann. Glaciol., 17*, 1–16, 1993.

Steffen, K., S. V. Nghiem, R. Huff, and G. Neumann, The melt anomaly of 2002 on the Greenland Ice Sheet from active and passive microwave satellite observations, *Geophys. Res. Lett., 31*, L20402, doi:10.1029/2004GL020444, 2004.

Stroeve, J., J. E. Box, F. Gao, S. Liang, A. Nolin, and C. Schaaf, Accuracy assessment of the MODIS 16-day albedo product for snow: comparisons with Greenland in situ measurements, *Rem. Sens. Environ., 94(1)*, 46–60, 2005.

Swithinbank, C., R. S. Williams Jr., J. G. Ferrigno, B. A. Seekins, B. K. Lucchitta, and C. E. Rosanova, Coastal-change and glaciological map of the Bakutis coast, Antarctica: 1972–1990, *Geological Investigations Map I-2600-F, Scale 1:1 000 000*, Washington, D. C., U. S. Geological Survey, 1997.

Thomas, R. T., R. A. Bindschadler, R. L. Cameron, F. D. Carsey, B. Holt, T. J. Hughes, C. W. M. Swithinbank, I. M. Whillans, and H. J. Zwally, Satellite remote sensing for ice sheet research, *NASA Tech. Memo., 86233*, 32 pp., 1985.

Unwin, B., and D. Wingham, Topography and dynamics of Austfonna, Nordaustlandet, Svalbard, from SAR interferometry, *Ann. Glaciol., 24*, 402–408, 1997.

Wendler G., K. Ahlnäs, and C. S. Lingle, On Mertz and Ninnis Glaciers, East Antarctica, *J. Glaciol. 42(142)*, 447–453, 1996.

Whillans, I. M., and Y. H. Tseng, Automatic tracking of crevasses on satellite images, *Cold Reg. Sci. Techn., 23(2)*, 201–214, 1995.

Williams, M., and J. A. Dowdeswell, Historical fluctuations of the Matusevich ice shelf, Severnaya Zemlya, Russian high Arctic, *Arctic Ant. Alp. Res. 33(2)*, 211–222, 2001.

Williams Jr., R. S., D. K. Hall, and C. S. Benson, Analysis of glacier facies using satellite techniques, *J. Glaciol. 37(125)*, 120–128, 1991.

Williams Jr., R. S., J. G. Ferrigno, C. Swithinbank, B. K. Lucchitta, and B. A. Seekins, Coastal-change and glaciological maps of Antarctica, *Ann. Glaciol., 21*, 284–290, 1995.

Winther, J-G., Landsat TM derived and in situ summer reflectance of glaciers in Svalbard, *Pol. Res., 12(1)*, 37–55, 1993a.

Winther, J-G., Studies of snow surface characteristics by Landsat TM in Dronning Maud Land, Antarctica, *Ann. Glaciol., 17*, 27–34, 1993b.

Winther, J-G., Elvehøy, H., Bøggild, C. E., Sand, K., and Liston, G., Melting, runoff and the formation of frozen lakes in a mixed snow and blue-ice field in Dronning Maud Land, Antarctica, *J. Glaciol., 42 (141)*, 271–278, 1996.

Winther, J-G., Gerland, S., Ørbæk, J. B., Ivanov, B., Blanco, A., and Boike, J., Spectral reflectance of melting snow in a high Arctic watershed on Svalbard: Some implications for optical satellite remote sensing studies, *Hydrol. Processes. 13 (12–13)*, 2033–2049, 1999.

Winther, J-G., M. N. Jespersen, and G. E. Liston, Blue-ice areas in Antarctica derived from NOAA AVHRR satellite data, *J. Glaciol., 47(157)*, 325–334, 2001.

Zeng, Q., M. Cao, X. Feng, F. Liang, X. Chen, and W. Sheng, A study of spectral reflectance characteristics for snow, ice and water in the north of China, in *Hydrological Applications of Remote Sensing and Remote Data Transmission: Proceedings of the Hamburg Symposium, IAHS Publ. 145*, 451–462, 1984.

Zwally, H. J., Microwave emissivity and accumulation rate of polar firn, *J. Glaciol., 18*, 195–215, 1977.

Zwally, H. J., and F. Fiegles, Extent and duration of Antarctic surface melt, *J. Glaciol., 40*, 463–476, 1994.

Zwally, H. J., and M. B. Giovinetto, Accumulation in Antarctica and Greenland derived from passive-microwave data: a compilation with contoured compilations, *Ann. Glaciol., 21*, 123–130, 1995.

Zwally, H. J., A. C. Brenner, J. A. Major, R. A. Bindschadler, and J. G. Marsh, Growth of the Greenland ice sheet: measurement, *Science, 246*, 1587–1589, 1989.

Zwally, H. J., B. Schutz, W. Abdalati, J. Abshire, C. Bentley, A. Brenner, J. Bufton, J. Dezio, D. Hancock, D. Harding, T. Herring, B. Minster, K. Quinn, S. Palm, J. Spinhirne, and R. Thomas, ICESat's laser measurements of polar ice, atmosphere, ocean and land, *J. Geodynamics, 34(3–4)*, 405–445, 2002.

Robert Bindschadler, NASA Goddard Space Flight Center, Greenbelt, Maryland 20771, USA. (Robert.A.Bindschadler@nasa.gov)

Max König and Jan-Gunnar Winther, Norwegian Polar Institute, Polar Environmental Centre, N-9296 Tromsø, Norway. (max.koenig@npolar.no; winther@npolar.no)

Dieter Scherer, Climatology Section, Institute of Ecology, Berlin University of Technology, Rothenburgstrasse 12, D-12165 Berlin, Germany. (Dieter.Scherer@TU-Berlin.DE)

Ice Characteristics and Processes, and Remote Sensing of Frozen Rivers and Lakes

Martin O. Jeffries, Kim Morris, and Nickolai Kozlenko

Geophysical Institute, University of Alaska Fairbanks, Fairbanks, Alaska

This chapter is a broad overview of ice characteristics and processes on northern rivers and lakes in the time between initial ice formation in autumn and final melt-out in spring. Using primarily synthetic aperture radar (SAR: ERS-1, ERS-2, JERS-1, RADARSAT-1) images supplemented by aerial photographs, passive microwave and Landsat images, and examples from the literature, the aim is to illustrate the potential for remote sensing to contribute to a better knowledge and understanding of river ice and lake ice in the context of their role in northern hydrology and their value as sensitive indicators of northern environmental variability and change. The following seasonal ice characteristics and processes are described: (1) autumn freeze-up; (2) growth, thickening, and grounding; (3) fracturing and motion, including the effect on Mentasta Lake, Alaska, of the magnitude 7.9 earthquake of 3 November 2002; (4) aufeis; and (5) spring break-up. They are followed by a description of perennial ice characteristics, processes, and recent (1997–2002) change on lakes and epishelf lakes in northernmost Ellesmere Island, Nunavut, Canada. The merits of different current and future remote sensing instruments are briefly discussed. We conclude that, as the constellation of increasingly sophisticated spaceborne instruments grows, multisensor remote sensing of frozen rivers and lakes has the potential to contribute more to the study of the role of bodies of water in northern hydrology and of the effects of environmental variability and change on the ice and hydrological system.

1. INTRODUCTION

Frozen rivers and lakes are common features of the northern landscape and integral components of the hydrological system. Yet, for all the "... obvious significance of 'floating ice hydrology', it is astounding to note the lack of interest shown in the subject by the hydrological community. ... More disconcerting is the almost complete absence of discussion in hydrological texts" [*Gerard*, 1990]. This lament for the poor state of knowledge and lack of appreciation for the role of river ice and lake ice in northern

hydrology still holds largely true, but two factors that date back to the 1990s could be catalysts for change: the mounting evidence for significant changes in the northern cryosphere [e.g., *Morison et al.*, 2000; *Serreze et al.*, 2000] and the growth in availability and variety of high-resolution remote sensing data for studies of the northern cryosphere [*Walsh et al.*, 2001].

Among the many changes observed in the northern cryosphere is a significant reduction in lake ice and river ice duration [*Magnuson et al.*, 2000]. Observations made between 1846 and 1995 show that the duration of the ice cover decreased at a rate of 12.3 days per 100 years due to a combination of later freeze-up in autumn and earlier break-up in spring [*Magnuson et al.*, 2000]. Changes in freshwater ice duration can have significant physical and biological

effects, as exemplified by the Experimental Lakes, northern Ontario, Canada, where ice duration decreased by 20 days in just the 18-year period 1970–88 [*Schindler et al.*, 1990].

The relationship between air temperature and other climate variables on the one hand, and surface observations of freshwater ice freeze-up, break-up, and duration (sometimes known as ice phenology) on the other hand, has been the subject of extensive study [e.g., *Williams*, 1965, 1971; *Tramoni et al.*, 1985; *Palecki and Barry*, 1986; *Robertson et al.*, 1992; *Skinner*, 1992; *Assel and Robertson*, 1995]. Lake ice phenology, ice thickness, and the effects of climate change have also been the subject of computer modelling, but, except for *Ménard et al.* [2002], validation of the simulations has largely relied on surface observations and measurements [e.g., *Liston and Hall*, 1995a,b; *Vavrus et al.*, 1996; *Fang and Stefan*, 1997a; *Walsh et al.*, 1998; *Zhang and Jeffries*, 2000; *Duguay et al.*, 2003].

The first to suggest the feasibility of using satellite data rather than surface observations to monitor ice phenology were probably *Tramoni et al.* [1985] and *Palecki and Barry* [1986]. Since then, the potential for monitoring lake ice phenology by remote sensing has been amply demonstrated by different sensors used at different locations [e.g., *Maslanik and Barry*, 1987; *Skorve and Vincent*, 1987; *Barry and Maslanik*, 1993; *Walker and Davey*, 1993; *Wynne and Lillesand*, 1993; *Wynne et al.*, 1996, 1998]. Apart from this, remote sensing remains underutilized in river ice and lake ice studies.

Freshwater ice freeze-up and break-up dates are important climate and environmental signals, but remote sensing of freshwater ice need not be limited to these variables. Indeed, the full potential of remote sensing of freshwater ice will not be realized if it is applied only to the beginning and end of the ice season. The literature on remote sensing of lake ice and river ice is not large. A sense of how the field has developed can be obtained from *Hall and Martinec* [1985], *Frankenstein et al.* [1986], and *Hall* [1999]. The long history of research and the development of knowledge and understanding of river ice and lake ice can be traced via *Barnes* [1906, 1928], *Michel* [1971], *Ashton* [1980, 1986], *Adams* [1981], *Gerard* [1990], *Gray and Prowse* [1993], and *Beltaos* [1995a] and the references therein.

In this chapter we describe some of the key river ice and lake ice characteristics and processes that occur during the period between initial ice formation in autumn and final melt-out in spring, and illustrate them where possible with remote sensing images and examples from the literature. We use primarily spaceborne synthetic aperture radar (SAR) images, supplemented by aerial photography, airborne and satellite passive microwave images, and Landsat images. Section 2 is a general overview of the physical and biological effects of river ice and lake ice. The aim is to show why river ice and lake ice are important and to set the stage for the subsequent description of ice characteristics and processes and remote sensing. Section 3 describes the freeze-up of rivers and lakes. Section 4 focuses on winter and describes ice characteristics and processes such as (a) growth, thickness, and grounding; (b) fracturing and motion; and (c) aufeis. Section 5 describes river ice and lake ice break-up. Sections 3–5 describe seasonal river ice and lake ice. Perennial lake ice, which occurs at a few locations in the Northern Hemisphere, is described in section 6. The seventh and final section is a discussion and conclusion.

2. PHYSICAL AND BIOLOGICAL EFFECTS OF RIVER ICE AND LAKE ICE

The hydrological significance of ice on rivers and lakes is due to its effect on water discharge and stage (water level) in a channel, the lake's water level, and through the seasonal storage represented by the ice itself, the snow cover it carries and the channel and lake storage it induces [*Gerard*, 1990]. The hydrological significance of floating ice can be substantial; indeed, it can be argued that the hydrological extremes of common interest—floods and low flows—are as much a function of stream processes through the action of snow and ice in the channel as they are of catchment processes of traditional concern [*Gerard*, 1990].

Floods and low flows in channels are most often associated with ice jams, which form where the passage of ice along a reach is obstructed. An ice jam increases the hydraulic resistance and decreases the flow conveyance of the channel; consequently, water upstream of the ice jam goes into storage and the stage increases, whereas downstream the stage decreases and low flow occurs [*Gerard*, 1990]. In some cases during freeze-up, downstream low flows are the annual minimum [*Gray and Prowse*, 1993], whereas upstream of an ice jam the stage can exceed the maximum summer stage [*Gerard and Stanley*, 1988]. Northern riverside communities often have more to fear from ice jam floods than from open water floods in summer [*Gerard*, 1990].

When an ice jam fails, the ensuing ice run is one of the most violent and spectacular events that can occur on a river. The stage rises very rapidly at downstream locations and water velocities far exceed even those attained during open water floods [*Beltaos*, 1995b]. Scouring of the river bed and banks during major ice runs can have significant ecological and geomorphological effects [*Prowse*, 1994; *Scrimgeour et al.*, 1994]. Not all ice jams fail catastrophically and cause a surge. Many simply melt in situ, sometimes rapidly, and become a significant point-source of additional flow that also cools the water downstream [*Prowse and Marsh*, 1989;

Prowse, 1990]. On the other hand, once the ice cover has been removed from a reach, water temperatures have been known to rise from near-freezing to almost 10°C in a matter of hours [*Parkinson*, 1982]. This warm water subsequently contributes to melting of the ice cover further downstream [*Prowse*, 1990].

Although it typically has negative connotations, ice-induced flooding also has its benefits. Such floods are a major component of the water balance of lakes on the Mackenzie River delta [*Marsh*, 1986], where the ecosystems are particularly dependent on the spring flux of sediments and nutrients that accompany the flood water [*Lesack et al.*, 1991]. Ice-induced flooding of deltas can cause meso-scale climatic effects such as air temperature increases that stimulate budding and early plant growth [*Gill*, 1974; *Prowse and Reedyk*, 1993]. Ice jam flooding is so integral to the function of delta ecosystems that artificial ice jams have been built on regulated rivers in attempts to restore deltas where lakes have dried up due to the decline in natural ice-induced spring flooding [*Prowse et al.*, 1993; *Prowse*, 1994].

Hydroelectric power generation companies and their customers incur significant costs as operations are tailored to avoid high discharges that might trigger ice jam floods downstream or low discharges that fall below the regulatory minimum [*Gerard*, 1990]. Low discharge decreases the water supply, increases contaminant levels, and depletes oxygen, all of which have potential ecological and socioeconomic impacts. High financial costs are also incurred as government, business, and industry strive to maintain navigation and commerce on ice-covered waterways, and recover from occasionally devastating damage to structures and vessels by ice and floods [e.g., *Gerard and Davar*, 1995].

As well as influencing the extremes, ice can have a major effect on the winter hydrograph of northern streams [*Gerard*, 1990]. The volume of water stored as ice, and as channel storage due to the increase in stage caused by the ice, can represent a significant portion of winter flow that does not become available until spring. This might be particularly so for the lake-dominated rivers of the Canadian Shield, where slight changes in the resistance to flow from the outlet can trigger enormous changes in lake storage [*Gerard*, 1990]. On the other hand, snowfall on lake ice will increase the discharge from a lake because the snow displaces the underlying water [*Jones*, 1969]. Thus, snow falling on lake ice increases the outflow, which can be significant in a stream in midwinter in a catchment with a large number of lakes [*Gerard*, 1990].

Through their influence on solar radiation transmission alone, a long-duration ice cover and the overlying blanket of snow can have a significant effect on the physics, chemistry,

and ecology of lakes and rivers [*Adams*, 1981; *Scrimgeour et al.*, 1994]. The transmission of solar radiation through the snow and ice affects the water heat budget [*Likens and Ragotskie*, 1965; *Adams and Lasenby*, 1978]; it can warm the near-surface waters to the temperature of maximum density and trigger convective mixing [*Matthews and Heaney*, 1987; *Malm et al.*, 1997]. This can suspend non-motile phytoplankton in the upper water column, where there is sufficient light for growth even during ice-covered periods [*Matthews and Heaney*, 1987; *Kelley*, 1997]. In permafrost regions, lakes and ponds have a significant effect on the ground thermal regime [*Brewer*, 1958; *Lachenbruch et al.*, 1962] and are the primary contributors to tundra landscape modification [*Sellmann et al.*, 1975a]. The growth and decay of ice on shallow lakes on the North Slope of Alaska play an important role in regional greenhouse gas budgets [*Phelps et al.*, 1998] and the winter surface energy balance [*Jeffries et al.*, 1999]. Shallow lakes are ubiquitous features of the tundra landscapes of Canada, e.g., the Hudson Bay Lowland [*Duguay and Lafleur*, 1997; *Duguay et al.*, 1999] and east Siberia [*Mellor*, 1994; *Jeffries et al.*, 1996], as well as northernmost Alaska.

Simulations of the effects of climate warming on northern lakes predict a number of consequences, including (1) shorter ice cover duration, resulting in higher water temperatures and increased thermocline depth [*McCormick*, 1990; *Assel*, 1991; *Huttula et al.*, 1992]; (2) the potential elimination of anoxia and winterkill in winter but increased duration of anoxia in summer [*Fang and Stefan*, 1997b]; and (3) decreases in fish populations and changes in species composition [*Meisner et al.*, 1987; *Hill and Magnuson*, 1990]. The current state of knowledge of river ice ecology is summarized by *Prowse* [2001a,b], and some possible effects of climate change on river ice processes and river ecology are discussed by *Scrimgeour et al.* [1994]. The likely effects of climate change on the freshwaters of Arctic and sub-Arctic North America are discussed by *Rouse et al.* [1997].

3. FREEZE-UP

3.1. Freeze-up of Rivers

In a river the first ice usually forms along the banks, where the flow is gentle, creating border ice that extends out into the channel. This is illustrated in the aerial photograph of the Susitna River, Alaska (Figure 1); there are also numerous examples of this in SAR images of rivers in northern Manitoba [*Leconte and Klassen*, 1991]. Predictive modelling of border ice growth is a prerequisite to forecasting the formation of a complete ice cover and the formation of freeze-up jams, because it is the reduction in channel surface width by border ice that often determines the bridging

Figure 1. Vertical aerial photograph (visible band) of freeze-up on the Susitna River between Curry and Talkeetna, Alaska, 17 November 1982. The centre of the photograph is at 62.62°N, 151.12°W. Reprinted with the kind permission of AeroMap U.S., Anchorage, Alaska.

point or channel constriction where moving ice floes are arrested [*Prowse*, 1995].

The quiet reaches of a channel can favor the formation of sheet ice, with a columnar crystal texture (Figure 2), which is transported downstream until the floes are arrested at a constriction [*Beltaos*, 1995b]. Away from the banks, in fast-flowing or turbulent reaches of the channel, once the well-mixed water column has cooled to 0°C, frazil ice crystals will form as the water cools further. Frazil ice crystals are typically small due to disintegration during crystal-to-crystal collisions in the turbulent water. Once formed, however, the frazil crystals accumulate to form slush, which, in turn, freezes completely to form polycrystalline ice with a fine-grained crystal texture (Figure 2). Often the slush will first consolidate into ice pans, which, in turn, combine and create larger ice floes. As the slush, pans, and floes are carried downstream (Figure 1), they can contribute to the expansion of the border ice.

Once a channel becomes congested and bridged by ice, the lodgement [*Gerard*, 1990] (Figure 1) or surface ice jam [*Beltaos*, 1995b] affects the flow of water and movement of ice from upstream. Frazil, pans, and floes can be carried under the lodgement and contribute to its thickening into a hanging jam or even a grounded jam [*Beltaos*, 1995b]. Or, the frazil, pans, and floes can remain at the surface and accumulate against the lodgement to form a pack [*Gerard*, 1990]. As more ice arrives from upstream and is arrested, the pack grows as it extends upstream (Figure 1). The river becomes progressively covered with ice by pack progression at a rate that depends on the prevailing weather conditions and by the discharge and geometry of the channel [*Gerard*, 1990]. Where a river enters a lake, the frazil ice, pans, and floes can be arrested by the lake ice cover and accumulate in an extensive and rough mass that can be seen clearly in SAR images because of their strong backscatter [*Leconte and Klassen*, 1991].

An autumn ice jam affects the stage upstream and downstream, as described earlier. However, because the air temperatures and discharge are generally lower in autumn than in spring, ice jam floods, and ice jam failures and surges are uncommon in autumn [*Gerard and Davar*, 1995]. Autumn ice jams can be identified in SAR images because deformation creates rough surfaces that cause strong backscatter and bright signatures for months after their initial formation, e.g., the Tanana River at Fairbanks, Alaska [*Melloh and Gatto*, 1990a,b,c, 1992]. The same ice jams also appear bright (radiometrically cold) in passive microwave images [*Melloh and Gatto*, 1990a,b,c, 1992].

Strong backscatter from rough ice probably explains the bright signature of the ice on the Churchill River, Manitoba (Figure 3), since areas of river ice that have not been

deformed appear moderately dark in SAR images [*Melloh and Gatto*, 1990a,c, 1992; *Leconte and Klassen*, 1991]. Alternatively, the bright signature of the Churchill River ice might be due to strong backscatter from juxtaposed layers of ice and slush, as proposed by *Leconte and Klassen* [1991] for river ice elsewhere in Manitoba.

3.2. Freeze-up of Lakes

As a lake cools from above 4°C—the temperature of maximum density of freshwater—the surface water loses heat, becomes more dense, and sinks. This process continues until all the water in the lake is at 4°C. With further cooling (and without mechanical mixing), a stable, lighter water layer forms at the surface. As this layer cools to the freezing point, ice begins to form on the lake surface [*Schwartz et al.*, 1986]. The first ice to form is known as the initial ice skim, which often appears first as border ice in shallow, protected areas. However, the entire lake surface can reach the freezing point simultaneously and a continuous ice cover will appear in a matter of a hours [*Ragotskie*, 1978].

Wind and wave action can break down the initial ice skim into small fragments, i.e., frazil ice, and the topmost layer

Figure 2. Vertical thin sections of ice on the Beauharnois Canal, Québec, illuminated between crossed polarizers. The sections are not to scale; the length of each is given at the bottom. The labels P3, S1, S2, and T1 identify ice according to the freshwater ice classification of *Michel and Ramseier* [1971]; i.e., P3 is frazil ice, S1 is congelation ice with vertical c-axis, S2 is congelation ice with horizontal c-axis, and T1 is snow ice. Originals provided by A. J. Gow and reprinted from *Schwarz et al.* [1986] with the kind permission of Water Resources Publications, LLC.

Figure 3. SAR subscene of the lowermost reaches of the Churchill River, Manitoba, 13 April 1998. The four white arrows indicate river ice that is frozen to the bottom. The very bright features in the upper right quadrant are ice-covered shallow lakes. Churchill (C) is located at 58.72°N, 94.12W°. North is at the top of the frame. The original ERS-2 image (©ESA) was radiometrically corrected then filtered to reduce speckle by C. R. Duguay, who provided the subscene.

0.22 m

0.43 m   0.43 m
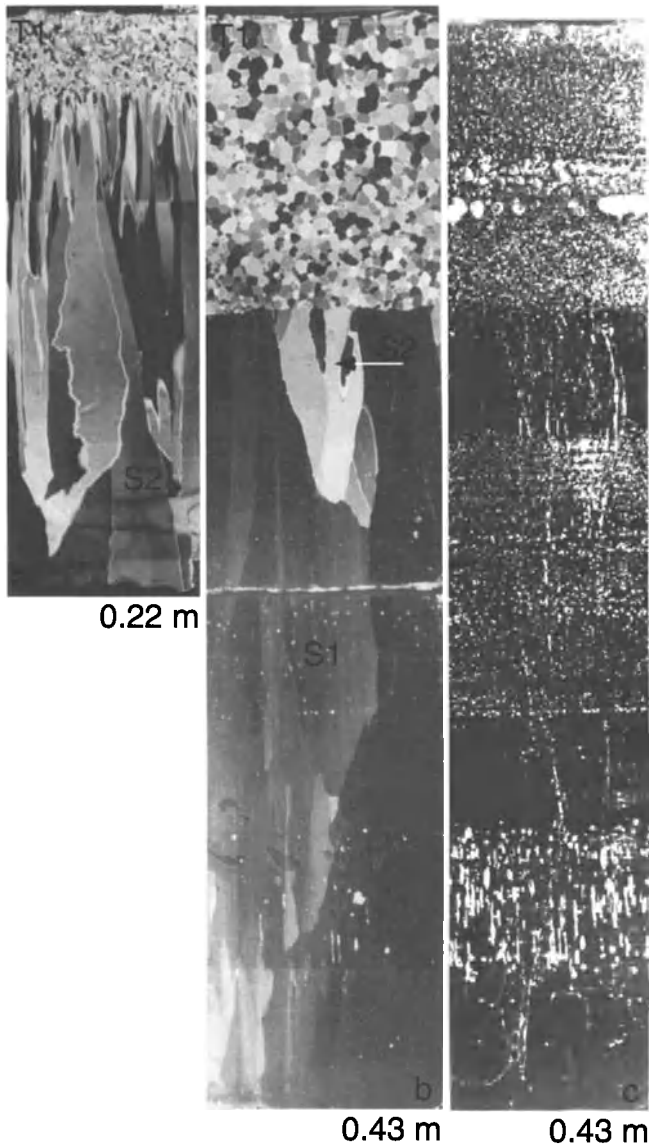
Figure 4. Vertical thin sections of ice on (a) Mascoma Lake and (b, c) Post Pond, New Hampshire, illuminated (a, b) between crossed polarizers and (c) in plain light. The labels S1, S2, and T1 identify ice as in Figure 2. Section (b) has a small amount of S2 ice that has been wedged out by the S1 ice. Originals provided by A. J. Gow and reprinted from *Gow and Langston* [1977] with the kind permission of the U.S. Army Cold Regions Research and Engineering Laboratory (USA-CRREL).

of the consolidated lake ice sheet will have a fine-grained texture. Regardless of whether the initial ice skim is affected by wind and wave action, it thickens further by the formation of congelation ice as water freezes on the bottom. The congelation ice crystals grow downward into the water and occur as two crystallographic types. One has horizontally

oriented c-axes and a distinctive columnar texture of vertically elongated crystals that increase in size as the ice thickness increases (Figure 4a). The other has vertically oriented c-axes characterized by massive crystals (macrocrystals) that have a striped or striated appearance (Figure 4b). Why congelation ice initially grows in this fashion is uncertain (it might be due to the meteorological conditions during initial ice formation [*Barns and Laudise*, 1985; *Gow*, 1986]), but the fact that it happens is significant from a perspective of lake ice geophysics and remote sensing in spring, as will be discussed in section 5.

The bulk water temperature (the average temperature between the lake surface and lake bottom) at which lakes freeze over has been related to fetch, with small lakes freezing at bulk temperatures of 2–3°C and large lakes freezing at bulk temperatures of 1°C [*Scott*, 1964]. Lake depth and volume are also important controls of freeze-up [*Stewart and Haugen*, 1990]. The combined effects of lake fetch, depth, and volume on initial ice formation are illustrated by Teshekpuk Lake and the surrounding smaller lakes on the North Slope of Alaska (Figure 5). The water in Teshekpuk Lake is >4 m deep [*Mellor*, 1985, 1987], with a maximum depth of 6.6 m, and it is ice-free. The smaller lakes are much
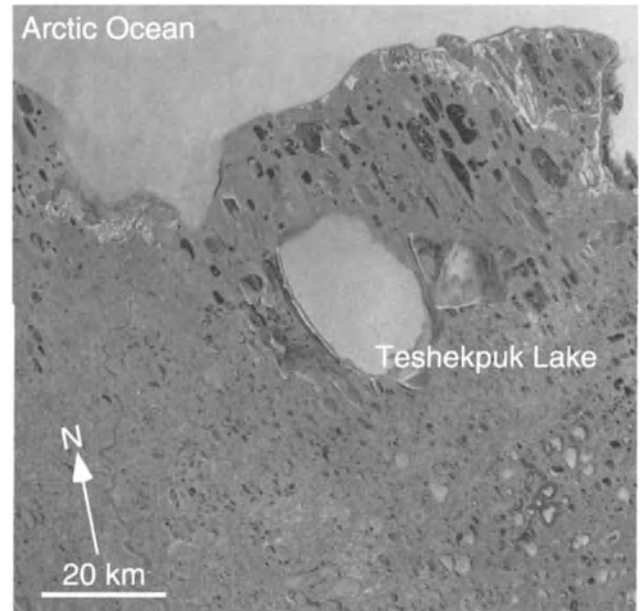
Figure 5. Freeze-up in the vicinity of Teshekpuk Lake on the North Slope of Alaska, 13 September 1996. The centre of Teshekpuk Lake is at 70.58°N, 153.50°W, 140 km southeast of Barrow. ERS-2 SAR image (©ESA) from the Alaska Satellite Facility (ASF). This and all subsequent SAR images presented in this chapter have been radiometrically calibrated, but they are not filtered to reduce speckle, and the gray scale that represents backscatter intensity is the same in each image.

shallower, typically no more than 4 m deep [*Mellor*, 1985, 1987] and are frozen over.

Teshekpuk Lake appears bright in Figure 5 due to strong backscatter from the wind-roughened water surface. A similar signature can be seen offshore on the Arctic Ocean. Smaller, shallower lakes to the west and northeast of Teshekpuk Lake appear dark because of specular reflection off the smooth air/ice and ice/water interfaces of the initial ice skim [*Bryan and Larson*, 1975; *Leconte and Klassen*, 1991; *Jeffries et al.*, 1994]. A snow-free initial ice skim also appears dark in the visible band but can be difficult to distinguish from open water; consequently, there can be problems in identifying the timing of initial ice formation with visible band data such as DMSP OLS [*Maslanik and Barry*, 1987]. It is possible to discriminate between open water and ice on lakes with passive microwave data and thus detect initial ice formation, as demonstrated at Great Slave Lake, Northwest Territories, Canada, using 37-GHz SMMR data [*Barry and Maslanik*, 1993] and 85-GHz SSM/I data [*Walker and Davey*, 1993].

On large lakes, a considerable thickness of ice is required to resist wind forces without breaking, and initial ice cover formation is much more dynamic than on small lakes [*Michel et al.*, 1986]. Fracturing, movement, and refreezing of the ice cover during the early stages of freeze-up are evident in the SAR signature changes at Teshekpuk Lake in autumn 1992 (Figure 6). Differences in the surface roughness of the ice probably account for the contrasting dark (smooth ice, low backscatter) and bright (rough ice, high backscatter) tones. The ice on the small lakes around Teshekpuk Lake appears to have remained undisturbed during the same period.

4. WINTER ICE CHARACTERISTICS AND PROCESSES

4.1. Ice Growth, Thickness, and Grounding

After initial ice formation and the establishment of a consolidated ice cover on a river, there often remain open areas that persist all winter. Sometimes known as polynyas, they recur on reaches of fast water and in areas of warm groundwater flow or lake outflow [*Gerard*, 1990]. Under favourable light conditions, open water is visible in Landsat images, although the level of detail depends on the size of the river and whether MSS or TM data are used [*Gatto*, 1990]. Open channels in an otherwise ice-covered river are also easily identified in active and passive microwave images [*Leconte and Klassen*, 1991; *Melloh and Gatto*, 1990a,b,c, 1992, 1993]. Like their polar ocean counterparts, river ice polynyas must be sites of significant heat and mass transfer to the atmosphere, but we are not aware of any studies of the magnitudes of these fluxes from rivers in winter.

Using Landsat MSS and TM data, *Gatto* [1990] identified four classes of ice on rivers in the American Midwest: ice-free/open water, partial gray ice, complete gray ice, and white ice; this classification, based entirely on the tonal variations, provided information on the presence or absence of ice but little information on ice types and processes. *Gatto* [1993] was subsequently able to identify open water, snow ice, clear ice, cracked ice, and ice ridges in ERS-1 SAR images of the St. Mary's River, Michigan, but concluded that the 30-m spatial resolution of the data was insufficient for monitoring ice conditions on small
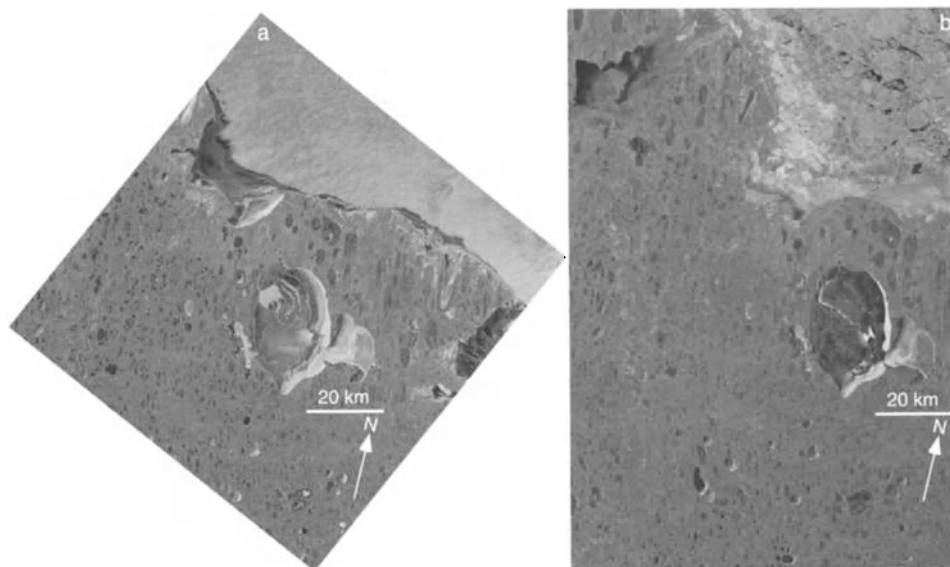
Figure 6. Teshekpuk Lake on (a) 17 September 1992 and (b) 3 October 1992. ERS-1 SAR images (©ESA) are from ASF.

rivers. *Weber et al.* [2003] developed a semi-automated classification of ice on the Peace River in British Columbia and Alberta, Canada; having identified seven ice types in 8-m spatial resolution RADARSAT Fine Beam images, they concluded that the ice maps would augment but not replace aerial and ground surveys for ice monitoring and decision-making related to water flow and ice stability in a heavily regulated river.

Leshkevich [1985] developed a lake ice classification scheme based on Landsat and in situ albedo data. Efforts are underway to develop automated, SAR-based ice classification algorithms for the Great Lakes [*Leshkevich et al.*, 1998; *Nghiem et al.*, 1998].

As in polar ocean polynyas, river polynyas are a significant source of frazil ice. Frazil ice can be swept below a river ice sheet downstream, where it can accumulate and consolidate (Figure 2a), thereby increasing the ice thickness. Where frazil ice is not present in large quantities, the ice will thicken by congelation ice growth, occasionally interrupted by the arrival of small quantities of frazil ice (Figure 2b). Figures 2a and 2b exemplify the often complex crystal texture and stratigraphic variability of river ice that is a consequence of the dynamic environment in which initial ice formation and subsequent consolidation and thickening occur.

The texture and stratigraphy of a lake ice sheet can be complex, too. Studies on lakes in Alaska and Russia have revealed that, after initial ice formation, S1 and S2 ice (Figure 4) can occur in multiple layers in the same ice sheet; on any given lake, S1 ice might dominate one year and S2 ice might dominate the next [*Knight*, 1962; *Weeks and Wettlaufer*, 1996]. The reasons for this variability are unclear, but they might include the thermal characteristics of the underlying water body [*Weeks and Wettlaufer*, 1996]. S2 ice is commonly observed in river ice (Figure 2), but much less is known about the occurrence of S1 ice in frozen rivers. The significance of S1 and S2 ice is discussed in section 5.

As congelation ice grows, it rejects dissolved salts and gases back into the water. As a general rule, when the gas content of the water is below the nucleation level, then clear, inclusion–free ice forms. But when the gas content of the water exceeds its nucleation level, thereby forcing the gases out of solution, inclusions (air bubbles, Figure 4c) form in the ice [*Ragle*, 1963; *Bari and Hallett*, 1974]. Bubbles in freshly formed lake ice are often characteristically tubular and oriented parallel to the direction of ice growth [*Gow and Langston*, 1977; *Weeks et al.*, 1978, 1981]. However, the size, shape, and distribution of bubbles established at the time of freezing can undergo significant changes (e.g., Figure 4c), particularly in response to thaw/freeze cycles [*Gow and Langston*, 1977]. Whether the ice is clear or contains bubbles, congelation ice is often referred to as black

ice because it appears that way against a dark background, e.g., the water below.

The presence or absence of air bubbles in the ice can have a significant effect on the radar backscatter and the interpretation of lake and ice processes. This is exemplified by the ice on Tazlina Lake, Chugach Range, Alaska (Figure 7) and on shallow lakes on the North Slope of Alaska (Figures 8 and 9). The ice on Tazlina Lake has many bright, linear features (fractures, to be discussed further in section 4.2) set against a background of dark to moderately dark tone. Those areas of low to moderate backscatter are believed to represent clear ice on this deep lake, where the gas content of the water does not reach the nucleation level and few bubbles form in the ice; consequently, there is minimal backscatter and the ice has a dark signature [*Morris et al.*, 1995].

In contrast to the low to moderate backscatter from the ice on Tazlina Lake, a large proportion of the ice-covered lakes on the North Slope (Figures 8 and 9) show strong backscatter. This is due to double-bounce reflection, first off vertically oriented, tubular bubbles in the lower layers of the ice and then off the ice/water interface, where there is a strong dielectric contrast between ice and water. The double-bounce results in the return of a significant part of the incident energy to the satellite at nearly the same angle as it was initially transmitted; consequently, the floating ice appears bright in radar images [*Weeks et al.*, 1978; *Mellor*, 1982; *Jeffries et al.*, 1994; *Wakabayashi et al.*, 1994]. The double-bounce mechanism also accounts for strong backscatter from ice-covered lakes on the Hudson Bay Lowland [*Duguay et al.*, 2002; *Duguay and Lafleur*, 2003] (Figure 3).

Figure 9 also shows that the area of floating ice with strong backscatter decreases during the course of the winter and the area of ice with a dark signature increases. This was first observed in airborne real aperture radar images [*Sellmann et al.*, 1975b; *Weeks et al.*, 1977]. It has since become clear that the dark signature represents low backscatter from grounded ice (i.e., ice that is frozen to the bottom of the lake); the low dielectric contrast between the ice and the sediments to which it has frozen results in signal loss in the sediments [*Weeks et al.*, 1978, 1981; *Mellor*, 1982, 1994; *Jeffries et al.*, 1994]. The increase in area of ice with low backscatter (decrease in area of ice with strong backscatter) is due to an increase in the area of ice that grounds on the bottom (decrease in the area of floating ice) as the ice thickness increases during the course of the winter. *Duguay et al.* [2002] describe the backscatter variability of floating and grounded lake ice as it relates to the RADARSAT-1 incidence angle.

ERS-2 and RADARSAT-1 SAR images of the ice on Lake El'gygytgyn, northeast Siberia, showed unusual concentric bright and dark rings [*Nolan et al.*, 2003]. The lake is too deep (maximum ~175 m) for the bright and dark rings
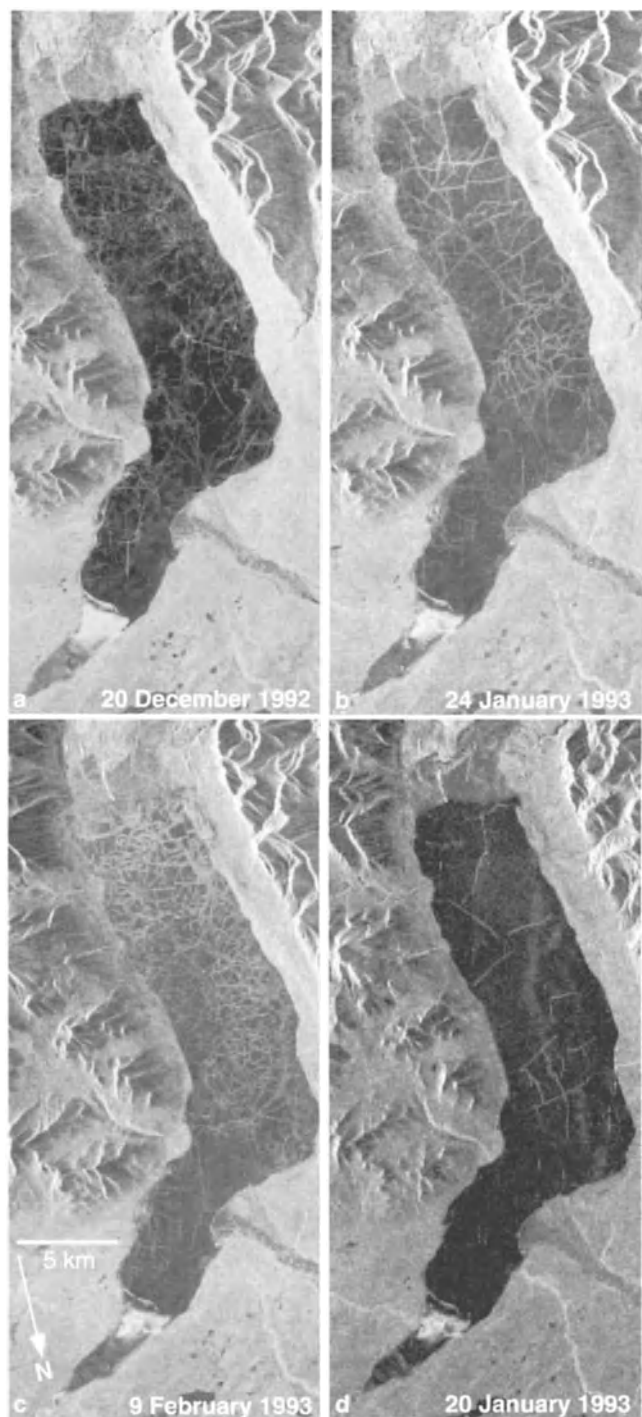
Figure 7. ERS-1 (a, b, c) and JERS-1 (d) SAR image subscenes of Tazlina Lake, Alaska. The centre of the lake is at 61.88°N, 146.50°W, 190 km east-northeast of Anchorage. From *Morris et al.* [1995] and reprinted with the kind permission of B. Riffenburgh (editor), *Polar Record*. The original images (©ESA, ©NASDA) are from ASF.

to represent floating and grounded ice zones, respectively. Instead, the rings are believed to represent spatial variations in the density, size, shape, and orientation of bubbles in the ice—characteristics that in turn are probably a function of depth-related variations in biological productivity in and gas release from the lake sediments [*Nolan et al.*, 2003].

River ice that freezes to the bottom can also have a dark signature in SAR images (Figure 3, and personal communication, C. R. Duguay, University of Alaska Fairbanks, July 2003). In contrast to the dark signature of the localized occurrences of grounded ice, most of the ice in the Churchill River channel has a bright signature (Figure 3). As noted in section 3.1, areas of river ice that have not been deformed appear moderately dark in SAR images; consequently, the strong backscatter that dominates the Churchill River channel is probably due to the rough ice surface rather than to scatter off the bottom of floating ice. The very dark signature of the grounded ice (Figure 3) suggests that it does not have a rough surface. We propose that there must be greater ambiguity in the detection of floating and grounded river ice than the detection of floating and grounded lake ice because of the widespread occurrence of deformation and the resulting presence of rough ice in frozen river channels.

The strong contrast between floating and grounded lake ice has been used to map water depth on the North Slope of Alaska, where there are thousands of shallow lakes covering as much as 25–40% of the land area in some places (Figure 8) [*Sellmann et al.*, 1975a]. *Mellor* [1985, 1987] used analogue (photographic) real aperture radar (RAR) imagery of over 20,000 lakes to identify how many fell into three depth categories: <1.6 m, 1.6–4 m, and >4 m; he verified the results with ice thickness measurements made in late winter and water depth data obtained by sonar in summer. *Mellor* [1982, 1985, 1987] also demonstrated a technique for creating bathymetric maps of lakes by using ice thickness measurements and a series of winter RAR images. Using digital SAR images of the North Slope and a numerical ice growth model, *Jeffries et al.* [1996] determined the maximum depth of 473 lakes, and *Kozlenko and Jeffries* [2000] developed a semi-automated bathymetric mapping technique (Plate 1).

A large proportion of Teshekpuk Lake has a dark signature (Figure 8). Consequently, on the basis of the previous description of light and dark lake ice SAR signatures, one might conclude that a large proportion of the ice cover is frozen to the bottom. But this is not the case. Ice growing on water >4 m deep in this region contains an insufficient number of tubular bubbles to cause strong double-bounce reflection and backscatter; consequently, the dark signature identifies the deepest (>4 m), not the shallowest, part of Teshekpuk Lake [*Mellor*, 1985, 1987].

Figure 8. SAR image subscene of the western region of the North Slope of Alaska, 12 May 1997. Barrow is located at 71.30°N, 156.82°W. The many small bright features are areas of floating lake ice. The length of the bottom of the image is equivalent to 480 km on the ground. The original RADARSAT-1 ScanSAR Wide B image (©CSA) is from ASF.
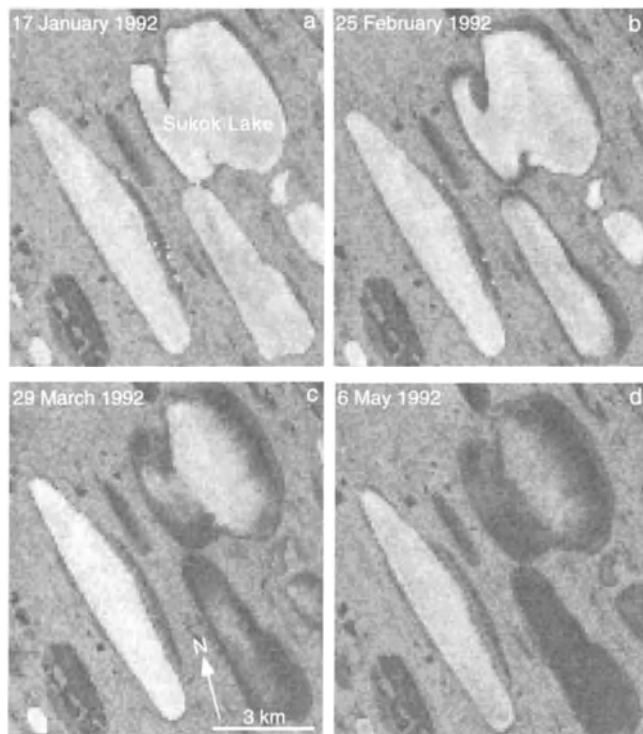
Figure 9. SAR image subscenes of lakes on the North Slope of Alaska showing changes in backscatter/tone as the ice thickened and froze to the bottom between January and May 1992. The centre of Sukok Lake is 71.05°N, 156.83°W, 28 km south of Barrow. From *Jeffries et al.* [1996] and reprinted with the kind permission of the Arctic Institute of North America. The original ERS-1 SAR images (©ESA) are from ASF.

Knowing that the deeper the lake, the longer it takes for the ice to melt completely in spring, *Sellmann et al.* [1975a] used Landsat MSS data to classify North Slope lakes into three depth categories: <1 m, 1–2 m, and >2 m deep. *Duguay and Lafleur* [2003] used Landsat TM data to establish a precise relationship between lake depth (based on field measurements) and band 2 radiance in summer; from these data they made bathymetric maps of shallow lakes on the Hudson Bay Lowland, including those in Figure 3. On the basis of those maps and a sequence of winter ERS–1 SAR images in which it was possible to differentiate between floating and grounded ice, *Duguay and Lafleur* estimated the ice thickness on the date each SAR image was acquired. Assuming that no significant changes in water depth occur over time, bathymetric maps developed using the *Kozlenko and Jeffries* [2000] or the *Duguay and Lafleur* [2003] techniques coupled with a series of winter SAR images could be used to monitor lake ice thickness variability and change over a period of years.

SAR interferometry is another possible approach to the determination of tundra lake depth and ice thickness [*Li et al.*, 2000]. Interferometry is usually used to map surface topography, but *Li et al.* argue that, because lake ice is a transparent material, SAR interferometry can be used to map the bottom topography of grounded ice, i.e., the lake bed. Floating ice has a noisy, decorrelated phase pattern because the bottom of the ice has shifted as a result of ice growth in the time between SAR orbits, whereas the grounded ice is identified by a clean phase pattern because no further ice growth occurs once the ice has frozen to the bottom.

Therefore, the phase difference between the grounded ice and the surrounding land is a measure of the topography of the lake bed [*Li et al.*, 2000]. This technique remains experimental and requires improvement, field measurements, and validation before it can be put into routine use.

Floating and grounded lake ice can also be identified in high-resolution passive microwave images (Figure 10a). The bright fringe in the upper right margin of the lake is believed to be ice that is frozen to the bottom because it is radiometrically colder than the floating ice [*Melloh et al.*, 1991]. Of greater potential value is the fact that passive microwave radiometers operating at low frequencies [1.41 to 7.2 GHz] are particularly effective for the determination of lake ice thickness, as demonstrated by airborne data from Lake Erie [*Swift et al.*, 1980] and Walden Reservoir, Colorado [*Hall et al.*, 1981].

The AMSR instrument aboard the NASA Aqua satellite has a 6.925-GHz channel that offers the possibility of being able to obtain lake ice thickness, albeit from only the largest lakes, since this very low frequency channel has an instantaneous field of view of 43 × 75 km. The potential to derive snow depth on floating ice by remote sensing has been demonstrated by *Markus and Cavalieri* [1998], who used the current 85-GHz SSM/I channel to estimate snow depth on Antarctic sea ice. The high-frequency channel (89 GHz) on AMSR offers the same possibility, and with an instantaneous field of view of 4 × 6 km it could be used to obtain data for medium-sized lakes. It might be possible in the near future to obtain the total thickness of snow and ice on medium to large lakes from snow surface elevation data acquired by spaceborne laser (ICESat) and radar altimeter (CryoSat). The successful application of any of these techniques to river ice seems a remote possibility in view of the large footprint of the sensors and the relatively narrow width of even the broadest river channels.

4.2. Fracturing and Motion

As freshwater ice thickens during the winter, it is subject to a number of different stresses, such as thermal pressure, wind and water drag, and water level changes, which all contribute to fracturing of the ice cover [*Carstens et al.*, 1986]. Using SAR interferometry, *Smith* [2002] identified a transverse crack and an associated 10–30 mm displacement in the ice on the Mackenzie River, Canada (Plate 2A) and an ice collapse on the Ob River, Russia (Plate 2B). Transverse
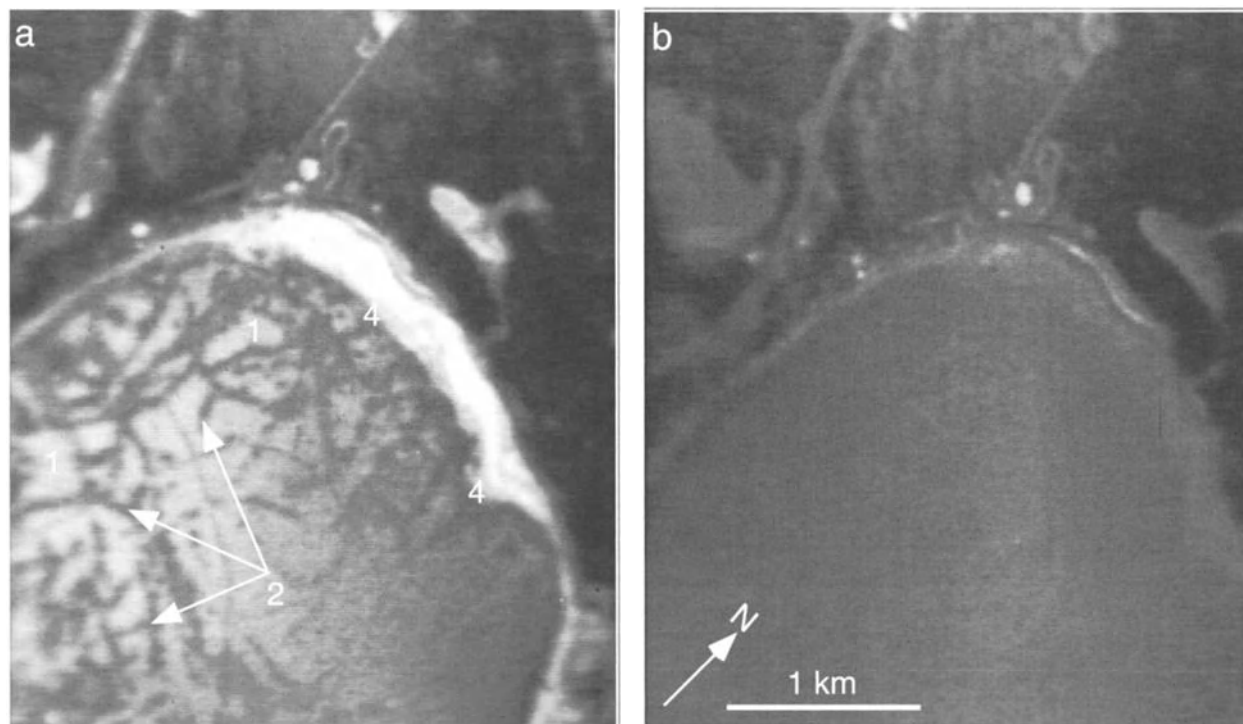
Figure 10. Airborne, 33.6-GHz frequency, passive microwave images of Harding Lake, Alaska, obtained on (a) 8 March 1988 and (b) 11 March 1988. The center of the lake is at 64.43°N, 146.85°W, 60 km southeast of Fairbanks. The annotations are (1) floating ice; (2) fractures; (3) grounded ice; (4) boundary between floating and grounded ice. Originals provided by R. A. Melloh and reprinted from *Melloh et al.* [1991] with the kind permission of USA-CRREL.
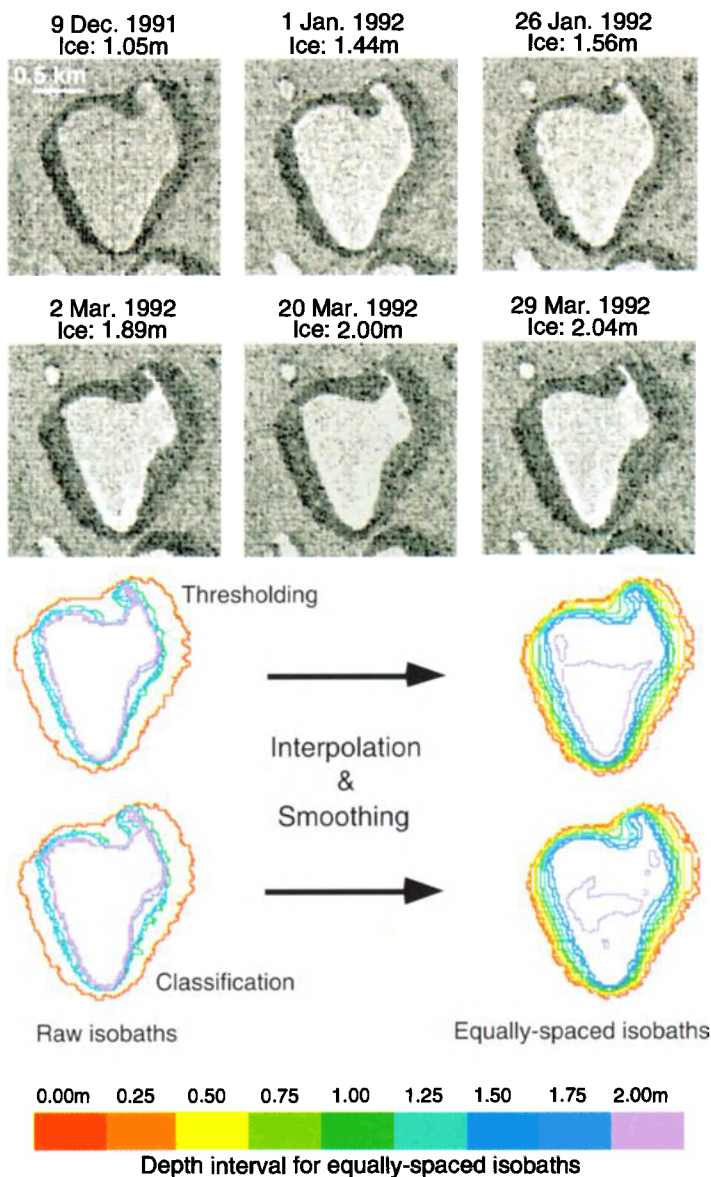
Plate 1. Derivation of a bathymetric map of the shallow water in a tundra lake using spaceborne SAR images and a simulated ice growth curve. The sequence of ERS-1 SAR image subscenes (originals ©ESA) at the top was used to map the boundary between floating ice (bright tone) and grounded ice (dark tone) by using either classification or thresholding. A simulated ice growth curve was used to convert the image acquisition date into ice thickness, i.e., water depth, at that boundary. The raw, irregularly spaced isobaths (lower left) are converted into regularly spaced (0.25 m) isobaths (lower right) by use of interpolation and smoothing. The legend at the bottom applies only to the bathymetric maps on the right. From *Kozlenko and Jeffries* [2000] and reprinted with the kind permission of the Arctic Institute of North America.
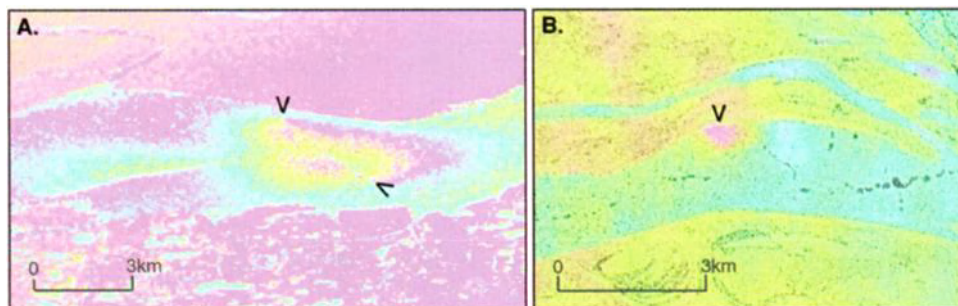
Plate 2. ERS-2 SAR interferograms of (A) ice displacement on the Mackenzie River delta between 22 and 23 January 1996, and (B) ice collapse on the Ob River between 26 and 27 March 1996. The two V symbols in (A) indicate the line of ice displacement. The V in (B) indicates the area of ice collapse. The scale bars represent a distance of 3 km. Originals provided by L. C. Smith and reprinted from *Smith* [2002] with the kind permission of Blackwell Publishing.

cracks, which are described further in section 5.1, are normally associated with the onset of spring break-up of a river ice cover [*Beltaos*, 1990, 1997]. However, the transverse cracks in Plate 2 occurred in mid- to late winter, which raises some interesting questions as to their origin and subsequent effect on the strength of the ice cover and its response to the onset of "true" break-up.

Fracture networks in lake ice can be detected by high-resolution passive microwave imagers (Figure 10a) [*Melloh et al.*, 1991]. The sensor is not detecting the fractures per se; rather, it is detecting the locations of former fractures through the occurrence of snow ice that is radiometrically warmer, and thus has a darker signature, than the surrounding ice cover where flooding and snow ice formation have not occurred [*Melloh et al.*, 1991]. Flooding and snow ice formation occur when the mass of snow is sufficient to overcome the buoyancy of the ice and depress the ice surface below water level; fractures present allow water to flow up to the ice surface and wet the snow cover, and the resulting slush freezes.

Snow ice is polycrystalline with a granular texture (Figure 4b) and contains many air bubbles (Figure 4c). It is often referred to as white ice because of light scattering off the densely packed bubbles. Snow ice need not be limited to the immediate vicinity of fractures in the ice. It can occur in a layer of variable thickness over broad areas and often occurs in greater quantities around the margins than in the center of the ice cover because of snow redistribution by the wind [*Adams and Roulet*, 1980; *Adams and Prowse*, 1981; *Bengtsson*, 1986].

An evolving network of fractures in the ice on Tazlina Lake is clearly identified by the bright, linear signatures in Figure 7a-c. Here, the development of the fractures probably relates primarily to katabatic winds blowing off Tazlina Glacier at the south end of the lake, where the wind stress would be greatest and the density of fractures is highest (Figure 7) [*Morris et al.*, 1995]. The roughly triangular bright area at the outlet at the north end of the lake is probably a plug of rough ice that blew into the constriction during freeze-up [*Morris et al.*, 1995]. As noted in section 3.1, bright features such as this also occur where a river enters a lake, and frazil ice, pans, and floes accumulate against the lake ice sheet [*Leconte and Klassen*, 1991].

There are two possible explanations for the bright tone of the fractures in the Tazlina Lake ice. First, after fracturing has occurred and refreezing has begun, compression of the newly formed ice and sometimes complete closure of the crack can lead to the formation of a small pressure ridge [*Metge*, 1976]. *Morris et al.* [1995] illustrated extensive pressure ridge networks on Great Bear Lake, Northwest Territories, and attributed their bright signature to strong

surface-scattering off the rough, blocky surfaces of the ridges. Second, flooding and snow ice formation might have occurred after fracturing, and volume scattering from the snow ice would contribute to strong backscatter and the bright tone of the fracture network [*Hall et al.*, 1994; *Morris et al.*, 1995]. Note that the JERS-1 SAR (Figure 7d) does not reveal the fractures as effectively as the ERS-1 SAR (Figure 7a-c), probably because the longer wavelength JERS-1 signal (235 mm versus 53 mm) is less affected by surface and volume scattering and penetrates as far as the ice/water interface, where specular reflection leads to minimal returns to the radar receiver.

Fractures are commonly observed early in the autumn in the ice on the North Slope lakes (e.g., Figure 6), but they are obscured later in the ice growth season as double-bounce scattering from the broadly distributed tubular bubbles and the bottom of the ice exceeds that from the localized fractures [*Jeffries et al.*, 1994]. The fractures in the Tazlina Lake ice cover remain visible against the darker background of the surrounding clear ice, from which there is minimal backscatter, as described in section 4.1 and *Morris et al.* [1995].

Fractures running parallel to and close to the shore occur in lake ice that has been affected by a seiche [*Ashton*, 1980]. Seiches are transient standing-wave oscillations that occur in response to air pressure fluctuations, changes in wind speed and direction, and events such as volcanic eruptions, landslides, and earthquakes [*Korgen*, 1995]. During a seiche, the water in a lake literally "sloshes" back and forth, and resonates. Seiche-induced fractures parallel and close to shore are not apparent in Tazlina Lake (Figure 7), but the more dramatic consequences of a seiche are evident in Figure 11, which shows a pair of SAR images of Mentasta Lake, Alaska, before and after the magnitude 7.9 earthquake of 3 November 2002. Nine days before the earthquake, the perimeter of Mentasta Lake is clearly visible due to the sharp contrast between the dark signature of
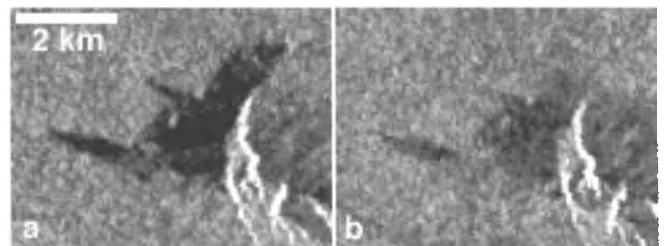
Figure 11. SAR image subscenes of Mentasta Lake, Alaska, on (a) 26 October 2002 and (b) 12 November 2002, i.e., before and after the magnitude 7.9 earthquake of 3 November 2002, respectively. The centre of the lake is at 62.92°N, 143.77°W, 290 km southeast of Fairbanks. North is at the top of each frame. The original RADARSAT-1 ScanSAR images (©CSA) are from ASF.

the generally smooth, young ice and the lighter signature of the surrounding land (Figure 11a). Nine days after the earthquake, the perimeter of the lake is largely obscured and the ice cover signature is brighter (Figure 11b). The lake lies directly on the Denali Fault, which ruptured and caused the earthquake. The resulting seiche fragmented the ice cover into thousands of small floes and shoved ice up onto the shore [personal communication, Barb Dalke, Principal, Mentasta Lake-Katie John School, June 2003]. The increase in backscatter from the ice and the obscuration of the lake perimeter (Figure 11b) can be attributed to an increase in surface roughness due to the disintegration and rafting of the ice and the widespread ice shoves onto the shore, respectively.

On the largest lakes, e.g., the Great Lakes, the ice cover rarely becomes firmly established and is subject to frequent disturbance throughout the winter, primarily by the wind [*Wiesnet*, 1979; *Assel et al.*, 1983; *Michel et al.*, 1986]. Using a pair of RADARSAT-1 SAR images, *Pilant and Agarwal* [1998a] illustrated a 20-km ice displacement on Lake Superior over a period of 12 h. It should be possible to derive ice motion vectors for the largest lakes, if needed, using SAR or high-frequency passive microwave data, as is routinely done for sea ice [*Kwok et al.*, 1995; *Agnew et al.*, 1997]. The simultaneous use of SAR, SSM/I, and AVHRR over the Great Lakes indicates the potential for learning about the ice cover on large lakes by multisensor remote sensing [*Pilant*, 1995; *Pilant and Agarwal*, 1998a,b].

4.3. Aufeis

In the previous section, we described flooding and snow ice formation due to depression of a lake ice surface by the snow mass with resulting water flow through fractures. This also occurs on river ice. Aufeis is a similar phenomenon, which forms when water overflows onto a river ice surface from tributaries, or from below the ice, or from groundwater springs. It occurs over broad areas but is often simply frozen water as opposed to the snow/water mixture that defines snow ice. The location and extent of aufeis deposits, also known as overflow, icings, or naleds, are of considerable hydrological interest and they are described in detail in *Michel et al.* [1986]. Melting aufeis can make up a significant proportion of summer flow [*Li et al.*, 1997], and during periods of significant runoff they largely determine the channel routing and can act as major flow restrictions that increase the flooding potential [*Prowse*, 1995].

Melloh and Gatto [1990a, 1992] identified possible areas of overflow on ice on the Tanana River, Alaska, in passive microwave images. *Dean* [1984] used Landsat MSS scenes acquired over a 9-year period to map aufeis deposits in northern Alaska; aufeis also is clearly visible in Landsat TM scenes

of the British Mountains, Yukon [personal communication, C. R. Duguay, July 2003]. *Li et al.* [1997] discussed some of the limitations of Landsat for aufeis studies and showed how aufeis deposits can be mapped more accurately during the course of a single winter by using SAR interferometry.

Aufeis can be detected with SAR because of changes in the surface properties and elevation of the ice that cause variations in amplitude (backscatter), phase, and coherence of the radar returns between orbits [*Li et al.*, 1997]. A phase diagram or interferogram (Plate 3a) shows fringes in those areas where change in topography has been minimal in the 6 days between the two satellite passes; also shown is a central linear area of decorrelation in the river channel where aufeis has accumulated and the surface elevation has thus changed during that time. A SAR amplitude difference image (Plate 3b) shows changes in backscatter (darker tones identify a reduction; lighter tones identify an increase) due to changes in wetness at the surface of the aufeis. The extent of the aufeis deposit can be seen more clearly in the phase coherence image (Plate 3c) that provides a measure of the resemblance of radar phase between days 1 and 6; i.e., if aufeis accretes in the time between the orbits, the coherence between phases from two acquisitions is low relative to the surroundings and is revealed as an area of dark tone. Coherence images can be summed to show aufeis deposit development in time and space (Plate 3d).

5. BREAK-UP

5.1. River Ice Break-up

Freshwater ice break-up involves decay, fracture, transport, and removal [*Prowse*, 1995]. The break-up of river ice is controlled by thermodynamic and dynamic processes, also referred to as hydrothermal and hydrodynamic processes, respectively [*Prowse*, 1994, 1995]. Thermodynamic, or over-mature, break-up is typically characterized by only moderate increases in water flow and by an ice cover that has thermally deteriorated and lost much of its mechanical strength, thereby posing little resistance to the flow. In contrast, dynamic, or pre-mature, break-up usually results from the interaction of a large, spring flood wave with a mechanically competent (intact and mechanically strong) ice cover.

During break-up, the channel is commonly ice-free in some reaches and ice-covered in others (Figure 12a), which can be attributed to both thermodynamic and dynamic processes. In the case of thermodynamic decay, the ice melts and disintegrates in situ, a process that often occurs more rapidly in the quieter reaches than in the more turbulent, steeper reaches due to differences in the optical properties of the ice [*Prowse*, 1995]. The ice cover on quiet reaches is often predominantly
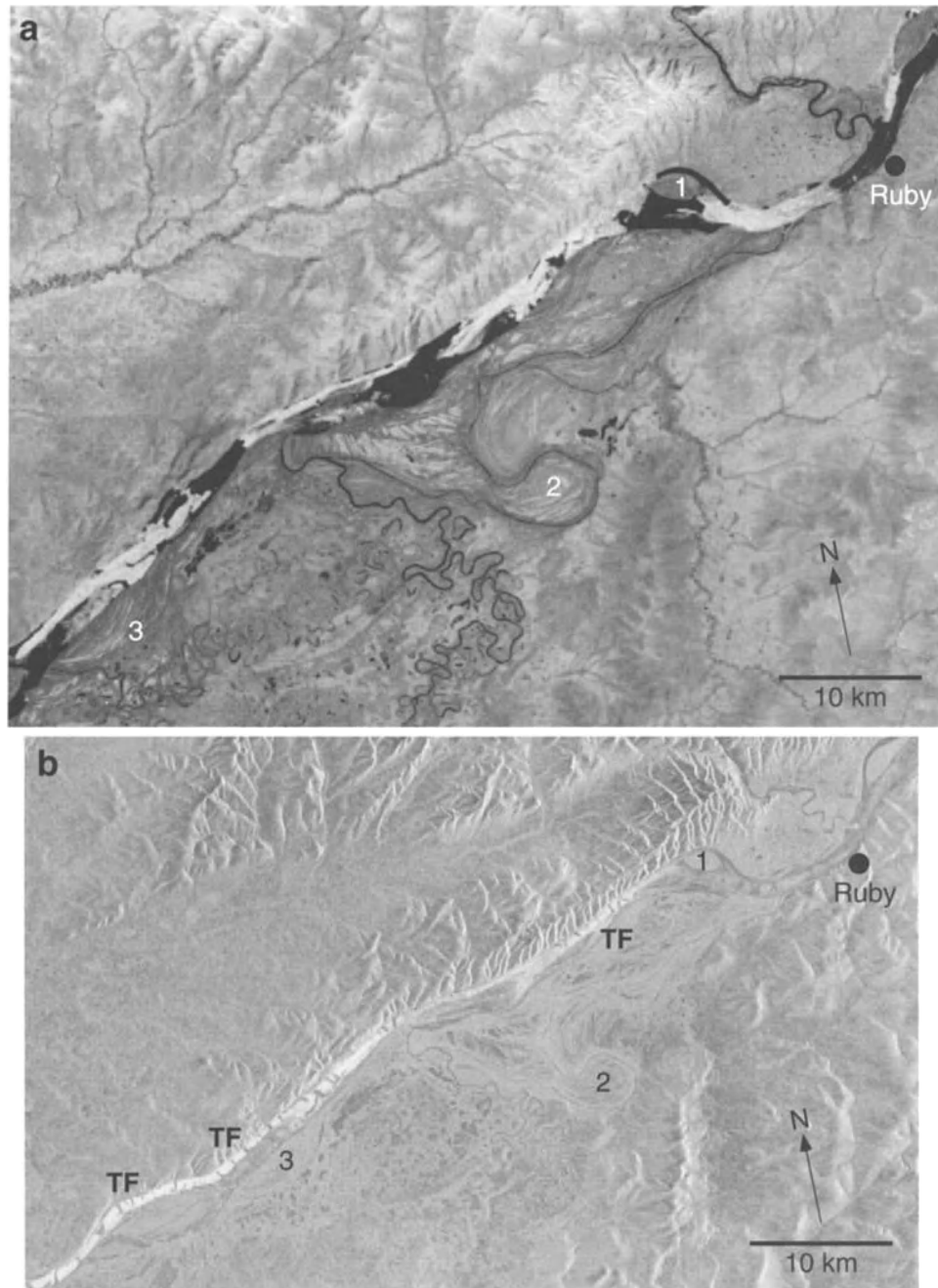
Figure 12. Ice break-up on the Yukon River downstream of Ruby, Alaska: (a) Landsat MSS Band 7 image, 10 May 1983, and (b) ERS-1 SAR image, 24 April 1994. Reference points 1, 2, and 3 identify the same location in each image. TF in (b) shows the location of transverse features in the ice cover. Ruby is located at 64.73°N, 155.48°W, 370 km west of Fairbanks. The Landsat image is reprinted with the kind permission of the Geophysical Institute, University of Alaska Fairbanks, where it was acquired by the now defunct Landsat Quick-Look Facility. The SAR image (©ESA) is from ASF.

congelation ice, which has a low albedo [0.1; *Bolsenga*, 1969], whereas the ice cover on turbulent reaches is predominantly frazil ice, which has an albedo similar to that of snow ice [*Prowse*, 1995]. *Bolsenga* [1969, 1977] reported snow ice albedo values of 0.39–0.46. Consequently, congelation ice absorbs more solar radiation and decays more rapidly than the more reflective frazil ice [*Prowse*, 1995]. Where snow ice is widespread, the underlying ice will be exposed and the ice

cover will decay more slowly than an ice cover with minimal snow ice [*Prowse*, 1995]. However, the effects of ice type and albedo are probably more complex than this, not the least because the albedo values cited by the above authors are for ice before the onset of melting. Ice types, albedo, and thermodynamic break-up are discussed further in section 5.2.

The role of dynamics in the opening of some reaches while others remain covered with ice is related primarily to the formation and failure of ice jams. Before an ice jam forms, the river ice sheet must fracture so that the ice can move. Fractures occur close to and parallel to the bank, down the center-line [*Prowse*, 1995], and most importantly, across the river ice sheet perpendicular to the banks, i.e., transverse cracks [*Beltaos*, 1990, 1997]. Transverse cracks occur when bending stresses exceed the flexural strength of the ice, sometimes in response to the passage of steep flood waves, which cause vertical bending, or where flow shear and the meandering planform of a channel cause horizontal bending. Transverse cracks have been reported in SAR images of the Moose River, northern Ontario [*Murphy et al.*, 2001], and as described in the previous section (Plate 2), detected by SAR interferometry [*Smith*, 2002].

Many transverse features are visible in the SAR image of the Yukon River (Figure 12b) and we hypothesize that they are a consequence of events that occurred after the initial formation of transverse cracks. Once the large slabs that are formed between the transverse cracks are set in motion, they quickly break down into small ice blocks, and when their downstream progress is halted by an intact, mechanically competent ice cover, an ice jam forms [*Beltaos*, 1997]. As the blocks move downstream, the river will open behind them, and it is transverse leads of open water that we believe are visible in Figure 12b.

Why and when an ice jam will fail is not fully known, but conditions at the toe (leading edge) of the jam, ice competence, discharge, and thermal effects probably all play a role [*Beltaos*, 1995b]. The surge that follows the failure of an ice jam can cause flooding downstream, ice fracture in situ as a breaking front propagates though the ice cover, or extensive clearing of the ice cover as the ice runs [*Prowse*, 1995]. When the ice run or breaking front is arrested by an intact ice cover further downstream, another ice jam will form. In fact, break-up over long distances in a river can be viewed as a series of surge–stall events related to the successive failure and formation of ice jams [*Scrimgeour et al.*, 1994]. It is this process that clears the ice from some reaches while others remain covered with ice. This might explain the state of the Yukon River in Figure 12a.

A similar pattern of open and ice-covered reaches has been observed on the Mackenzie River, using AVHRR data [*Dey et al.*, 1977]. AVHRR images have somewhat low spatial resolu-tion (maximum 1.1 km) and are appropriate for studying wide river channels such as those of the Mackenzie River. Because AVHRR images cover a broad area (swath width 2,580–4,000 km) it is possible to study ice break-up along the entire length of large rivers and place it in the context of catchment processes.

This is precisely what *Pavelsky and Smith* [2004] did with AVHRR and MODIS data in a study of break-up patterns along the entire length of the Mackenzie, Lena, Yenisey, and Ob' rivers. They were able to map break-up at any point along the rivers with a mean precision of ±1.75 days and a high degree of correlation with ground observations. Break-up patterns were governed primarily by latitude, timing of the spring flood wave, and location of confluences with major tributaries. Moreover, the pattern of break-up along the Russian rivers was shown to be similar from year to year, indicating that point-based river ice break-up records [e.g., *Magnuson et al.*, 2000] can indeed be used to reliably infer regional climate variations [*Pavelsky and Smith*, 2004].

Although relatively low spatial resolution data such as AVHRR and MODIS can be used to study river ice variability over large areas, higher spatial resolution data, e.g., Landsat (Figure 12) and SAR, make it possible to examine river ice processes at smaller scales. For example, *Murphy et al.* [2001] used RADARSAT-1 Fine Beam data (9-m spatial resolution) of the Hudson Bay Lowland to describe the progressive fracturing and shearing of river ice, the formation of leads and ice-push ridges, and a gradual change in ice characteristics that indicate increased wetness due to either melting or overflow onto the ice cover.

5.2. Lake Ice Break-up

Unlike initial ice formation and subsequent ice growth, which can be understood relatively easily in terms of heat conduction driven by the energy balance at the top surface, the thermodynamic decay of lake ice is more complex because the top and bottom surfaces melt simultaneously as the ice becomes isothermal at 0°C [*Larsen et al.*, 1986]. The exception is grounded ice, which often melts only at the top without ever becoming afloat [*Brewer*, 1958]. Furthermore, melting is influenced by the albedo of the ice, which, as was discussed briefly in the previous section, is affected by the often variable ice crystal texture.

Lake ice break-up begins when the snow cover starts to melt, an event that is quite straightforward to detect with microwave remote sensing. For example, the change in the appearance of the airborne passive microwave images (Figure 10) is due to increased emission from the snow cover, which had become wet (Figure 10b), obscuring the features that were so clearly visible only 3 days before (Figure 10a) [*Melloh et al.*, 1991]. Thaw/freeze events that cause spikes in

SSM/I 85-GHz brightness temperatures have been reported at Great Slave Lake [*Walker and Davey*, 1993].

In the case of active microwave remote sensing, the microwave penetration depth rapidly decreases as snow wetness increases, and absorption becomes the dominant loss mechanism [*Stiles and Ulaby*, 1980]. This results in a significant reduction in backscatter and, in the case of North Slope lakes, a loss of the strong contrast between the bright and dark tones of the ice cover, which appear almost equally dark (Figure 13). Likewise, the peculiar concentric bright and dark rings in SAR images of ice-covered Lake El'gygytgyn, northeast Siberia, were obscured once snowmelt was underway [*Nolan et al.*, 2003].

Jeffries et al. [1994] reported a curious phenomenon as melt progressed on the shallow lakes on the North Slope: the floating and grounded ice signatures reversed completely, as the backscatter from grounded ice increased while the backscatter from floating ice decreased. Observations and modelling suggest that the backscatter reversal occurs while the ice remains blanketed with a snow cover that is undergoing thaw/freeze cycles, which leads to a roughening of the surface of the grounded ice (backscatter increase) and the development of a water film at the surface of the floating ice (backscatter decrease) [*Wakabayashi et al.*, 1999].

If snow ice formed during the winter, it will be the first ice to be exposed once the snow melts completely. Because of its high albedo, a layer of snow ice can slow the break-up of a lake ice cover [*Michel et al.*, 1986]. Once the congelation ice is exposed, absorption of shortwave radiation is particularly effective in promoting the decay of S2 congelation ice (Figures 2 and 4), as melting occurs along the vertically oriented crystal boundaries in a process known as "candling" that can originate simultaneously at the top and bottom of the ice [*Larsen et al.*, 1986]. Candling does not occur in S1 congelation ice; instead, tubules and air bubbles form when solar radiation causes melting in the macrocrystals [*Knight*, 1962].

Important factors with respect to ice decay are the crystal texture of the congelation ice and whether S1 and S2 ice occur in the same ice cover, because melting S1 ice has a higher albedo than melting S2 ice, as observed at Peters Lake, Alaska (Figure 14) [*Knight*, 1962]. Few data are available on the albedo of melting congelation ice, but *Heron and Woo* [1994] reported albedos of 0.45 and 0.2 for melting S1 and S2 ice, respectively, i.e., higher than the value (0.1) for frozen congelation ice [*Bolsenga*, 1969]. *Prowse and Marsh* [1989] reported albedo values of 0.39 for candled ice and 0.55 for granulated congelation ice (we interpret this as melting S1 congelation ice based on our experience during lake ice melt). It is because of the albedo changes that occur as the ice melts that we suggested earlier that the thermodynamic break-up of river ice might not be as simple as described in section 5.1.
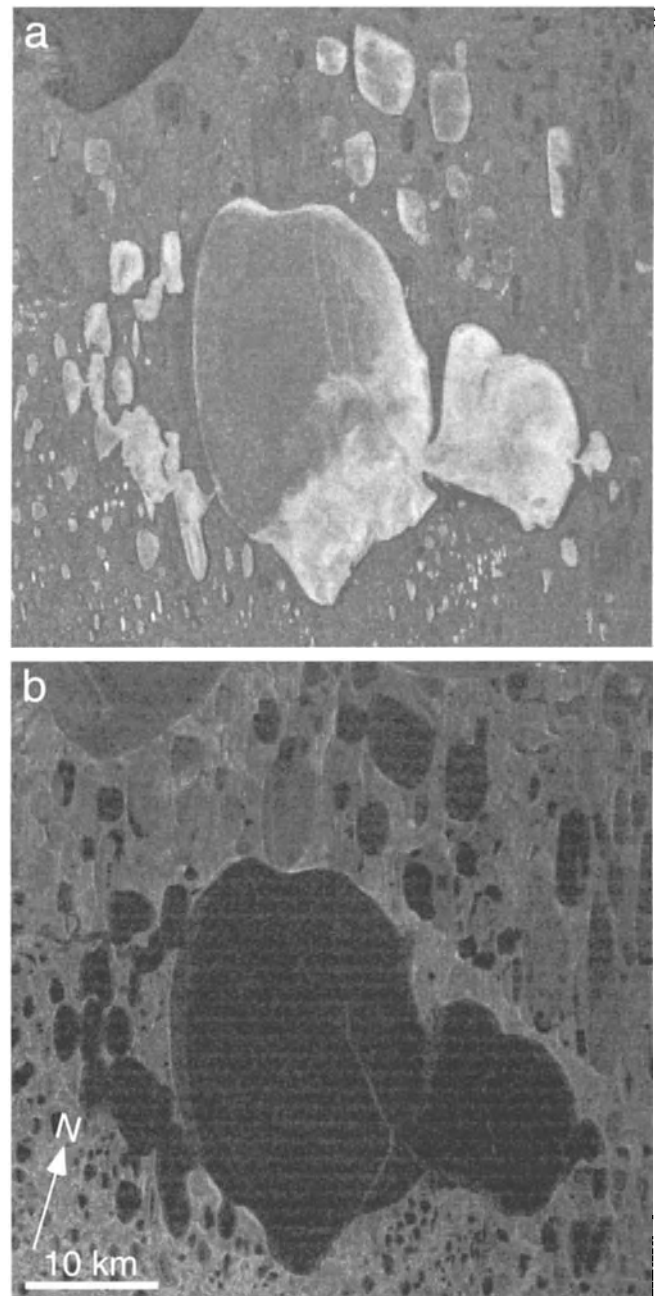
Figure 13. SAR image subscenes of Teshekpuk Lake showing the onset of melt between (a) 25 May and (b) 5 June 1997. Original RADARSAT-1 ScanSAR Wide B images (©CSA) are from ASF.

Figure 15a is a Landsat MSS band 5 (visible) image that shows subtle shades of gray. In light of the two previous paragraphs, it is possible that these reflect spatial variability in the exposure of different ice types, but we shall never know. Figure 15b is a MSS band 7 (near-infrared; NrIR) image that confirms the ice surface is wet and also shows the pooling
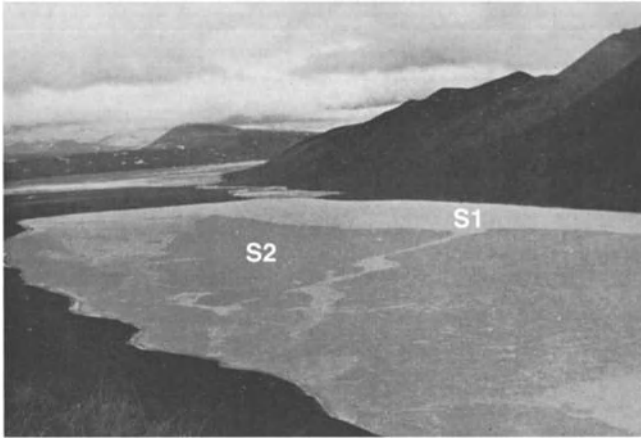
Figure 14. Oblique aerial photograph of Peters Lake, Alaska, showing S1 and S2 congelation ice exposed during the spring melt period. Peters Lake is located at 69.33°N, 145.05°W, in the easternmost Brooks Range, 100 km south-southwest of Kaktovik. Reprinted from *Knight* [1962] with the kind permission of the International Glaciological Society and C. A. Knight.

of water around the lake margin [*Hall and Martinec*, 1985]. This is common during the break-up period and leads to more rapid melting and release of the main ice cover from the shore, thereby allowing it to be moved about the lake by the wind [*Michel et al.*, 1986]. As the ice moves and simultaneously thins and weakens, it fractures, and once fractured, it disappears quickly [*Larsen et al.*, 1986; *Michel et al.*, 1986].

Figure 16 shows extensive ice fractures at Teshekpuk Lake during break-up. *Nolan et al.* [2003] illustrate ice fracturing and shrinkage during break-up at Lake El'gygytgyn with a sequence of Landsat and SAR images.

The rapidity with which an ice cover can break up is illustrated in Plate 4, a sequence of SSM/1 85-GHz images of Great Slave Lake. Open water first appeared in the southeastern region on 7 June and spread rapidly to the north and west until the lake was almost completely ice-free on 22 June. The potential for passive microwave remote sensing of lake ice break-up was originally suggested by *Barry and Maslanik* [1993; their Figure 6], who illustrated the SMMR 37-GHz brightness temperature changes and polarization differences associated with the break-up of the Great Slave Lake ice cover.

Figure 16 illustrates another important aspect of lake ice break-up: the ice disappears earlier from some lakes than from others. On the North Slope of Alaska, it is the shallow lakes with a relatively thin ice cover that become ice-free before the deeper lakes with a thicker ice cover do [*Sellmann et al.*, 1975a]. *Bilello* [1980] describes the role that thickness plays in the break-up of an ice cover.

6. MULTIYEAR LAKE ICE

As noted in the Introduction, some lakes in the Northern Hemisphere have perennial (multiyear) ice covers because they do not melt completely each summer. These include
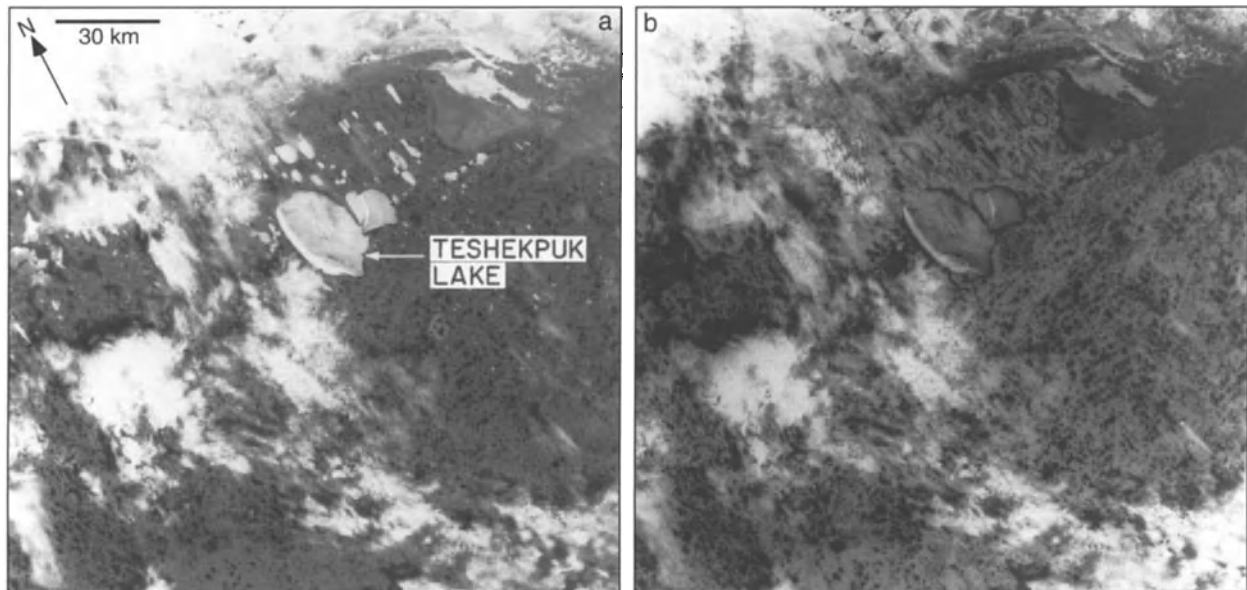
Figure 15. Teshekpuk Lake and surrounding area on 6 July 1978 in (a) Landsat MSS Band 5 image, and (b) Landsat MSS Band 7 image. Original provided by D. K. Hall and reprinted from *Hall and Martinec* [1985] with the kind permission of Kluwer Academic Publishers.
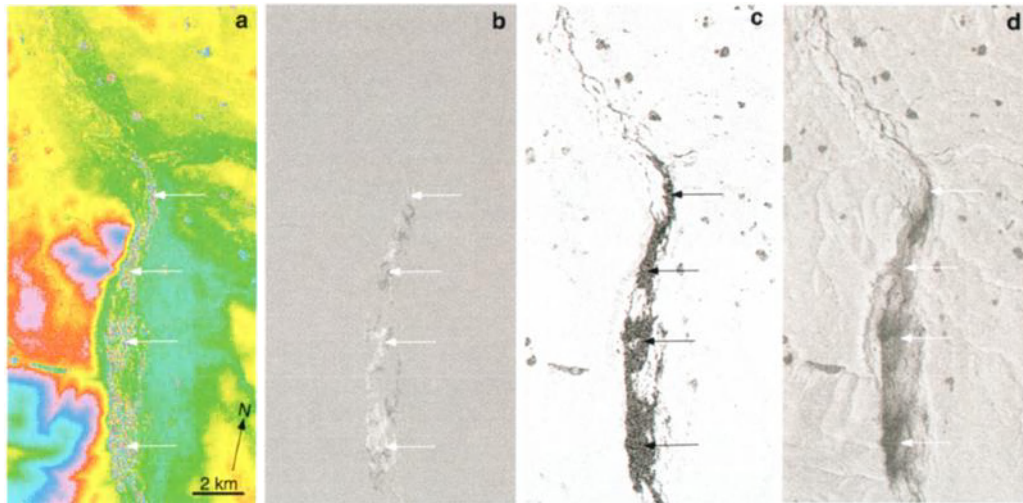
Plate 3. ERS-1 SAR interferometry of aufeis on the Ivishak River, North Slope of Alaska, for the period 20–26 January 1994: (a) phase difference image or interferogram; (b) amplitude/backscatter difference image; (c) coherence image; and (d) accumulated coherence image for the period 8 January to 13 February 1994. The four arrows in each panel show the general course of the aufeis deposit. The centre of each panel is at 69.34°N, 148.22°W. Originals provided by S. Li and reprinted from *Li et al.* [1997] with the kind permission of Elsevier.
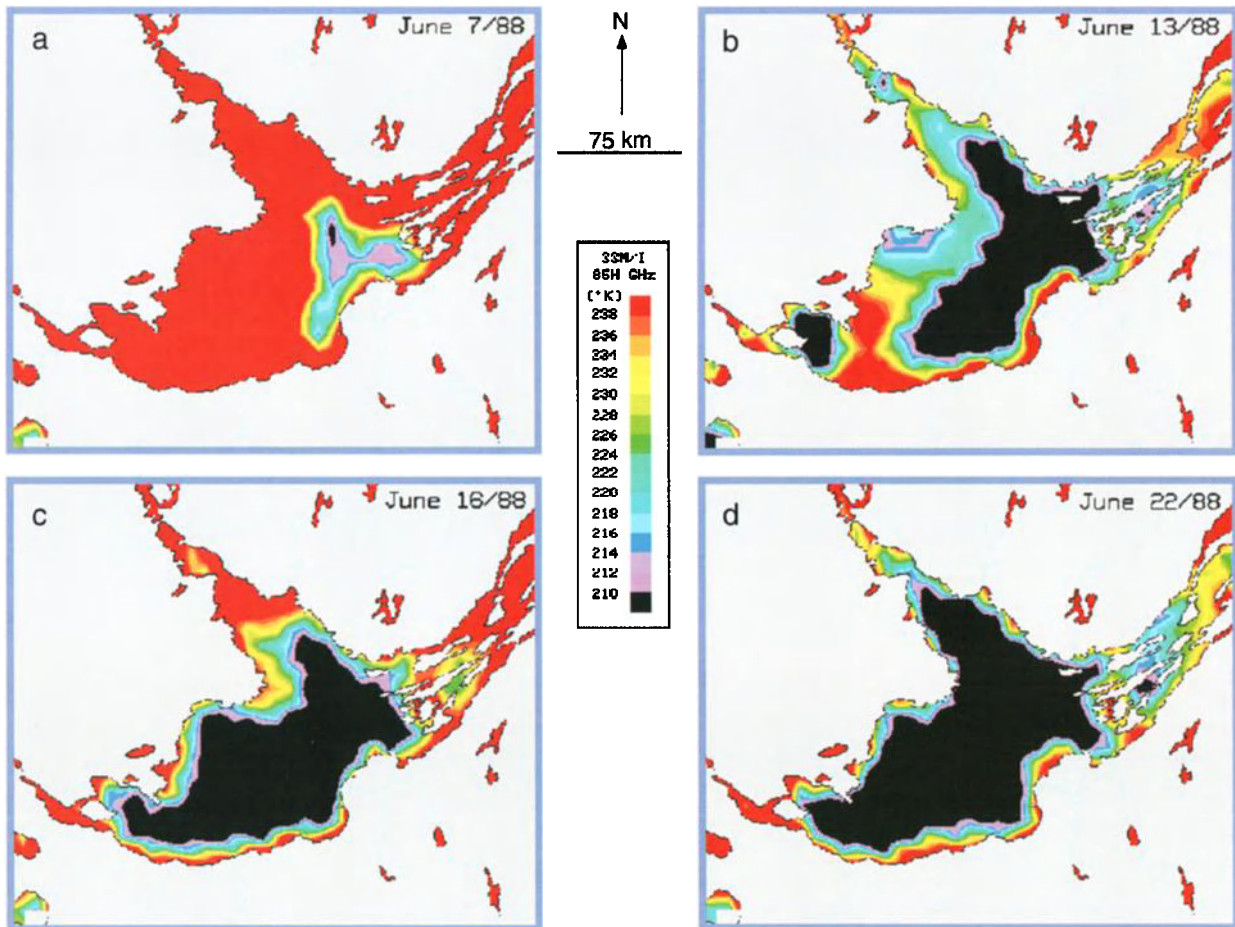
Plate 4. SSM/I 85-GHz brightness temperature images illustrate the break-up of the ice cover on Great Slave Lake, Northwest Territories, in June 1988. The centre of Great Slave Lake is at 61.54°N, 114.21°W. Original provided by A. E. Walker, Meteorological Service of Canada, and reprinted with her kind permission.
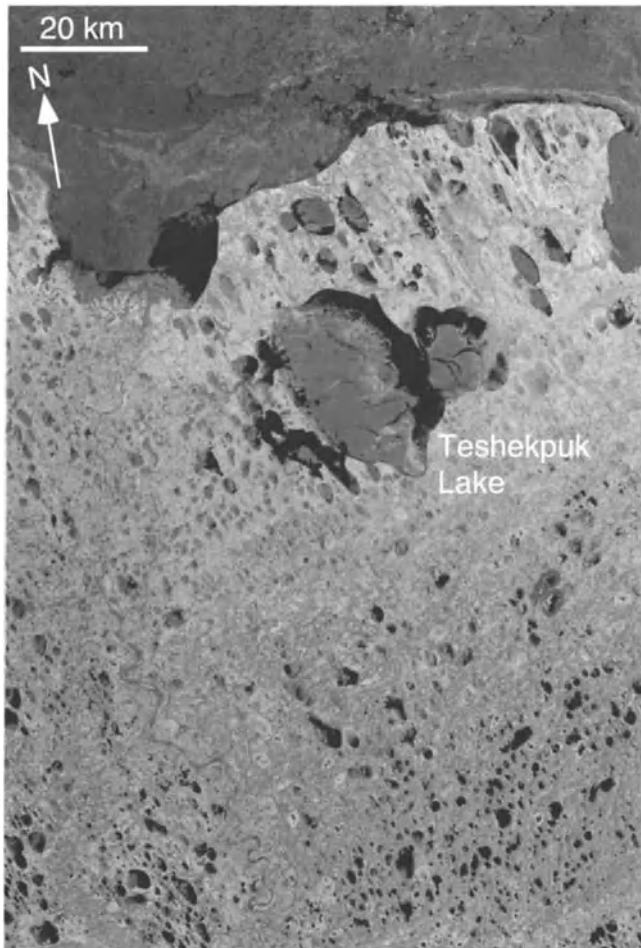
Figure 16. Ice break-up in the vicinity of Teshekpuk Lake, 9 July 1992. ERS-1 SAR image (©ESA) from ASF.

Colour Lake, Axel Heiberg Island, Nunavut, Canada [*Doran et al.*, 1996], and a few lakes in northernmost Ellesmere Island, Nunavut. The Ellesmere Island lakes, marked in the RADARSAT-1 ScanSAR image (Figure 17), are easily identified by the bright signature of the ice. The signature resembles the floating ice on the shallow, thaw lakes on the Hudson Bay Lowland (Figure 3) and the North Slope of Alaska (Figures 8 and 9; Plate 1) but has different origins. The perennial ice has a candled surface [*Hattersley-Smith et al.*, 1970; *Belzile et al.*, 2001; *Jeffries*, unpublished observations made in 1982 and 1983] and contains many internal melt features [*Jeffries*, 1985] that must cause strong surface and volume scattering, respectively.

Lakes A, B, C1, and C2 are physically and biologically interesting because they are meromictic, i.e., permanently stratified, with an upper freshwater layer overlying a deep layer of modified seawater [*Hattersley-Smith et al.*, 1970; *Jeffries et al.*, 1984; *Belzile et al.*, 2001; *Gibson et*

al., 2002]. The lakes are meromictic because the perennial ice cover isolates the water from wind-induced mixing and perhaps also convective mixing. Whether the lakes remain meromictic or the meromixis is altered will be determined by the ice cover, which has experienced significant changes in recent years. In summer 1998 and 2000 no ice was observed on Lakes C1 and C2 (Figure 18; see also *Belzile et al.* [2001]) and in summer 2000 there was a considerable reduction in the area of ice on Lakes A and B (Figure 19). Any effects on the meromixis have yet to be determined.

Like the ice on the meromictic lakes and the ice on Taconite Inlet, M'Clintock Inlet and Disraeli Fiord have a bright signature that indicates strong backscatter (Figure 17). Since the inlets and fiord are connected to the nearby Arctic Ocean, this raises a question as to why the ice does not have a backscatter signature similar to that of the sea ice a short distance to the north, beyond the Ward Hunt Ice Shelf (Figure 17). The answer is simple: at the time Figure 17 was obtained, and for at least 31 years before that, Disraeli Fiord was highly stratified, with a surface layer of freshwater overlying the deeper seawater [*Keys*, 1978; *Jeffries*, 1992; *Vincent et al.*, 2001]. That is, Disraeli Fiord contained an epishelf lake [*Vincent et al.*, 2001; *Mueller et al.*, 2003] with a perennial lake ice cover that had been growing from the surface freshwater layer. Like the perennial ice on the nearby meromictic

Figure 17. SAR image subscene of the Ward Hunt Ice Shelf, Disraeli Fiord, and vicinity, including the location of perennially ice-covered Lakes A, B, C1, C2, and C3, northern Ellesmere Island, Nunavut, 26 May 1998. The center of Lake A is located at 83.00°N, 74.50°W. The center of Lake C2 is located at 82.83°N, 78.00°W. The original RADARSAT-1 Standard Beam (ST5) SAR image (©CSA) is from ASF.

Figure 18. SAR image subscenes of Lakes C1, C2, and C3 between summer 1997 and summer 2002 showing advanced to complete melting of the ice on all three lakes in 1998 and 2000, advanced melting on Lake C3 in 2002, and the development of a modest moat in other years. North is at the top of each frame. The original RADARSAT-1 Standard Beam images (©CSA) are from ASF.

cover at a number of locations along the northernmost coast of Ellesmere Island [*Jeffries*, 2002].

The epishelf lake in Disraeli Fiord was composed of snow and ice meltwater runoff impounded in the fiord to a depth equivalent to the draft of the Ward Hunt Ice Shelf [*Keys*, 1978; *Jeffries*, 1992; *Vincent et al.*, 2001]. Between 1967 and 1999, the depth of the epishelf lake decreased by 14 m, implying that either the Ward Hunt Ice Shelf had uniformly thinned that much or a more localized conduit had formed in that time [*Vincent et al.*, 2001]. *Jeffries* [2002] predicted that further significant changes in the hydrography of Disraeli Fiord and other epishelf lakes in this region, e.g., complete flushing of the freshwater and breakdown of the strong stratification, might be detected by changes in the backscatter from the ice cover, which would appear darker in SAR images if seawater began to freeze on the bottom. This is what occurred between January and May 2002 (Figure 20). Salinity and temperature measurements in Disraeli Fiord in July 2002 confirmed that the epishelf lake had drained completely [*Mueller et al.*, 2003]. The sudden drainage of the epishelf lake probably occurred through a large fracture in the ice shelf [*Mueller et al.*, 2003] and a unique biological community [*Van Hove et al.*, 2001] was probably lost.

Meromictic lakes A, B, C1, and C2 and the epishelf lakes of the fiords, bays, and inlets of northernmost Ellesmere Island lie at the northern limit of Arctic lakes, where future climate changes and effects are likely to be pronounced [*Belzile et al.*, 2001]. The response of the water bodies to climate change is intimately linked to the response of their ice covers, and it is clear that they have been changing in recent years. Since there have been significant changes in other ice components of the Arctic cryosphere in recent years

lakes, there was strong backscatter from the epishelf lake ice (Figure 17) due to surface scattering from candled ice and volume scattering from internal melt features. From the bright signatures of Taconite and M'Clintock inlets, we can reasonably infer that they also have epishelf lakes with a perennial lake ice cover. Ice shelf and multiyear landfast sea ice dams cause epishelf lakes with perennial lake ice

Figure 19. SAR image subscenes of Lakes A and B between summer 1999 and summer 2002 showing advanced to complete melting of the ice cover in 2000, and the development of a modest moat in other years. North is at the top of each frame. The original RADARSAT-1 Standard Beam images (©CSA) are from ASF.
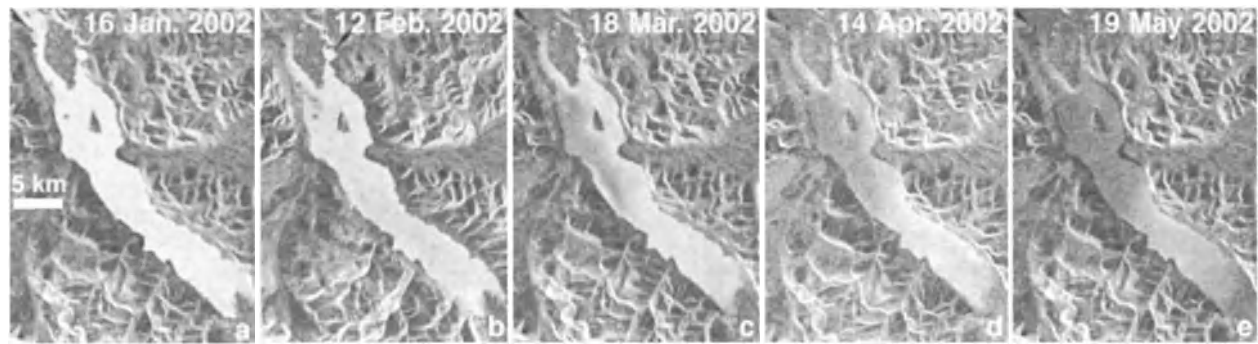
Figure 20. SAR image subscenes of Disraeli Fiord, January to May 2002, showing the decrease in backscatter associated with the drainage of freshwater from the fiord and the onset of sea ice growth at the bottom of the previously freshwater ice cover. The southernmost end of the fiord is located at 82.70°N, 72.66°W. North is at the top of each frame. The original RADARSAT-1 ScanSAR images (©CSA) are from ASF.

[e.g., *Morison et al.*, 2000; *Serreze et al.*, 2000], we suggest that the changes observed in the perennial lake ice covers are additional evidence of Arctic change. For this reason alone, continued monitoring of the ice on the lakes and epishelf lakes is warranted [*Jeffries*, 2002].

7. DISCUSSION AND CONCLUSION

We have described ice characteristics and processes and have used remote sensing images to illustrate a number of aspects of the evolution of the ice cover from the time of initial ice formation, through winter thickening, to the onset of melt and the final disappearance of ice on northern (Alaska, Canada) rivers and lakes. Most northern freshwater ice is seasonal in nature, but we have also illustrated some of the perennially ice-covered lakes and freshwater ice-covered fiords of northernmost Ellesmere Island, Nunavut. The illustration of ice variability and change, some dramatic in remote locations, underscores the importance of frequent data acquisition and the value of time series of images to follow the course of events and processes.

River ice and lake ice characteristics and processes have been illustrated primarily with active microwave (SAR) images, together with some aerial photography and passive microwave and Landsat images. The focus on SAR reflects our particular interests and expertise, and also a belief that, in the long term, these are the most useful data for remote sensing of freshwater ice processes at high latitudes. Most northern freshwater ice occurs in remote locations, where field studies are costly and where darkness and poor weather interfere with data acquisition in the visible and IR/NrIR/TIR bands. SAR data have high spatial resolution and, in particular, allow one to "see" the ice rather than the snow cover for the entire winter. Even in the spring, when the snow wetness increases, SAR gives a useful signal of the onset of snow and ice melt. Wide-swath imaging, which is now a standard feature of current (RADARSAT-1, Envisat-ASAR) and planned (RADARSAT-2, ALOS-PALSAR) spaceborne SAR instruments, increases their value for all-season remote sensing of lake ice and river ice. The multi-polarization capability of RADARSAT-2 and PALSAR is an exciting prospect that ought to reveal new information about freshwater ice.

Passive microwave complements SAR in having all-weather, all-season capabilities but also has the advantage of daily to sub-daily data acquisition. However, because passive microwave has a coarser spatial resolution, it is best suited to the study of medium to large lakes. Passive microwave also offers potential opportunities for the determination of freshwater ice thickness and the depth of snow that it supports. Lake ice studies could benefit from the continuing concern about the state of the Arctic and Antarctic sea ice covers, as efforts are made to develop spaceborne laser- and radar altimeter-based methods to determine ice thickness.

Although poor weather and illumination often limit the use of visible and IR/NrIR/TIR imagery, there is no question that much has been achieved with these data, particularly with respect to monitoring the duration of the ice cover on lakes. AVHRR and DMSP OLS, and successor instruments, will no doubt continue to be used because they cover large areas on a daily to sub-daily basis and are often available at minimal cost. When cloud-free visible and IR/NrIR/TIR are available, they provide a useful complement to microwave imagery. Even cloudy imagery has its uses, particularly with respect to the use and understanding of data at the highest passive microwave frequencies, which are subject to atmospheric interference.

We began the chapter with a lament by *Gerard* [1990] about the poor state of knowledge and lack of appreciation for the role of river ice and lake ice in northern hydrology. Remote sensing has the potential to improve the situation by allowing us to see from above, often on a frequent basis over broad areas, various ice characteristics and processes on riv-

ers and lakes that would otherwise be difficult to see on the ground. Remote sensing can (1) support field investigations, (2) enable monitoring of the evolution of the ice cover and process studies between freeze-up and break-up, (3) allow scaling up from small to large (local to regional to continental to hemispheric), and (4) contribute to the calibration and validation of computer simulations.

As new satellites are launched, a growing constellation of ever more sophisticated instruments will make it possible to pursue multisensor remote sensing investigations of river ice and lake ice in conjunction with field programs and computer modelling. The need to know and understand more about the role of river ice and lake ice in northern hydrology is more important then ever in a region where significant environmental change is occurring on the sea and on the land in response to the changing climate. There are potentially significant physical, biological, and human consequences associated with changing patterns in the growth and decay of river ice and lake ice, and remote sensing of the ice cover has a vital role to play in assessing the occurrence and magnitude of the consequences of climate change.

REFERENCES

Adams, W. P., Snow and ice on lakes, in *Handbook of Snow and Ice: Principles, Processes, Management and Use*, edited by D. M. Grey and D. H. Male, pp. 437–474, Pergamon Canada, 1981.

Adams, W. P., and D. C. Lasenby, The role of ice and snow in lake heat budgets, *Limnol. Oceanogr.*, 23(5), 1025–1028, 1978.

Adams, W. P., and T. D. Prowse, Evolution and magnitude of spatial patterns in the winter cover of temperate lakes, *Fennia*, 159(2), 343–359, 1981.

Adams, W. P., and N. T. Roulet, Illustration of the roles of snow in the evolution of the winter ice cover, *Arctic*, 33(1), 100–116, 1980.

Agnew, T. A., H. Le, and T. Hirose, Estimation of large-scale sea ice motion from SSM/I 85 GHz imagery, *Ann. Glaciol.*, 25, 305–311, 1997.

Ashton, G. D., Freshwater ice growth, motion and decay, in *Dynamics of Snow and Ice Masses*, edited by S. C. Colbeck, pp. 261–304, Academic Press, 1980.

Ashton, G. D. (editor), *River and Lake Ice Engineering*, Water Resources Publications, Littleton, CO, 1986.

Assel, R. A., Implications of CO$_2$ global warming on Great Lakes ice cover, *Climatic Change*, 18(4), 377–395, 1991.

Assel, R. A., and D. M. Robertson, Changes in winter air temperatures near Lake Michigan, 1851–1993, as determined from regional lake ice records, *Limnol. Oceanogr.*, 40(1), 165–176, 1995.

Assel, R. A., F. H. Quinn, G. A. Leshkevich, and S. J. Bolsenga, *Great Lakes Ice Atlas*, Great Lakes Environmental Research Laboratory, Ann Arbor, Michigan, U.S.A., 1983.

Bari, S. A., and J. Hallett, Nucleation and growth of bubbles at an ice–water interface, *J. Glaciol.*, 13(69), 489–520, 1974.

Barns, R. L., and R. A. Laudise, Size and perfection of crystals in lake ice, *J. Crystal Growth*, 71(1), 104–110, 1985.

Barnes, H. T., *Ice Formation with Special Reference to Anchor-ice and Frazil*, John Wiley and Sons, New York, 1906.

Barnes, H. T., *Ice Engineering*, Renouf Publishing Company, Montreal, Québec, 1928.

Barry, R. G., and J. A. Maslanik, Monitoring lake freeze–up/break–up as a climatic indicator, in *Snow Watch '92*, edited by R. G. Barry, B. E. Goodison and E. F. LeDrew, *Glaciological Data Report GD-25*, pp. 66–79, NSIDC, University of Colorado, Boulder, CO, 1993.

Beltaos, S., Fracture and break-up of river ice cover, *Can. J. Civ. Eng.*, 17(2), 173–183, 1990.

Beltaos, S. (editor), *River Ice Jams*, Water Resources Publications, LLC, Highlands Ranch, CO, 1995a.

Beltaos, S., Ice jam processes, in *River Ice Jams*, edited by S. Beltaos, pp. 71–104, Water Resources Publications, LLC, Highlands Ranch, CO, 1995b.

Beltaos, S., Onset of river ice break-up, *Cold Reg. Sci. Tech.*, 25(3), 183–196, 1997.

Belzile, C., W. F. Vincent, J. A. E. Gibson and P. Van Hove, Bio-optical characteristics of the snow, ice, and water column of a perennially ice-covered lake in the High Arctic, *Can J. Fish Aquat. Sci.*, 58(12), 2405–2418, 2001.

Bengtsson, L., Spatial variability of lake ice covers, *Geogr. Annaler*, 68A(1–2), 113–121, 1986.

Bilello, M. A., Maximum thickness and subsequent decay of lake, river and fast sea ice in Canada and Alaska, *CRREL Rep. 80-6*, 160 pp., U.S. Army Cold Reg. Res. and Eng. Lab., Hanover, NH, 1980.

Bolsenga, S. J., Total albedo of Great Lakes ice, *Water Res. Res.*, *5*(5), 1132–1133, 1969.

Bolsenga, S. J., Preliminary observations on the daily variation of ice albedo, *J. Glaciol.*, *18*(80), 517–521, 1977.

Brewer, M. C., The thermal regime of an Arctic lake, *Trans. AGU*, *39*(2), 278–284, 1958.

Bryan, M. L., and R. W. Larson, The study of fresh–water lake ice using multiplexed imaging radar, *J. Glaciol.*, *14*(72), 445–457, 1975.

Carstens, T., L. Bergdahl, R. L. Gerard, M. Määttänen, D. Nevel, D. Sodhi, and P. Tryde, Ice mechanics, in *River and Lake Ice Engineering*, edited by G. D. Ashton, pp. 87–201, Water Resources Publications, Littleton, CO, 1986.

Dean, K. G., Stream-icing zones in Alaska, *Report No. 84-16*, 20 pp., Division of Geological Surveys, Department of Natural Resources, State of Alaska, 1984.

Dey, B., H. Moore, and A. F. Gregory, The use of satellite imagery for monitoring ice break-up along the Mackenzie River, N.W.T., *Arctic*, *30*(4), 234–242, 1977.

Doran, P. T., C. P. McKay, W. P. Adams, M. C. English, R. A. Wharton, Jr., and M. A. Meyer, Climate forcing and thermal feedback of residual ice covers in the high Arctic, *Limnol. Oceanogr.*, *41*(5), 839–848, 1996.

Duguay, C. R., and P. M. Lafleur, Monitoring ice freeze–up and break-up of shallow tundra lakes and ponds, in *Proceedings of GER'97 (International Symposium: Geomatics in the Era of RADARSAT)* (on CD–ROM), 24–30 May 1997, Ottawa, Ontario, 1997.

Duguay, C. R., and P. M. Lafleur, Determining depth and ice thickness of shallow subarctic lakes using spaceborne optical and SAR data, *Int. J. Remote Sens*, *24*(3), 475–489, 2003.

Duguay, C. R., W. R. Rouse, P. M. Lafleur, D. L. Boudreau, Y. Crevier, and T. J. Pultz, Analysis of multi–temporal ERS–1 SAR data of subarctic tundra and forest in the northern Hudson Bay Lowland and implications for climate studies, *Can. J. Remote Sens.*, *25*(1), 21–33, 1999.

Duguay, C. R., T. J. Pultz, P. M. Lafleur, and D. Drai, RADARSAT backscatter characteristics of ice growing on shallow sub-arctic lakes, Churchill, Manitoba, Canada, *Hydrol. Proc.*, *16*(8), 1631–1644, 2002.

Duguay, C. R., G. M. Flato, M. O. Jeffries, P. Ménard, W. R. Rouse, and K. Morris, Ice cover variability on shallow lakes at high latitudes: Model simulations and observations, *Hydrol. Proc.*, *17*(17), 3465–3483, 2003.

Fang, X., and H. G. Stefan, Simulated climate change effects on ice and snow covers on lakes in a temperate region, *Cold Reg. Sci. Tech.*, *25*(2), 137–152, 1997a.

Fang, X., and H. G. Stefan, Simulated climate change effects on dissolved oxygen characteristics in ice-covered lakes, *Ecol. Model.*, *103*(2–3), 209–229, 1997b.

Frankenstein, G., D. Hall, D. McGinnis, C. Merry, V. Salomonsen, and J. Welker, Remote sensing, in *River and Lake Ice Engineering*, edited by G. D. Ashton, pp. 427–443, Water Resources Publications, Littleton, CO, 1986.

Gatto, L. W., Monitoring river ice with Landsat images, *Remote Sens. Environ.*, *32*(1), 1–16, 1990.

Gatto, L. W., River ice conditions determined from ERS-1 SAR, in *Proceedings of the 50th Eastern Snow Conference and the 61st Western Snow Conference*, 7–10 June 1993, Québec City, Québec, edited by M. Ferrick and T. Pangburn, U.S. Army, Cold Reg. Res. and Eng. Lab., Hanover, NH, pp. 113–122, 1993.

Gerard, R., Hydrology of floating ice, in *Northern Hydrology: Canadian Perspectives*, edited by T. D. Prowse and C. S. L. Ommanney, *NHRI Science Report No. 1*, pp. 103–134, National Hydrology Research Institute, Saskatoon, Saskatchewan, Canada, 1990.

Gerard, R. L., and K. S. Davar, Introduction, in *River Ice Jams*, edited by S. Beltaos, pp. 1–28, Water Resources Publications, LLC, Highlands Ranch, CO, 1995.

Gerard, R. L., and S. Stanley, Ice jams and flood forecasting, Hay River, N.W.T., *Water Resources Engineering Report No. 88-6*, 199 pp., Department of Civil Engineering, University of Alberta, Edmonton, Alberta, 1988.

Gibson, J. A. E., W. F. Vincent, P. Van Hove, C. Belzile, X. Wang, and D. Muir, Geochemistry of ice-covered, meromictic Lake A in the Canadian High Arctic, *Aquat. Geochem.*, *8*, 97–119, 2002.

Gill, D., Significance of spring break-up to the bioclimate of the Mackenzie Delta, in *The Coast and Shelf of the Beaufort Sea*, edited by J. C. Reed and J. E. Slater, pp. 543–544, The Arctic Institute of North America, Arlington, VA, 1974.

Gow, A. J., Orientation textures in ice sheets of quietly frozen lakes, *J. Crystal Growth*, *74*(2), 247–258, 1986.

Gow, A. J., and D. Langston, Growth history of lake ice in relation to its stratigraphic, crystalline and mechanical structure, *CRREL Rep. 77-1*, 24 pp., U.S. Army Cold Reg. Res. and Eng. Lab., Hanover, NH, 1977.

Gray, D. M., and T. D. Prowse, Snow and floating ice, in *Handbook of Hydrology*, edited by D. Maidment, pp. 7.1–7.58, McGraw Hill, New York, 1993.

Hall, D. K., Remote sensing of snow and ice, in *Principles and Applications of Imaging Radar*, edited by F. M. Henderson and A. J. Lewis, pp. 677–703, John Wiley and Sons, Inc., New York, 1999.

Hall, D. K., and J. Martinec, *Remote Sensing of Snow and Ice*, Chapman and Hall, New York, 1985.

Hall, D. K., J. L. Foster, A. T. C. Chang, and A. Rango, Freshwater ice thickness observations using passive microwave sensors, *IEEE Trans. Geosci. Remote Sens.*, *GE–19*(4), 189–193, 1981.

Hall, D. K., D. B. Fagre, F. Klasner, G. Linebaugh, and G. E. Liston, Analysis of ERS–1 synthetic aperture radar data of frozen lakes in northern Montana and implications for climate studies, *J. Geophys. Res.*, *99*(C11), 22,473–22,482, 1994.

Hattersley–Smith, G., J. E. Keys, H. Serson, and J. E. Mielke, Density stratified lakes in northern Ellesmere island, *Nature*, *225*(5227), 55–56, 1970.

Heron, R., and M.-K. Woo, Decay of a High Arctic lake ice cover: Observations and modelling, *J. Glaciol.*, *40*(135), 283–292, 1994.

Hill, D. K., and J. J. Magnuson, Potential effects of global climate warming on the growth and prey consumption of Great Lakes fish, *Trans. Amer. Fish. Soc., 119* (2), 265–275, 1990.

Huttula, T., A. Peltonen, A. Bilaletdin, and M. Saura, The effects of climatic change on lake ice and water temperature, *Aqua Fennica, 22*(2), 129–142, 1992.

Jeffries, M. O., Physical, chemical and isotopic investigations of Ward Hunt Ice Shelf and Milne Ice Shelf, Ellesmere Island, N.W.T., Ph.D. thesis, Univ. of Calgary, 1985.

Jeffries, M. O., Arctic ice shelves and ice islands: Origin, growth and disintegration, physical characteristics, structural–stratigraphic variability and dynamics, *Rev. Geophys., 30*(3), 245–267, 1992.

Jeffries, M. O., Ellesmere Island ice shelves and ice islands, in *Satellite Image Atlas of Glaciers of the World: Glaciers of North America*, edited by R. S. Williams, Jr. and J. G. Ferrigno, *USGS Prof. Paper 1386-J*, U. S. Geological Survey, Reston, VA, J147–J164, 2002.

Jeffries, M. O., H. R. Krouse, M. A. Shakur, and S. A. Harris, Isotope geochemistry of stratified Lake "A", Ellesmere Island, N.W.T., *Can. J. Earth Sci., 21*(9), 1008–1017, 1984.

Jeffries, M. O., K. Morris, W. F. Weeks, and H. Wakabayashi, Structural–stratigraphic features and ERS–1 SAR backscatter characteristics of ice growing on shallow lakes in N.W. Alaska, winter 1991–92, *J. Geophys. Res., 99*(C11), 22,459–22,471, 1994.

Jeffries, M. O., K. Morris, and G. E. Liston, A method to determine lake depth and water availability on the North Slope of Alaska with spaceborne imaging radar and numerical ice growth modelling, *Arctic, 49*(4), 367–374, 1996.

Jeffries, M. O., T. Zhang, K. Frey, and N. Kozlenko, Estimating late winter heat flow to the atmosphere from the lake–dominated Alaskan North Slope, *J. Glaciol., 45*(150), 315–324, 1999.

Jones, J. A. A., The growth and significance of white ice at Knob Lake, Québec, *Can. Geogr., 8*(4), 354–372, 1969.

Kelley, D. E., Convection in ice-covered lakes: Effects on algal suspension, *J. Plankton Res., 19*(12), 1859–1880, 1997.

Keys, J. E., Water regime of Disraeli Fiord, Ellesmere Island, *DREO Report No. 792*, 62 pp., Defence Research Establishment Ottawa, Department of National Defence, Research and Development Branch, Canada, 1978.

Knight, C. A., Studies of Arctic lake ice, *J. Glaciol., 4*(33), 319–335, 1962.

Korgen, B., Seiches, *Amer. Sci., 83*(4), 330–341, 1995.

Kozlenko, N., and M. O. Jeffries, Bathymetric mapping of shallow water in thaw lakes on the North Slope of Alaska with spaceborne imaging radar, *Arctic, 53*(3), 306–316, 2000.

Kwok, R., D. A. Rothrock, H. L. Stern, and G. F. Cunningham, Determination of the age distribution of sea ice from Lagrangian observations of ice motion, *IEEE Trans. Geosci. Remote Sens., 33*(2), 392–400, 1995.

Lachenbruch, A. H., M. C. Brewer, G. W. Greene, and B. V. Marshall, Temperatures in permafrost, *Temperature–Its Measurement and Control in Science and Industry, 3*(1), 791–803, 1962.

Larsen, P., G. Ashton, J. Gosink, N. Marcotte, A. Müller, and T. E. Osterkamp, Thermal regime of lakes and rivers, in *River and Lake Ice Engineering*, edited by G. D. Ashton, pp. 203–260, Water Resources Publications, Littleton, CO, 1986.

Leconte, R., and P. D. Klassen, Lake and river ice investigations in northern Manitoba using airborne SAR imagery, *Arctic, 44*(Supp. 1), 153–163, 1991.

Lesack, L. W. F., R. E. Hecky, and P. Marsh, The influence of frequency and duration of flooding on the nutrient chemistry of Mackenzie Delta lakes, in *Mackenzie Delta, Environmental Interactions and Implications of Development*, edited by P. Marsh and C. S. L. Ommanney, *NHRI Symposium No. 4*, pp. 19–36, National Hydrology Research Institute, Saskatoon, Saskatchewan, Canada, 1991.

Leshkevich, G. A., Machine classification of freshwater ice types from Landsat-1 digital data using ice albedos as training sets, *Remote Sens. Environ., 17*(3), 251–263, 1985.

Leshkevich, G., S. V. Nghiem, and R. Kwok, Algorithm development for satellite synthetic aperture radar (SAR) classification and mapping of Great Lakes ice cover, in *Proceedings of the International Geoscience and Remote Sensing Symposium* (IGARSS'98), 6–10 July 1998, Seattle, WA, pp. 1397–1399, 1998.

Li, S., C. Benson, L. Shapiro, and K. Dean, Aufeis in the Ivishak River, Alaska, mapped from satellite radar interferometry, *Remote Sens. Environ., 60*(2), 131–139, 1997.

Li, S., M. O. Jeffries, and K. Morris, Mapping the bathymetry of shallow tundra lakes using INSAR techniques, in *Proceedings of the International Geoscience and Remote Sensing Symposium (IGARSS 2000)*, 24–28 July 2000, Honolulu, HI, pp. 2230–2232, 2000.

Likens, G. E., and R. A. Ragotskie, Vertical water motion in a small, ice-covered lake, *J. Geophys. Res., 70*(10), 2333–2344, 1965.

Liston, G. E., and D. K. Hall, An energy balance model of lake ice evolution, *J. Glaciol., 41*(138), 373–382, 1995a.

Liston, G. E., and D. K. Hall, Sensitivity of lake freeze-up and break-up to climate change: A physically based modelling study, *Ann. Glaciol., 21*, 387–393, 1995b.

Magnuson, J. J., and thirteen others, Historical trends in lake and river ice cover in the northern hemisphere, *Science, 289*(5485), 1743–1746, 2000.

Malm, J., A. Terzhevik, L. Bengtsson, P. Boyarinov, A. Glinsky, N. Palshin, and M. Petrov, Temperature and salt content regimes in three shallow ice-covered lakes: 1. Temperature, salt content and density structure, *Nordic Hydrol., 28*(2), 99–128, 1997.

Markus, T., and D. J. Cavalieri, Snow depth distribution over sea ice in the Southern Ocean from satellite passive microwave data, in *Antarctic Sea Ice: Physical Processes, Interactions and Variability*, edited by M. O. Jeffries, pp. 19–39, *Antarctic Res. Ser., 74*, AGU, Washington, D.C., 1998.

Marsh, P., Modelling water levels for a lake in the Mackenzie Delta, in *Proceedings of the Cold Regions Hydrology Symposium*, edited by D. L. Kane, pp. 23–29, American Water Resources Association, Bethesda, MD, 1986.

Maslanik. J. A., and R. G. Barry, Lake ice formation and break-up as an indicator of climate change: Potential for monitoring using remote sensing, in *The Influence of Climate Change and Climate Variability on the Hydrologic Regime and Water Resources*, International Association for the Hydrological Sciences, *IAHS Publ. No. 168*, pp. 153–161, 1987.

Matthews, P. C., and S. I. Heaney, Solar heating and its influence on mixing in ice-covered lakes, *Freshwater Biol.*, *18*(1), 135–149, 1987.

McCormick, M. J., Potential changes in thermal structure and cycle of Lake Michigan due to global warming, *Trans. Am. Fish Soc.*, *119*(2), 183–194, 1990.

Meisner, J. D., J. L. Goodier, H. A. Regier, B. J. Shuter, and W. J. Christie, An assessment of the effects of climate warming on Great Lakes basin fishes, *J. Great Lakes Res.*, *13*(3), 340–352, 1987.

Melloh, R., and L. W. Gatto, Interpretation of passive and active microwave imagery over snow-covered lakes and rivers near Fairbanks, Alaska, in *Proceedings of a Workshop on Applications of Remote Sensing in Hydrology*, 13–14 February 1990, Saskatoon, Saskatchewan, edited by G. W. Kite and A. Wankiewicz, pp. 259–278, Environment Canada, Saskatoon, 1990a.

Melloh, R., and L. W. Gatto, River and lake ice conditions as determined from AirSAR imagery, *JPL Publication No. 90-56*, pp. 37–42, Jet Propulsion Laboratory, California Institute of Technology, 1990b.

Melloh, R., and L. W. Gatto, Interpretation of synthetic aperture radar imagery of snow-covered river ice, in *Proceedings of the U.S. Army Corps of Engineers Seventh Remote Sensing Symposium: Integration of Remote Sensing with Physical Sciences*, 7–9 May 1990, Portland, Oregon, pp. 429–441, 1990c.

Melloh, R., and L. W. Gatto, River and lake ice conditions as interpreted from microwave imagery, in *Proceedings of the Army Science Conference*, 22–25 June 1992, Vol. 2, pp. 381–395, 1992.

Melloh, R. A., D. T. Eppler, L. D. Farmer, L. W. Gatto, and E. F. Chacho, Interpretation of passive microwave imagery of surface snow and ice, Harding Lake, Alaska, *CRREL Rep. 91–11*, 30 pp., U.S. Army Cold Reg. Res. and Eng. Lab., Hanover, NH, 1991.

Mellor, J. C., Bathymetry of Alaskan Arctic lakes: a key to resource inventory with remote sensing methods, Ph.D. thesis, Univ. of Alaska, Fairbanks, 1982.

Mellor, J. C., Radar interpreted lake depths – Barrow, Harrison Bay, Howard Pass, Ikpikpuk River, Killik River, Lookout Ridge, Meade River, Misheguk Mountain, Teshekpuk Lake, Umiat, Utukok River and Wainwright quadrangles, *BLM-AK-PT-85-(020 through 031)-7200-029*, U.S. Department of the Interior, Bureau of Land Management, Anchorage, Alaska (12 quadrangle maps individually published with lake depths and statistical data), 1985.

Mellor, J. C., A statistical analysis and summary of radar-interpreted Arctic lake depths: An addendum to 12 map products, *BLM-Alaska Tech. Rep. 11*, 33 pp., U.S. Department of the Interior, Bureau of Land Management, Anchorage, Alaska, 1987.

Mellor, J. C., ERS-1 SAR use to determine lake depths in arctic and subarctic regions, in *Proceedings of the Second ERS-1 Symposium—Space at the Service of our Environment*, 11–14 October 1993, Hamburg, Germany, *Special Publication SP–361*, European Space Agency, Paris, pp. 1141–1146, 1994.

Ménard, P., C. R. Duguay, G. M. Flato, and W. R. Rouse, Simulation of ice phenology on Great Slave Lake, Northwest Territories, Canada, *Hydrol. Proc.*, *16*(18), 3691–3706, 2002.

Metge, M., Thermal cracks in lake ice, Ph.D. thesis, Queen's Univ., Kingston, Ontario, Canada, 1976.

Michel, B., Winter regimes of lakes and rivers, *CRREL Monogr. 111-B1a*, 130 pp., U.S. Army Cold Reg. Res. and Eng. Lab., Hanover, NH, 1971.

Michel, B., and R. Ramseier, Classification of river and lake ice, *Can. Geotech. J.*, *8*(1), 36–35, 1971.

Michel, B., G. Ashton, S. Beltaos, K. Davar, R. Frederking, R. L. Gerard, B. Pratte, G. Tsang, and G. Williams, Hydraulics, in *River and Lake Ice Engineering*, edited by G. D. Ashton, pp. 261–371, Water Resources Publications, Littleton, CO, 1986.

Morison, J., K. Aagaard, and M. Steele, Recent environmental changes in the Arctic: A review, *Arctic*, *53*(3), 359–371, 2000.

Morris, K., M. O. Jeffries, and W. F. Weeks, Ice processes and growth history on arctic and sub-arctic lakes using ERS-1 SAR data, *Polar Rec.*, *31*(177), 115–128, 1995.

Mueller, D.R., W. F. Vincent, and M. O. Jeffries, Break-up of the largest Arctic ice shelf and associated loss of an epishelf lake, *Geophys. Res. Lett.*, *30(20)*, 2031, doi: 10.1029/2003GL017931, 2003.

Murphy, M. A., I. P. Martini, and R. Protz, Seasonal changes in subarctic wetlands and river ice break-up detectable on RADARSAT images, southern Hudson Bay Lowland, Ontario, Canada, *Can. J. Remote Sens.*, *27*(2), 143–158, 2001.

Nghiem, S. V., G. A. Leshkevich, and R. Kwok, C–band polarimetric backscatter observations of Great Lakes ice, in *Proceedings of the International Geoscience and Remote Sensing Symposium* (IGARSS'98), 6–10 July 1998, Seattle, WA, pp. 1400–1402, 1998.

Nolan, M., G. Liston, P. Prokein, J. Brigham-Grette, V. L. Sharpton, and R. Huntzinger, Analysis of lake ice dynamics and morphology on Lake El'gygytgyn, NE Siberia, using synthetic aperture radar (SAR) and Landsat, *J. Geophys. Res.*, *108*(D2), 8162, doi: 10.1029/2001JD000934, 2003.

Palecki, M. A., and R. G. Barry, Freeze–up and break–up of lakes as an index of temperature changes during the transition seasons: A case study for Finland, *J. Climate Appl. Meteorol.*, *25*(7), 893–902, 1986.

Parkinson, F. E., Water temperature observations during break-up on the Liard-Mackenzie river system, in *Proceedings of the Workshop on Hydraulics of Ice-Covered Rivers*, Edmonton, Alberta, 1–2 June 1982, pp. 261–295, 1982.

Pavelksky, T. M., and L. C. Smith, Spatial and temporal patterns in Arctic river ice break-up observed with MODIS and AVHRR time series, *Remote Sens. Environ.*, *93*(3), 328–338, 2004.

Phelps, A. R., K. Peterson, and M. O. Jeffries, Methane efflux from high latitude lakes during spring ice-melt, *J. Geophys. Res.*, *103*(D2), 29,029–29,036, 1998.

Pilant, A. N., SSM/I time series observations of Great Lakes ice and snow, in *Proceedings of the 52nd Eastern Snow Conference*, Toronto, Canada, pp. 21–25, 1995.

Pilant, A. N., and A. Agarwal, A study of Lake Superior ice features and dynamics using RADARSAT-1 ScanSAR imagery, in *Proceedings of the RADARSAT ADRO Final Symposium*, 13–15 October 1998, Montreal, Québec, Canada (on CD–ROM), 1998a.

Pilant, A. N., and A. Agarwal, Lake Superior ice viewed using RADARSAT-1 ScanSAR imagery and low-altitude oblique air photos, in *Proceedings of the International Geoscience and Remote Sensing Symposium* (IGARSS'98), 6–10 July 1998, Seattle, WA, pp. 583–585, 1998b.

Prowse, T. D., Heat and mass balance of an ablating ice jam, *Can. J. Civ. Eng.*, *17*(4), 629–635, 1990.

Prowse, T. D., Environmental significance of ice to streamflow in cold regions, *Freshwater Biol.*, *32*(2), 241–259, 1994.

Prowse, T. D., River ice processes, in *River Ice Jams*, edited by S. Beltaos, pp. 29–70, Water Resources Publications, LLC, Highlands Ranch, CO, 1995.

Prowse, T. D., River-ice ecology. I: Hydrologic, geomorphic and water quality aspects, *J. Cold Reg. Eng.*, 15(1), 1–16, 2001a.

Prowse, T. D., River-ice ecology. II: Biological aspects, *J. Cold Reg. Eng.*, 15(1), 17–33, 2001b.

Prowse, T. D., and P. Marsh, Thermal budget of river ice covers during break-up, *Can. J. Civ. Eng.*, *16*(1), 62–71, 1989.

Prowse, T. D., and S. Reedyk, Thermal and climatologic effects, in *Environmental Aspects of River Ice*, edited by T. D. Prowse and N. C. Gridley, *NHRI Science Report No. 5*, pp. 60–75, National Hydrology Research Institute, Saskatoon, Saskatchewan, Canada, 1993.

Prowse, T. D., M. N. Demuth, and M. Peterson, Proposed artificial river ice damming to induce flooding of a delta ecosystem, in *Proceedings of the 50th Eastern Snow Conference*, Québec City, Québec, pp. 331–338, 1993.

Ragle, R. H., Formation of lake ice in a temperate climate, *CRREL Res. Rep. 107*, 22 pp., U.S. Army Cold Reg. Res. and Eng. Lab., Hanover, NH, 1963.

Ragotskie, R. A., Heat budgets of lakes, in *Lakes: Chemistry, Geology, Physics*, edited by A. Lerman, pp. 1–19, Springer–Verlag, New York, Inc., U.S.A., 1978.

Robertson, D. M., R. A. Ragotskie, and J. J. Magnuson, Lake ice records used to detect historical and future climatic changes, *Climatic Change*, *21*(4), 407–427, 1992.

Rouse, W. R., and ten others, Effects of climate change on the freshwaters of Arctic and Subarctic North America, *Hydrol. Proc.*, *11*(8), 873–902, 1997.

Schindler, D. W., K. G. Beaty, E. J. Fee, D. R. Cruikshank, E. R. DeBruyn, D. L. Findlay, G. A. Linsey, J. A. Shearer, M. P. Stainton, and M. A. Turner, Effects of climatic warming on the lakes of the central boreal forest, *Science*, *250*(4983), 967–970, 1990.

Schwarz, J., R. Frederking, D. J. Goodman, A. Gow, H. Kohnen, H. Reuter, B. Schwerdtfeger. and N. K. Sinha, Ice physics, in *River*

and Lake Ice Engineering, edited by G. D. Ashton, pp. 19–85, Water Resources Publications, Littleton, CO, 1986.

Scott, J. T., A comparison of the heat balance of lakes in winter, Ph.D. thesis, Univ. of Wisc., Madison, 1964.

Scrimgeour, G. J., T. D. Prowse, J. M. Culp, and P. A. Chambers, Ecological effects of river ice break-up: A review and perspective, *Freshwater Biol.*, *32*(2), 261–275, 1994.

Sellmann, P. V., J. Brown, R. I. Lewellen, H. McKim, and C. Merry, The classification and geomorphic implications of thaw lakes on the Arctic Coastal Plain, Alaska, *CRREL Res. Rep. 344*, 21 pp., U.S. Army Cold Reg. Res. and Eng. Lab., Hanover, NH, 1975a.

Sellmann, P. V., W. F. Weeks, and W. J. Campbell, Use of sidelooking airborne radar to determine lake depth on the Alaskan North Slope, *CRREL Spec. Rep. 230*, 6 pp., U.S. Army Cold Reg. Res. and Eng. Lab., Hanover, NH, 1975b.

Serreze, M. C., J. E. Walsh, F. S. Chapin, III, T. Osterkamp, M. Dyurgerov, V. Romanovsky, W. C. Oechel, J. Morison, T. Zhang, and R. G. Barry, Observational evidence of recent change in the northern high-latitude environment, *Climatic Change*, *46*(1–2), 159–207, 2000.

Skinner, W. R., Lake ice conditions as a cryospheric indicator for detecting climate variability in Canada, *Report No. 92-4* (unpublished manuscript), Canadian Climate Centre, Atmospheric Environment Service, Downsview, Ontario, 46 pp., 1992.

Skorve, J., and P. Vincent, Some models of ice melt on high level lakes in southwest Norway, *Photogramm. Eng. Remote Sens.*, *53*(11), 1565–1570, 1987.

Smith, L. C., Emerging applications of interferometric synthetic aperture radar in geomorphology and hydrology, *Ann. Assoc. Amer. Geogr.*, *92*(3), 385–398, 2002.

Stewart, K. M., and R. K. Haugen, Influence of lake morphometry on ice dates, *Ver. Int. Ver. Limnol.*, *24*, 122–127, 1990.

Stiles, W. H., and F. T. Ulaby, Active and passive microwave response to snow parameters: 1. Wetness, *J. Geophys. Res.*, *85*(C2), 1037–1044, 1980.

Swift, C. T., W. L. Jones, Jr., R. F. Harrington, J. C. Fedore, and R. H. Couch, Microwave radar and radiometric remote sensing measurements of lake ice, *Geophys. Res. Lett.*, *7*(4), 243–246, 1980.

Tramoni, F. R., R. G. Barry, and J. Key, Lake ice cover as a temperature index for monitoring climate perturbations, *Zeitschr. Gletscherk. Glazialg.*, *21*, 43–49, 1985.

Vincent, W. F., J. A. E. Gibson, and M. O. Jeffries, Ice shelf collapse, climate change and habitat loss in the Canadian High Arctic, *Polar Rec.*, *37*(201), 133–142, 2001.

Van Hove, P., K. M. Swadling, J. A. E. Gibson, C. Belzile, and W. F. Vincent, Farthest north lake and fjord populations of calanoid copepods *Limnocalanus macrurus* and *Drepanopus bungei* in the Canadian high Arctic, *Polar Biol.*, *24*(4), 303–307, 2001.

Vavrus, S. J., R. H. Wynne, and J. A. Foley, Measuring the sensitivity of southern Wisconsin lake ice to climate variations and lake depth using a numerical model, *Limnol. Oceanogr.*, *41*(5), 822–831, 1996.

Wakabayashi, H., M. O. Jeffries, and W. F. Weeks, C band backscatter variation and modelling for lake ice in northern Alaska

(in Japanese with English abstract), *J. Remote Sens. Soc. Japan*, *14*(3), 18–27, 1994.

Wakabayashi, H., F. Nishio, and M. O. Jeffries, C band backscattering characteristics of lake ice in northern Alaska during spring thaw period, *J. Remote Sens. Soc. Japan*, *19*(4), 18–27, 1999.

Walker, A. E., and M. R. Davey, Observation of Great Slave Lake ice freeze–up and break–up processes using passive microwave satellite data, in *Proceedings of the 16th Canadian Remote Sensing Symposium*, 7–10 June, 1993, Sherbrooke, Québec, Canada, pp. 233–238, 1993.

Walsh, J. E., J. Curry, M. Fahnestock, M. C. Kennicutt, II, A. D. McGuire, W. B. Rossow, M. Steele, C. J. Vorosmarty, and R. Wharton, Enhancing NASA's contributions to polar science: A review of polar geophysical data sets, National Academy Press, Washington, DC, 2001.

Walsh, S. E., S. J. Vavrus, J. A. Foley, V. A. Fisher, R. H. Wynne, and J. D. Lenter, Global patterns of lake ice phenology and climate: Model simulations and observations, *J. Geophys. Res.*, *103*(D22), 28,825–28,837, 1998.

Weber, F., D. Nixon, and J. Hurley, Semi-automated classification of river ice types on the Peace River using RADARSAT-1 synthetic aperture radar (SAR) imagery, *Can. J. Civ. Eng.*, *30*(1), 11–27, 2003.

Weeks, W. F., and J. S. Wettlaufer, Crystal orientations in floating ice sheets, in *Proceedings of the Johannes Weertman Symposium*, Anaheim, CA, 4–8 February 1996, edited by R. J. Arsenault and six others, pp. 337–350, Minerals, Metals & Materials Society, Warrendale, PA, 1996.

Weeks, W. F., P. V. Sellmann, and W. J. Campbell, Interesting features of radar imagery of ice-covered North Slope lakes, *J. Glaciol.*, *18*(78), 129–136, 1977.

Weeks, W. F., A. J. Fountain, M. L. Bryan, and C. Elachi, Differences in radar returns from ice–covered North Slope lakes, *J. Geophys. Res.*, *83*(C8), 4069–4073, 1978.

Weeks, W. F., A. J. Gow, and R. J. Schertler, Ground–truth observations of ice–covered North Slope lakes imaged by radar, *CRREL Res. Rep. 81–19*, 17 pp., U.S. Army Cold Reg. Res. Eng. Lab., Hanover, NH, 1981.

Wiesnet, D. R., Satellite studies of fresh–water ice movement on Lake Erie, *J. Glaciol.*, *24*(90), 415–426, 1979.

Williams, G. P., Correlating freeze–up and break–up with weather conditions, *Can. Geotech. J.*, *2*(4), 313–326, 1965.

Williams, G. P., Predicting the date of lake ice break–up, *Water Resour. Res.*, *7*(2), 323–333, 1971.

Wynne, R. H., and T. M. Lillesand, Satellite observation of lake ice as a climate indicator: Initial results from statewide monitoring in Wisconsin, *Photogramm. Eng. Remote Sens.*, *59*(6), 1023–1031, 1993.

Wynne, R. H., J. J. Magnuson, M. C. Clayton, T. M. Lillesand, and D. C. Rodman, Determinants of temporal coherence in the satellite-derived 1987–1994 break-up dates of lakes on the Laurentian Shield, *Limnol Oceanogr.*, *41*(5), 832–838, 1996.

Wynne, R. H., T. M. Lillesand, M. K. Clayton, and J. J. Magnuson, Satellite monitoring of lake ice break-up on the Laurentian Shield (1980–1994), *Photogramm. Eng. Remote Sens.*, *64*(6), 607–617, 1998.

Zhang, T., and M. O. Jeffries, Modelling inter-decadal variations of lake ice thickness and sensitivity to climatic change in northernmost Alaska, *Ann. Glaciol.*, *31*, 339–347, 2000.

M. O. Jeffries, K. Morris, and N. Kozlenko, Geophysical Institute, University of Alaska Fairbanks, 903 Koyukuk Drive, P. O. Box 757320, Fairbanks, Alaska 99775-7320. (martin.jeffries@gi.alaska.edu)

Satellite Remote Sensing of Permafrost
and Seasonally Frozen Ground

Claude R. Duguay[1], Tingjun Zhang[2], David W. Leverington[3],
and Vladimir E. Romanovsky[1]

Permafrost consists of ground materials that have remained at or below 0°C for two or more years, while seasonally frozen ground refers to ground that freezes and thaws annually. Permafrost and seasonally frozen ground parameters are difficult to measure directly from remote sensing data since they are related to subsurface phenomena. Until recently, relatively few studies had examined the potential of remote sensing techniques for mapping the spatial distribution of near-surface permafrost, the properties of the active layer (the uppermost portion of the ground that freezes and thaws on an annual basis), and seasonally frozen ground in non-permafrost regions. In addition, few studies had made use of satellite imagery to map features indicative of the presence of near-surface permafrost or of the occurrence of permafrost degradation. Currently, high-resolution satellite images, such as those generated by sensors on board the IKONOS and QuickBird satellites, as well as declassified images generated by the CORONA spy satellite, are being used in conjunction with older aerial photographs to identify changes that have occurred in permafrost terrain in recent decades. Some of the most important advances in recent years have involved (1) the use of parameters related to permafrost conditions (including digital databases of topography and surface cover) to indirectly infer permafrost conditions over large areas by using remote-sensing classification algorithms and ground-truth data and (2) the development of active and passive microwave techniques to monitor near-surface soil freeze/thaw status at regional to continental scales. These recent advances, as well as potential areas of future development, are covered in this chapter.

1. INTRODUCTION

Permafrost, or perennially frozen ground, is soil or rock that has remained cryotic (at or below 0°C) for a minimum of 2 years [*ACGR*, 1988]. Climate is the dominant factor influencing the continental distribution of permafrost, generally resulting in an increase in permafrost occurrence with increasing latitude. At more local scales, particularly within the discontinuous permafrost zone, the distribution of permafrost is strongly influenced by factors that affect local microclimate and surface energy balance, such as slope, aspect, local hydrology, vegetation cover, geology, and snow cover [e.g., *Mackay*, 1970; *Smith*, 1975; *Goodrich*, 1982]. Permafrost may vary in thickness from a few centimeters to several hundred meters.

Seasonally frozen ground refers to ground that freezes and thaws annually [*ACGR*, 1988]. Seasonally frozen ground

[1]Geophysical Institute, University of Alaska Fairbanks, Fairbanks, Alaska.
[2]National Snow and Ice Data Center, University of Colorado, Boulder, Colorado.
[3]Department of Geosciences, Texas Tech University, Lubbock, Texas.

includes the active layer in permafrost regions and the seasonally frozen layer in non-permafrost regions; the active layer is the layer of ground in areas underlain by permafrost that is subject to annual freezing and thawing. The depth (or thickness) of the active layer varies as a function of air and soil temperatures, soil texture, soil moisture content, soil thermal properties, soil ice content, vegetation, site topography, and microclimate. The active layer may have a lower limit that extends slightly below the permafrost table if impurities within the upper permafrost allow annual thawing and refreezing under cryotic conditions. The active layer may also have a lower limit situated above that of the permafrost table should a residual thaw layer between the permafrost and the active layer exist [*ACGR*, 1988]. Thus, it is important to note that "depth to permafrost" is not always a synonym for active layer thickness [*French*, 1996]. The active layer generally ranges in thickness from about 15 cm or more in the zone of continuous permafrost to 3 m and more in mountainous regions of discontinuous permafrost zones.

The thermal regime of permafrost, and therefore its ice content, its strength, and its landforms, are affected by both natural ecological processes, such as vegetation and snow cover changes, forest fires, surface erosion and soil accretion (e.g., in peatlands and by windborne sedimentation), and human activities (e.g., clearance of vegetation and borrow pits). Permafrost is also very sensitive to climatic variations, on both short (several years) and long timescales [e.g., *Burn*, 1992, 1994], largely because conduction is the dominant mechanism for heat transfer through the various mixes of earth materials and ice. The depth of the active layer, the thermal profile, the thickness of permafrost, and topography all change simultaneously with local and regional climate changes. Due to the complexity of the exchange system at the surface–atmosphere interface, the factors controlling heat flux to and from the subarctic and arctic permafrost are poorly understood, although the physical processes involved and their mathematical solutions are well known [*Williams and Smith*, 1989].

Knowledge of the spatial distribution of permafrost conditions is necessary for both economic and environmental reasons. From a resource management perspective, the spatial distribution of permafrost must be understood in order to assess the sensitivity of specific regions to environmental changes, both anthropogenic and natural. The evolution of ground thermal conditions that can accompany climate and microclimate change can result in aggradation or, often more adversely, the degradation of permafrost [e.g., *French*, 1975; *Burn and Smith*, 1990]. Only by identifying especially sensitive permafrost regions can informed decisions be made for the management and use of northern regions by government and industry. Permafrost conditions strongly determine the suitability of land for development. Because of the typically confounding effects

of permafrost on engineering projects, baseline information regarding the presence or absence of permafrost, the active-layer thickness, and permafrost ice content must be collected to adequately assess the appropriateness of a prospective location for the construction of structures and roads [*Hall and Martinec*, 1985]. Beyond this minimum knowledge, more detailed information concerning the local hydrology, vegetation characteristics, distribution of frost-susceptible materials, and the likely behavior of local materials to thaw must also be acquired as necessary background information for engineering projects.

Data revealing the spatial distribution of near-surface permafrost conditions are also important because of the major influence of permafrost on northern hydrological processes. For example, freezing reduces the hydraulic conductivity of soil, leading to either more runoff due to decreased infiltration or higher soil moisture content due to restricted drainage [*Williams and Smith*, 1989]. Changes in active-layer thickness and in permafrost continuity impact surface runoff, directly affecting groundwater storage and river discharge [*Kane*, 1997]. Permafrost limits subsurface water storage and infiltration, resulting in wet soils and standing surface water. Thickening of the active layer and thawing of ice-rich permafrost enhance the development of thaw lakes, in turn influencing the thermal regime of permafrost [*Ling and Zhang*, 2003, 2004].

The creation of regional databases of permafrost information would be useful for the development and management of northern areas. Remote sensing techniques have the potential to provide a valuable and cost-effective means for mapping and monitoring near-surface permafrost conditions as well as seasonally frozen ground [see *Zhang et al.*, 2004]. However, of all cryospheric parameters (i.e., snow, glaciers/ice caps/ice sheets, sea ice, and lake and river ice), frozen ground, particularly permafrost, is the most difficult to map and monitor through the use of remote sensing imagery since it is a subsurface phenomenon.

The success achieved to date, the current limitations, and the future prospects for remote sensing of frozen ground are described in this chapter. The following section provides some background on the geographical distribution of permafrost and the factors controlling its distribution. Features indicative of permafrost presence and degradation are also reviewed. Later sections review progress in mapping permafrost extent and active layer depth and in monitoring seasonally frozen ground. The chapter concludes with a discussion of areas for future research.

2. BACKGROUND

Permafrost may be found where mean annual air temperatures (MAAT) are at or below 0°C. It is generally continuous

where MAAT are below -7°C. In addition, its extent and thickness are affected by ground moisture content, surface and ground water presence and movement, vegetation cover, winter snow depth, and terrain aspect (i.e., slope orientation). The global extent of permafrost is still not completely known, but it occupies about 24% of the terrestrial surface of the Northern Hemisphere [*Brown et al.*, 1997; *Zhang et al.*, 1999]. Thicknesses exceed 600 m along the Arctic coasts of northeastern Siberia and Alaska [e.g., *Lachenbruch et al.*, 1982]; toward its margins, however, permafrost becomes thinner and horizontally discontinuous. The marginal zones are more immediately subject to any thawing caused by climate warming. Some extant permafrost was formed during previous colder conditions and is therefore relic [*Mackay et al.*, 1972]. However, permafrost may form under present-day polar climates where glaciers retreat or land emergence exposes unfrozen ground. *Washburn* [1973] concluded that most continuous permafrost is in balance with the present climate at its upper surface, but changes at its base depend on the present climate and geothermal heat flow. In contrast, discontinuous permafrost is already unstable and most of it is in such delicate equilibrium that the slightest climatic or surface change will have drastically disequilibrating effects [e.g., *Anisimov and Nelson*, 1997].

In the presence of permafrost, mass exchange between land and atmosphere in the cold period of the year is negligibly small. In summer, this exchange is limited to the water and gas fluxes between the atmosphere and the relatively shallow near-surface layer of seasonal thaw: the active layer. The deeper the active layer, the larger its storage capacity and the amount of substance potentially available for exchange with the atmosphere. Frozen ground plays a significant role in the terrestrial portion of the hydrological cycle because it restricts moisture exchanges between surface water and deep ground water [*Prowse and Ommanney*, 1990]. The occurrence of frozen ground and permafrost is, therefore, an important factor controlling drainage and the areal and spatial distributions of wetlands [*Rouse et al.*, 1997]. To northern hydrologists, knowledge of the spatial distribution of permafrost and the seasonal evolution of the active layer is crucial for gaining a better understanding of the hydrological cycle of the Arctic and for generating improvements to hydrological models.

2.1. Geographical Distribution of Permafrost and Environmental Controls

Roughly 25% of the continents (nearly 50% of Canada and 80% of Alaska) are underlain by permafrost [*Williams and Smith*, 1989], precluding extensive ground surveys of permafrost conditions because of expense, logistical difficulties, short field seasons, and time constraints [*Ferrians and Hobson*, 1973; *Morrissey*, 1983]. As shown in Plate 1 [*Zhang et al.*, 1999], four small-scale permafrost zones have been delineated in the Northern Hemisphere [*Brown et al.*, 1997; *Heginbottom*, 2002]: (1) zone of continuous permafrost (>90% of area is underlain by permafrost); (2) zone of discontinuous permafrost (50–90% of area is underlain by permafrost); (3) zone of sporadic permafrost (10–50% of area is underlain by permafrost); and (4) zone of isolated patches of permafrost (<10% of area is underlain by permafrost). In areas of continuous permafrost, frozen ground is present at all localities except for localized thaw zones, or taliks, existing beneath lakes, river channels, and other large water bodies that do not freeze to their bottoms in winter [e.g., *Mackay*, 1985]. In discontinuous permafrost regions, bodies of frozen ground are separated by areas of unfrozen ground. At the southern limit of this zone, permafrost becomes restricted to isolated "islands" occurring beneath peaty organic sediments [e.g., *Brown*, 1967].

The long-term average maximum extent of seasonally frozen ground is about 54.39×106 km^2, or 57.1% of the exposed land areas in the Northern Hemisphere [*Zhang et al.*, 2003a] (Plate 2). Essentially, all climatic and environmental factors controlling permafrost conditions and freezing/thawing processes of the active layer have a similar impact on seasonally frozen ground.

Although cold climate and deep-freezing air temperatures for long periods of the year are hallmarks of permafrost existence, permafrost is nonetheless nonhomogeneous and its characteristics are very variable across a landscape due to geological, ecological, and regional climatic factors. Essentially, five factors determine the presence of permafrost [*Ferrians and Hobson*, 1973]: (1) climatic factors (mean annual temperature at the bottom of the active layer is below 0°C); (2) geological factors (the character of soil and rock materials); (3) hydrological factors (amount of soil moisture available and the rate of freezing determine the amount of ice in permafrost); (4) topographic factors (altitude, slope, and aspect influence the amount of solar radiation received by the ground); and (5) biological factors (vegetation acts as a ground insulator, and its disturbance can cause permafrost to thaw).

Local factors (i.e., vegetation cover, snow cover distribution and thickness, topography, and soil moisture conditions) commonly override the influence of larger-scale macroclimatic factors (i.e., air temperature and precipitation) on ground thermal conditions [e.g., *Brown*, 1967]. Therefore, in the discontinuous zone, the detection of permafrost from surface indicators assumes that a good relationship has been established between the indicator and the presence or absence of permafrost. This is also true for the mapping of active-layer
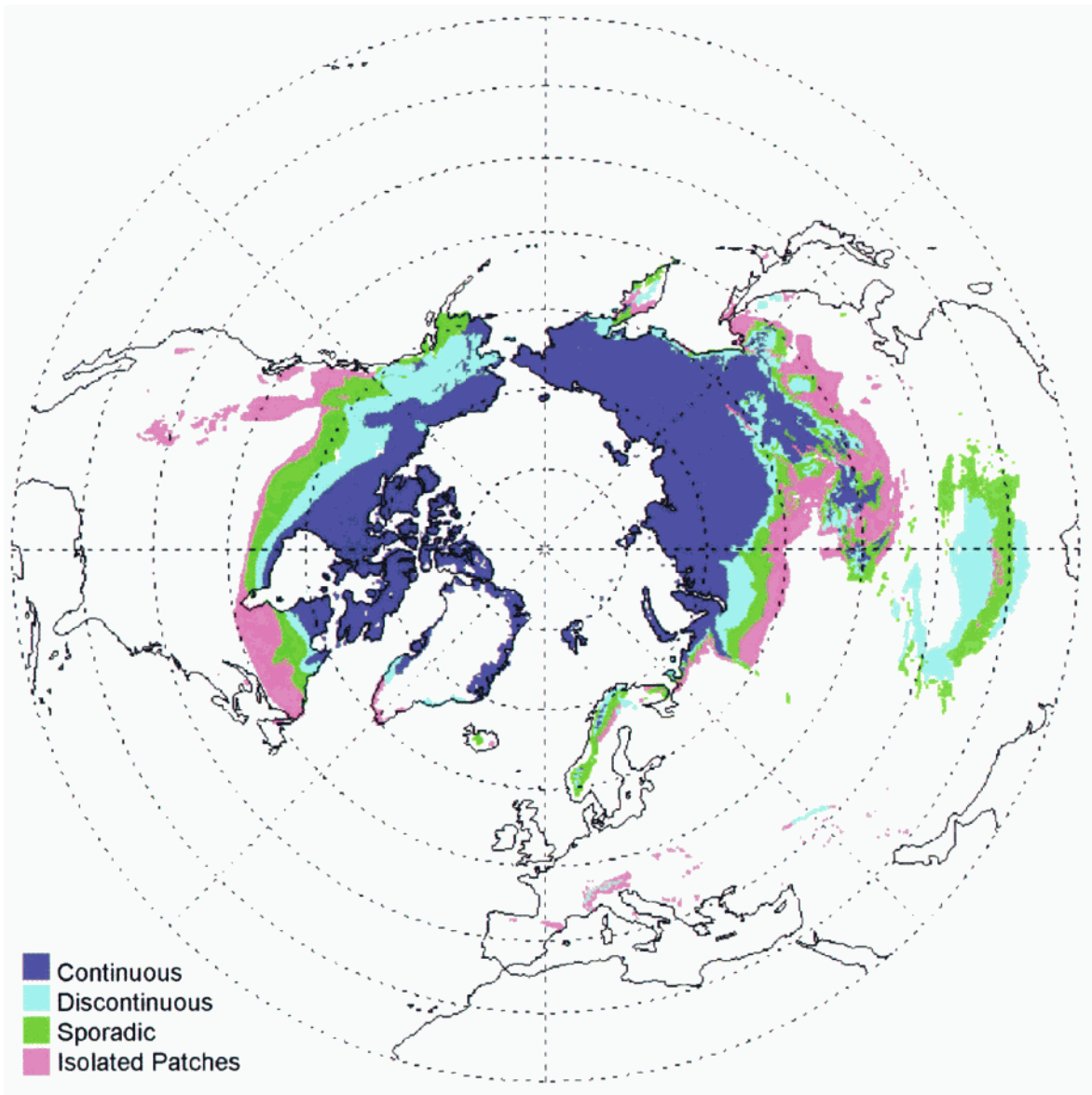
Plate 1. Permafrost distribution in the Northern Hemisphere, based on the NSIDC EASE-grid version of the International Permafrost Association Circum-Arctic Map of Permafrost and Ground-Ice Conditions (from *Zhang et al.* [1999]; reproduced with the kind permission of Bellwether Publishing).
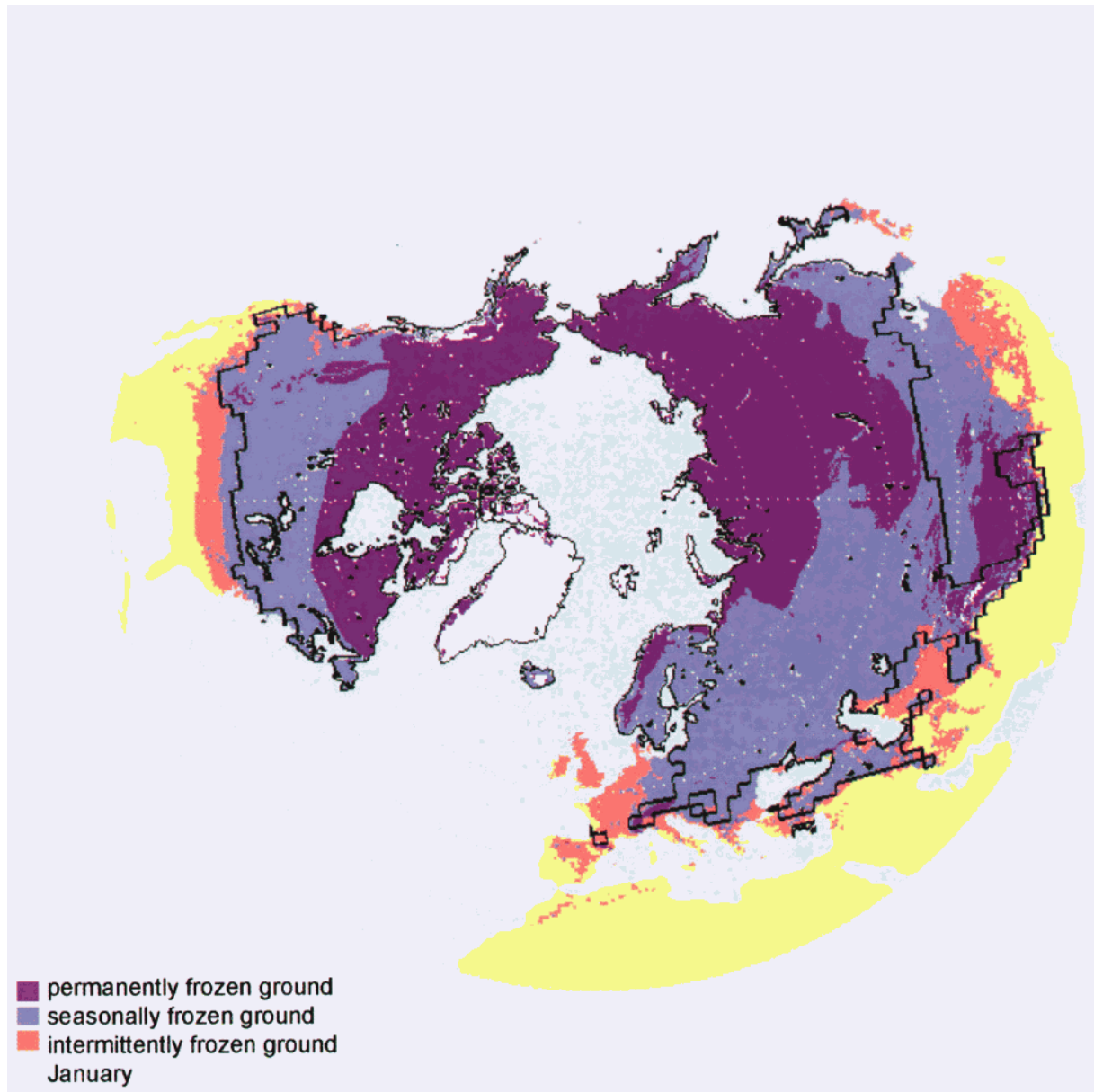
Plate 2. Distribution of permafrost, average maximum extent of seasonally and intermittently frozen ground (1950–1996), and average maximum snow cover extent (solid line, 1972–1995) in the Northern Hemisphere (from *Zhang et al.* [2003a]; reproduced with the kind permission of the International Permafrost Association).

thickness in both discontinuous and continuous permafrost zones.

Luthin and Guymon [1974] visualized boundary-layer interactions in terms of a complex buffer layer interposed between atmosphere and ground (Figure 1). Atmospheric mass and energy flows, together with geothermal heat flux, constitute the boundary conditions; the vegetation canopy, snow cover (when present), and surface organic layer act as buffers between atmosphere and ground [*Smith*, 1993]. Clearly, the presence of the buffer layer makes the *direct* mapping of permafrost and its ground thermal regime from satellite remote sensing alone a significant, if not insurmountable challenge. However, information obtainable from satellite sensors (e.g., vegetation canopy, snow cover, and topography) provides an *indirect* means of mapping the presence or absence of permafrost and the thickness of the active layer from space.

2.1.1. Vegetation cover. Vegetation cover (or canopy) is one of the best indicators of the spatial distribution of permafrost conditions within the upper 2 m of ground. This is because near-surface permafrost commonly acts as a cold and impervious ground mass that maintains low summer ground temperatures through which roots and water can-

not penetrate. The predominance of certain tree and shrub species in an area underlain by discontinuous permafrost can be strong indicators of the presence of permafrost and the relative thickness of the active layer. For example, shallow-rooted, generally coniferous species such as tamarack and white and black spruce tend to be dominant in subarctic permafrost localities characterized by relatively thin active layers; as the active layer thickness diminishes, these species tend to become increasingly scattered and shorter [*Mollard*, 1960; *Tarnocai and Thie*, 1974; *Morrissey*, 1983; *Morrissey et al.*, 1986; *Leverington*, 1995].
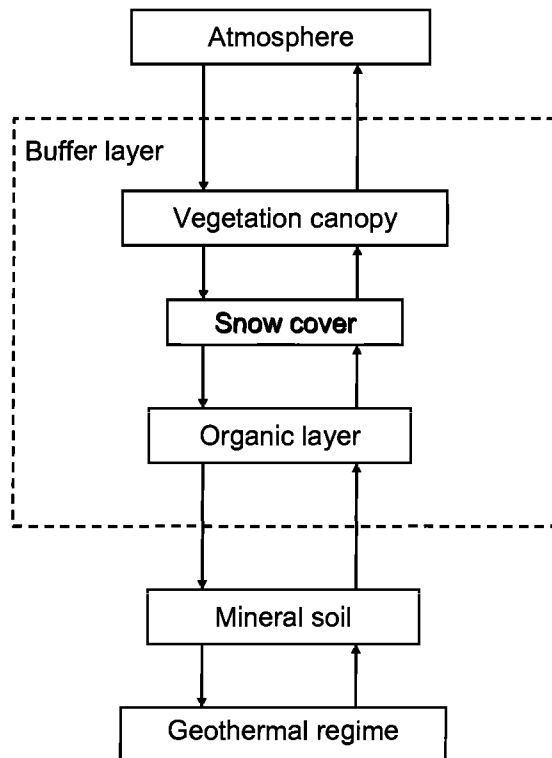
Deep-rooted, generally broad-leafed tree species such as poplar, white birch, and aspen tend to be found in localities characterized by relatively thicker active layers, and trees grow taller and become more densely spaced with increasing active-layer thickness [*Mollard*, 1960; *Tarnocai and Thie*, 1974; *Morrissey*, 1983; *Morrissey et al.*, 1986]. Pure dense willow stands tend to grow in areas unfrozen to even greater depths and are commonly indicative of water-saturated soils [*Mollard*, 1960; *Schreier and Selby*, 1981].

Exceptions to the tree-species generalizations given above are not uncommon. For example, birch trees can sometimes be found in isolated small groups within localities characterized by thin active layers and otherwise dominated by shallow-rooted tree species. Forest fires can introduce boundaries in vegetation that may, with time, not accurately reflect differences in the active layer of the affected locality. Moreover, the presence of specific tree species may correspond to different ground conditions, depending on regional climate. As an extreme example, a spruce stand located at a particular high-latitude locale may be suggestive of permafrost conditions and a shallow active layer, whereas the presence of a similar spruce stand located at low-elevation midlatitudes is clearly meaningless with regard to permafrost conditions. Thus, the predominance of specific tree species by itself should never be used as an indicator of permafrost conditions.

Layers of surface organic material such as peat can have seasonally dependent ground-insulating abilities. They are poor conductors of energy in their drier summer states, and better conductors in their moister or frozen autumn and winter states [*Williams and Smith*, 1989; *Williams and Burn*, 1996]. Whereas sphagnum, lichen, and peat are good ground insulators and tend to be associated with thin active layers in regions both with and without forest cover [e.g., *Leverington*, 1995; *Williams and Burn*, 1996], feather mosses and marsh sedges have been found to be much less protective of permafrost.

Figure 1. Model of climate–permafrost relationship (from *Luthin and Guymon* [1974]).

2.1.2. Topography. The important topographic factors that control permafrost conditions are elevation, slope and aspect (i.e., orientation of the slope). Permafrost conditions and

climate vary with changes in elevation. At high elevations, permafrost can exist at latitudes where it does not normally occur. Noteworthy, however, are the formation of strong air temperature inversions during the winter in highlands and low mountain regions (typically in the elevation range between several hundreds and several thousands of meters). These temperature inversions may have a strong effect on the spatial heterogeneity of mean annual air temperatures and can be responsible for a reduced spatial distribution or even complete absence of permafrost within some specific elevation belts in such regions.

Slope and aspect strongly affect permafrost distribution, since they both influence the amount of solar radiation received by the ground. In the discontinuous permafrost zone, for example, south-facing slopes are sometimes free of permafrost, whereas north-facing slopes are underlain by it [*Ferrians and Hobson*, 1973]. Also, everything else being equal, the permafrost would be thicker and colder (and active layer thinner) under north-facing slopes than under south-facing slopes in the continuous permafrost zone.

2.1.3. Geology. Different ground materials have different thermal conductivities, porosities, and permeabilities. Thus, geology can be an important factor in the distribution of permafrost. A dry coarse-grained sediment bed, for example, has a greater thermal conductivity than a dry fine-grained sediment bed. High ground thermal conductivities can allow for relatively thick active layers and support greater annual ground temperature amplitudes at greater depths [*Goodrich*, 1982]. The porosity and permeability of ground materials, which influence the ability of the ground to contain and conduct air and moisture, are also important with regard to permafrost conditions. These factors are strong determinants of the nature of ground ice, influencing, for example, ice injection and segregation processes [*Williams and Smith*, 1989].

2.1.4. Hydrology. Because water has a high specific heat, 4,186 J kg^{-1} °C^{-1} (at 25°C and 1 atm), local hydrological factors such as soil moisture content and proximity to water bodies can greatly affect ground thermal regimes. Water at the ground surface can affect surface temperatures by transferring latent or sensible heat to or from the atmosphere through boundary-layer convective processes. Furthermore, water at or below the ground surface can interact thermodynamically with ground materials, behaving as a significant energy source or sink. Thus, lakes and rivers strongly influence ground thermal conditions and can cause the formation of discrete unfrozen zones in permafrost regions (taliks) [e.g., *Mackay*, 1985]. Streams of water that can course through or over ground materials for extended periods of

time can be effective in maintaining unfrozen ground conditions. Finally, when soil water freezes, latent heat is released into surrounding ground materials. Similarly, when ground ice melts, latent heat is absorbed from surrounding ground materials. The significant amount of energy involved in the solid–liquid phase changes of water, along with the increased ground conductivity that accompanies the freezing of water, strongly influences the rate at which surface temperature waves penetrate the ground and therefore the maximum thickness of the active layer.

2.1.5. Snow cover. Snow cover, because of its low thermal conductivity, insulates ground surfaces against cold winter temperatures. Meanwhile, because of its absence in summer months, warmer temperatures are permitted to influence the ground thermal regime unhindered. The net effect is that increasing amounts of snow on the ground (i.e., snow depth) can increase permafrost temperature and decrease permafrost thicknesses [*Zhang et al.*, 1997]; snowfall can therefore strongly influence the distribution of permafrost, particularly in the discontinuous zones [*Smith*, 1975; *Goodrich*, 1982]. The distribution of permafrost in some areas is also closely related to the accumulation of seasonal snow cover. Lack of thermal insulation of the ground by snow cover has a first-order effect on the presence of permafrost. At this time, no easily applied and accurate algorithms of snow depth have been developed for use with remotely sensed data. Fortunately, both vegetation and topography strongly influence snow parameters such as drift thicknesses and distributions [*Smith*, 1975]. Thus, although snow depth cannot be determined with remote sensing with much confidence at present, it can be assumed to be at least indirectly involved in any statistical relationships (or permafrost models) that consider vegetation and topography.

2.2. Permafrost-Related Features

Typical permafrost and periglacial (environments where frost action dominates) features include frost mounds, earth hummocks, ice wedges, sorted circles, thermokarst features, and features produced by gelifluction. Frost mounds are mound-shaped landforms produced in a variety of ways by the combined processes of ground freezing and groundwater movement [*ACGR*, 1988]. Although large frost mounds such as pingos [*Mackay*, 1977, 1990] are greater than 10 m in height and 100 m in horizontal dimension, frost mounds can be as small as several meters across. Earth hummocks are hummocks that have a core of silty and clayey mineral soil and show evidence of cryoturbation [*Mackay*, 1980; *ACGR*, 1988]. These features are believed to form only in permafrost regions; individual earth hummocks are typically 50 to 150

cm across, and often occur in dense clusters. Ice wedges are formed mainly in zones of continuous permafrost through the combined and repeated processes of thermal contraction-caused cracking and the penetration of surface water into these cracks by water flow and by the formation of hoar frost [*Mackay*, 1974; *Burn*, 1990]. Ice wedges can be about 10 cm to 3 m or more in width at the surface, tapering to zero width at a depth of 1–20 m. Ice wedges, and their sand wedge counterparts [*Murton and French*, 1993], are typically expressed at the surface in planar view as a network of polygons. Sorted circles are tightly spaced circular domains of fine-grained materials surrounded by gravel ridges and are formed by freeze–thaw action [*Kessler and Werner*, 2003]. The circular domains are typically about 2–4 m across, and the gravel ridges are about 20 cm high [*Hallet*, 1990]. Nonsorted circles are also very typical surficial features in the Arctic [*Walker et al.*, 2004]. Thermokarst features such as thaw lakes [*Burn and Smith*, 1990], active layer detachment slides, and retrogressive thaw slumps [e.g., *Burn and Friele*, 1989] are caused by changes in ground thermal regimes that result in ice thaw and ground subsidence. Gelifluction features are formed by downslope creep of frozen ground; individual lobes can be up to tens of meters wide and hundreds of meters long. Table 1 provides a list of surface indicators of permafrost com-monly found in the discontinuous and continuous permafrost zones, including the features described above.

3. MAPPING OF PERMAFROST WITH REMOTE SENSING

Climatic models of permafrost distribution [*Anisimov and Nelson*, 1997; *Stendel and Christensen*, 2002] tend to ignore local influences of microclimate such as topography and vegetation cover, and are thus only applicable at small scales. The remote sensing of northern terrain, meanwhile, can potentially provide rapidly accessible and accurate high-resolution permafrost information over broad areas in short periods of time. In the case of satellite and airborne imagery, remote sensing can provide relevant georeferenced data in an easily updatable and manipulatable digital format. Remote sensing is less expensive than complete ground surveys and can provide additional environmental information beyond that directly related to permafrost distribution [*Tarnocai and Thie*, 1974].

Although earth resources satellite data from Landsat have been available since 1972, relatively few investigations have been conducted to evaluate the potential of remotely sensed data for permafrost studies compared with the number of studies of other cryospheric parameters such as snow cover,

Table 1. Surface Indicators of Permafrost Commonly Found in the Discontinuous and Continuous Zones.

Discontinuous permafrost zone	Continuous permafrost zone
Beaded drainage (i.e., thermokarst along a stream)	Beaded drainage (present but not as common)
Frost mounds 　Palsas 　Open-system pingos	Frost mounds 　Palsas 　Closed-system pingos
Seasonal frost mounds (may also form in areas of deep seasonal frost)	River icings and mounds adjacent to pingos
Peat plateaus	Peat plateaus
Thermokarst 　Active layer detachment slides 　Retrogressive thaw slumps 　Thermo-erosion 　Lakes and ponds (sometimes oriented)	Thermokarst 　Active layer detachment slides 　Retrogressive thaw slumps 　Thermo-erosion 　Lakes and ponds (sometimes oriented)
Thermal contraction cracks (active or inactive—note that cracks can form in seasonally frozen ground; i.e., these features can be found in areas without permafrost)	Thermal contraction cracks (generally active ice wedges and ice-wedge polygons)
Alpine environments 　Rock glaciers 　Ice-cored moraines	Alpine environments 　Rock glaciers 　Ice-cored moraines
Many temperature controls (vegetation, snow cover, lithology, etc.)	Relatively few controls (mainly water bodies that promote taliks and snow distribution and cover)

glaciers and ice sheets, and sea ice. This is because the numerous processes related to permafrost conditions are not to date detectable from satellite imagery. Because permafrost and the active layer are subsurface phenomena, they cannot be directly photographed or imaged with airborne or satellite-based sensors.

In the interpretation of remotely sensed data, the surface depth to which the electromagnetic energy responds is, in reference to target parameters, a function of the surface characteristics. These include the composition of the surface layer and its corresponding moisture content, as well as the presence or absence of vegetative cover. In addition, the sensor configurations related to frequency, polarization, and incidence angle are important in determining penetration depth or depth of sensitivity. In general, however, earth observation sensors respond to only the top few millimeters (visible and infrared wavelengths) or centimeters (microwave wavelengths) of the surface. Consequently, since permafrost is usually located below an active layer ranging in depth from 15 cm to 5 m thick, most remote sensing studies to date have used surface indicators for identifying the presence and spatial distribution of permafrost. Inferences regarding the presence of permafrost can be made from indicators such as periglacial phenomena, vegetation cover, and snow cover.

Aerial photographs remain very valuable tools in permafrost research [e.g., *Mollard and Janes*, 1984; *Mollard*, 1986]. However, in the next subsections we emphasize the use of digital remote sensing and do not discuss the use of air photographs in permafrost mapping. A number of studies have been published describing the use of optical and microwave (active and passive) sensors for mapping permafrost terrain and near-surface soil freeze/thaw status. Still, the number and range of research initiatives regarding this remote-sensing application remain somewhat limited.

3.1. Permafrost-Related Features

Annual freezing and thawing of the active layer causes frost heaving, slumping, surface collapse, drainage impedance, cryoturbations, and periglacial features such as palsas, pingos, rock glaciers, thaw lakes, and ice-wedge polygons. As discussed earlier, these features indicate the presence of subsurface permafrost and are often detectable in aerial photographs and high-resolution satellite imagery obtained at visible to infrared wavelengths. Early efforts in permafrost mapping and characterization used Landsat Multi-Spectral Scanner (MSS) imagery [e.g., *Tarnocai and Thie*, 1974]. The spatial and spectral resolution of MSS (about 80 m and four spectral bands), coupled with limitations in digital image processing techniques, resulted in unsatisfactory digital permafrost maps (northern Manitoba and Northwest Territories,

Canada). Nevertheless, the qualitative (visual) detection of large permafrost-related landscape features such as peat plateaus was found to be easily performed by using Landsat MSS data [*Tarnocai and Thie*, 1974].

Less favorable results have been reported in relation to the use of synthetic aperture radar (SAR) for permafrost features. *Granberg et al.* [1994] reported that permafrost features such as active and collapsed palsas, peat plateaus, and frost boils do not generate strong backscatter signals and therefore are not easily mapped with SAR, unless SAR images are combined with other image data. A multitemporal SAR or multispectral approach was suggested.

Dean and Morrissey [1988] confirmed that multispectral data were significantly better than radar data alone for detection and recognition of arctic landforms in northern Alaska. In their study, landforms observed on remotely sensed data were compared against baseline geomorphic maps. The identification of a number of landforms was investigated (thaw lakes, submerged margins of lakes, floodplains, polygonal ground, pingos, drainages, dunes, and escarpments); also, the scale required to detect that lakes was examined by sensor type. Both visible–infrared (VIR) and satellite/airborne SAR data were used in this study. In reference to the VIR data, the sensor with the highest spatial resolution (simulated SPOT or Système Probatoire d'Observation de la Terre; 18.5 m pixels) produced the best results. Most of the landscape features were observed on the simulated SPOT image. However, polygonal ground was the most difficult to distinguish; only very large patterns could be observed. In exploring the detection of landforms with use of radar data, *Dean and Morrissey* [1988] reported that with shallow incidence angles (80°) most of the larger landforms such as thaw lakes, drained lake beds, and large dunes could be detected. Small permafrost features such as pingos could also be detected but could not be distinguished from other surface relief features in the surrounding terrain. Seasat (L-band or 23.5 cm; nominal range resolution of 25 m; acquired July 19, 1978) with its high incidence angle (80°) was only marginally capable of detecting large thaw lakes due to speckle, but drained lakes and ponds were clearly evident. The authors concluded that, in general, radar with low incidence angles revealed subtle surface undulations but the undulations were difficult to associate with a landform. In addressing scale requirements, *Dean and Morrissey* [1988] discovered that recognizable thaw lakes had to be approximately three times larger than the resolution of the VIR data and six times larger than the resolution of the Seasat data.

The lack of availability of high-resolution imagery (spatial resolution at or finer than 10 m) from civilian satellite missions during much of 1970s and 1980s, and the high cost of such images when they became available in the mid-1980s (e.g., SPOT-1), provide the most probable explanation for the

paucity of research papers published on the use of remote sensing to map permafrost-related features over this period.

Lewkowicz and Duguay [1999] investigated the potential use of SPOT 10-m panchromatic imagery to detect and identify features indicative of permafrost for 16 sites on Ellesmere Island, Northwest Territories, Canada. A SPOT satellite image acquired in early summer (June 21, 1990) was digitally enhanced by histogram stretching and compared with field observations and aerial photographs for localities in the northern and central regions of the Fosheim Peninsula. The investigation showed that in this area SPOT imagery could be used to detect the following features: (1) large, well-developed, high-centered ice-wedge polygons (diameters of 30–60 m) and large, low-centered polygons containing shallow ponds; (2) anthropogenically induced thermokarst 40 years after the original terrain disturbance (e.g., old airport runway); (3) recent active-layer detachment slides >500 m long; and (4) active retrogressive thaw slumps where they had previously been known to be present. The authors concluded that the 10-m pixel size of SPOT generally led to an underestimation of polygonized terrain in the study area, compared with results from the interpretation of aerial photographs.

The availability of high-resolution satellite images from new sensors such as IKONOS (four VIR channels at 4 m; one panchromatic channel at 1 m) and QuickBird (four VIR chan-

nels at 2.44 m; one panchromatic channel at 61 cm), as well as relatively inexpensive declassified photographs/ images (<US$100 per frame) from earlier satellite missions such as CORONA, the KH-7 Surveillance System and the KH-9 Mapping System, available from the United States Geological Survey (USGS) EROS Data Center, may revive interest in the application of remote sensing to map permafrost-related (geomorphic) features at the local scale. CORONA satellite photography consists of approximately 880,000 photographs that were taken between 1959 and 1972, whereas the photographic images collected by the KH-7 Surveillance System and the KH-9 Mapping System—approximately 50,000 images—were taken from 1963 to 1980.

Yoshikawa and Hinzman [2003] used historical aerial photographs (1950 and 1981) and IKONOS imagery (2000) to map changes in the areal extent of thermokarst ponds in an area of discontinuous permafrost near Council, Alaska. Their analysis revealed that many ponds have undergone recent dramatic decreases in their areal extent (Figure 2). The loss in surface water has been associated with internal drainage due to the initiation of large taliks that completely penetrated the permafrost, causing ponds to shrink under recent climatic conditions [*Yoshikawa and Hinzman*, 2003]. In another investigation, *Smith et al.* [2005] compared satellite imagery acquired across two large tracts of western Siberia in the
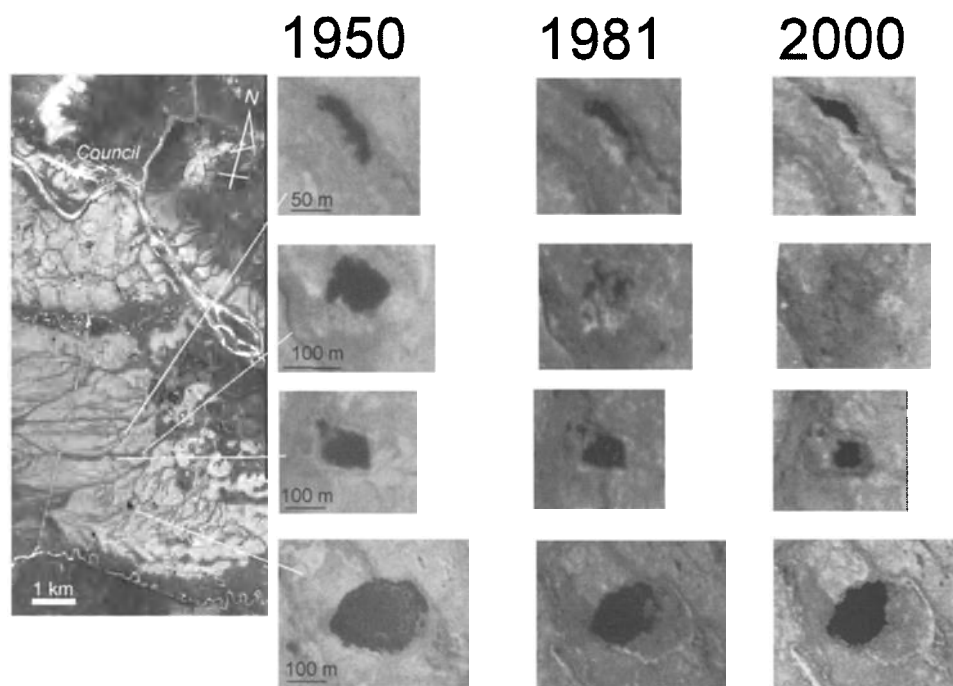
Figure 2. Numerous tundra ponds near Council, Alaska (64°51' N, 163°42' W) have decreased in surface area over the last 50 years. A probable mechanism for these shrinking ponds is internal drainage through the degradation of shallow permafrost. Images courtesy of L. Hinzman.

early 1970s with recent satellite data (1997–2004), to inventory and track dynamic changes of large lakes after three decades of rising soil and air temperatures in the region. As shown in Plate 3, this analysis has revealed a widespread decline in lake abundance and area in the discontinuous, sporadic, and isolated permafrost zones, despite slight precipitation increases. It also demonstrates a net increase in lake area and in the number of lakes exceeding 40 ha in the continuous permafrost zone.

Recently, *Grosse et al.* [2005] evaluated the potential of declassified CORONA images (1967 and 1972) to distinguish and map periglacial features in northeast Siberia. Using a mosaic of CORONA panchromatic images taken over the Bykovsky Peninsula and adjacent Khorogor Valley, the authors were able to map thermo-erosional valleys, depressions, thermokarst lakes, thermo-erosional cirques, thermokarst lagoons, and pingos (Figure 3). A logical next step in this study would be to examine the evolution of the features mapped with CORONA with a similar exercise using recent IKONOS or QuickBird panchromatic images.

Incidentally, coincident with the increasing use of high-resolution optical data for identifying terrestrial permafrost features, the recent availability of high-resolution images (up to ~1 m per pixel) over widely distributed areas of Mars has allowed remote sensing techniques to be used in the identification of probable permafrost features such as local-scale polygonal networks and hummocky terrain [e.g., *Siebert and Kargel*, 2001; *Leverington*, 2003]. In combination with gamma-ray spectrometer data used to identify Martian regions where the near-surface layers are likely to be underlain by water ice [*Boynton et al.*, 2002], investigations utilizing high-resolution optical imagery have led to substantial improvements in our understanding of probable past and present permafrost processes operating at and near the surface of Mars.

In addition to the progress made in mapping terrestrial permafrost-related features with high-resolution panchromatic and multispectral satellite images, new developments have also taken place in the use of SAR to map surface deformation. Some studies have demonstrated the potential of differential SAR interferometry (D-InSAR) to estimate the surface velocity of rock glaciers [e.g., *Kenyi and Kaufmann*, 2001; *Strozzi et al.*, 2004] as well as frost-heaving of the active layer [e.g., *Wang and Li*, 1999].

Using ERS-1/2 single-look complex (SLC) image data sets acquired over the Hohe Tauern range in Austria, *Kenyi and Kaufmann* [2001] estimated an average deformation rate of –7.7 mm/35 days in the radar line of sight for a small, active rock glacier. Typical of dry and cold mountain regions, rock glaciers are lobate, or tongue-shaped, bodies of frozen debris with interstitial ice and ice lenses, that move downslope or
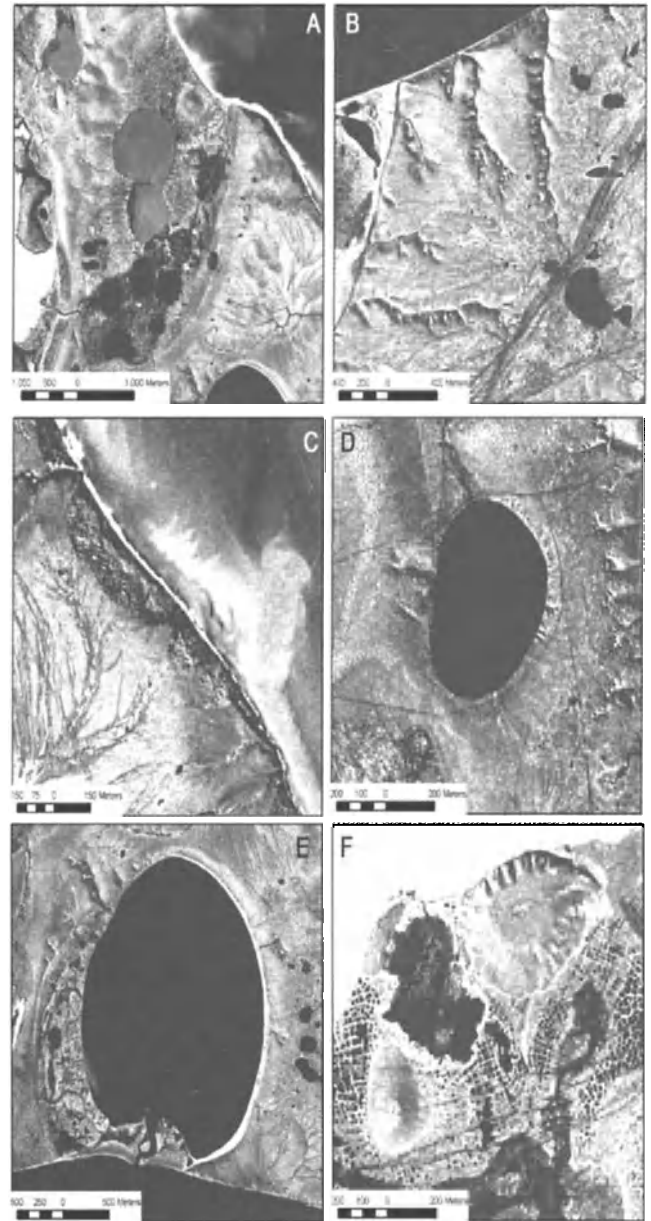
Figure 3. Geomorphological features identified from the CORONA images: (A) partially drained thermokarst depression due to coastal erosion with lake remnants and pingo; (B) gullies discharging from an upland surface and human-induced vehicle tracks; (C) large thaw slumps along the east shore of the Bykovsky Peninsula; (D) thermokarst lake with subsidence features on an upland plain; (E) lagoon in an early stage formed by coastal erosion and the drainage of a thermokarst lake (Ivashkina lagoon); (F) pingos and partially drained, low-centered ice-wedge polygon terrain (from *Grosse et al.* [2005]; reproduced with the kind permission of John Wiley & Sons, Inc.).

downvalley by deformation of the ice contained within them [*French*, 1996]. *Kenyi and Kaufmann* [2001] found that the spatial distribution of the rock glacier surface deformation
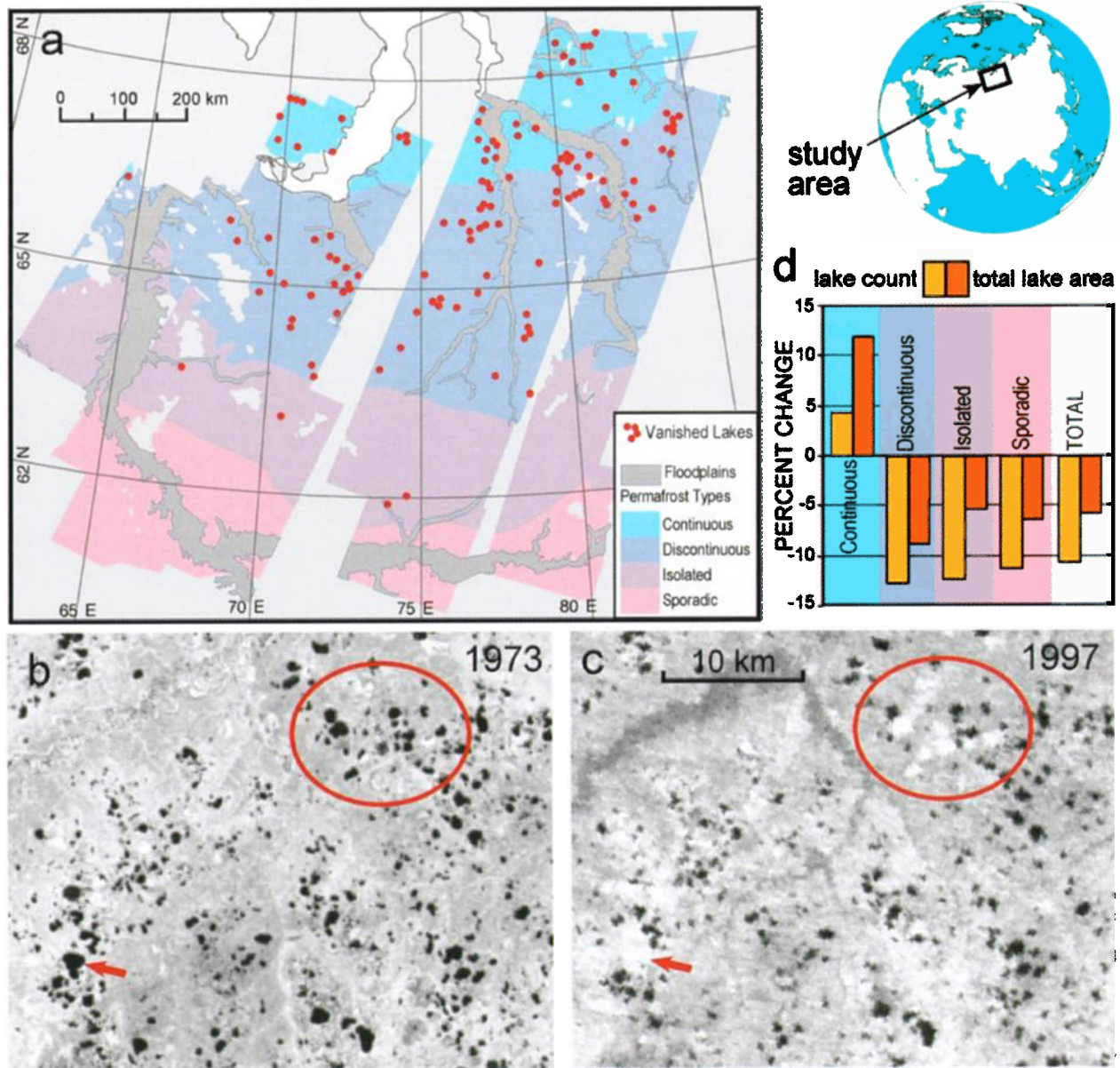
Plate 3. (a) Geographic coverage of western Siberian lake inventories, current permafrost distribution, and recently vanished large lakes. Total lake abundance and inundation area have declined since 1973 (b), including permanent drainage and revegetation of former lakebeds (c). Net *increases* in lake abundance and area have occurred in continuous permafrost (d), suggesting an initial but transitory increase in surface ponding in response to rising air and permafrost temperatures in the region (from *Smith et al.* [2005]; reproduced with the kind permission of the American Association for the Advancement of Science).

derived from the D-InSAR data corroborated with results generated from photogrammetric and geodetic measurements. *Strozzi et al.* [2004] drew similar conclusions regarding the potential of D-InSAR for detecting and quantifying surface deformation of rock glaciers. They also found that D-InSAR provided a good estimate of deformation rates in their study of four active rock glacier systems in the Swiss Alps.

Wang and Li [1999] report they were able to use D-InSAR successfully to detect winter frost-heaving of the active layer in a study area in the foothills of the Brooks Range, Alaska. From the deformation pattern derived from analysis of a pair of ERS-1 images acquired in August and October 1995, they estimated a maximum differential uplift of about 3 cm.

3.2. Permafrost Extent and Active Layer Thickness

Improvements in the spatial and spectral resolution of satellite imagery have resulted in the development of procedures for its use in near-surface active-layer and permafrost mapping. For example, *Morrissey et al.* [1986] prepared maps of near-surface permafrost conditions in a 106 km^2 area in Alaska, using various combinations of three variables as input to logistic discriminant functions: equivalent latitude (a measure derived from actual latitude as well as surface slope), a Landsat Thematic Mapper (TM)–derived vegetation map, and TM thermal Band 6. Terrain was mapped into three categories (frozen, discontinuously frozen, and unfrozen) and compared with a permafrost map prepared by using terrain analysis and ground temperatures. The highest classification accuracy (78%) was obtained when using the TM thermal data and the TM-derived vegetation classification. An accuracy of 75.5% was obtained with equivalent latitude method (potential insolation index) and a TM vegetation classification. Lower accuracies ranging between 62% and 70% were achieved with each of the three input variables alone.

Using SPOT multispectral (HRV) and digital terrain data, and an evidential reasoning classifier, *Peddle and Franklin* [1993] were able to predict four early-summer frozen ground classes within a 100 km^2 study site in the Ruby Range, Yukon Territory, Canada, based on land cover, terrain aspect, and equivalent latitude. Both aspect and equivalent latitude were directly extracted from a digital elevation model (DEM) created from stereoscopic air photos. Land cover was classified from a July SPOT multispectral scene of the study area. The four frozen ground classes used in the study were as follows: class 1: <25 cm; class 2: 25–50 cm; class 3: >50 cm; and 4: an absent class. A classification accuracy of 79% obtained was based on evidence generated from the remotely sensed information listed above. A classification accuracy of 87% was later achieved with a neural network classifier [*Peddle et al.*, 1994].

In another study, *Leverington and Duguay* [1996] evaluated three supervised classification schemes (maximum likelihood, evidential reasoning, and a back-propagation neural network) for their predictive and mapping capabilities of depth to late-summer frozen ground (DTFG; a field-derived measurement that approximates the thickness of the active layer) in the widespread discontinuous permafrost zone of the boreal forest of central Yukon, Canada. Source imagery used in the classifications consisted of TM- and DEM-derived data known to be correlated with DTFG. Results of a two-class DTFG experiment indicated that all tested classifiers were suitable for generating two-class correlative DTFG data products in the Mayo region. The neural network classifier was found to be most successful, producing a two-class DTFG image with a 93% agreement rate between predicted and field-measured DTFG classes. Land cover and equivalent latitude were consistently found to be especially useful sources for use in the classifications. When three DTFG classes were used, agreement rates greatly decreased for all classifiers. The map showing the two classes (frozen and unfrozen) derived by using the neural network classifier with Landsat TM-derived land cover and equivalent latitude as input variables is shown in Figure 4.

In a follow-up study, *Leverington and Duguay* [1997] showed that the correlative relations between surface cover and permafrost table developed at the study site of their 1996 study could not be extended to a second study area located only 15 km away (only 60% agreement was obtained). Results from this study stressed that in situ reconnaissance of any study area of interest is mandatory in the correlative generation of any meaningful permafrost database.

Also on the basis of their research, *Leverington and Duguay* [1996, 1997] concluded that the monitoring of near-surface permafrost using remote sensing must overcome a number of obstacles before it can be used for large-scale climate monitoring over high latitudes. For example, (1) the vertical resolution in estimates of depth to frozen ground is currently insufficient for detecting changes over time; (2) land-cover permafrost correlative relationships may change over time; and (3) there is a significant time lag between changes in climate and changes in surface cover and permafrost (this time lag may be on the order of decades). In equilibrium conditions, vegetation cover, like permafrost, is soil- and microclimate-dependent and may show correlation with permafrost presence/absence, with depth of the active layer, and with near-surface ground ice content. However, as argued by *Granberg* [1994], vegetation depends not only on microclimate, soil, and ground ice conditions, but also on other factors such as history of forest fires. Therefore, the correlative relationships can have local rather than general validity. As seen above, combining remote sensing data with regional climate and topographic data can

LEGEND

■ Frozen

□ Unfrozen

■ Burned

■ Water
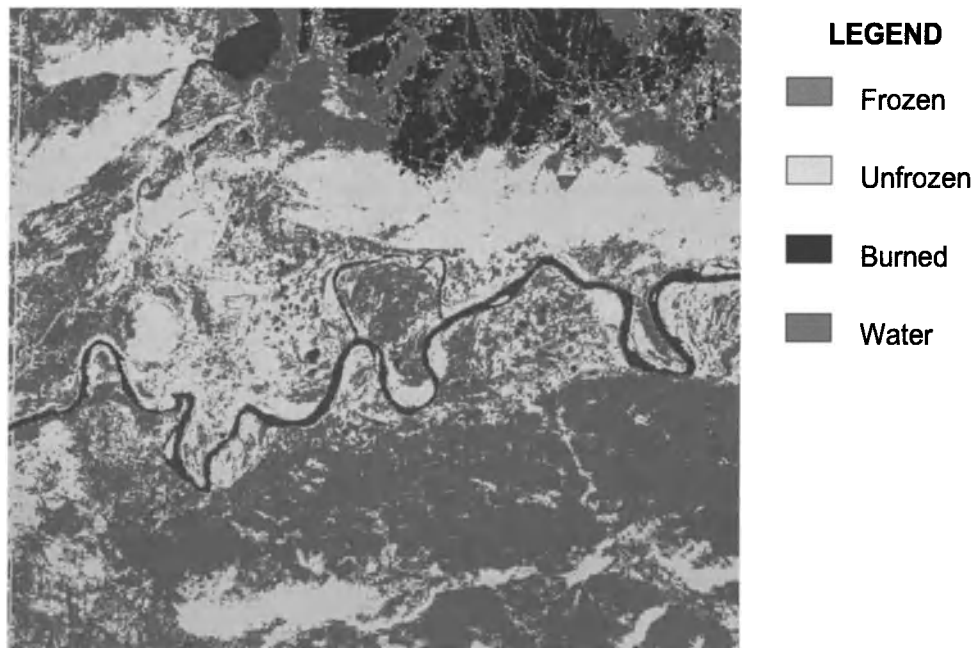
Figure 4. Map showing two classes of depth to late-summer frozen ground (DTFG) predicted by using a neural network with land cover and equivalent latitude used as input variables (93%) agreement between predicted and field-measured DTFG classes. The map was derived based on the approach described in *Leverington and Duguay* [1996]. The mapped region, located in central Yukon Territory, is approximately 23 km across.

aid in predicting permafrost presence/absence and to some extent depths of the active layer at a particular time during the summer season.

McMichael et al. [1997] examined the feasibility of estimating active layer depth (ALD) at multiple spatial scales (tower and toposequence) on the Alaskan North Slope, using the Normalized Difference Vegetation Index (NDVI). They used NDVI as a measure of the aboveground vegetation production since previous studies had shown that spatial variations in ALD are strongly related to vegetation production in the subarctic tundra. Using an Exotech hand-held radiometer, Landsat TM data, and ground measurements of ALD acquired during two summers (1994 and 1995) on the North Slope, they showed that (1) there was no relation between NDVI and ALD in areas with little variation in relief, and (2) NDVI accounted for approximately 40% of the variability in ALD in areas where topography strongly controlled the flow and distribution of water. The authors concluded that local environmental factors (radiation, soil characteristics, and temperature) exert variable degrees of control over the spatial distribution of ALD at both the tower and toposequence scales and should therefore be considered in future studies.

Although measurements of reflected solar radiation from satellite sensors (e.g., Landsat TM and SPOT HRV) have provided the main source of data for the permafrost studies described above, at least one study has examined the potential of SAR imagery for mapping permafrost distribution. *Granberg* [1994] related C-HH radar backscatter to the presence of snow abrasion damage to vegetation and suggested that this information could be indicative of the presence of permafrost near Schefferville, Québec, Canada. C-band radars are sensitive to the structure and dielectric properties of vegetation and can easily detect vegetated versus nonvegetated areas. Strong backscatter responses are characteristic of brush vegetation and trees [*Granberg et al.*, 1994]. On the airborne C-band images, areas where snow abrasion strongly suppressed brush vegetation were clearly distinguishable by the absence of bright returns. *Granberg* [1994] suggested that these areas experience strong wintertime heat loss and therefore probably correspond to areas of permafrost. To test this hypothesis, permafrost zones identified from the SAR image were compared against a map of permafrost derived from air photos interpreted for topography, drainage, and vegetation. On the SAR image, medium-gray speckle-free areas approximately coincided with those areas delimited by the 0.4-m critical snow depth for permafrost development. Although the SAR-produced map suggested a somewhat smaller area of permafrost, *Granberg* [1994] concluded that radar returns, including those from RADARSAT, could be used to accurately map zones of wintertime heat loss and therefore the approximate distribution of permafrost.

4. MAPPING AND MONITORING OF SEASONALLY FROZEN GROUND

Freezing and thawing of the soil and vegetation are the most critical hydrological processes occurring in response to disturbances in the thermal regime of northern latitude terrestrial ecosystems. Whether or not moisture in the soil is frozen affects the rate of energy transfer to the atmosphere by limiting evapotranspiration and affects rainfall or snowmelt runoff potential by reducing the infiltration capacity of the soil [*England*, 1990]. Global warming may significantly alter the duration of the freeze–thaw periods at high- and mid-latitude locations. A modification of the length of the frost-free period could have significant hydrological, ecological, engineering, and economical implications. Active and passive microwave instruments have been shown to be particularly useful for monitoring the freeze–thaw state of northern landscapes.

4.1. Active Microwave

Inasmuch as freezing and thawing represent a state change in water, freezing (thawing) results in a large decrease (increase) in the dielectric constants of vegetation and soil under the canopy. Using a field-based scatterometer, *Wegmüller* [1990] showed a 3–4-dB decrease in backscatter as freezing occurred in bare soil at a 4.6-GHz frequency (VV-polarization; 30° look angle). To microwave instruments, frozen soil is indistinguishable from dry soil, because its liquid water content is small. Measurements from airborne SAR missions have also shown the sensitivity of radar backscatter to freeze–thaw events that occur within forest canopies. For example, decreases in the order of 4–6 dB have been observed with the freezing of spruce and poplar canopies at L-band in a study area near Fairbanks, Alaska [*Way et al.*, 1990]. Results from these experiments have led to the interest of using spaceborne radar systems (SAR and scatterometry) for monitoring the frozen/thawed state of large areas covered by different types of natural vegetation [e.g. *Rignot and Way*, 1994; *Way et al.*, 1994; *Duguay et al.*, 1999].

Rignot and Way [1994] presented an approach for monitoring freeze–thaw cycles of terrestrial ecosystems by using ERS-1 C-band (5.3-GHz) SAR imagery. Using 3-day repeat-pass images (ERS-1 1991 commissioning phase) processed at 100-m pixel spacing, the authors were able to provide a regional picture (100 km × 1,400 km) of the frozen/thawed state of the Alaskan landscape between August and November 1991. Plate 4 shows the temporal series of ERS-1 SAR mosaics along a north–south transect. The mosaics were processed with a simple freeze detection algorithm that determines whether the vegetation and soil are frozen or thawed, based on a radar backscatter decrease of 3 dB relative to a known thawed state of the landscape (the August 12 mosaic). Using data from meteorological stations along the north–south transect, *Rignot and Way* [1994] determined that the decrease in backscatter could be attributable to the large decrease in the dielectric constants of soil and vegetation with freezing. They cautioned however, that radar backscatter can increase in areas of standing water (wetlands, ponds, lakes) with freezing due to the formation of a rough ice–water or ice–soil interface.

In another study, *Duguay et al.* [1999] used ERS-1 data to analyze annual variations in backscatter from subarctic tundra and forest in the northern Hudson Bay Lowland (HBL) near Churchill, Manitoba. Field observations on the physical, ecological, and meteorological conditions gathered were used in the interpretation of variations in backscatter from five sites representing typical terrain types found in the northern HBL (sedge fen, raised beach ridge, willow/birch shrubs, open forest, and lake). The authors determined that the largest variations in backscatter observed within individual terrain types were associated with freezing/thawing and surface wetness (soil moisture and the amount of standing water). The magnitude of changes in backscatter with freezing/thawing (2–9 dB) between sites was largely explained by the nature of the surfaces, which determines the importance of the scattering process (volume or surface). The decrease in backscatter with freezing (2.6 dB) over open forest sites observed in this study agreed well with the value of 3 dB reported by *Rignot and Way* [1994] for the high boreal forest of Alaska, as well as more recent results by *Lagacé et al.* [2002], who used RADARSAT-1 (HH-polarization) images to map the progression of freezing in the taiga zone of Québec, Canada. These authors reported a decrease of 2 dB with freezing of forested areas.

In recent years, scatterometers have also become an important source of data for monitoring the freeze–thaw state of northern landscapes. Unlike SAR sensors, scatterometers provide a much coarser spatial resolution (25–50 km) but have the distinct advantage of offering a much larger spatial coverage and higher temporal resolution. The more frequent temporal coverage and lower spatial sampling of spaceborne scatterometers make them particularly suitable for continental- to global-scale applications. Some characteristics of scatterometers aboard various satellite platforms are summarized in Figure 5.

Using backscatter measurements from C-band (5.3-GHz) scatterometers aboard the ERS-1/2 satellites, *Wismann* [2000] developed a technique to retrieve the date of transition from the frozen to thawed state of the Siberian landscape. In areas covered with snow, the radar return first decreases with melt
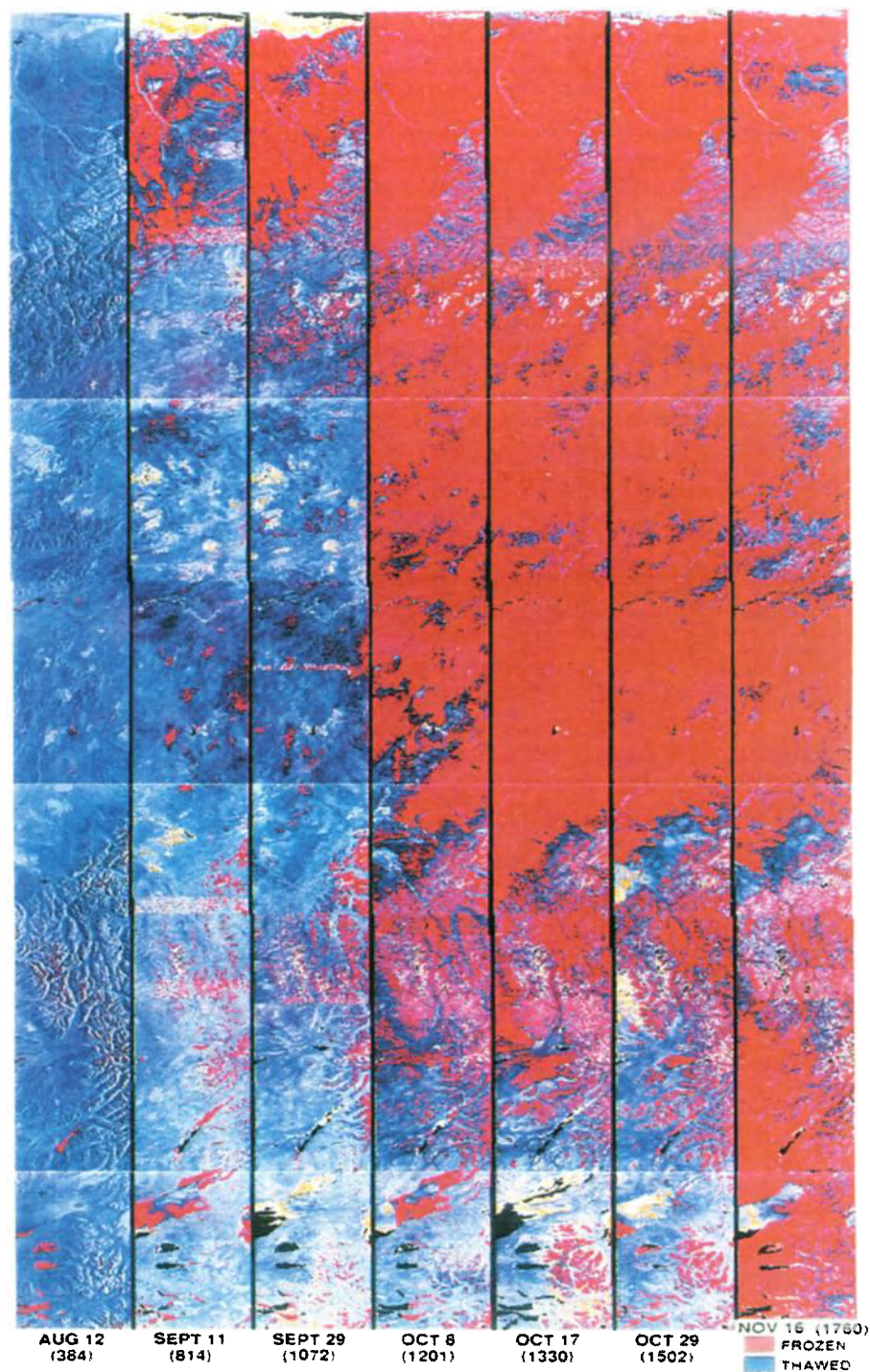
Plate 4. North–south transects across Alaska acquired by ERS-1 SAR during its 1991 commissioning (3-day overpass) phase. Each transect covers an area of 100 × 1,400 km. From left to right are seven transects created from August 12 to November 16. The change from blue to red indicates freeze-up of the landscape (modified from *Rignot and Way* [1994]).

due to enhanced absorption of the microwaves in the wet snow cover. Once soil and vegetated areas become snow-free, back-scatter increases by several dB. The temporal change detection technique proposed by *Wismann* [2000] was applied to a time series of scatterometer data obtained for a period of 8 years (1992–1999) over Siberia. The sequence of images produced with this technique is shown in Plate 5. The time series allows one to visualize the spatial and interannual variability in the onset of thaw, which marks the start of snowmelt, and in the high latitude permafrost region also marks the beginning of thawing of the active layer. Such maps, showing the onset of thaw at a coarse resolution, are of utmost interest to climate and hydrologic modeling groups.

Similar research has also taken place on the development of techniques to determine the frozen/thawed state of the landscape from shorter wavelength Ku-band (2.14 cm; 25-km spatial resolution) spaceborne NASA scatterometer (NSCAT) data. NSCAT, which flew onboard the Japanese Advanced

Earth Observing System (ADEOS) (see Figure 5), provided 9 months of high-quality data (August 16, 1996, to June 30, 1997) until a failure in the ADEOS solar array forced the termination of NSCAT operations [*Kimball et al.*, 2001]. *Running et al.* [1999] produced NSCAT mosaics to map the progression of landscape thawing over Alaska during spring of 1997. These mosaics are compared with interpolated surface temperature records in Plate 6. As described by *Kimball et al.* [2001], the Ku-band is very sensitive to the presence of unfrozen water on the surface of the snow or ground. Thus, with spring thaw, radar backscatter measurements show pronounced decreases in backscatter relative to frozen state conditions (about 2–5 dB). More recently, *Kimball et al.* [2004] used the same temporal change detection technique applied to daily NSCAT backscatter measurements to characterize the 1997 spring thaw transition period over a boreal forest study area in central Canada. They found that air temperature transitions from frozen to nonfrozen conditions and
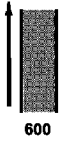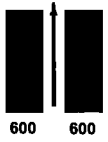
	SASS	ESCAT	NSCAT	SeaWinds
Frequency	14.6 GHz	5.3 GHz	14.0 GHz	13.4 GHz
Antenna azimuth orientations				
Polarizations	V-H, V-H	V Only	V, V-H, V	V-Outer/H-Inner
Beam resolution	Fixed Doppler	Range gate	Variable Doppler	Pencil-beam
Modes	Many	SAR, wind	Wind only	Wind/hi-res
Resolution	50/100 km	25/50 km	25/50 km	25 km/6 × 25 km
Swath, km	750 750	600	600 600	1400,1800
Incidence angles	0–70°	18–59°	17–60°	46° & 54°
Daily coverage	Variable	<41%	78%	92%
Dates	SEASAT: 06/78–10/78	ERS-1: 1992–96 ERS-2: 1995–	ADEOS I: 08/98–06/97	QuikSCAT: 06/99–

Figure 5. Characteristics of four spaceborne scatterometers flown on Seasat (SASS), ERS-1/2 (ESCAT), ADEOS (NSCAT), and QuikSCAT (SeaWinds or QSCAT) (from *Long et al.* [2001]).
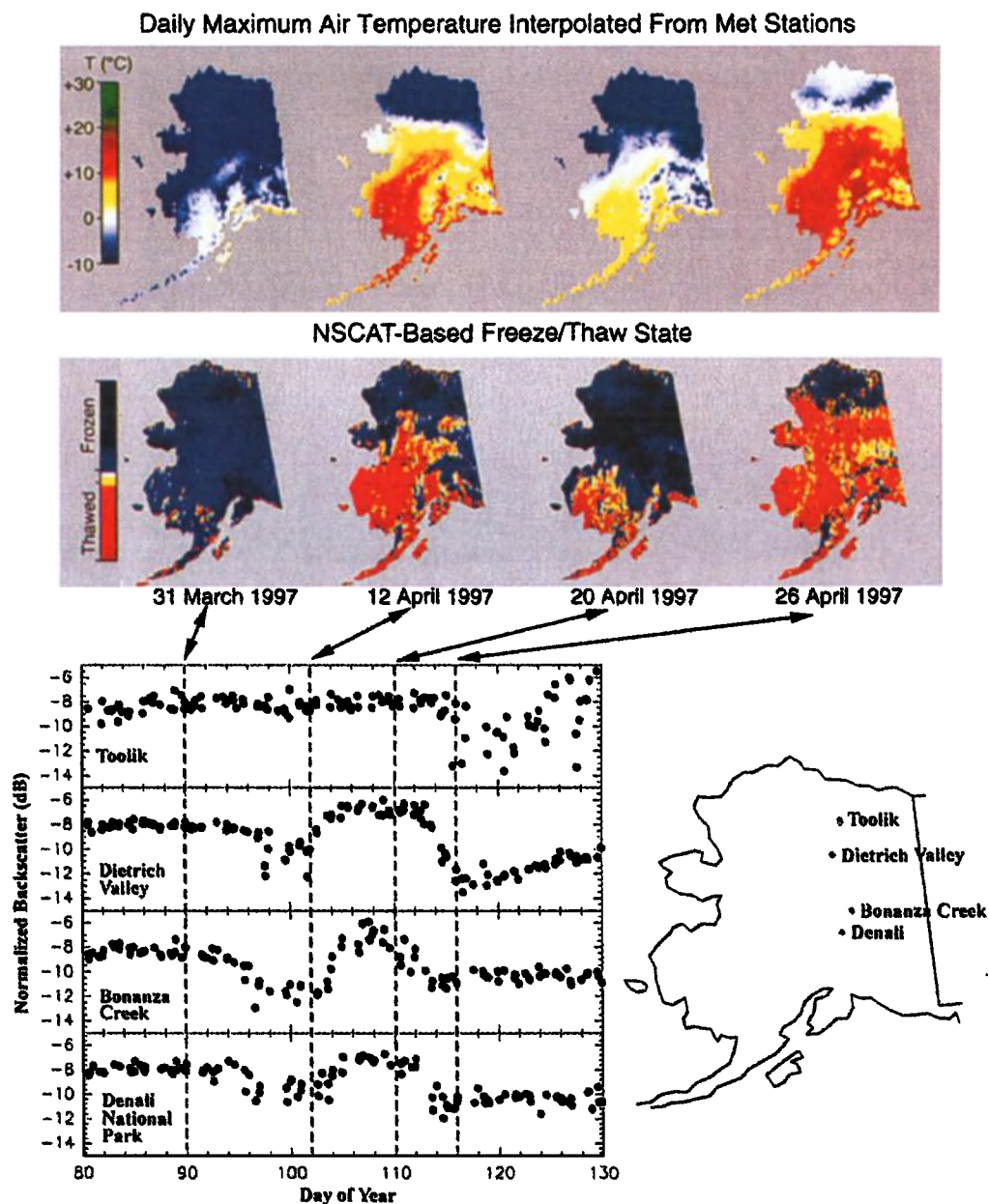
Plate 5. Comparison of maximum air temperature with freeze/thaw state maps derived from 2-day NASA Scatterometer (NSCAT) composite mosaics for 4 days in March and April 1997. The surface temperature maps were spatially interpolated with measurements from 72 meteorological stations in Alaska. The NSCAT images used a 4-dB shift in backscatter to define the freeze/thaw transition. The bottom four graphs show temporal series of the NSCAT backscatter at four locations along a north–south transect. Vegetation temperature measurements obtained in situ at four sites are compared with NSCAT backscatter extracted from 50-km regions centered at each of the ground stations. The broken vertical lines mark the times initiating the 2-day NSCAT composites. Comparison of in situ data with normalized backscatter reveals that the scatterometer observes a combination of vegetation and snow thaw as conditions in the Alaskan interior progress from a short warming trend, through a brief refreezing transition, to the final initiation of springtime thaw and progression to a snow-free state (from *Running et al.* [1999]).
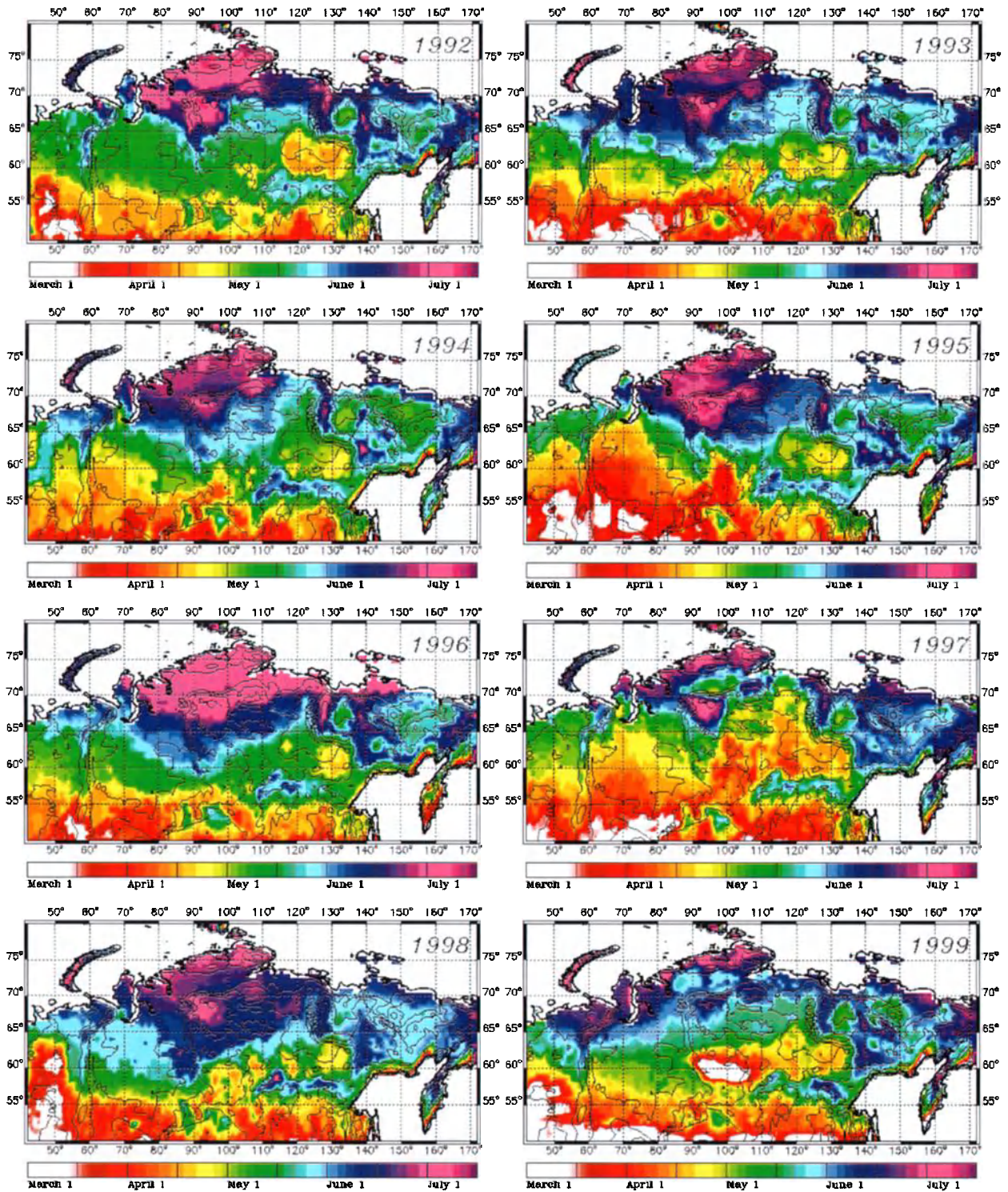
Plate 6. Maps depicting the onset of thawing from ERS-1/2 scatterometer data (1992–1999) over Siberia. The maps were produced based on the technique described in *Wismann* [2000]. Source: http://www.ifars. de/thawing/thawing.htm.

surface observations of snow cover depletion were generally coincident with decreases in radar backscatter of more 2.9 dB, regardless of the land cover type within the study area. These results further illustrate the potential of spaceborne radar-based measurements for monitoring the freeze–thaw state of vast areas of the Northern Hemisphere.

4.2. Passive Microwave

Some important advances have also been achieved in the mapping of the freeze–thaw state by using passive microwave imagery. Using data from the Nimbus 7 Scanning Multi-channel Microwave Radiometer (SMMR; available from October 1978 through August 1987), *Zuerndorfer and England* [1992] showed that two criteria— the 10.7, 18, and 37-GHz spectral gradient ($\partial T_b/\partial f$ in K GHz^{-1}, where T_b is the brightness temperature and f is frequency) and the 37-GHz brightness temperature—can be utilized to classify snow-free soils as either frozen or unfrozen. *Judge et al.* [1997] explain that the SMMR spectral gradient of frozen soils is negative because heterogeneities in the frozen soil scatter microwave radiation more severely at 37 GHz than at 10.7 GHz. However, for soils that contain liquid water, the SMMR spectral gradient is positive because the Debye process has a greater darkening effect at 10.7 GHz than 37 GHz. The 37-GHz brightness temperature is used because it is more strongly correlated with ground surface and air temperatures than are the 10.7- and 18-GHz frequencies [*Zhang and Armstrong*, 2001].

The freeze indicator method developed by *Zuerndorfer and England* [1992] was used to classify frozen surfaces in the northern Great Plains of the contiguous United States with good results. *Cao and Chang* [1999], using SMMR data, applied a similar algorithm with a special gradient of -0.17 K GHz^{-1} between 37 and 18 GHz and a cutoff brightness temperature $T_b(37) = 222.5$ K to detect the near-surface soil freeze–thaw status for the spring and autumn of 1983 on the Qinghai-Xizang (Tibetan) Plateau. The accuracy of *Cao and Chang*'s results compared with ground-based soil temperature measurements was about 70%. *Toll et al.* [1999] used the horizontal polarized brightness temperatures at 37 and 18 GHz of the SMMR data to assess seasonally frozen soils between spring 1985 and fall 1987 for the north-central United States and southern Canada. They applied a negative spectral gradient between 37 and 18 GHz and a cutoff brightness temperature of $T_b(37H) = 257.5$ K. The overall accuracy is 85.9% as compared with 5-cm soil temperature data at both 0800 CST and 1600 CST from 14 Canadian field stations [*Toll et al.*, 1999].

Special Sensor Microwave Imager (SSM/I) data collected on a series of Defense Meteorological Satellites since July 1987 are available. SSM/I data are acquired at frequencies 19.35, 22.235, 37, and 85.5 GHz; dual polarizations are used at all frequencies except the 22.235-GHz, horizontal polarization, water vapor channel. Although the SSM/I frequencies are well above the Debye relaxation frequency of liquid water, *Judge et al.* [1997] showed that frozen soils could be discriminated from unfrozen soils in the northern Great Plains of the United States by using a combination of the 37-GHz V-polarization brightness temperature and 19–37-GHz V-polarization spectral gradient. The vertically polarized brightness temperature at 19 and 37 GHz is expressed as $T_b(19V)$ and $T_b(37V)$, respectively. The V-polarization was favored over the H-polarization because it is less sensitive to variations in soil moisture content at the SSM/I incidence angle of 53°, thus providing superior discrimination between frozen and unfrozen soils. Therefore, two decision criteria must be met to classify soils as frozen [*Judge et al.*, 1997]: (1) $T_b(37V) < 247$ K, and (2) a negative spectral gradient between $T_b(19V)$ and $T_b(37V)$.

Chang and Cao [1996] conducted an analysis by averaging the vertical and horizontal components of the SSM/I brightness temperature to discriminate the seasonal freeze–thaw boundary on the Qinghai-Xizang (Tibetan) Plateau, as *Zuerndorfer and England* (1992) did using SMMR data in the northern United States. They used a negative spectral gradient between $T_b(37)$ and $T_b(19.35)$ with a cutoff $T_b(37) = 231$ K for the morning overpass and $T_b(37) = 238$ K for the afternoon overpass, respectively. The overall accuracy was about 85% when compared with the 5-cm soil temperatures.

Zhang and Armstrong [2001] proposed a variation to the approach developed by *Zuerndorfer and England* (1992). By examining the relation between soil temperature measurements taken at 5-cm depth from more than 20 sites (winter 1997/1998) throughout the contiguous United States and $T_b(37V)$, they found that a cutoff brightness temperature of 258.2 K should be used instead of 247 K. Also, the authors suggest using the snow algorithm of *Goodison* [1989], written as $GW = -2.74[T_b(37V) - T_b(19V)] - 20.7$, to discriminate between snow-free frozen and snow-covered soils, where $GW > 0$ indicates that snow is present on the ground. The application of the two new criteria allowed *Zhang and Armstrong* [2001] to estimate the variation in the duration of soil freezing from 5 to 7 months over most of the study area shown in Plate 7.

Other authors, such as *Lagacé et al.* [2002], have proposed further modifications to the algorithm of *Judge et al.* [1997] to detect the onset of freezing of the landscape. In the *Lagacé et al.* [2002] approach, the spectral gradient is adjusted to take into account the presence of lakes (and other water reservoirs), which can occupy a significant fraction of SSM/I pixels in lake-rich areas of the Northern Hemisphere. The
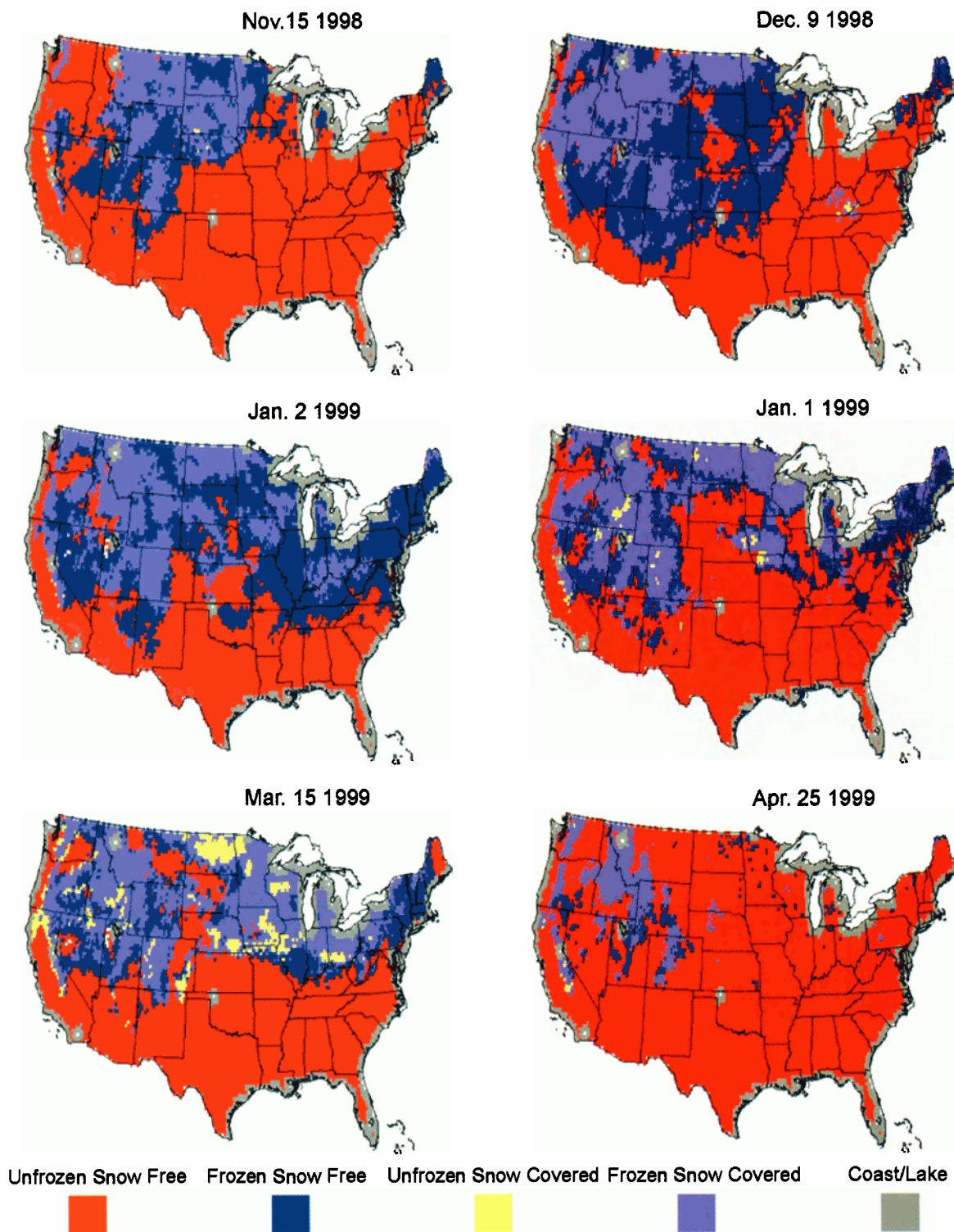
Plate 7. Advance and retreat of the area extent of near-surface freezing soils and seasonal snow cover, detected by using the NSIDC Frozen Soil Algorithm, during the winter of 1998–1999 in the contiguous United States (from *Zhang et al.* [2003b]).

percentage of water bodies occupying each SSM/I pixel is first determined based on a land cover map produced from NOAA AVHRR at the 1-km spatial resolution. The spectral-gradient equation is then weighted to correct for the effect of water bodies on the SSM/I brightness temperatures at both the 19- and 37-GHz frequencies. Also noteworthy is the cutoff brightness temperature of 274 K used by *Lagacé et al.* [2002], which is 27 K and 25.8 K higher than the values of 247 K and 258.2 K suggested by *Judge et al.* [1997] and *Zhang and Armstrong* [2001], respectively. *Lagacé et al.* [2002], however, do not provide a clear explanation as to the reason for choosing the new cutoff value. Maps resulting from the application of this method to a large area in the taiga zone of the province of Québec, Canada, are presented in Plate 8. The series of maps depicts the seasonal progression of landscape freezing in fall 1996, beginning in the northeast, followed by the western region near James Bay/Hudson Bay, and then in the central and southern regions of the territory.

The freeze indicator originally developed by *Zuerndorfer and England* [1992], and revised by others [*Chang and Cao*, 1996; *Judge et al.*, 1997; *Toll et al.*, 1999; *Zhang and Armstrong*, 2001; and *Lagacé et al.*, 2002], applies only to snow-free land surfaces. However, knowing the freeze–thaw status of the soil under the seasonal snow cover is particularly important for studies on soil moisture, spring surface runoff, and potential flood forecasting. *Zhang et al.* [2003b] developed a combined algorithm, namely, the National Snow and Ice Data Center Frozen Soil Algorithm (NSIDC FSA), which detects the freeze–thaw status of near-surface soil over both snow-free and snow-covered land areas. The NSIDC FSA consists of two parts: (1) Over snow-free land areas, a passive microwave satellite remote sensing algorithm is used to detect the near-surface soil freeze–thaw status; and (2) over snow-covered land areas, a one-dimensional numerical heat transfer model with phase change is used to detect the freeze–thaw status of the soil under snow cover. Using soil temperature data measured from 26 stations across the contiguous United States for the period July 1, 1998, through June 30, 1999, the NSIDC FSA provides an accuracy of about 76% for frozen soil detection and the correct classification of both frozen and unfrozen soils of approximately 83%, with a percentage error of about 17%. Using the validated NSIDC FSA, *Zhang et al.* [2003b] further investigated the timing, duration, number of days, and daily areal extent of the near-surface frozen soils from July 1, 1997, through June 30, 1999, over the contiguous United States. They found that the maximum areal extent of frozen ground during the winter of 1997–1998 was about 4.4×10^6 km² or 63% of the total area of the contiguous United States, whereas during the winter of 1998–1999, the maximum areal extent was

about 5.2×10^6 km² or 74%. The duration of seasonally frozen ground ranges from less than 1 month in the south to longer than 8 months in the Rocky Mountains. The actual number of days of soil freezing varies from a few weeks to more than several months. The number of the near-surface soil freeze–thaw cycles varied from 1 to more than 11 times during the winters of 1997–1998 and 1998–1999, while the average length of frozen period varied from fewer than 20 days to more than 120 days.

More recently, *Smith et al.* [2004] presented for the first time the application of a freeze/thaw detection algorithm to a long time series of passive microwave data covering the regions north of 45°N. The authors used 6-day daily means of SMMR and SSM/I data in the NSIDC-EASE (Equal Areal Scalable Earth) Grid format (25 km × 25 km pixels) available from the NSIDC for the entire period of analysis between 1978 and 2002. The detailed analysis, however, focused on the 1988-2002 SSM/I period. Briefly, the algorithm involves a two step process of fitting a line by ordinary least squares to the plateau of a spline-fitted spectral gradient curve ($T_{b(37)}^-$ $T_{b(18/19)}$). The reader is invited to consult the original paper for further details on the elaboration and validation of the algorithm. For global analysis (i.e., north of 45°N), *Smith et al.* [2004] compute freeze/thaw dates for each of four time series (horizontally or vertically polarized and ascending or descending orbits) from EASE-Grid data previously aggregated to 1° × 1° grid cells, giving four independent estimates of freeze and thaw dates which are then averaged to provide a single date for each grid cell. An analysis of the spatial patterns and trends in freeze–thaw dates reveals, as examples, a trend toward earlier spring thaw in Eurasian larch and tundra biomes, and a trend toward later fall freeze in evergreen conifer forests of North America over the period 1988–2002.

McGuire et al. [2004] and *McDonald et al.* [2004] employ a step-edge detection scheme to identify the predominant springtime thaw transition event on an annual basis using SSM/I data from 1988 through 2001 over the pan-Arctic basin and Alaska. The technique is based on the application of an optical edge detector for determining edge transitions in noisy signals [*Canny*, 1986]. Unlike the freeze–thaw algorithm by *Smith et al.* [2004], which ignores snow cover and cannot detect the repeated freeze–thaw cycles, the freeze–thaw algorithm by *McGuire et al.* [2004] and *McDonald et al.* [2004] accounts for the occurrence of frequently repeated freeze/thaw events in spring. Based on this freeze–thaw algorithm, *McDonald et al.* [2004] found that the timing of seasonal thawing and subsequent initiation of the growing season in early spring has advanced by approximately 8 days from 1988 to 2001 for the pan-Arctic basin and Alaska. However, using the ground-based measurements, *Stone et al.* [2002] found that
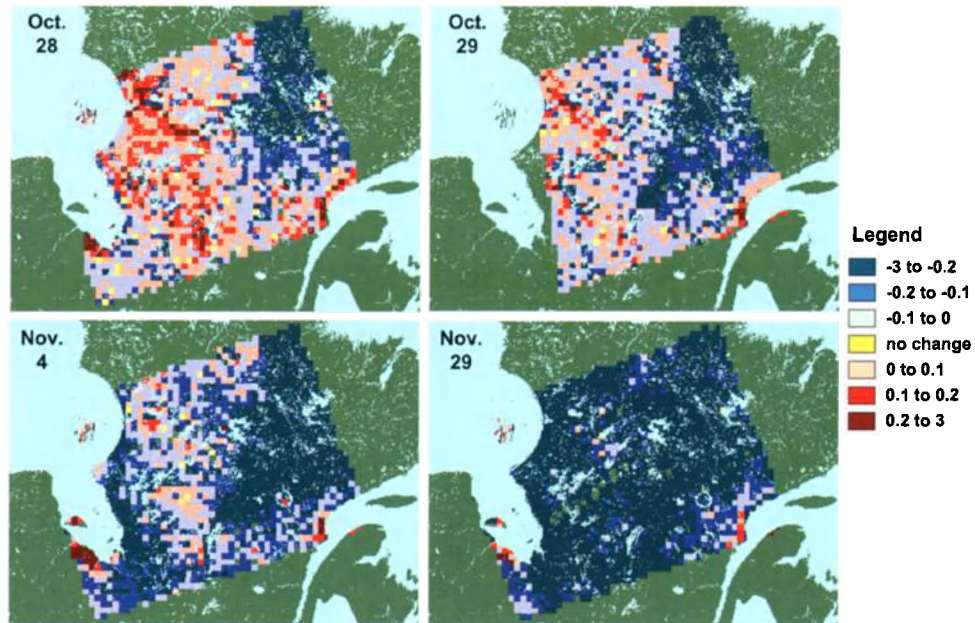
Plate 8. Maps showing the progression of soil freezing in the taiga region of the province of Quebec, Canada, during fall 1996. The maps were produced based on the weighted brightness temperature gradient algorithm of *Lagacé et al.* [2002] from SSM/I data (negative values in the legend correspond to frozen soils). Images courtesy of M. Bernier.

snowmelt date in northern Alaska has advanced by about 8 days from the mid-1960s to 2000. The freeze–thaw algorithm developed by *McGuire et al.* [2004] and *McDonald et al.* [2004] needs further validation and calibration from ground-based measurements and other available data.

5. CONCLUSIONS AND OUTLOOK

Success in the development of remote-sensing techniques for use in mapping near-surface permafrost conditions has been limited relative to the success in mapping of other cryospheric variables of interest. Nevertheless, some advances have been made in satellite-based mapping techniques, including the use of correlative relationships between surface parameters and permafrost conditions to generate digital databases of near-surface permafrost conditions using such databases as SPOT and TM images, as well as digital topography. Recent improvements in the spectral and spatial resolution of optical imagers (e.g., the Hyperion and IKONOS sensors), as well as SAR sensors (e.g., the RADARSAT series) and topographic databases (e.g., the databases of the Shuttle Radar Topography Mission) provide a strengthened foundation from which substantial improvements in permafrost mapping may now be made. The surface expression of permafrost conditions and processes (e.g., polygonal networks of frost wedges) can be most easily detected in high-resolution images, which are now available at relatively low cost. The surface parameters that are correlated with permafrost conditions (e.g., vegetation cover) can be most accurately generated by using data with both a high spatial and spectral resolution: data that are increasingly available as advanced sensors are placed in orbit.

The permafrost- and frozen-ground-related databases generated with remote sensing techniques demonstrate considerable potential for use as tools in regional-scale permafrost research, environmental management, and hydrological modeling. With nearly 25% of the continents underlain by permafrost, extensive ground surveys of permafrost conditions are precluded due to expense, logistical difficulties, short field seasons, and time constraints. On the other hand, many numerical heat-transfer models have been used to understand the detailed physics of the permafrost–climate relationship. With a few exceptions, however, because of the extremely limited databases characterizing the microclimates of a broad range of vegetation and terrain conditions, these models are impractical beyond the site scale. In contrast, satellite remote sensing techniques provide the means to generate both local and regional permafrost-related databases. In combination with direct in situ measurements, these techniques may have the potential to more effectively identify evidence of climate change by identifying regional changes in permafrost conditions over extended time periods of decades or centuries.

The constellation of recently launched and planned satellites is expected to produce important developments in the permafrost applications of remote sensing techniques over the next decade, many more than have been realized in the past 30 years. In particular, significant future advancements are foreseen on at least four fronts: (1) mapping/monitoring of the evolution of permafrost-related features by using archived imagery or aerial photographs and more recent high-resolution satellite imagery (e.g., IKONOS, QuickBird, and declassified images generated by the CORONA spy satellite); (2) increased use and development of new land-surface "skin" temperature data products from thermal infrared and passive microwave satellite sensors [e.g., *Prigent et al.*, 2003; *Hachem et al.*, 2004] to examine the impact of climate variability and change on permafrost terrain; (3) increased use and development of new land-surface freeze–thaw products from both active and passive microwave satellite sensors [e.g., *Zhang et al.*, 2003b, 2004; *Entekhabi et al.*, 2004] to examine variability and trends in the onset of freezing and thawing in relation to climate; and (4) integration of the land surface products derived from satellite remote sensing data (e.g., land surface temperature, vegetation cover, snow cover, etc.) in spatially distributed permafrost models [e.g., *Hinzman et al.*, 1998; *Etzelmüller et al.*, 2001; *Gruber and Hoelzle*, 2001; *Henry and Smith*, 2001; *Shiklomanov and Nelson*, 2002; *Oelke et al.*, 2003; *Sazonova and Romanovsky*, 2003; *Oelke and Zhang*, 2004]. Finally, it is anticipated that further developments will also be made in the application of D-InSAR to monitor the deformation of landscape features associated with the presence of permafrost.

REFERENCES

Anisimov, O. A. and Nelson, F. E., Influence of climate change on continental permafrost in the northern hemisphere. *Meteorol. Gidrol.* 1997/5: 71–80 (In Russian; English translation appears in *Russian Meteorol. Hydrol.* 1997/5), 1997.

Associate Committee on Geotechnical Research (ACGR). Glossary of Permafrost and Related Ground-Ice Terms. Permafrost Subcommittee, National Research Council of Canada, Ottawa, Technical Memorandum 142, 156 pp, 1988.

Boynton, W.V. and 24 others, Distribution of hydrogen in the near surface of Mars: Evidence for subsurface ice deposits, *Science, 297,* 81–85, 2002.

Brown, R. J. E., Permafrost Investigations in British Columbia and Yukon Territory, *National Research Council of Canada Publication 9762,* 1967.

Brown J., O. J. J. Ferrians, J. A. Heginbottom, and E. S. Melnikov, *International Permafrost Association Circum-Arctic Map of*

Permafrost and Ground Ice Conditions, Washington, DC: U.S. Geological Survey, scale 1:10,000,000, 1997.

Burn, C. R., Recent ground warming inferred from the temperature in permafrost near Mayo, Yukon Territory. In *Periglacial Geomorphology*, Edited by J.C. Dixon and A.D. Abrahams, John Wiley & Sons, Chichester, U.K., pp.327–350, 1992.

Burn, C. R., Permafrost, tectonics, and past and future regional climate change, Yukon and adjacent Northwest Territories, *Can. J. Earth Sci.*, *31*, 182–191, 1994.

Burn, C. R., Implications for paleoenvironmental reconstruction of recent ice-wedge development at Mayo, Yukon Territory, *Permafrost Periglacial Process.*, *1*, 3–14, 1990.

Burn, C. R., and P. A. Friele, Geomorphology, vegetation succession, soil characteristics and permafrost in retrogressive thaw slumps near Mayo, Yukon Territory, *Arctic*, *42*, 31–40, 1989.

Burn, C. R., and M. W. Smith, Development of thermokarst lakes during the Holocene at sites near Mayo, Yukon Territory, *Permafrost Periglacial Process.*, *1*, 161–176, 1990.

Canny, J. F., A computational approach to edge detection, *IEEE Trans. Pattern Anal. Machine Intell.*, *8*, 679–698, 1986.

Cao, M. S. and A. T. C. Chang, Monitoring terrain soil freeze/thaw condition on Qinghai-Plateau in spring and autumn using microwave remote sensing, *J Remote Sens.*, *1*, 139–144, 1999. (in Chinese with English abstract).

Chang, A. T. C. and M. S. Cao, Monitoring soil condition in the northern Tibetan Plateau using SSM/I data, *Nord. Hydrol.*, *27*, 175–184, 1996.

Dean, K. G. and L. A. Morrissey, Detection and identification of Arctic landforms: An assessment of remotely sensed data, *Photogramm. Eng. Remote Sens.*, *54*, 363–371, 1988.

Duguay, C. R., W. R. Rouse, P. M. Lafleur, D. L. Boudreau, Y. Crevier, and T. J. Pultz, Analysis of multi-temporal ERS-1 SAR data of subarctic tundra and forest in the northern Hudson Bay Lowland and implications for climate studies, *Can. J. Remote Sens.*, *24*, 21–33, 1999.

England, A. W., Radiobrightness of diurnally heated, freezing soil, *IEEE Trans. Geosci. Remote Sens.*, *28*, 464–476, 1990.

Entekhabi, D., and 20 others, The Hydrosphere State (Hydros) satellite mission: an earth system pathfinder for global mapping of soil moisture and land freeze/thaw, *IEEE Trans. Geosci. Remote Sens.*, *42*, 2184–2195, 2004.

Etzelmüller, B, R.S. Ødegård, I. Berthling, and J. L. Sollid, Terrain parameters and remote sensing data in the analysis of permafrost distribution and periglacial processes: principles and examples from southern Norway, *Permafrost Periglacial Process.*, *12*, 79–92, 2001.

Ferrians, O. J. and G. D. Hobson, Mapping and predicting permafrost in North America: A review, 1963–1973, in *Permafrost: Second International Conference*, Yakutsk, U.S.S.R., 479–498, 1973.

French, H. M., Man-induced thermokarst, Sachs Harbour airstrip, Banks Island, N.W.T., Canada, *Can. J. Earth Sci.*, 12, 132–144, 1975.

French, H. M., *The Periglacial Environment*, Second edition, Longman: Singapore, 341 p., 1996.

Goodison, B. E., Determination of areal snow water equivalent on the Canadian prairies using passive microwave satellite data,

IGARSS'89, 12th Canadian Symposium on Remote Sensing, Quantitative Remote Sensing: An Economic Tool for the Nineties, Vancouver, Canada, July 10-14, Vol. 3, 1243–1246, 1989.

Goodrich, L. E., The influence of snow cover on the ground thermal regime, *Can. J. Earth Sci.*, *19*, 421–432, 1982.

Granberg, H. B., Mapping heat loss zones for permafrost prediction at the northern/alpine limit of the boreal forest using high-resolution C-band SAR, *Remote Sens. Environ.*, *50*, 280–286, 1994.

Granberg, H. B., A. S. Judge, K. Fadaie, and R. Simard, C-band SAR backscatter from northern terrain with discontinuous permafrost: The Schefferville Digital Transect, *Can. J. Remote Sens.*, *20*, 245–256, 1994.

Grosse, G., L. Schirrmeister, V. Kunitsky, and H.-W. Hubberten, The use of CORONA images in remote sensing of periglacial geomorphology: an illustration from the NE Siberian coast, *Permafrost Periglacial Process.*, *16*, 163–172, 2005.

Gruber, S. and M. Hoelzle, Statistical modelling of mountain permafrost distribution: local calibration and incorporation of remotely sensed data, *Permafrost Periglacial Process.*, *12*, 69–77, 2001.

Hachem, S., C. R. Duguay, V. Romanovsky, M. Allard, and M. Fukuda, Evaluation of the MODIS land surface temperature daily global 1-km product in permafrost areas of northern Canada and Alaska, *Workshop on Spatially Distributed Modeling and Remote Sensing of Permafrost –Program and Abstracts*, Fairbanks, Alaska, 17–20 October, 2004.

Hall, D. K. and J. Martinec, *Remote Sensing of Snow and Ice*, Chapman and Hall: London, 1985.

Hallet, B. Self-organization in freezing soils: From microscopic ice lenses to patterned ground, *Can. J. Phys.*, *68*, 842–852, 1990.

Heginbottom, J. A., Permafrost mapping: a review, *Progr. Phys. Geogr.*, *26*, 623–642, 2002.

Henry, K. and M. Smith, A model-based map of ground temperatures for the permafrost regions of Canada, *Permafrost Periglacial Process.*, *12*, 389–398, 2001.

Hinzman, L. D., D. J. Goering, and D. L. Kane, A distributed thermal model for calculating soil temperature profiles and depth of thaw in permafrost regions, *J. Geophys. Res.*, *103*(D22), 28,975–28,991, 1998.

Judge, J., J. F. Galantowicz, A. W. England, and P. Dahl, Freeze/thaw classification for prairie soils using SSM/I radiobrightnesses, *IEEE Trans. Geosci. Remote Sens.*, *35*, 827–832, 1997.

Kane, D. L., The impact of arctic hydrologic perturbations on arctic ecosystems induced by climate change, In Oechel, W. C., *Global Change and Arctic Terrestrial Ecosystems*, Springer-Verlag, *Ecological Studies*, *124*, 63–81, 1997.

Kenyi, L. W. and V. Kaufmann, Estimation of alpine permafrost surface deformation using InSAR data, *Proc. IEEE 2001 International Geoscience and Remote sensing Symposium*, 3p., 2001.

Kessler, M. A. and B. T. Werner, Self-organization of sorted patterned ground, *Science*, *299*, 380–383, 2003.

Kimball, J. S., K. C. McDonald, S. Frolking, and S. W. Running, Radar remote sensing of the spring thaw transition across a boreal landscape, *Remote Sens. Environ.*, *89*, 163–175, 2004.

Kimball, J. S., K. C. McDonald, A. R. Keyser, S. Frolking, and S. W. Running, Application of the NASA scatterometer (NSCAT)

for determining the daily frozen and nonfrozen landscape of Alaska, *Remote Sens. Environ.*, 75, 113–126, 2001.

Lachenbruch, A. H., J. H. Sass, B. V. Marshall, and T. H. Moses, Permafrost, heat flow, and the geothermal regime at Prudhoe Bay, Alaska, *J. Geophys. Res.*, 87, B11, 9301–9316, 1982.

Lagacé, C., M. Bernier, and Y. Gauthier, Cartographie du gel saisonnier du sol en zone de taïga à partir d'images RSO de RADARSAT-1 et SSM/I de DMSP F-8, *Télédétection*, 2, 161–175, 2002.

Leverington, D. W., A field survey of late-summer depths to frozen ground at two study areas near Mayo, Yukon Territory, Canada, *Permafrost Periglacial Process.*, 6, 373–379, 1995.

Leverington, D. W., Preliminary results from a survey of candidate permafrost and periglacial features on Mars, Third Mars Polar Science Conference, Abstract 8013, Lunar and Planetary Institute, 2003.

Leverington, D. W. and C. R. Duguay, Evaluation of three supervised classifiers in mapping "depth to late-summer frozen ground," Central Yukon Territory, *Can. J. Remote Sens.*, 22, 163–174, 1996.

Leverington, D. W. and C. R. Duguay, A neural network method to determine the presence or absence of permafrost near Mayo, Yukon Territory, Canada, *Permafrost Periglacial Process.*, 8, 205–215, 1997.

Lewkowicz, A. G. and C. R. Duguay, Detection of permafrost features using SPOT panchromatic imagery, Fosheim Peninsula, Ellesmere Island, N.W.T., *Can. J. Remote Sens.*, 25, 34–44, 1999.

Ling, F. and T. Zhang, Numerical simulation of permafrost thermal regime and talik formation under shallow thaw lakes in the Alaskan Arctic, *J. Geophys. Res.*, 108(D16), 4511, doi:10.1029/2002JD003014, 2003.

Ling, F., and T. Zhang, Numerical simulation of talik freeze-up and permafrost response under drained thaw lakes on the Alaskan Arctic Coastal Plain, *J. Geophys. Res.*, 109, D01111, doi:/10.1029/2003JD3886, 2004.

Long, D. G., M. R. Drinkwater, B. Holt, S. Saatchi, and C. Bertoia, Global ice and land climate studies using scatterometer image data, *EOS, Trans. American Geophys. Union*, 82(43), 503, 2001.

Luthin, J. N. and G. L. Guymon, Soil moisture-vegetation-temperature relationships in central Alaska, *J. Hydrol.*, 23, 233–246, 1974.

Mackay, J. R., Disturbances to the tundra and forest tundra environment of the western Arctic, *Can. Geotech. J.*, 7, 420–432, 1970.

Mackay, J. R., Ice wedge cracks, Garry Island, N.W.T., *Can. J. Earth Sci.*, 11, 1366–1383, 1974.

Mackay, J. R., Pulsating pingos, Tuktoyaktuk Peninsula, N.W.T., *Can J. Earth Sci.*, 14, 209–222, 1977.

Mackay, J. R., The origin of hummocks, western Arctic coast, *Can. J Earth Sci.*, 17, 996–1006, 1980.

Mackay, J. R., Permafrost growth in recently drained lakes, Western Arctic Coast, *In* Current Research, Part B, Geological Survey of Canada, Paper 85-1B, 177–189, 1985.

Mackay, J. R., Seasonal growth bands in pingo ice, *Can. J. Earth Sci.*, 27, 1115–1125, 1990.

Mackay, J. R., Rampton, V.N., and Fyles, J.G., Relic Pleistocene permafrost, western Arctic, Canada, *Science*, 176, 1321–1323, 1972.

McDonald, K. C., J. S. Kimball, E. Njoku, R. Zimmermann, M. Zhao, Variability in springtime thaw in the terrestrial high latitudes: monitoring a major control on the biospheric assimilation of atmospheric CO_2 with spaceborne microwave remote sensing, *Earth Interactions*, 8, 1–23, 2004.

McGuire, A. D and 15 others, Land cover disturbances and feedbacks to the climate system in Canada and Alaska. In *Land Change Science: Observing, Monitoring, and Understanding Trajectories of Change on the Earth's Surface*. G. Gutman, A.C. Janetos, C.O. Justice, E.F. Moran, J.F. Mustard, R.R. Rindfuss, D. Skole, B.L. Turner II, and M.A. Cochrane (editors). Dordrecht, Netherlands, Kluwer Adademic Publishers, 139–161, 2004.

McMichael, C. E., A. S. Hope, D. A. Stow, and J. B. Fleming, The relation between active layer depth and a spectral vegetation index in arctic tundra landscapes of the North Slope of Alaska, *Int. J. Remote Sens.*, 18, 2371–2382, 1997.

Mollard, J. D., Guides for the interpretation of muskeg and permafrost conditions from aerial photographs, *Oilweek*, 23 July, Calgary, Alberta, 1960.

Mollard, J. D., *Landforms and Surface Materials of Canada: A Stereoscopic Airphoto Atlas and Glossary*, J. D. Mollard and Associates Limited, Regina, Saskatchewan, 1986.

Mollard, J. D., and J. R. Janes, Permafrost terrain and peatland features, In *Airphoto Interpretation and the Canadian Landscape*, Department of Energy Mines and Resources Canada, Ottawa, 117–136, 1984.

Morrissey, L. A., The utility of remotely sensed data for permafrost studies, *Proc. of the Fourth International Permafrost Conference*, National Academy Press: Washington, 45–63, 1983.

Morrissey, L. A., L. L. Strong, and D. H. Card, Mapping permafrost in the boreal forest with Thematic Mapper satellite data, *Photogramm. Eng. Remote Sens.*, 52, 1513–1520, 1986.

Murton, J. B., and H. M. French, Thaw modification of frost-fissure wedges, Richards Island, Pleistocene Mackenzie Delta, Western Arctic Canada, *J. Quatern. Sci.*, 8, 185–196, 1993.

Oelke, C. and T. Zhang, A model study of circum-Arctic soil temperature, *Permafrost Periglacial Process.*, 15, 103–122, 2004.

Oelke, C., T. Zhang, M. C. Serreze, and R. L. Armstrong, Regional-scale modeling of soil freeze/thaw over the Arctic drainage basin, *J. Geophys. Res.*, 108(D10), 4314, doi:10.1029/2002JD002722, 2003.

Peddle, D. R. and S. E. Franklin, Classification of permafrost active layer depth from remotely sensed and topographic evidence, *Remote Sens. Environ.*, 44, 67–80, 1993.

Peddle, D. R., G. M. Foody, A. Zhang, S. E. Franklin, and E. F. LeDrew, Multi-source image classification II: An empirical comparison of evidential reasoning and neural network approaches, *Can. J. Remote Sens.*, 20, 396–406, 1994.

Prigent, C., F. Aires, and W. B. Rossow, Land surface skin temperatures from a combined analysis of microwave and infrared satellite observations for an all-weather evaluation of the dif-

ferences between air and skin temperatures, *J. Geophys. Res.*, *108*(D10), 4310, doi:10.1029/2002JD002301, 2003.

Prowse, T. D. and C. S. L. Ommanney, *Northern Hydrology: Canadian Perspectives.* NHRI Science Report No.1, Environment Canada, 308 p., 1990.

Rignot, E. and J. B. Way, Monitoring freeze-thaw cycles along north-south Alaskan transects using ERS-1 SAR, *Remote Sens. Environ.*, *49*, 131–137, 1994.

Rouse, W. R. and 10 others, Effects of climate change on the freshwaters of Arctic and Subarctic North America, *Hydrol. Process.*, *11*, 873–902, 1997.

Running, S. W., J. B. Way, K. C. McDonald, J. S. Kimball, S. Frolking, A. R. Keyser, and R. Zimmerman, Radar remote sensing proposed for monitoring freeze-thaw transitions in boreal regions, *EOS, Trans., American Geophys. Union, 80*, 213, 1999.

Sazonova, T. S. and V. E. Romanovsky, A model for regional-scale estimation of temporal and spatial variability of active layer thickness and mean annual ground temperatures, *Permafrost Periglacial Process., 14,* 125–139, 2003.

Schreier, H. and C. Selby, Predicting permafrost conditions with infrared sensing techniques, *Proc. of the Seventh Canadian Symposium on Remote Sensing,* 323–331, 1981.

Shiklomanov, N. I. and F. E. Nelson, Active-layer mapping at regional scales:a 13-year spatial time series for the Kuparuk region, north-central Alaska, *Permafrost Periglacial Process., 13,* 219–230, 2002.

Siebert, N. M. and J. S. Kargel, Small-scale Martian polygonal terrain: implications for liquid surface water, *Geophys. Res. Lett., 28,* 899–902, 2001.

Smith, L. C., Y. Sheng, G. M. MacDonald, and L. D. Hinzman, Disappearing Arctic lakes, *Science, 308,* 1429, 2005.

Smith, M. W., Microclimate influences on ground temperatures and permafrost distribution, Mackenzie Delta, Northwest Territories, *Can. J. Earth Sci., 12,* 1421–1438, 1975.

Smith, M. W., Climatic change and permafrost, In *Canada's Cold Environments,* H. M. French and O. Slaymaker (editors), McGill Queen's University Press: Montreal & Kingston, 292–311, 1993.

Smith, N. V., S. S. Saatchi, and J. T. Randerson, Trends in high northern latitude soil freeze and thaw cycles from 1988 to 2002, *J. Geophys. Res., 109,* D12101, doi:10.1029/2003JD004472, 2004.

Stendel, M., and Christensen, J. H., Impact of global warming on permafrost conditionsin a coupled GCM. *Geophys. Res. Lett., 29,* 101–104, 2002.

Stone, R. S., E. G. Dutton, J. M. Harris, and D. Longenecker, Earlier spring snowmelt in northern Alaska as an indicator of climate change, *J. Geophys. Res., 107*(D10), doi:10.1029/2000JD000286, 2002.

Strozzi, T., A. Kääb, and R. Frauenfelder, Detecting and quantifying mountain permafrost creep from *in situ* inventory, spaceborne radar interferometry and airborne digital photogrammetry, *Int. J. Remote Sens., 25,* 2919–2931, 2004.

Tarnocai, C. and J. Thie, Permafrost and remote sensing, *Proc. of the Second Canadian Symposium on Remote Sensing,* Guelph, Ontario, Canadian Remote Sensing Society, Ottawa, Vol. 2, 438–447, 1974.

Toll, D. L., M. Owe, J. Foster, and E. Levine, Monitoring seasonally frozen soils using passive microwave satellite data and simulation modeling, in *Proc. of IGARSS'99, 28 June–2 July 1999, Hamburg, Germany,* 1149–1151, 1999.

Walker, D. A., H. E. Epstein, W. A. Gould, A. Kade, A. M. Kelley, J. A. Knudson, W.B. Krantz, R.A. Peterson, G. Michaelson, R.A. Peterson, C.L. Ping, M.A. Raynolds, V.E. Romanovsky, Y. Shur, and M. D. Walker, Frost-boil ecosystems: complex interactions between landforms, soils, vegetation, and climate, *Permafrost Periglacial Process., 15,* 171–188, 2004.

Wang, Z. and S. Li, Detection of winter frost heaving of the active layer of Arctic permafrost using SAR differential interferograms, *Proc. IEEE 1999 International Geoscience and Remote Sensing Symposium,* 3 pp., 1999.

Washburn, A. L., *Periglacial Processes and Environments.* Edward Arnold Publishers: London, 1973.

Way, J. B. and 15 others, The effect of changing environmental conditions on microwave signatures of forest ecosystems: Preliminary results of the March 1988 Alaskan Aircraft SAR experiment, *Int. J. Remote Sens., 11,* 1119–1144, 1990.

Way, J. B., E. Rignot, K. C. McDonald, R. Oren, R. Kwok, G. Bonan, M. C. Dobson, L. Viereck, J. F. Roth, Evaluating the type and state of Alaska taiga forests with imaging radar for use in ecosystem flux models, *IEEE Trans. Geosci.Remote Sens., 32,* 353–370, 1994.

Wegmüller, U., The effect of freezing and thawing on the microwave signatures of bare soil, *Remote Sens. Environ., 33,* 123–135, 1990.

Williams, P. J. and M. W. Smith, *The Frozen Earth: Fundamentals of Geocryology,* Cambridge University Press: New York, 1989.

Williams, D. J., and C. R. Burn, Surficial characteristics associated with the occurrence of permafrost near Mayo, Central Yukon Territory, Canada, *Permafrost Periglacial Process., 7,* 193–206, 1996.

Wismann, V., Monitoring of seasonal thawing in Siberia with ERS scatterometer data, *IEEE Trans Geosci. Remote Sens., 38,* 1804–1809, 2000.

Yoshikawa, K. and L. D. Hinzman, Shrinking thermokarst ponds and groundwater dynamics in discontinuous permafrost near Council, Alaska, *Permafrost Periglacial Process., 14,* 151–160, 2003.

Zhang, T. and R. L. Armstrong, Soil freeze/thaw cycles over snow-free land detected by passive microwave remote sensing, *Geophys. Res. Let., 28,* 763–766, 2001.

Zhang, T., R. L. Armstrong, and J. Smith, Investigation of the near-surface soil freeze-thaw cycle in the contiguous United States: Algorithm development and validation, *J. Geophys. Res., 108*(D22), 8860, doi:10.1029/2003JD003530, 2003b.

Zhang, T., R. G. Barry, and R. L. Armstrong, Application of satellite remote sensing techniques to frozen ground studies, *Polar Geogr., 28,* 2004.

Zhang, T., R. G. Barry, K. Knowles, J.A. Heginbottom, and J. Brown, Statistics and characteristics of permafrost and ground ice distribution in the Northern Hemisphere, *Polar Geogr., 23*, 132–154, 1999.

Zhang, T., R. G. Barry, K. Knowles, F. Ling, and R. L. Armstrong, Distribution of seasonally and perennially frozen ground in the Northern Hemisphere, in M. Phillips, S. M. Springman, and L. U. Arenson, eds., *Proceedings of the 8th International Conference on Permafrost*, July 21–25, 2003, Zurich, Switzerland, Rotterdam, Netherlands: A.A. Balkema Publishers, Vol. 2, 1289–1294, 2003a.

Zhang, T., T. E. Osterkamp, and K. Stamnes, Effects of climate on the active layer and permafrost on the North Slope of Alaska, *Permafrost Periglacial Process., 8*, 45–67, 1997.

Zuerndorfer, B. W. and A. W. England, Radiobrightness of decision criteria for freeze/thaw boundaries, freezing terrain, *IEEE Trans. Geosci. Remote Sens., 30*, 89–101, 1992.

C. R. Duguay and V.E. Romanovsky, Geophysical Institute, University of Alaska Fairbanks, 903 Koyukuk Drive, P.O. Box 757320, Fairbanks, Alaska 99775-7320, USA. (claude.duguay@gi.alaska.edu)

D. W. Leverington, Department of Geosciences, Texas Tech University, Box 41053, Lubbock, Texas 79409-1053, USA. (david.leverington@ttu.edu)

T. Zhang, NSIDC/CIRES, University of Colorado, Boulder, Colorado 80309-0449, USA. (tzhang@nsidc.org)

Remote Sensing of Surface Water and Soil Moisture

Alain Pietroniro and Jessika Töyrä

National Water Research Institute, Saskatoon, Saskatchewan, Canada

Robert Leconte

Département de génie de la construction, École de technologie supérieure, Montréal, Québec, Canada

Geoff Kite

International Water Management Institute, Colombo, Sri Lanka

Historically, there has been a strong research effort to apply remote sensing techniques to hydrological understanding. Northern environments are particularly well-suited to remote sensing applications because of the lack of systematic and comprehensive coverage in many cold regions. Heterogeneity in the landscape has forced hydrologists to conceptualize the physics and to seek effective parameterizations to describe various hydrological processes in northern environments. General algorithms that deal with wetlands, permafrost and organic soils are difficult to resolve because of the difficulty of dealing with multiple scales. Therefore, the hydrologist typically uses simple objective functions to describe complex terrains. Remote sensing approaches offer unique opportunities to assess the complexities of the hydrological phenomenon with repeatable spaceborne or airborne measurements. This chapter examines two very important liquid-phase storage features on the landscape, namely, surface water bodies and soil moisture. Theoretical considerations for the detection of surface water and soil moisture, along with examples of experiments and applications in northern environments, are presented.

1. INTRODUCTION

The land surface presents northern hydrologists with a litany of storage features, including snow, permafrost, ice, and liquid water. This chapter examines two very important liquid-phase storage features on the landscape, namely, surface water bodies and soil moisture. Naturally, these features are detectable only during prolonged warming periods and perhaps represent a limited temporal window

in which they can be detected. Surface water, including wetlands and soil moisture, provides important storage components on the landscape that can have dramatic effects on the hydrological response of a particular region. Also, as noted by *Bowling et al.* [2003], the arctic land-surface water balance plays an important role in regulating the heat balance within Northern environments. Therefore, understanding the water cycle within the northern environments has important implications for the planetary heat and water balance. This chapter describes theoretical considerations for the detection of surface water and soil moisture and provides examples wherever possible of experiments and applications in northern environments.

2. SURFACE WATER

The extent, level, and volume of water bodies are important parameters for assessing the state of lakes, reservoirs, or wetlands. This type of information is critical in assessing water management strategies as well as observing changes in hydrologic and ecological regimes. Surface water detection is of particular importance in northern latitudes due to the lack of in situ measurements. Certainly, the potential impacts of climate change are best monitored through time-series assessments of surface water boundaries for areas that are predicted to change most dramatically.

This section looks at the issue of detecting surface water extent in northern regions with remote sensing. Although a more complete review would look at all aspects of surface water, including aquatic vegetation, sedimentation, and geomorphology, this endeavor would fill a textbook all by itself. The focus here is limited to detecting and delineating surface water boundaries and extrapolation to volume estimates. This is likely the most straightforward of all remote-sensing applications, yet it is still often fraught with problems for proper delineation and interpretation of these water bodies.

There are many excellent previously published overviews written on this topic. These citations are not necessarily focused on northern regimes but still provide excellent descriptions of the electromagnetic interactions with surface water. *Lewis* [1998] provides an excellent overview of microwave sensing of surface waters, while *Hess et al.* [1990] examine the use of microwave remote sensing in flooded vegetation. Other interesting articles focusing on remote sensing of surface waters can be found in *Kite and Pietroniro* [2000], *Engman and Gurney* [1991], and *Smith* [1997b]. An overview of recent remote sensing research in Canada focusing on surface waters and other aspects of the hydrological cycle can be found in *Pietroniro and Leconte* [2005].

2.1. General Approaches

Remote sensing of surface water can be achieved based on three different sources of electromagnetic energy: energy transmitted from a manmade source (active microwave), energy from the sun (visible and infrared), and energy emitted from the Earth (thermal infrared and passive microwave). The resolution for spaceborne visible infrared and active microwave systems is generally around 25 m, and typically in the 5–50 km range for passive microwave sensors. This section will focus mainly on the visible and infrared and active microwave mapping, the sensors most often used for surface water detection and mapping because of their high spatial resolution.

2.1.1. Remote sensing of open water surfaces. Water absorbs most of the incident electromagnetic energy in the near infrared (0.7–1.3 μm) and middle infrared (1.3–3.0 μm) wavelengths; energy in the visible (0.4–0.7 μm) wavelengths is primarily transmitted, but also is absorbed and reflected in small amounts [*Curran*, 1985]. Therefore, the reflectance of water is very low in the near and middle infrared wavelengths and moderate to low in the visible wavelengths (Figure 1). The reflectance may increase if the incident energy is scattered or reflected by a rough water surface, bottom sediments in shallow water, or high concentrations of suspended materials [*Hoffer*, 1978; *Curran*, 1985; *Kuittinen*, 1992]. Vegetation and soil, on the other hand, have low to intermediate reflectance in visible light. The infrared wavebands are scattered by leaves, resulting in high reflectance by vegetation [*Szekielda*, 1988]. The middle infrared energy is absorbed by water in the vegetation and the soil [*Szekielda*, 1988], and the amount of reflected energy is dependent upon the water content. Thus, on grayscale infrared images or on multispectral scanner images in the infrared portion of the spectrum, water bodies appear dark and stand out in stark contrast to surrounding vegetative and soil features [*Swain and Davis*, 1978]. The use of visible and infrared imagery to map open water bodies is relatively straightforward and has been applied since the 1970s [*Deutsch and Ruggles*, 1974; *Rango and Salomonson*, 1974; *Wiesnet et al.*, 1974]. The major drawback is the nonselective scattering of visible and infrared wavelengths by clouds or dense smoke. Therefore, monitoring using visible and infrared radiation must take place during clear sky conditions.

Thermal infrared sensing (10.0–12.5 μm) of water surfaces exploits the high thermal inertia of water compared to land, which results in a large radiant temperature difference between the two surface types around midday.
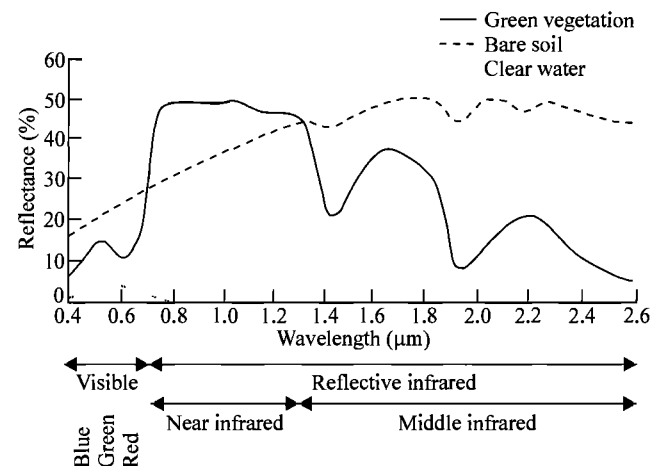
Figure 1. Reflectance vs. wavelength for soil, vegetation, and water [after *Hoffer*, 1978].

Table 1. Microwave Bands Used in Remote Sensing [after *Sabins*, 1997].

Band	Frequency (GHz)	Wavelength (cm)
P	0.3–1.0	100.0–30.0
L	1.0–2.0	30.0–15.0
S	2.0–4.0	15.0–7.5
C	4.0–8.0	7.5–3.8
X	8.0–12.5	3.8–2.4
K	12.5–40.0	2.4–0.8

Radar sensors operate in the microwave spectrum at wavelengths between 0.8 and 100.0 cm, which corresponds to frequencies between 0.3 and 40.0 GHz. The microwave bands commonly used in remote sensing are listed in Table 1. Microwave sensors are responsive to changes in moisture content and have the distinct advantage of nearly all-weather viewing. A wet and unfrozen ground target results in a very strong radar return signal because of the high dielectric constant of water. The resulting backscatter is also influenced by local roughness of the ground target. Although the presence of water enhances the radar signal, a smooth water surface, such as on a calm lake, acts as a specular reflector of microwaves and the energy is reflected away from the sensor, resulting in a very low backscatter signal. Most other natural targets, such as vegetation canopies, are inhomogeneous and the microwave energy is scattered diffusely. A portion of the energy is scattered back to the sensor, generating an intermediate backscatter signal for most natural land surfaces. Active sensors such as the ERS (European Remote Sensing Satellite)-1 and -2, JERS-1 (Japanese Earth Resources Satellite) and Radarsat have all shown potential for estimating open water boundaries because of the contrast between the water and land [*Yamagata and Yasuoka*, 1993; *Hall*, 1996; *Crevier and Pultz*, 1997].

Water targets, however, can induce Bragg resonance effects in the radar image due to surface wave action. These surface waves generate a backscatter response, thereby increasing the backscatter values of the water target. The resonance effect can cause confusion between land and open water, and in some cases, the increased backscatter of open water can make the coastline obscure [*Dean and Morrissey*, 1988]. In general, X- and C-band radar are sensitive to centimeter surface waves, while L-band radar is sensitive to decimeter surface wave heights. The vertically polarized transmit-and-receive signal (VV) is more susceptible to surface waves than is a horizontally polarized transmit-and-receive signal (HH) at the same frequency [*Ulaby et al.*, 1986]. The use of larger incidence angles for mapping open water surfaces is also recommended, because smaller angles are more sensitive to the Bragg resonance effects. This was clearly shown by *Barber et al.* [1996] for flood delineation along the Assiniboine River, Manitoba, Canada. They concluded that C-HH data acquired at large incidence angles (greater than 45°) maximized their ability to detect flooded areas through specular reflection of the incident wave. *Töyrä et al.* [2001] also found that Radarsat imagery acquired at an incidence angle of 47° could differentiate between open water and land, whereas Radarsat imagery acquired at 23.5° experienced increased backscatter of open water due to surface waves, which resulted in confusion between the two classes.
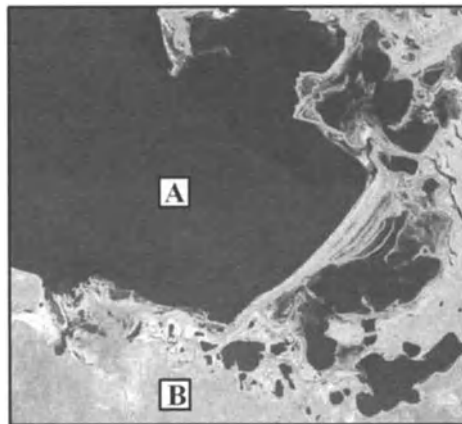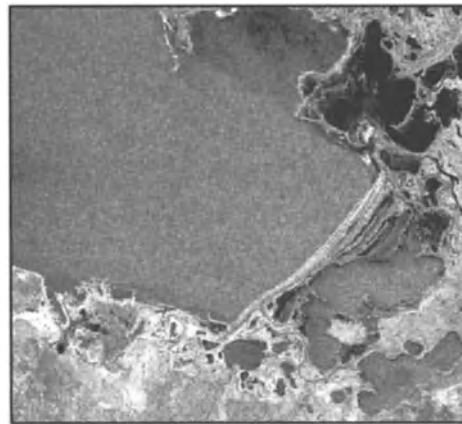
Radarsat S7   Radarsat S1

Figure 2. Subsets of a 47° incidence angle (Radarsat, Standard Beam S7) and a 23.5° incidence angle (Radarsat, Standard Beam S1) image of a northern lake. The size of the image subsets is approximately 20 × 20 km. The two images were taken 1 day apart under similar conditions. In the Radarsat S7 image, the lakes (A) stand out as very dark areas compared with the surrounding land (B), whereas the difference in backscatter between water and land is much less in the Radarsat S1 image.

Figure 2 illustrates the difference in lake surface backscatter between high and low incidence angle Radarsat images.

A disadvantage to using large incidence angles to reduce the Bragg effect in mountainous terrain is that the likelihood of radar shadows increases. The radar shadows appear as dark areas in the imagery and are, therefore, often mistaken for open water surfaces [Bryan et al., 1977; Bryan, 1979]. Lewis [1998] pointed out that the confusion between radar shadows and open water can be overcome by imaging from two perpendicular look directions, where open water will be consistently dark regions in both images.

Passive microwave sensors operate on the same principle as thermal infrared sensing, and they discriminate between water and land based on the differences in emissivity between the two surface types in the microwave region [Ulaby, 1977; Schmugge, 1980]. However, as with all sensors, there are practical limitations that limit their use, the main one being the low resolution.

2.1.2. Remote sensing of flooded areas and wetlands.

In northern environments, flooding events are unlikely to inundate large population centers and extensive agricultural areas; rather, they affect vegetated flood plains and sometimes smaller communities. The flood boundaries are often obscured by vegetation, which makes it difficult to separate inundated areas from dry land. The same is true for monitoring the surface water extent in vegetation-laden wetlands. Plate 1 shows a 10 × 10 km subset of a Landsat TM image taken during midsummer conditions. It illustrates the inability of the Landsat image to detect standing water through the thick vegetation cover. Carter [1982] suggested

that the extent of flooding can be most efficiently detected on visible and infrared imagery when vegetation is absent or during the dormant, leafless season in forested wetlands and flood plains. As the vegetation becomes foliated, tree canopies obscure the inundated areas, and most flood boundaries become difficult to distinguish. On the other hand, the vegetation cover, composition, and condition can be used as indicators of the presence of water beneath the canopy. Some studies have suggested that the Landsat TM middle infrared bands would be more appropriate than the near infrared band for detecting inundated areas [Work and Gilmer, 1976; Bennett, 1987].

In contrast to the short wavelengths of visible and infrared energy, the longer microwave wavelengths have the capability to penetrate vegetation. Since the launch of the Seasat satellite in 1978, many studies have tested the ability of L-band radar to map flooded vegetation. Studies using L-band spaceborne or airborne radar sensors have illustrated that the backscatter from various forest stands is enhanced when there is standing water beneath the canopy [MacDonald et al., 1980; Waite et al., 1981; Place, 1984; Ormsby et al., 1985; Harris and Digby-Argus, 1986; Richards et al., 1987a,b]. According to Richards et al. [1987a,b] and Wang et al. [1995], four components should be included when developing a backscatter model for wetland forests using L-band microwave sensing. These components, illustrated in Figure 3, are not limited to the longer L-band frequency. They include (1) diffuse scattering from the forest floor, (2) volume scattering from the canopy, (3) scattering from the canopy to the forest floor and specular reflectance back to the sensor, and (4) scattering from the trunk to the for-
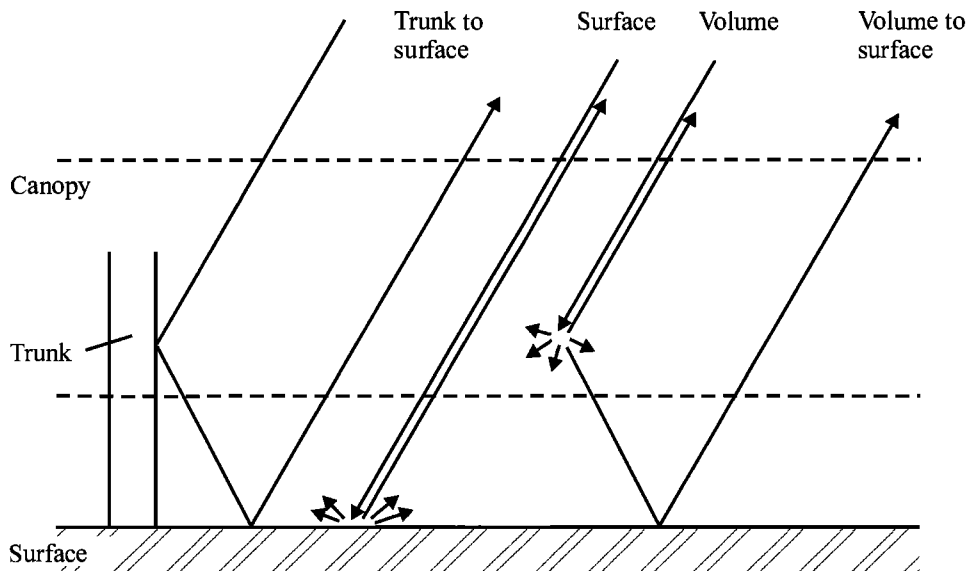
Figure 3. Four components of backscatter from a forest stand [after Richards et al., 1987a, ©IEEE].

est floor and specular reflectance to the sensor. *Wang et al.* [1995] suggested that the total backscatter for a nonflooded forest stand is dominated by surface scattering by the forest floor and volume scattering in the canopy. *Wang et al.* [1995] also pointed out that it is the corner reflection between the tree trunks and the ground, amplified by the high dielectric constant of the standing water, that causes the high returns of flooded forest stands. This phenomenon is limited to wavelength that will penetrate the vegetation canopy. The longer L-band wavelengths can generally penetrate thicker vegetation than the C-band microwaves because the shorter wavelengths are scattered by smaller features. However, as Plate 1 and Figure 4 illustrate, C-band microwaves also can produce enhanced backscatter due to corner reflection in flooded vegetated areas when the radar signal is able to penetrate the canopy.

Wedler and Kessler [1981], *Harris and Digby-Argus* [1986], and *Crevier and Pultz* [1997] demonstrated that like-polarised scenes are better for forest flood mapping than cross-polarised scenes are. In addition, *Hess et al.* [1995] and *Crevier and Pultz* [1997] showed that the contrast between flooded and nonflooded forests is higher for HH-polarised scenes compared with VV-polarized scenes. *Crevier and Pultz* [1997] suggested that canopy volume scattering is the dominating scattering component at HV and VV polarization as opposed to the trunk–surface component.

An increase in incidence angle lengthens the path the radar signal has to travel through the canopy layer, which means that the canopy attenuation on the radar signal also increases. *Crevier and Pultz* [1997], *Adam et al.* [1998], *Sokol et al.* [2000], and *Töyrä et al.* [2001] found that HH-polarized C-band images acquired at smaller incidence angles have a greater enhancement in flooded forest stands than those acquired at larger angles. *Sokol et al.* [2000] recorded a 7-dB decrease in backscatter values of northern bogs and fens when the incidence angle was changed from 20° to 49°. *Ford and Casey* [1988] and *Wang and Imhoff* [1993] noted the same trends using L-band radar. On the other hand, *Ormsby et al.* [1985] and *Imhoff et al.* [1986] concluded that the incidence angle has no effect on the enhancement of the signal in L-band frequencies. One possible explanation is that the incidence angle does not have as much influence on longer wavelengths in low-density stands where the canopy attenuation is less substantial.

2.2. Applications in Northern Environments

2.2.1. Visible infrared (VIR) sensors. Many studies have utilized visible and infrared imagery to map and monitor surface water bodies in northern environments. For example, *Brook* [1983] used Landsat MSS imagery to obtain a flood record of the Nahanni karst in northern Canada. The Nahanni karst is one of the most complex subarctic karst landscapes and the valuable hydrologic data could not have been obtained by any other source [*Brook*, 1983]. *Mouchot et al.* [1991] used the middle infrared Landsat Thematic Mapper (TM) channel to map the extent of the water bodies in the Mackenzie Delta, in Arctic Canada. The Mackenzie Delta has an area of 12,000 km^2 and contains a complex interconnected network of many thousands of lakes, ponds, channels, and waterways [*Mouchot et al.*, 1991; *Roberts et al.*, 1995]. The area is particularly well suited to remote sensing appli-
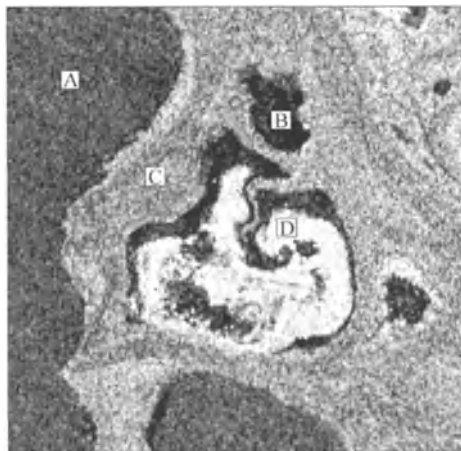
| Original unfiltered Radarsat S2 | Average filter (5 x 5) applied to Radarsat S2 |
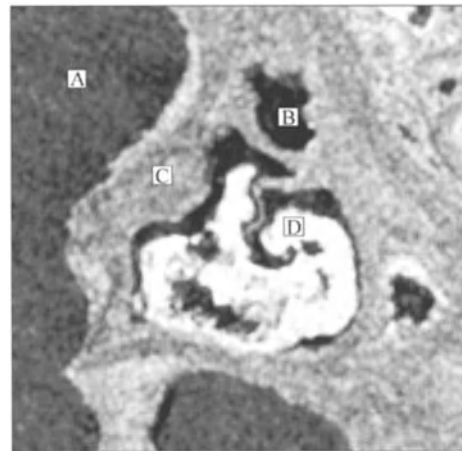
Figure 4. An unfiltered and filtered Radarsat S2 (standard beam, 27.5° incidence angle) image subset of a wetland basin in the Peace–Athabasca Delta, Canada. The image subset illustrates C-band backscatter over (A) open water with waves; (B) open water with no waves; (C) dry land covered by grasses, sedges, and willows; and (D) standing water beneath willows (no leaves).

cations because of its remoteness, size, and lack of accessibility. After using a gray-level threshold to separate water from land, *Mouchot et al.* [1991] applied a mathematical morphological algorithm to ensure that the narrow streams were included in the water class. This allowed them to identify all water bodies that were connected to the drainage network and divide them into levels of connectedness based on the width of the connecting channel. In the same delta, *Roberts et al.* [1995] used a sequence of airborne multispectral video (MSV) imagery to provide data for understanding the frequency, timing, and duration of flooding events during an 18-day period of annual ice breakup. Because floodwater contains higher suspended sediment content (SSC) than the local water in the lakes does, the time of flooding could be determined for 3,216 lakes by estimating the SSC of each lake from the sequential MSV imagery. In a similar fashion, *Mertes* [1997] applied a spectral mixture analysis procedure to a SPOT image to estimate the SSC of the floodplain wetlands between the Ob' and Irtysh Rivers in Siberia. *Mertes* [1997] concluded that the wetlands were only partially inundated with river floodwater and that the SSC of the floodwater was comparable to that of the Ob' River.

The Peace–Athabasca Delta in northern Alberta, Canada, is one of the largest freshwater deltas in the world; much like many northern wetlands and deltas, this dynamic ecosystem is affected by seasonal, annual, and longer-term changes in water levels and extents that are rarely documented. *Pietroniro et al.* [1999] used a time series of Landsat MSS bands 4–7, Landsat TM bands 1–7 and SPOT panchromatic data to document changes in areal water extent over a 15-year period. In their study, the satellite images were classified as water/no water by using a parallelepiped scheme with training areas of known water bodies. The time-series of images highlighted the extent of surface water change that occurred in this ecologically sensitive region during a significant drying trend. To define hydrologically connected areas, *Pietroniro et al.* [1999] applied an algorithm to find all pixels satisfying a four-point connectivity. The images were converted to vector polygons and overlaid on the original scenes. The vectors could then be compared with existing lake level estimates and a simple relationship between lake areal extent and lake level was determined. Both these applications provided vital hydrologic information that was otherwise unavailable for this remote site.

Remote sensing has also been used for estimating extents of very large water bodies. In a study of the Great Lakes of the Mackenzie River Basin (i.e., Great Bear Lake, Great Slave Lake, and Lake Athabasca), *Birkett and Kite* [1997] used NOAA AVHRR images in the visible, near infrared, and thermal infrared bands to estimate surface water extent. Lake extent measurements can be troublesome since the Mackenzie lakes are often cloud-covered; for example, during the month of August 1994, only 6 images of 50 were cloud-free. Errors in measured areas were determined to be unacceptable within the order of 3–4% when compared with ground measurements.

Relationships between water depth and some other measurable parameter can be used to convert remotely sensed lake areas into lake volumes [*Pietroniro et al.*, 1999]. This was done in the Peace–Athabasca Delta, where detailed survey information was obtained for a small isolated ephemeral basin representative of the myriad of small-perched lakes in the region [*Pietroniro et al.*, 1999]. Areal extent measurements, coupled with area–depth and area–volume relationships derived from field surveys, provided a surrogate water balance estimate and confirmation of a water balance model for the basin. Analysis of the perched basins showed that, even with the relatively coarse resolution of Landsat images, satellite remote sensing of water conditions is a viable technique, when changes in surface water extent are readily detected. The strong spatial correlation between flooded areas (defined by image classification) and a digital elevation model showed that remote sensing could be used in ecological studies of changes to the aquatic and riparian regimes of these basins. This is particularly true of basins in which small changes in depth produce large changes in perimeter and areal extent.

Visible and infrared remote sensing techniques have also been used for direct estimations of lake depth. *Duguay and Lafleur* [2003] used Landsat summertime imagery to estimate lake depth and winter ice depth for small sub-arctic lakes. They established a relationship between summertime TM-2 radiances and observed lake depth to generate a lake bathymetry map in the region. This relationship proved adequate for lakes that were up to about 3 m in depth; however, lakes with large concentrations of dissolved organic carbon (DOC) were problematic.

Melloh et al. [1999] evaluated different Landsat TM band combinations and transformations (tasseled-cap, principal component, and NDVI) for discriminating wetlands from upland in both coastal and interior Alaska. The different combinations were classified by using an unsupervised algorithm, and the generated wetland maps were compared with National Wetland Inventory (NWI) maps. In the coastal area, estuarine marshes could be discriminated, but there were difficulties with palustrine scrub–shrub and forested wetlands on the coastal plain. The coefficient of agreement between the Landsat wetland map and the NWI map was 0.72. *Melloh et al.* [1999] recommended that at least one visible band and the near infrared band be used for best results. In the interior mountainous area, a composite of the thermal, the near infrared, and the green band was most useful. The

combination resulted in a κ = 0.67. The forested wetlands were often confused with the upland forest.

Töyrä et al. [2001] used SPOT multispectral data acquired in the spring and summer to classify a northern wetland as to open water, flooded vegetation, and nonflooded land. A supervised algorithm was used to classify the imagery, and the classification accuracy was determined on the basis of 300 semirandomly selected pixels that were compared against ground verification data. The overall   was 0.80 for the classified spring image, and 0.67 for the summer image. *Töyrä et al.* [2001] found that the SPOT image could not discriminate between flooded versus dry willows, grasses, or sedges in the summer when the vegetation was fully foliated. There were also problems with separating flooded willows from dry deciduous vegetation.

Vanderbilt et al. [1997] used multispectral, multi-angle, polarized airborne POLDER (POLarization and Directionality of the Earth Reflectance) data to discriminate northern wetland fens from nonwetland vegetation. The image flight lines were flown either toward or away from the solar azimuth direction. *Vanderbilt et al.* [1997] observed that open water has a peak reflectance in the forward scattering direction (specular direction), whereas dry vegetation is characterized by high reflectance in the backscattering direction (hot spot direction). The presence of emergent vegetation in the water increased the reflectance in the backscatter direction, whereas the forward scattering remained high.

2.2.2. Microwave remote sensing. The low resolution of passive microwave sensors limits their use to delineating very large surface features. Therefore, this section will focus on active microwave sensors. However, passive microwave systems have been used in continental-scale studies to retrieve the fraction of water surface within pixels [*Basist et al.*, 1998, 2001; *Fily et al.*, 2003]. For example, *Fily et al.* [2003] showed that the fraction of water surface could be mapped over the Canadian subarctic continental area within a 6 % correspondence to the 1 km² Canadian National Topographic Database of water-covered areas.

Mapping open water bodies using active microwave sensors is relatively straightforward. As mentioned above, the use of large incidence angles and HH polarization is recommended to reduce the Bragg effects caused by wave action. Since ERS synthetic aperture radar (SAR) images are acquired at VV polarization and a steep incidence angle, they are very susceptible to scattering by surface waves. *Smith* [1997a], for example, found that only 8 of 88 temporal ERS-1 and ERS-2 SAR images of the Ob' River in Siberia were acquired in wind conditions that permitted clear distinction between open water and land. *Smith* [1997a] found that by deriving interferometric phase coherence images from ERS-1 and ERS-2 pairs, the open water surfaces could be clearly delineated. This is because the water surfaces are constantly in motion and have low phase coherence compared to the relatively high coherence of the surrounding land.

In addition to waves, the presence of ice on the water surface will often increase the backscatter values for stable lake ice cover. The amount of backscatter produced by freshwater ice is determined by the amount of tubular air bubbles within the ice layer and by whether the ice layer overlies water or frozen bottom sediment [*Weeks et al.*, 1977, 1978; *Leconte and Klassen*, 1991; *Jeffries et al.*, 1994, 1996; *Duguay et al.*, 1999, 2002; and *Duguay and Lafleur*, 2003]. Freshwater ice and frozen sediments have low dielectric constants (3.2 and 8, respectively), whereas water is characterized by a high dielectric constant (80) [*Leconte and Klassen*, 1991]. In cases where the water body is not frozen all the way to the bottom, the microwave energy will penetrate the ice layer and reflect strongly at the ice/water interface. Due to scattering by tubular air bubbles within the ice layer, part of the strong radar signal is reflected back to the sensor. A lower radar backscatter return is produced when shallow lakes and ponds are frozen to the bottom. Since the dielectric contrast between ice and frozen sediment is small, the radar signal will penetrate the frozen soil instead of being reflected at the interface. *Jeffries et al.* [1996] used this information, together with a numerical ice growth model, to determine lake depth and water availability in northwestern Alaska. ERS-1 SAR images were used to identify when and how many lakes froze completely to the bottom. The lake depths were determined by using the numerical ice growth model to calculate the ice thickness when the lakes were frozen completely. Details can be found in *Jeffries et al.* [this volume].

Radar altimeter data from sensors such as Geosat, Seasat, ERS-1, ERS-2, and TOPEX/POSEIDON have also been used to estimate water level changes in lakes. The sensor transmits and receives nadir radar pulses and the elevation is calculated based on the travel time of the pulse and the exact satellite position. *Birkett and Kite* [1997] used the TOPEX/POSEIDON altimeter to derive water levels of three large lakes in northern Canada. Plate 2 illustrates the 1992–1995 observed water levels versus the TOPEX/POSEIDON–derived water levels for one of these lakes. Altimeter estimates proved reliable with a root mean square error of ±4 cm, which can be considered acceptable for some hydraulic analysis. *Birkett and Kite* [1997] noted, however, that the role of lake ice in altimeter level estimates was not clearly understood and that these effects may have induced serious errors in the early spring analysis. The inaccuracies of the winter and spring measurements are clearly shown in Plate 2. A similar approach was used by *Kouraev et al.*

Landsat TM (MIR, NIR, red)   Radarsat S1 (5x5 average filter)
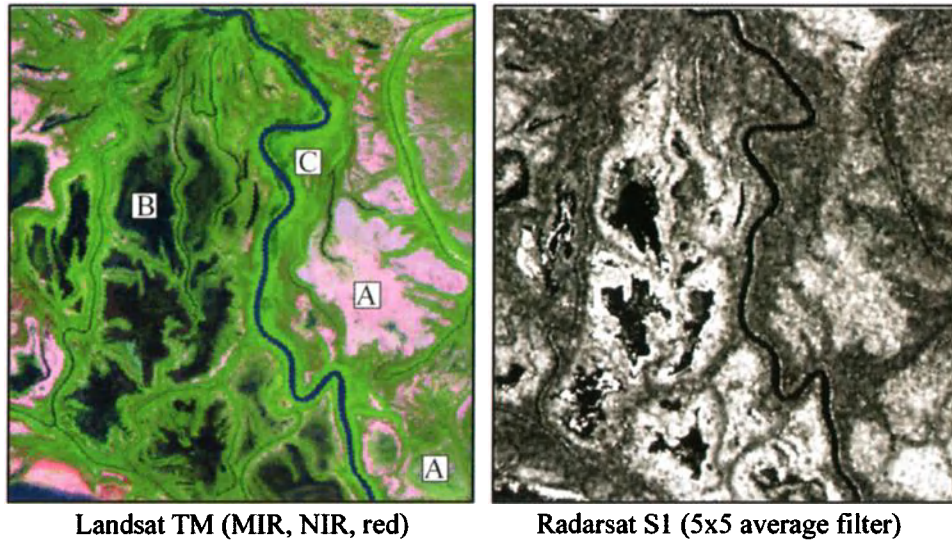
Plate 1. 10 × 10 km Landsat and Radarsat image subsets illustrating the reflectance/backscatter of inundated areas covered by (A) dense vegetation, (B) open water, and (C) dry vegetation. The Landsat TM image did not detect the standing water in the densely vegetated areas (A); however, the higher radar backscatter in the Radarsat S1 image, caused by the double-bounce effect between the water surface and the vegetation, demonstrated that these areas were in fact inundated.

**Observed Lake Level vs Lake Level from TOPEX/Poseidon (NRA and SSALT)
for Great Bear Lake, Oct. 92 - Dec. 95**
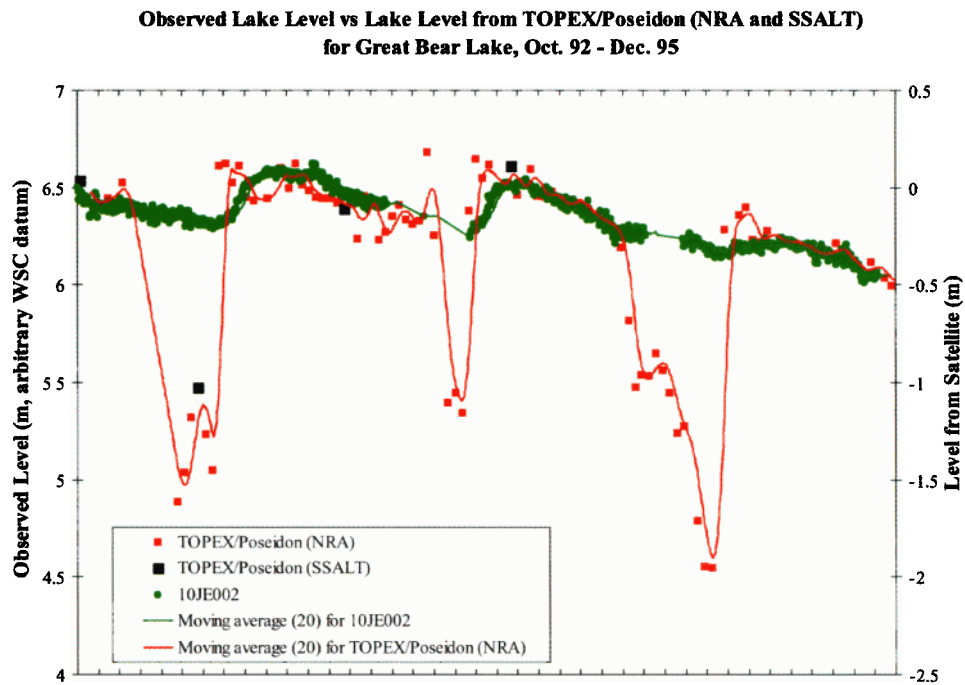
Plate 2. Observed lake elevations, as measured by the Water Survey of Canada (WSC) gauge 10JE002, versus lake levels from TOPEX/POSEIDON for Great Bear Lake in northern Canada over the time period September 1992–December 1995 [from *Birkett and Kite*, 1997; reprinted with permission from Environment Canada Publications].

[2004] to estimate discharge from the Ob' River in Northern Russia. This work is especially compelling given the importance of quantifying terrestrial freshwater fluxes into the Arctic Ocean in order to understand and describe oceanic circulation patterns and the resulting impact on weather circulation patterns. *Kouraev et al.* [2004] note that river discharge measurements in Arctic catchments have been declining since the mid-1980s [*Shiklomanov et al*, 2002] and that remote sensing technology can fill the data void with a reasonable degree of confidence. They argue that TOPEX/ POSEIDON altimetry data could be used successfully to estimate annual discharge to within 8% of in situ estimates. For monthly estimates, the average error increased to 17%, largely due to the lack of altimetry overpasses within the required months. Although this methodology is limited to large rivers with wide channel bottoms (several kilometers), *Kouraev et al.* [2004] point out that with the new generation of altimeters it may be possible to estimate elevation on rivers with widths on the order of hundreds of meters rather than thousands of meters.

Smith et al. [1995, 1996] used a temporal series of ERS-1 imagery to estimate discharge of braided rivers in northern Canada and Alaska. The images were calibrated and a threshold of −10.5 dB was applied to the image to separate river water from the surrounding land. A 3 × 3 bimodal majority filter was applied to remove speckle, and the total water area was calculated within a control section. By dividing the total area by the length of the river in the control section, an effective river width was achieved. *Smith et al.* [1995, 1996] found a power law correlation between the effective width and discharge, such that a width–discharge rating curve could be generated for each river.

Since canopy penetration is reduced at shorter wavelengths, forest flood mapping is best performed by using longer wavelengths [*Richards et al.*, 1987b; *Hess et al.*, 1990; and *Hall*, 1996]. *Hess et al.* [1990] recommended the use of L- or P-band SAR sensors for this purpose. However, *Adam et al.* [1998] showed that C-band imagery from the Radarsat sensor can be used to map the extent of flooding in a northern wetland basin during spring conditions when the vegetation is dormant and no leaves are present. This work identified floodwater distribution by segmenting the images into three distinct classes: open water, flooded willow, and nonflooded areas. Flooded willows were recognized by the characteristic strong backscatter caused by the double bounce of the radar signal between the surface water and the willow stems. Supervised classification results of the original Radarsat images were not acceptable because of the large local variance introduced by speckle. The speckle was minimized with a 7 × 7 Gamma MAP (Maximum A Posteriori) filter, significantly improving the resulting classifications. In the same wetland complex, *Töyrä et al.* [2001] used a combination of Radarsat and multispectral SPOT imagery to map the extent of flooding in both spring and summer conditions. The images were classified into open water, flooded vegetation, and nonflooded land by using a Mahalanobis distance classifier. On their own, the classified Radarsat spring and summer scenes achieved κ values of 0.76 and 0.56, respectively. *Töyrä et al.* found that the Radarsat sensor could generally detect standing water beneath willows, grasses, and sedges, but there were some problems with wind-induced Bragg effect on the lakes and with detecting water beneath very dense willows and thatch layers. In addition, compared with other dry vegetation, some dry deciduous areas generated high radar backscatter and were therefore confused with flooded vegetation. Although a 7 × 7 Kuan speckle filter had been applied to the Radarsat scenes before classification, the remaining speckle was sufficient to give the classified images very noisy appearances. When the Radarsat scenes were classified in combination with the SPOT scenes, increased significantly to 0.92 and 0.83 for spring and summer conditions, respectively. The SPOT images provided complementary information because the visible and infrared bands could easily map open water and the areas of dry deciduous vegetation that were problematic for the Radarsat scenes.

In another study, *Morrissey et al.* [1996] found that differential freezing between wetland and nonwetland areas can be used to separate the two classes. They used multitemporal ERS-1 data to differentiate wetlands from nonwetland areas in the Arctic Coastal Plains of the Alaskan North Slope. Herbaceous sedges and grasses with a few scattered shrubs dominate the vegetation in the area. The authors noted that when the air temperature was well above freezing at the time of the satellite overpass, the wetlands appeared marginally brighter than the surrounding land. When the temperatures dropped near or below freezing shortly before image acquisition, the difference in backscatter between the two classes increased. *Morrissey et al.* [1996] concluded that the high thermal inertia of the standing water caused the wetland areas to freeze more slowly, whereas the nonwetland areas froze rapidly in response to the temperature drop. Since ice has a very low dielectric constant, freezing reduces the backscatter of vegetation and wet soils. In cases where the air temperature was below freezing for an extended time before image acquisition and the wetlands were given enough time to freeze, the backscatter from wetlands and nonwetlands was not separable.

More recently, *Sokol et al.* [2000] studied the radar backscatter of bogs and fens over a summer season in Labrador, northern Atlantic Canada, using multitemporal ERS-2 and Radarsat imagery. They found that the wetland bogs and

fens of the region have similar vegetation structure and could not be separated by using the radar imagery. The plants do not lose their foliage over the year and the growth rate is slow, resulting in little changes in backscatter values over the growing season. Instead, *Sokol et al.* [2000] noted that the greatest variations in backscatter values were caused by different angles of incidence. Similar work is discussed by *Bowling et al.* [2003], who estimated the role of surface storage in the overall water balance of a low-gradient watershed by using a temporal series of Radarsat images. The remote sensing techniques were standard supervised classification techniques for delineating surface water features. The time series, however, provided a unique opportunity to estimate the surface water balance for the Putuligayuk river basin in Alaska over a 1- year period. The authors note that storage in the basin can, in large part, be explained through base-flow drainage and excess evaporation from open water bodies. Changes in the extent of surface water indicated that evaporation from open water accounted for 50% of snowmelt storage between 1999 and 2000 [*Bowling et al.*, 2003].

2.3. Conclusions and Future Directions

Northern environments are characterized by significant distributions of wetlands and open water bodies. Northern boreal shields and tundra regions are often characterized by a myriad of small bodies of surface water, while boreal regions are often characterized by wetland bogs and fens along with transitional forests. Detecting and quantifying these features is extremely important, because these features can exert strong control on the hydrological regime. Open water bodies are easily detected by VIR and microwave remote sensing. Similarly inundated areas can be reasonably delineated provided the vegetation cover allows some penetration of the active microwave signal. Wetland cover is much more difficult to estimate because of the vegetation structure, and investigation into quantifying wetland cover in northern environments remains an important research objective. Time series of water extent can be readily delineated using a combination of microwave and visible infrared satellite imagery. The derived maps could provide useful quantitative estimates of the hydrological conditions in a northern region. Also, altimeter estimates of water level elevation are showing increasing promise for hydrological assessments. Using TOPEX/Poseidon water level estimates for large rivers provides very good estimates of discharge and is an effective complement to conventional methods.

The European Envisat satellite was launched in March 2002 and the onboard C-band Advanced SAR (ASAR) sensor has the added benefit of being able to transmit and receive in multiple polarizations (horizontal or vertical polarizations). Images acquired in multiple polarizations may potentially enhance surface water delineation, possibly by increased separation between wetland and upland vegetation; to date, however, this approach has not been examined. The upcoming launches of the Canadian Radarsat-2 and the Japanese Advanced Land Observing Satellite (ALOS) could provide improved mapping capabilities. Radarsat-2 is being designed to acquire data in multiple polarizations as well as obtain fully polarimetric data (i.e., transmitting and receiving in any polarization). The Phased Array type L-band Synthetic Aperture Radar (PALSAR) sensor onboard the ALOS satellite will also be able to transmit and receive in multiple polarizations, and the longer L-band wavelengths will allow for improved detection of standing water beneath dense canopies because of the increased capability of this band to penetrate vegetation. In addition to the PALSAR sensor, the ALOS satellite will be equipped with a Panchromatic Remote sensing Instrument for Stereo Mapping (PRISM). The PRISM could potentially be useful for generating digital elevation models and estimating lake elevations. The already operational IKONOS and Quickbird satellites may also prove to be beneficial in mapping water extent in higher detail, given their very high spatial resolution (2–4 m for multispectral data), but their usefulness in northern environments has yet to be fully exploited.

3. SOIL MOISTURE

Estimating the amount of water stored in a soil profile is essential for most water management projects and for assessing the hydrologic state of a basin. Soil moisture is a dynamic quantity, changing rapidly with distance and in time. Implementation of appropriate techniques for water management and of conservation practices requires quantitative assessment of the soil water status. In many cases, particularly watershed scale monitoring or modeling, soil moisture is inferred from more easily obtainable hydrologic variables such as rainfall, runoff, and temperature. More recently, amelioration of atmospheric models has led to the use of sophisticated land surface schemes to better represent interactions with the atmosphere. Such modeling schemes have highlighted the need for better soil moisture representations on a global or regional scale. Conventional in situ measurements of soil moisture are costly and provide information at only a few selected points. However, soil moisture networks are rarely found in highly populated temperate zones and are rarely if ever implemented in high latitude areas. Despite this lack of measurement, the soil moisture component in most hydrologic and atmospheric models is the

most important intermediary component within the water balance equation. As noted by *Engman* [1990], soil moisture is a system state that must be initiated and recomputed if precipitation is added or if decreased by drainage and evapotranspiration. *Engman* [1990] also notes that in most models, the representation of soil moisture is simply a step to make the model work and is not a physical representation of true soil moisture. In fact, soil moisture is ubiquitous by its very nature, since correlation lengths are often on the order of 100–300 m [*Bardossy and Lehmann*, 1998] and are highly dependent on soil conductivity and texture—two parameters that are highly variable in space. Nonetheless, to obtain spatial and temporal estimates of soil moisture on a watershed, regional, or continental scale, nontraditional approaches to this mapping must be used. Remote sensing techniques are seen as the most promising approach, particularly at northern latitudes, where there is already a lack of sufficient traditional data sources.

Moisture in the upper 10-cm layer of the soil profile is the typical variable considered in soil moisture remote sensing applications or algorithm development. This layer is an important component of the total water balance of the Earth–atmosphere system and is a vital state variable in any hydrological or atmospheric land surface model. In model applications, the soil layer usually considered is that which can interact with the atmosphere through evapotranspiration. The depth of this layer depends on the type and stage of maturity of the plant cover but is typically 1–2 m.

3.1. General Approaches

Remote sensing has the advantage of providing an overall picture of a particular region or basin. However, the signal received from a remote sensing platform is usually the result of a mixture of land cover and topographic and atmospheric effects. Reasonable knowledge of electromagnetic energy interaction within the biosphere and the atmosphere is required to separate these components. The soil moisture models developed over the last two decades are usually divided into four main groups, categorized by the specific band width of the electromagnetic spectrum the model is concerned with. These four groups are divided by the following wavelength regions: the reflected visible and infrared, the thermal infrared, active microwave, and passive microwave. A summary of the property observed, advantages, disadvantages and sources of error for each group—modified from *Colwell* [1983] and *Engman and Gurney* [1991]—is given in Table 2.

Soil moisture measurements by remote sensing are limited to the 0–10-cm surface layer, since this is generally the maximum penetration depth of the sensors. The penetration depth is limited by wavelength and soil moisture. The penetration depth increases with longer wavelengths and lower soil moisture. The shorter visible and infrared wavelengths are reflected by the surface and do not penetrate the soil, whereas the microwaves are longer and can penetrate the soil up to 10 cm. The penetration depth is reduced as the soil moisture increases. However, if the water in the soil

Table 2. Summary of Remote Sensing Techniques for Soil Moisture (adapted from *Colwell* [1983] and *Engman and Gurne* [1991]).

Wavelength	Property	Advantages	Disadvantages	Sources of error
Reflected visible and infrared (0.3–3.0 μm)	Reflectance	High resolution	Cloud cover limitations No direct relationship between reflection and soil moisture	Vegetative cover Surface roughness Atmosphere
Thermal infrared (10–12 μm)	Temperature	High resolution Large swath Soil texture insignificant	Bare soil only Cloud cover limitation	Vegetation Topography Atmosphere
Active microwave (1–100 cm)	Backscatter coefficient	All-weather High resolution Vegetation penetration	Noisy data stream Complex interaction with surface	Roughness Vegetation Topography
Passive microwave (1–100 cm)	Microwave emission (brightness temperature)	Nearly all-weather Large area coverage Vegetation penetration	Poor spatial resolution	Surface roughness Soil temperature Vegetative cover Atmosphere

freezes, the dielectric constant is reduced and the microwaves can penetrate deeper.

3.1.1. The optical, thermal, and dielectric properties of soil.

The interaction between shortwave radiation and soil surface plays an important role in the soil-forming process and the heat balance of the soil. Hence it has been long studied by soil scientists before the widespread application and experimentation of remote sensing. Spectral and thermal soil properties, as influenced by texture and moisture, have been examined since the mid-1950s [see *Mulders*, 1987]. In general, the albedo of soil increases with increasing wavelength between 0.4 and 0.8 μm wavelengths. The slope of the albedo curve between these wavelengths is shallower for high organic soils, an albedo of about 20% being recorded for silty clay loam containing 10% organic matter, compared with an albedo of about 40% for a clay loam containing 1.6% organic matter [*Mulders*, 1987, after *Obukhov and Orlov*, 1964]. The five characteristics of soil that will determine the albedo are as follows: moisture content, organic matter, texture, structure, and iron oxide content [*Curran*, 1985]—soil moisture being the dominant factor. In the visible wavelengths, the presence of soil moisture reduces the albedo considerably. As an example, the albedo of a silt loam soil can decrease from 60% at 0.8% moisture content to less than 20% at 21% moisture content, as illustrated in Figure 5 [after *Bowers and Hanks*, 1965].

Remote sensing devices sensitive to the thermal infrared emissivity of the Earth's surface can be used to discriminate objects. The radiation temperature of the object is a function of the object's emissivity, temperature, thermal properties, and rate of heating. Soil moisture is one of the most important factors controlling the thermal properties of soils [*Mulders*, 1987]. The thermal conductivity of soil increases with increasing soil moisture because air is an insulating thermal material and air-filled pores will not conduct heat as efficiently as the water-filled matrix of a wet soil. As the soil matrix saturates, only slight increases in conductivity are produced. Raising the moisture content of a very dry soil will result in much higher conductivity because of the presence of thin water films conducting the energy.

The dielectric constant of soil is a measure of the amount of polarization upon interaction with an electromagnetic field [*Mulders*, 1987]. Temperature, pressure, and composition all impact on the dielectric property of a material; for alternating electromagnetic fields, the frequency also influences the dielectric constant [*Mulders*, 1987]. The large difference between the dielectric constant for soil minerals and soil water makes the microwave approach for determination of soil moisture possible. When no liquid water is present, the real part of the soil dielectric
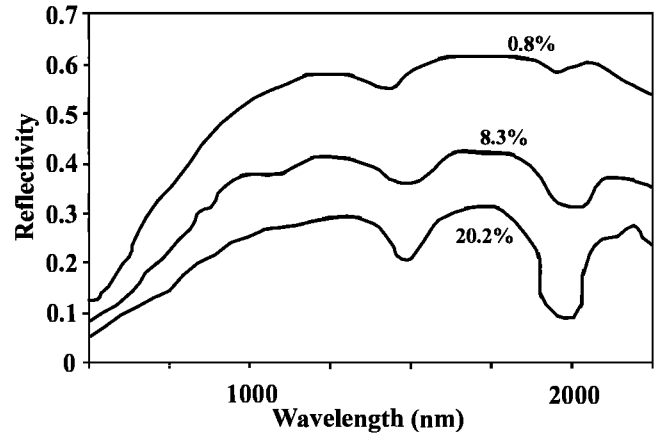
Figure 5. Spectral reflectance of silt-loam at various wavelengths [adapted from *Bowers and Hank*, 1965].

constant, ε', varies between 2 and 4 and is independent of frequency and temperature. The imaginary component of the dielectric constant, ε'', is typically less than 0.05 [*Ulaby et al.*, 1986]. The total dielectric constant for an alternating electromagnetic field is

$$= \varepsilon' + j\varepsilon'' \qquad (1)$$

where $j = \sqrt{-1}$.

Wet soil is a mixture of three components: soil particles, air, and water. The water is divided into bound water, which is tightly held to the soil particles, and free water, which is free to rotate and align itself with an applied electric field. *Wang and Schmugge* [1980] developed an empirical model relating soil texture parameters to the dielectric constant [*Ulaby et al.*, 1986] and showed that the differences between dielectric constants are primarily the result of the variations in water retention capacity rather than mineral type. The effect of soil type is reduced when soil moisture is normalized and is expressed as a ratio of volumetric soil moisture content to field capacity. Studies using portable dielectric probes have shown there is little difference in the dielectric constants of different textured soils and, moreover, the dielectric constant is affected only by changes in soil moisture [*Brisco et al.*, 1992; and *Topp et al.*, 1980]. *Brisco et al.* [1992] also suggested that texture effects were not significant for C-, L-, P-, and X-band frequencies.

The dielectric properties of a medium have important consequences for the reflectivity and emissivity of incoming electromagnetic radiation. For a semi-infinite medium, the reflectivity is determined by the Fresnel reflectivity equations for vertical and horizontal polarization. These equations were derived by *Stratton* [1941]:

$$R_v = \left| \frac{\cos(\theta) - \sqrt{\varepsilon - \sin^2(\theta)}}{\cos(\theta) + \sqrt{\varepsilon - \sin^2(\theta)}} \right| \qquad (2)$$

$$R_h = \left| \frac{\cos(\theta) - \sqrt{\varepsilon - \sin^2(\theta)}}{\cos(\theta) + \sqrt{\varepsilon - \sin^2(\theta)}} \right| \qquad (3)$$

where ε is the dielectric constant of the semi-infinite solid and θ is the angle of incidence. For angles of 0° (i.e., looking vertically down at the object), polarization has no effect and the Fresnel reflectivity is given by the following [from *Schmugge*, 1985]:

$$r = \left| \frac{\sqrt{\varepsilon} - 1}{\sqrt{\varepsilon} + 1} \right|^2 \qquad (4)$$

Using the dielectric values given by *Ulaby et al.* [1986] for vernon clay with a volumetric moisture of 0.2 and 0.4, the reflectivity can be plotted for like polarizations by using equations (2) and (3) as shown in Figure 6. Because dielectrics are sensitive to surface soil moisture, which can vary significantly both spatially and temporally, it is important to take field measurements over a short period of time for as many fields as possible.

3.1.2. Field measurements of soil moisture.

Ground data are used to assess the accuracy of any remote sensing algorithm and are a fundamental component of data analysis [*Foody*, 1991]. *Curtis and Trudghill* [1974] note that a wide variety of techniques exist for soil moisture determination, the oven-drying technique being the most common. In all cases, if the wet weight, dry weight, and volume of the sample and the weight of the container are known, one can estimate the bulk density and the gravimetric and volumetric soil moisture for each sample. Bulk density, defined as the mass of a unit volume of dry soil [*Brady*, 1972] is calculated as follows:

$$BD = \frac{DW_s}{Vol} \qquad (5)$$

where DW_s is the mass of dry soil in grams and Vol is the volume of the sampling device. If consistent volume measurements were taken at each sampling point, the volumetric moisture (m_v, cm³/cm³) could also be calculated directly as

$$m_v = \frac{WW_s - DW_s}{Vol} \rho_w \qquad (6)$$

where WW_s is the wet weight of the soil and ρ_w is the density of water, which is assumed to be 1.0 g/cm³. Thus m_v
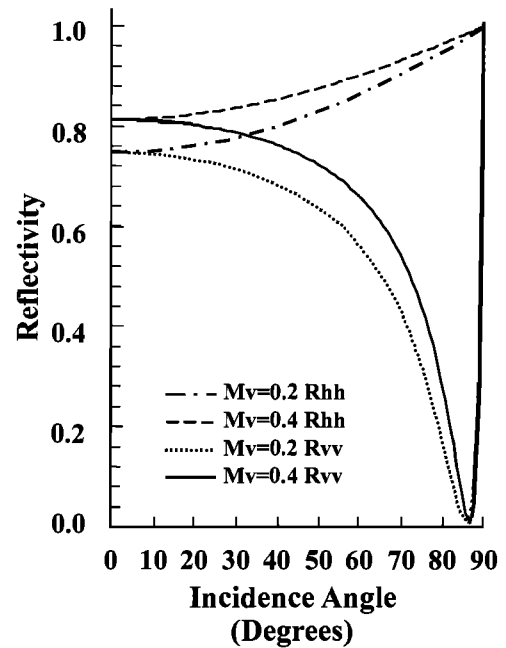
Figure 6. Fresnel reflectivity for Vernon clay [after *Ulaby et al.*, 1986].

is expressed in cm³ of water per unit volume of soil. The gravimetric moisture content (m_g) is defined as

$$m_g = \frac{WW_s - DW_s}{DW_s} \qquad (7)$$

and is expressed as a ratio or percentage of mass of water per unit dry mass of soil. When only gravimetric samples are taken and bulk density is known, conversion to volumetric moisture is estimated by rearranging equation (6) and combining it with equation (7). This results in an expression for converting between gravimetric and volumetric moisture:

$$m_v = \frac{1}{\rho_w} m_g BD \qquad (8)$$

Because conventional gravimetric measurements are time consuming, other methods, such as Time Domain Reflectometry instruments (TDR) and Portable Dielectric Probes (PDP), have been used in the field. Both instruments measure the soil dielectric constant, which is a function of soil moisture. *Brisco et al.* [1992] have developed the following equation relating volumetric soil moisture to the soil dielectric constant. This equation is independent of soil texture:

$$m_v = -0.0101 + 0.0262\varepsilon' - 0.000471\varepsilon'^2 + 0.00000412\varepsilon'^3 \qquad (9)$$

where ε' is the real part of the dielectric constant.

An important issue that arises is the correlation between these soil moisture sampling techniques and radar [*Boisvert et al.*, 1995b]. Generally, the three methods provide comparable moisture values. However, when the penetration depth of the radar signal is less than 5 cm, TDR instruments show some limitations. TDR instruments use rods or waveguides in the soil and rely on the speed of an electromagnetic pulse through these guides to estimate the dielectric constant. Good contact between the soil and wave guides is essential and can prove troublesome at shallow depths. The choice of the instrument should therefore be based on the expected penetration depth, which in turn depends on radar configuration and soil moisture content [*Boisvert et al.*, 1997]. Ground-based evaluations of near-surface soil moisture are highly variable in space and time [*Pietroniro*, 1993; *Famliglietti et al.*, 1999] and show skewed distributions in very wet and very dry conditions. Volumetric soil moisture content is a bounded distribution, with both upper and lower limits on moisture content, and tends to follow a   distribution. Another important issue to consider is the number of samples that must be collected to account for the spatial variability of surface soil moisture. *Famliglietti et al.* [1999] show that as sampling density increases from $n = 14$ to $n = 49$ samples, errors in spatial estimates can be decreased by a factor of two. Sampling strategies should consider factors such as the spatial dependency of soil moisture and the geometric resolution of the remote sensing instrument. Correlation lengths in mineral soils are often in the order of 30 to 50 m. Northern environments are much more heterogeneous, and sampling strategies should take this into account.

3.1.3. Optical and thermal infrared remote sensing of soil moisture.

Optical remote sensing methods depend on reflected energy and albedo estimates for measuring soil moisture. Typically, these techniques have yielded only qualitative results and are not truly viable for quantitative estimates of moisture in the ground. Although wet soil will have a much lower albedo than dry soil, this signal is easily confused with factors such as organic matter, roughness, and, to some degree, texture and incidence angle. Vegetation is a transient phenomenon that obscures the moisture signal, thus making this approach impractical [*Jackson et al.*, 1987].

Thermal infrared imagery has been used to infer soil moisture from each of satellite-, aircraft-, and truck-mounted platforms. Most of these methods were developed in the late 1970s and early 1980s and have recently lost favor, primarily due to advancements in microwave remote sensing and the limitations imposed by these methods. For the sake of completeness, a brief description of the theoretical basis for soil moisture discrimination using optical and infrared techniques is described. To the best of the authors' knowledge,

these techniques have not been applied to northern environments. All of the thermal infrared methods that have been developed are based on surface temperature measurements and the changes in temperature that result from changes in incident radiation and sensible, latent, and ground heat fluxes [*Price*, 1980]. The thermal inertia approach to soil moisture estimation was adapted from early work established by *Jeager* [1953], in which he derived an analytical solution to the periodic heating of a semi-infinite solid. The solution was used to discriminate lunar surface materials based on their thermal response during lunation. This relationship was later adapted for geologic discrimination on Earth by *Watson* [1973]. In both cases, a relationship between the thermal properties of the rock and the diurnal surface temperatures was examined. It was proposed that because rock types have different thermal properties, and cool down and warm up at different rates, it is possible to discriminate between different rock types [*Van de Griend and Engman*, 1985]. This principle was applied to soil moisture detection.

Early experiments on the application of thermal inertia for soil moisture assessment were carried out by *Idso et al.* [1975]. In their study, soil moisture estimates were correlated with the maximum diurnal soil-surface temperature differences for a bare Avondale loam site. The volumetric water content of the soil was found to be a linear function of the amplitude of the surface temperature curve. This prompted both several research projects examining the thermal infrared discrimination of soil moisture and the development of the Heat Capacity Mapping Mission satellite (HCMM) from 1978 to 1980. All the models developed use an energy balance approach to solve for moisture availability. Some use a direct analytical solution, whereas others solve implicitly for a finite difference formulation.

Analytical models are such that the thermal inertia is directly related to the maximum and minimum surface temperature, which is typically estimated from a satellite or aircraft platform. The early models of *Jeager* [1953] and *Watson* [1973] were both analytical. These were followed by the *Price* [1977] model and one proposed by *Pratt and Ellyett* [1979]. In all cases, the heat flow equation was solved analytically by using a simplified energy balance equation. The virtue of these models is their computational efficiency; their limitations stem from a simplified expression for thermal processes occurring at the surface [*Carlson*, 1986].

Other models using the same equations, but a more elaborate accounting of sensible and latent heat, have also been proposed and fall into the predictive category. The model developed by *Kahle* [1977] is one such example. *Kahle* [1977] developed a finite difference model that included both sensible and latent heat terms to determine surface heating. When the model was combined with field measurements of

meteorological values and remotely sensed temperature data, a map of thermal inertia of the Mojave Desert, California, was produced. In this case, the basic approach to thermal inertia mapping was to model the surface heat-exchange process and derive the surface temperature changes with time. Using the appropriate thermal characteristics of the medium, the modeled diurnal temperature curve should match the temperature curve obtained from the remote sensing instrument. These models do not yield a direct solution to estimates of thermal inertia or moisture availability but rather a family of curves [*Carlson and Boland*, 1978; *Rosema et al.*, 1978; *Soer*, 1980] that can be compared with the satellite estimate of ground temperature.

3.1.4. The microwave sensing of soil moisture.

Because of their cloud-penetrating capabilities and greater penetration depths, passive and active microwave remote sensing of soil moisture have an advantage over thermal sensors. In the case of both active and passive microwaves, the soil dielectric property is an indicator of surface soil moisture content. In the case of active sensors, the dielectric is related to the returned signal of the radar, whereas for passive sensors, the brightness temperature is a function of the surface emissivity of the bare surface or canopy and the atmospheric transmission, the surface emissivity being related to the dielectric constant and hence soil moisture. In both cases, the large dielectric constant for water, as opposed to a relatively low constant for soil minerals, is what makes the microwave approach to monitoring soil moisture feasible.

In active radar sensing, other factors such as incidence angle, soil roughness, canopy cover, and canopy moisture have a direct bearing on the radar backscatter coefficient of the target. Therefore, it is necessary to "remove" these effects so as to isolate the soil moisture component [*Schmugge*, 1984]. Measurements of thermal emission require sensitive radiometers with large antennas, thus limiting the ground resolution capabilities. For example, a 1.4-GHz radiometer with a 10-m antenna flown in a 500-km orbit would have a resolution of 10 km [*Schmugge*, 1984]. Canopy cover and moisture can also influence the measured signal, and optimum configurations for passive sensors have been established using field measurements and airborne radiometers. *Schmugge* [1984] concluded that radiometers operating at the 21-cm wavelength, or 1.4-GHz frequency, and in HH mode are the most effective for passive remote sensing of soil moisture.

Active remote sensing using SAR has an advantage over passive sensing because of the increased spatial resolution. The backscatter coefficient is the measure of the intensity of the return signal and describes the scattering properties of the sensing surface. The factors that contribute to a particular backscatter response are incident angle and roughness, soil type, and vegetation cover [*Schmugge*, 1984].

3.1.5. Passive microwave approaches.

Microwave radiometers measure the thermal emission from the surface of the Earth. This requires sensitive radiometers with large antennas and consequently large sampling areas, given the weak signal produced by the Earth's surface at microwave wavelengths. The emission measured from the surface of the Earth is referred to as the brightness temperature and is given as follows by *Wang and Schmugge* [1980]:

$$T_b = \tau(H)\left[rT_{sky} + (1-r)T_{soil}\right] + T_{atm} \qquad (10)$$

where T is the temperature, r is the surface reflectivity, and $\tau(H)$ is the atmospheric attenuation. At longer wavelengths (C-band microwaves or longer), atmospheric effects can be neglected [*Engman and Gurney*, 1991], thereby simplifying the equation to a function of reflectivity and soil temperature:

$$T_b = eT_{soil} \qquad (11)$$

where e is the surface emissivity.

The surface emissivity for a semi-infinite media, which allows no transmission, is

$$e = 1 - r \qquad (12)$$

where the reflectivity r is determined from the Fresnel relationship [*Schmugge*, 1985]. Using this relationship to calculate the emissivity for a smooth soil surface and the dielectric constant, the emissivity (and reflectivity) can be estimated as a function of incidence angle and volumetric moisture. The behavior of the response to moisture is approximately linear, decreasing in emissivity with increasing soil moisture. *Schmugge* [1985] reported that this linear behavior has been observed in truck-mounted and tower experiments.

Using equation (10), *Njoku et al.* [2003] proposed a soil moisture retrieval approach using a combination of microwave frequencies and polarisations from the Advanced Microwave Scanning Radiometer (AMSR-E) onboard the Aqua satellite, which was launched in 2002. Validation of the methodology is currently underway.

3.1.6. Active microwave approaches.

The potential of active microwave sensors for measuring surface moisture conditions was demonstrated by *Ulaby* [1974]. Since that time, there has been considerable research in this field, particularly for bare soil moisture discrimination [*Ulaby and Batlivala*, 1976; *Bernard et al.*, 1982] and vegetated surfaces [*Ulaby et al.*, 1984;

Dobson and Ulaby, 1986]. Incidence angle and roughness are major factors that govern the backscatter of a bare soil surface. For smooth surfaces, the behavior is specular, and the surface essentially behaves as a mirror. Only incidence angles near $0°$ will have a strong backscatter intensity. For example, still water behaves as a smooth (specular) surface and will appear dark on most radar images. A rough surface will behave as an isotropic scatterer and will be less sensitive to changes in incidence angle. Some sensor configurations are less sensitive to these effects. *Ulaby et al.* [1982] noted that the optimum configuration for surface (10-cm depth) soil moisture discrimination for bare and vegetated surfaces was for shallow incidence angles between $10°$ and $23°$ and a C-band radar. These results were based on extensive scatterometer studies carried out in the 1970s. L-band data have also been shown to be very sensitive to changes in soil moisture and shallow incidence angles.

Empirical and physical models, which relate backscatter to the surface roughness of the medium, incidence angle, and wavelength, have been developed. These surface-scattering models—such as the Kirchoff (physical optics) model, the geometric optics model, and the small perturbation model—express the backscatter coefficient as a function of reflectivity, surface roughness, incidence angle, and wavelength and are described in great detail in *Ulaby et al.* [1986]. These models also provide the physical basis for observed phenomena in active microwave remote sensing. However, due to their complexity, they are not easily applied on a watershed scale. More empirical approaches to bare soil surface sensing have been developed. These approaches are valid for sensor configuration in which the effects of roughness are not visible to the radar. The least-squares linear regression equation given in *Ulaby et al.* [1982] relates the surface-scattering coefficient (dB) to moisture (% field capacity). Similar linear relationships were developed by *Bernard et al.* [1986] for volumetric soil moisture. In both cases, the incidence angle and wavelength were at optimum values (C-band and $20°$) while roughness was minimized. However, for examining soil moisture over a large area, roughness effects, incidence angle effects, and vegetation effects must be eliminated from the measured backscatter in order to isolate the soil moisture effects. The generalized equations for simple bare soil regression can be given as

$$\sigma^0 (dB)_{soil} = \alpha m_x + \beta \qquad (13)$$

where α and β are regression coefficients and m_x is the surface soil moisture, expressed volumetrically or gravimetrically.

Vegetation absorbs and scatters some of the microwave energy incident on the canopy. Absorption is strongly affected by the water content of the canopy, but the mechanism is not well understood. *Ulaby et al.* [1982] have expressed the effect of vegetation as a function of the vegetation backscatter $(\theta°_v)$ and a loss factor. These two values have been tabulated from tower measurements for several different types of vegetation. The vegetation layer can be treated as a uniform cloud of particles with volume scattering being the end effect. The simple regression equation takes the following form:

$$\sigma^0_{total} = \sigma^0_{surface} + \sigma^0_{vegetation} + \sigma^0_{interaction} \qquad (14)$$

where the surface term is a function of the one-way transmissivity through the vegetation canopy and is

$$\sigma^0_{surface} = T(\theta, \tau) \sigma^0_{soil} \qquad (15)$$

The above equations can be reduced to a simple regression model if interaction terms are ignored and total backscatter is estimated as follows:

$$\sigma^0_{total} = \sigma^0_{vegetation} + T(\theta, \tau) \sigma^0_{soil} \qquad (16)$$

Using this form of the equation, *Ulaby et al.* (1982) tabulated the vegetation backscatter and the transmissivity factor for several different vegetation types.

In summary, as noted by *Brun et al.* [1990], the ability of active microwave remote sensing to provide an estimate of mean surface soil moisture (0–5-cm depth) has been fully demonstrated both theoretically and experimentally. The radar return is a function of the surface roughness, moisture content, and vegetation cover, but the radar specifications can be chosen in such a way so as to minimize these effects. The optimum radar for soil moisture discrimination is C-band with incidence angles below $20°$ and above $10°$ [*Dobson and Ulaby*, 1986]. In this case, an empirical model relating radar cross-section as an exponential function of surface moisture is satisfactory.

3.2. Algorithms and Applications in Northern Environments

Because SAR systems allow fine (10–30-m)-resolution coverage at the watershed scale, and with the launches of the ERS, JERS, Envisat, and Radarsat series of satellites over the last 10 years, researchers of northern hydrology have focused their studies in the microwave portion of the electromagnetic spectrum. The interaction between a propagating wave and a bare soil surface is represented by surface-scattering models [*Engman*, 1991]. Bare surface backscatter models relate surface characteristics to the observed signal received from the SAR. These models are a function of the surface roughness conditions, dielectric properties of the soil, and the angle

of incidence. Roughness measurements are defined by the root-mean-square (rms) slope of the surface (m), which is defined as

$$m = \frac{s}{l} \qquad (17)$$

for an exponent autocorrelation function, and

$$m = \frac{\sqrt{2}}{l} \qquad (18)$$

for a Gaussian autocorrelation function.

The range of applicability of these models is a function of the normalized correlation length (ks) and normalized rms (kl) roughness measurements, where

$$k = \frac{2\pi}{\lambda} \qquad (19)$$

and λ is the wavelength. The validity ranges are outlined by *Ulaby et al.* [1986], *Engman and Wang* [1987], and *Oh et al.* [1992] and are listed in Table 3.

The classical surface-scattering models, the small perturbation model, the physical optics model, and the geometric optics model are all similar in their representation of the surface backscatter as a product of the dielectric and surface roughness functions [*Shi et al.*, 1991]. These equations are of the following form [*Shi et al.*, 1991]:

$$\sigma^{pp}(\theta, f) = D(f, pp, \theta) S(f, pp, \theta, s, l) \qquad (20)$$

where pp is the polarization, f is the frequency, s and l are the roughness parameters, and θ is the incidence angle. D and S represent dielectric and surface roughness functions, respectively.

A study evaluating the three backscatter models was performed by *Engman and Wang* [1987]. They reported that the small perturbation model gave the best results for SIR-B L-Band radar flown over a test site in Fresno, California. Scatterometer studies performed by *Oh et al.* [1992] have concluded that none of the three backscatter models provided consistently good agreement with measured data. *Oh et al.* [1992] proceeded to develop empirical relationships that modeled the backscatter relationships for the polarization, frequencies, roughness, and incidence angle ranges considered. The three classical backscatter models originally tested by *Oh et al.* [1992] simulated the backscatter behavior reasonably well under some conditions. *Oh et al.* [1992] noted that, overall, the small perturbation model provided a reasonable fit for a HH polarization at 1.5-GHz frequency, but this was not the case for the VV polarization. The validity range of the small perturbation model was also a limiting factor, as is true of most surface-scattering models. *Oh et al.* [1992]

Table 3. Limits of Roughness and Correlation Lengths for Dielectric Model Applications (see text for explanation of symbols).

Model	Validity conditions	
Physics optics	m < 0.25	kl < 6
Geometric optics	[2kcos(θ)]^2 > 10	l^2 > 2.76 sλ
Small perturbation	m < 0.3	ks < 0.3

showed that their empirical model could simulate backscatter behavior for a wider range of frequencies and roughness values. This equation does not consider the correlation length as a parameter and limits the roughness component in the models to the rms value. The range of ks values for which the model was tested was 0.1–6. This corresponds to an rms value of 0.4 cm at L-band frequency and to an rms of 3.02 cm for the X-band frequency. The empirical model [*Oh et al.*, 1992] is expressed as follows:

$$\sigma^{hh} = g\sqrt{p}\cos^3(\theta)\left[R_v(\theta) + R_v(\theta)\right] \qquad (21)$$

where g is defined as

$$g = 0.7\left[1 - \exp\left(-0.65(ks)^{1.8}\right)\right] \qquad (22)$$

and p is defined as

$$\sqrt{p} = \sqrt{\frac{\sigma_{hh}^0}{\sigma_{vv}^0}} = 1 - \left(\frac{2\theta}{\pi}\right)^{\frac{1}{3R}} \exp(-ks) \qquad (23)$$

Data from *Oh et al.* [1992] are plotted in Figure 7 for L-band scatterometer data for a smooth field, where the small perturbation model is valid.

Near-surface soil moisture (usually 0–5 cm) has been extracted from SAR imagery with the use of statistical, semi-empirical, and physically based models [*Boisvert et al.*, 1996a]. Statistical models, for example, linear regression models between radar backscatter and soil moisture, are still the most commonly used approach [e.g., *Boisvert et al.*, 1995a; *Crevier et al.*, 1996; *Geng et al.*, 1996; *Pultz et al.*, 1997; *Biftu and Gan*, 2000]. *Pietroniro* [1992] showed that both the small perturbation optics model and a semi-empirical approach are easily replicated by a cosine approximation to a simple regression equation, as shown in Figure 8. A major drawback of these approaches is that the models cannot be transposed to other sites. Semi-empirical and theoretical models, on the other hand, can be applied to a variety of surfaces. However, there are no existing algorithms for the routine determination of soil moisture from single-frequency, single-polarization radars. These models have mainly been used in ground scatterometer studies to study the radar backscattering mechanisms in relation to soil moisture, surface roughness, and vegetation [*Dubois et al.*, 1995; *Boisvert et*
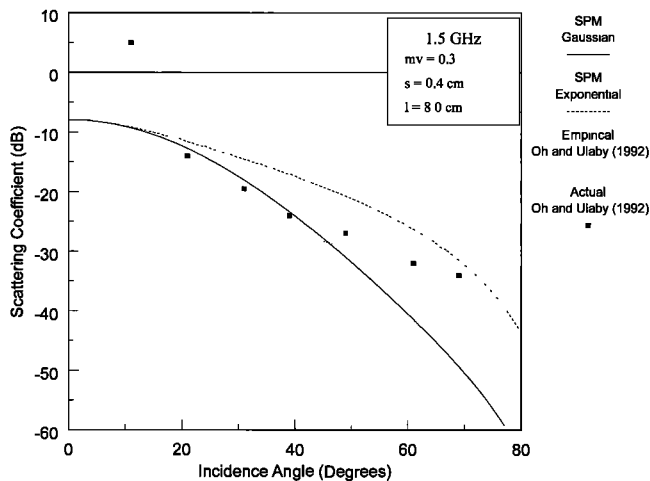
Figure 7. Comparison of small perturbation models (SPM) and empirical model for a bare field [original data adapted from *Oh et al.*, 1992].

al., 1997], although attempts to use the models for extracting soil moisture values at the field and watershed scale have produced encouraging results [*Biftu and Gan*, 2000; *Galarneau et al.*, 2000; *Leconte et al.*, 2004].

Xu et al. [1998a] studied the potential of Radarsat for applications in organic soils with a truck-mounted scatterometer. They concluded that soil moisture should be monitored at a 25° incidence angle before plant establishment. They obtained a linear relation between the radar signal and the soil dielectric constant (which varies with soil moisture) and demonstrated that roughness effect was more important at higher soil moisture content. *Colpitts* [1998] applied the Integral Equation Model (IEM) to ground scatterometer data for plots having a variety of soil moisture conditions and tillage practices and found that bare field surface (10-cm depth) soil moisture could be achieved with inaccuracies of less than 2% if external information, such as local precipitation, was used to initially constrain the moisture to ±10% of the actual level. Data collected during the 1994 SIR C/X SAR experiment in Altona, Manitoba, were used to evaluate the effect of incidence angle on the accuracy of soil moisture estimation [*Boisvert et al.*, 1996b]. The results showed that an increase in incidence angle by 1° could decrease the C-HH signal by 0.25 dB, which would translate into a change of 2% in soil moisture information. Such findings illustrate the importance of obtaining accurate topographic information to extract information on surface soil moisture in sloped surfaces.

The effects of other factors, such as soil texture, surface roughness, radar penetration depth, and environmental factors (frost, rain) on the radar backscatter have also been investigated [*Pultz et al.*, 1997]. *Pultz et al.* [1997] showed that effects of soil texture on the estimation of soil moisture from radar

backscatter were relatively small and that roughness could be neglected when measuring soil moisture over relatively short periods of time at a given site. However, as surface roughness is spatially and temporally variable, this variation must be taken into account to produce soil moisture maps at the watershed scale. *Jackson et al.* [1997] described a procedure that utilizes land cover, rainfall, and associated parameter data bases to provide an estimate of soil surface roughness. *Geng et al.* [1996] suggested that the effect of roughness could be a constant in agricultural areas in some cases. *Leconte et al.* [2000] used a semi-empirical radar backscatter model with a reference SAR image to infer a soil surface roughness map that was used to estimate soil moisture from other SAR images of the same area. Although attractive, this approach assumes that surface roughness is time-invariant, which is not the case for agricultural fields because of tillage practices and erosion. To circumvent this problem, some researchers have focused on pastures as index fields for the determination of soil moisture [*Crevier et al.*, 1996; *Rotunno Filho et al.*, 1996; *Pultz et al.*, 2000; *Seglenieks et al.*, 2000], from which soil moisture maps could be produced by using geostatistical approaches [*Rotunno Filho et al.*, 1996; *Biftu and Gan*, 2000], since roughness on those targets can be considered approximately time-invariant.

Statistical analyses relating radar backscatter (from airborne, ERS-1, and Radarsat images) to soil moisture content have shown that the best correlations are found if daily means of field average backscatter and soil moisture are used. Very few studies have examined estimating soil moisture by using SAR in permafrost regions to monitor the movement of the active layer. *Meade et al.* [1999] used neural network analysis to develop the necessary constituent equations to relate observed surface soil moisture to radar backscatter. Not surprisingly, the correlations were poor (r^2 from 0.36 to 0.06) since backscatter was highly

$$\log\left(\sigma^0(dB)_{soil}\right) = \alpha m_x + \beta \log(\cos(\theta)) + \chi \log(s) + \delta$$
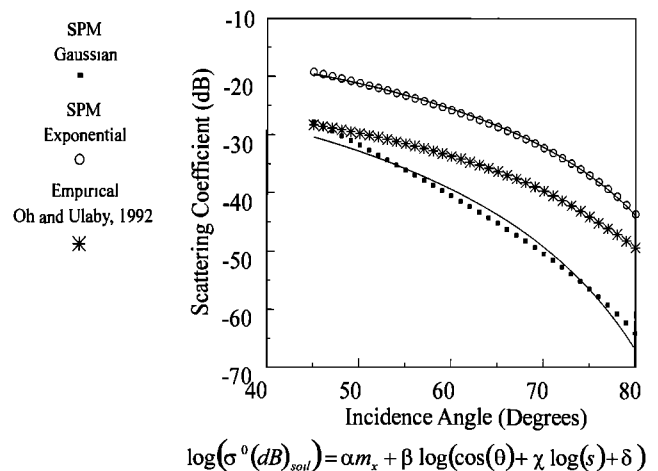
Figure 8. Simple regression approximation to the small perturbation models and empirical model.

influenced by vegetation, soil type, and surface roughness. Also, the inherent spatial variability of moisture between tussocks minerals and intertussock organic soils at a resolution much finer than the satellite footprint (about 25 m) makes it difficult to characterize the soil moisture. The overall pattern of backscatter within the basin provided a reasonable qualitative assessment of the soil moisture patterns, with ridges, hill slopes, and valley bottoms showing the characteristic patterns expected in this region [*Meade et al.*, 1999]. *Duguay et al.* [1999] suggest that surface wetness can be mapped but that the potential for soil moisture mapping in these types of environments is limited with C-band SAR.

Although most research has focused on radar data, some research has also involved the use of passive microwave sensors to retrieve surface soil moisture estimates. *Xu et al.* [1998b] obtained a linear relationship between the brightness temperature and the surface volumetric soil moisture at 0–3-cm depth over bare fields, using an airborne whiskbroom radiometer operating in L-band and VV polarization. No apparent effects of roughness were detected in the collected data.

In the case of forest canopies, researchers usually contend that the retrieval of surface soil moisture from remote sensing is not possible because the vegetation is masking the underlying ground. However, because boreal forests are typically relatively sparse, electromagnetic energy, particularly in the microwave region, can at least partially penetrate through the vegetation canopy. Many of the studies involving passive and active microwave sensors have dealt with the estimation of forest biomass [*Ahern et al.*, 1993; *Pulliainen et al.*, 1996]. Seasonal changes in backscattering properties of boreal forests were found to be the result of the presence of seasonal snow cover, soil freezing/thawing, and variations in soil and canopy moisture content. However, there have been comparatively very few attempts to extract quantitative information on soil moisture. For example, *Pulliainen et al.* [1996] used a semi-empirical backscattering model

$$\sigma^0 = \sigma_v^0 + t^2 \cdot \sigma_g^0 \qquad (24)$$

to extract soil moisture and biomass volume from ERS-1 SAR images, where $\sigma_v^{\,o}$ is the backscattering coefficient of the forest canopy, t is the forest canopy transmissivity, and $\sigma_g^{\,o}$ is the backscattering coefficient of the ground—which depends on surface soil moisture, among other things. Because ERS-1 is a single-channel instrument, retrieval of the two-state variables required the use of reference sample plots in which values for these variables were known. Another possible approach for estimating soil moisture in boreal forest would be to estimate surface moisture in open areas and use geostatistical techniques to interpolate soil moisture between these "point" measurements.

A unique approach applied to the Alaskan Boreal forests used recent burns as target areas to estimate soil moisture. *French et al.* [1996, 1999] noted a strong relationship between radar backscatter and observed soil moisture in regions that had been fire-scarred for up to 10 years. *Wang et al.* [2000] developed and tested a backscatter model for willow shrubs (*Salix sp.*), the dominant regrowth species after fire. The model is based on the vegetation scattering model proposed by *Wang et al.* [1993] and is given as follows [*Wang et al.*, 2000]:

$$\sigma_{total}^0 = \sigma_s^0 + C\sigma_v^0 + C\sigma_m^0 \qquad (25)$$

where C is the willow ground cover and s, v, and m are the surface, volume, and multipath scattering contributions, respectively.

Wang et al. [2000] designed a sensitivity study to investigate variations of modeled backscatter from a range of measured surface properties. This study focused on the sensitivity of modeled C- and L-band backscatter to soil moisture, surface roughness, and willow ground coverage, height, and stem density. They concluded that, when investigating soil moisture content alone, C-HH and C-VV appeared to be more sensitive than L-band over a range of incidence angles between 20° and 60°.

Deriving soil moisture from passive microwave radiometers under vegetated canopies is exceedingly difficult due to the large ground footprint and the sensitivity of the signal to canopy moisture. *Haboudane et al.* [1996], using a truck-mounted radiometer operating at a range of frequencies (1.4–90 GHz), studied the microwave radiation emitted from a surface partially covered with vegetation. They concluded that the volumetric water content of the soil surface could be estimated at lower frequencies with an acceptable accuracy level, provided the vegetation water content is known. *Du et al.* [2000] recently addressed the question of active and passive microwave sensitivities to soil moisture under a vegetated canopy by applying a radiative transfer model under three canopy conditions: a smooth soil surface, a grass canopy, and a soybean canopy. They concluded that radar and radiometric soil moisture sensitivities decreased with an increase in optical depth, the rates being approximately the same for both sensors. It is difficult to extrapolate such a study to northern regimes and is clear that further testing of both passive and active systems in northern regimes is required. The limited studies to date show some promise. However, much is left unresolved.

3.3. Conclusions and Future Research

Estimation of soil moisture using active microwave sensors is probably the avenue that offers the most potential. However,

many issues need to be resolved before this technique can be used in an operational basis. Research is needed to better understand the interaction of microwaves with soil moisture, particularly in moderately vegetated areas. The Hydrosphere State Mission (Hydros), scheduled for launch in 2010, will be invaluable in providing global-scale estimates of surface soil moisture and land surface freeze/thaw conditions at the watershed scale. To estimate soil moisture, Hydros radiometer and radar measurements will be used in combination, taking advantage of the simultaneous, coincident, and complementary nature of the measurements. It is implausible to map soil moisture on a pixel basis over entire watersheds because of the difficulties associated with speckle. An approach based on the determination of soil moisture in reference plots, or index fields, with interpolation using geostastical techniques [*Bardossy and Lehman*, 1998; *Pietroniro and Leconte*, 2005] should be pursued. Although surface moisture (0–5-cm depth) is important to know because it influences soil surface temperature, which in turn affects evaporation, the partitioning of rainfall into infiltration and runoff depends on soil moisture over a deeper layer, typically the root zone. Research is needed to infer soil moisture over 1–2-m depths from surface measurements. Currently, few hydrologic models have been used in conjunction with soil moisture estimates obtained from remotely sensed data. The reasons for this include the inability of many models to effectively incorporate surface soil moisture to calculate runoff and the lack of reliable estimates of surface soil moisture from remotely sensed data. At this point, it is not known if, and by how much, the use of remotely sensed soil moisture estimates will improve the accuracy of hydrological simulations and forecasts. Such an assessment needs to be performed on a variety of watersheds before using remote sensing in hydrological models in an operational way.

REFERENCES

Adam, S., J. Wiebe, M. Collins, and A. Pietroniro, RADARSAT flood mapping in the Peace-Athabasca Delta, Canada, *Can. J. Remote Sens.*, 24(1), 69–79, 1998.

Ahern, F., D. Leckie, and J. Drieman, J, Seasonal changes in relative C-band backscatter of northern forest cover types, *IEEE Trans. Geosci. Remote Sens.*, 31(3), 668–680, 1993.

Barber, D. G., K. P. Hochheim, R. Dixon, D. R. Mosscrop, and M. J. McMullan, The role of earth observation technologies in flood mapping: A Manitoba case study, *Can. J. Remote Sens.*, 22(1), 137–143, 1996.

Bardossy, A., and W. Lehman, Spatial distribution of soil moisture in a small catchment. Part 1: geostatistical analysis, *J. Hydrol.*, 206, 1–15, 1998.

Basist, A., N. C. Grody, T. C. Peterson, C. N. Williams, Using the special sensor microwave/imager to monitor land surface temperatures, wetness, and snow cover, *J. Appl. Meteorol.*, 37(9): 888–911, 1998.

Basist, A., C. Williams, N. Grody, T. F. Ross, S. Shen, A. T. C. Chang, R. Ferraro, M. J. Menne, Using the special sensor microwave imager to monitor surface wetness, *J. Hydrometerol.*, 2(3), 297–308, 2001.

Bennett, M. W. A., Rapid monitoring of wetland water status using density slicing, in *Proceedings of the Fourth Australasian Remote Sensing Conference*, pp. 682–691, 1987.

Bernard, R., P. Martin, J. L. Thony, M. Vauclin, and D. Vidal-Madjar, C-band radar for determining surface soil moisture, *Remote Sens. Environ.*, 12, 189–200, 1982.

Bernard, R., J. V. Soares, and D. Vidal-Madjar, Differential bare field drainage properties from airborne microwave observation, *Water Resour. Res.*, 22(6), 189–200, 1986.

Biftu, G.F., and T. Y. Gan, Retrieving soil moisture over a basin of the Canadian prairies from RADARSAT SAR data, in *Proceedings of the Workshop on Applications of Remote Sensing in Hydrology*, edited by A. Pietroniro, R. Granger, and T. J. Pultz, pp. 1–14, Santa Fe, New Mexico, 2000.

Birkett, C., G., and G. Kite, Derivation of lake areas and elevations for the Mackenzie Basin using satellite remote sensing, in *Applications of Remote Sensing in Hydrology*, pp. 19–32, Proceedings of the Third International Workshop, NHRI Symposium No. 17, 1997.

Boisvert, J.B., Q. H. J. Gwyn, B. Brisco, D. J. Major, and R. J. Brown, Evaluation of soil moisture estimation techniques and microwave penetration depth for radar applications, *Can. J. Remote Sens.*, 21(2), 110–123, 1995a.

Boisvert J.B., T J. Pultz, Y. Crevier, and R. J. Brown, Potential of multi-date imagery for soil moisture, texture and drainage classification: preliminary results, pp. 511–515, 17th Canadian Symposium on Remote Sensing, Saskatoon, Saskatchewan, June 13–15, 1995b.

Boisvert J.B., Y. Crevier, and T. J. Pultz, Estimation régionale de l'humiditédu so par télédétection, *Can. J. Soil Sci.*, 76, 325–334, 1996a.

Boisvert, J.B., T. J. Pultz, R. J. Brown, and B. Brisco, Potential of synthetic aperture radar for large scale soil moisture monitoring: a review, *Can. J. Remote Sens.*, 22(1), 2–13, 1996b.

Boisvert, J.B., Q. H. J. Gwyn, A. Chanzy, D. J. Major, B. Brisco, and R. J. Brown, Effect of surface moisture gradients on modelling radar backscattering from bare soil, *Int. J. Remote Sens.*, 18(1), 153–170, 1997.

Bowers, S.A., and R. J. Hanks, Reflection of radiant energy from soils, *Soil Sci.*, 100(2), 130–138, 1965.

Bowling, L.C., D.L. Kane, R.E. Gieck, L.D. Hinzman, and D.P. Lettemaier, The role of surface storage in a low-gradient Arc-

tiv watershed, *Water Resour. Res.*, 39(4), 1087, doi:10.1029/2002WR001466, 2003.

Brady, N.C., *The Nature and Properties of Soil,* 639 pp., Macmillan, New York. 1974.

Brisco, B., T. J. Pultz, R.J. Brown, G. C. Topp, M.A. Hares, and W. D. Zebchuk, Soil moisture measurement using portable dielectric probes and time domain reflectometry, *Water Resour. Res.*, 28(5), 1339–1346, 1992.

Brook, G. A., Application of Landsat imagery to flood studies in the remote Nahanni karst, Northwest Territories, Canada, *J. Hydrol.*, 61, 305–324, 1983.

Brun, C., R. Bernard, D. Vidal-Madjar, C. Gascuel-Odoux, P. Merot, P., J. Duchesne, and H. Nicolas, Mapping saturated areas with a helicopter-borne C band scatterometer, *Water Resour. Res.*, 26(5), 945–955, 1990.

Bryan, M. L., The use of radar imagery for surface water investigations, in *Proceedings of the Fifth Annual William T. Pecora Memorial Symposium on Remote Sensing, Satellite Hydrology*, pp. 238–251, 1979.

Bryan, M. L., W. D. Stromberg, and T. G. Farr, Computer processing of SAR L-band imagery, *Photogram. Eng. Remote Sens.*, 43(10), 1283–1294, 1977.

Carlson, T. N., Regional-scale estimates of surface moisture availability and thermal inertia using remote thermal measurement, *Remote Sens. Rev.*, 1(2), 197–247, 1986.

Carlson, T. N. and F. E. Boland, Analysis of urban-rural canopy using a surface heat flux temperature model, *J. Appl. Meterol.*, 17, 998–1013, 1978.

Carter, V., 1982. Applications of remote sensing to wetlands, in *Remote Sensing for Resource Management,* edited by C. J. Johannsen, and J. L. Sanders, pp. 284–300, Soil Conservation Society of America, Ankeny, 1982.

Colpitts, B. G., The integral equation model and surface roughness signatures in soil moisture and tillage type determination, *IEEE Trans. Geosci. Remote Sens.*, 36(3), 833–837, 1998.

Colwell, R., *Manual of Remote Sensing. Vol. 1 and 2*, 2440 pp., Society of Photogrammetry, Falls Church, 1983.

Crevier, Y., and T. J. Pultz, Analysis of C-band SIR-C radar backscatter over a flooded environment, Red River, Manitoba, in *Applications of Remote Sensing in Hydrology*, pp. 47–60, Proceedings of the Third International Workshop, NHRI Symposium No. 17, 1997.

Crevier, Y., T. J. Pultz, T. I. Lukowski, and T. Toutin, Temporal analysis of ERS-1 SAR backscatter for hydrology applications, *Can. J. Remote Sens.* 22(1), 65–76, 1996.

Curran. P. J., *Principles of Remote Sensing,* 282 pp. Longman Group Limited, London, 1985.

Curtis, L. F., and S. Trudgill, The Measurement of Soil Moisture, *Technical Bulletin 13*, British Geomorpholoical Research Group, Geo Abstracts, Norwich, 1974.

Dean, K. G., and L. A. Morrissey, Detection and identification of arctic landforms: An assessment of remotely sensed data, *Photogram. Eng. Remote Sens.*, 54(3), 363–371, 1988.

Deutsch, M., and F. Ruggles, Optical data and projected applications of the ERTS-1 imagery covering the 1973 Mississippi River Valley floods, *Water Resour. Bull.*, 10(5), 1023–1039, 1974.

Dobson, M.C., and F. T. Ulaby, Active microwave soil moisture research, *IEEE Trans. Geosci. Remote Sens.*, GE-24, 23–36, 1986.

Du, Y., F. T. Ulaby, and M. C. Dobson, Sensitivity to soil moisture by active and passive microwave sensors, *IEEE Trans. Geosci. Remote Sens.*, 38(1), 105–114, 2000.

Dubois, P. C., J. van Zyl, and T. Engman, Measuring soil moisture with imaging radars, *IEEE Trans. Geosci. Remote Sens.*, 33(4), 915–926, 1995.

Duguay, C. R., and P. M. Lafleur, Estimating depth and ice thickness of shallow subarctic lakes using spaceborne optical and SAR data, *Int. J. Remote Sens* , 24(3), 475–489, 2003.

Duguay, C. R., W. R. Rouse, P. M. Lafleur, L. D. Boudreau, Y. Crevier, and T. J. Pultz, Analysis of multi-temporal ERS-1 SAR data of subarctic tundra and forest in the northern Hudson Bay Lowland and implications for climate studies. *Can. J. Remote Sens.*, 25(1), 21–33, 1999.

Duguay, C. R., T. J. Pultz, P. M. Lafleur, and D. Drai, RADARSAT backscatter characteristics of ice growing on shallow sub-arctic lakes, Churchill, Manitoba, Canada, *Hydrol. Processes, 16*(8), 1631–1644, 2002.

Engman, E. T., Use of microwave remotely sensed data in hydrologic modelling, in *Proceedings of the Workshop on Applications of Remote Sensing in Hydrology*, pp. 259 – 278, Saskatoon, Saskatchewan, 1990.

Engman, E. T., Applications of microwave remote sensing of soil moisture for water resources and agriculture, *Remote Sens. Environ.*, 35, 213–230, 1991.

Engman, E. T., and R. J. Gurney, *Remote Sensing in Hydrology*, 225 pp. Chapman Hall, London, 1991.

Engman, E. T. and J. R. Wang, Evaluating roughness models of radar backscatter, *IEEE Trans. Geosci. Remote Sens.*, GE-25(6), 709–713, 1987.

Famiglietti, J. S., J. A. Devereaux, C. A. Laymon, T. Tsegaye, P. R. Houser, T. J. Jackson, S. T. Graham, M. Rodell, and P. J. van Oevelen, Ground-based investigation of soil moisture variability within remote sensing footprints during the Southern Great Plains 1997 (SGP97) hydrology experiment, *Water Resour. Res.*, 35(6), 1839–1851, 1999.

Fily, M., A. Royer, K. Goïta, and C. Prigent, A simple retrieval method for land surface temperature and fraction of water surface determination from satellite microwave brightness temperatures in sub-arctic areas, *Remote Sens. Environ.*, 85: 328–338, 2003.

Foody, G. M., Soil moisture content ground data for remote sensing investigations of agricultural regions, *Int. J. Remote Sens.*, 12(7), 1461–1469, 1991.

Ford, J. B., and D. J. Casey, Shuttle radar mapping with diverse incidence angles in the rainforest of Borneo, *Int. J. Remote Sens.*, 9(5), 927–943, 1988.

French, N. H. F., E. S. Kasischke, L. L. Bourgeau-Chavez, P. Harrell, and N. L. Christensen, Jr., Sensitivity of ERS SAR to variations in soil-water in fire-disturbed boreal forest ecosystem, *Int. J. Remote Sens.*, 17, 3037–3053, 1996.

French, N. H. F., L. L. Bourgeau-Chavez, Y. Wang, and E. S. Kasischke, Initial observations of Radarsat SAR imagery at fire-disturbed sites in interior Alaska, *Remote Sens. Environ.*, 68, 89–94, 1999.

Galarneau, M., R. Leconte, F. Brissette, and T. J. Pultz, The determination of soil moisture at the field scale using RADARSAT data, in *Proceedings of the Workshop on Applications of Remote Sensing in Hydrology*, edited by A. Pietroniro, R. Granger, and T. J. Pultz, pp. 77–85, Santa Fe, New Mexico, Santa Fe, New Mexico, 4–6 November, 1998, 2000.

Geng, H., Q. H. J. Gwyn, B. Brisco, J. B. Boisvert, and R. J. Brown, Mapping of soil moisture from C-band radar images, *Can. J. Remote Sens.*, 22(1), 117–126, 1996.

Gill, C. J., The flooding tolerance of woody species—a review. *For. Abstr.*, 31, 671–688, 1970.

Haboudane, D., A. Chanzy, J. C. Calvet, J. P. Wigneron, and F. Bonn, Radiométrie micro-onde dans le cas des couverts végétaux partiels: estimation de la teneur en eau du sol, *Can. J. Remote Sens.*, 22(2), 208–217, 1996.

Hall, D. K., Remote sensing applications to hydrology: imaging radar. *Hydrol. Sci.*, 41(4), 609–624, 1996.

Harris, J., and S. Digby-Argus, The detection of wetlands on radar imagery, in *10th Canadian Symposium on Remote Sensing*, pp. 529–543, 1986.

Hess, L., J. M. Melack, and D. S. Simonett, Radar detection of flooding beneath the forest canopy. *Int. J. Remote Sens.*, 11(7), 1313–1325, 1990.

Hess, L. L., J. M. Melack, S. Filoso, and Y. Wang, Delineation of inundated area and vegetation along the Amazon floodplain with the SIR-C synthetic aperture radar. *IEEE Trans. Geosci. Remote Sens.*, 33(4), 896–904, 1995.

Hoffer, R. M., Biological and physical considerations in applying computer-aided analysis techniques to remote sensor data, in *Remote Sensing: The Quantitative Approach*, edited by P. H. Swain, and S. M. Davis, pp. 227–287, McGraw-Hill, New York, 1978.

Idso, S.B., T. J. Schmugge, R. D. Jackson, and R.J. Reginato, The utility of surface temperature measurements for the remote sensing of surface soil water status, *J. Geophys. Res.*, 80, 3044–3049, 1975.

Imhoff, M., M. Story, C. Vermillion, F. Khan, and F. Polcyn, Forest canopy characterization and vegetation penetration assessment with space-borne radar, *IEEE Trans. Geosci. Remote Sens.*, 24, 535–542, 1986.

Jackson, T.J., M. E. Hawley, and P. E. O'Neill, Preplanting soil moisture using passive microwave sensors, *Water Resour. Bull.*, 23(1), 11–19, 1987.

Jackson, T.J., H. McNairn, M. A. Weltz, B. Brisco, and R. J. Brown, First order surface roughness correction of active microwave observations for estimating soil moisture, *IEEE Trans. Geosci. Remote Sens.*, 35(4), 1065–1069, 1997.

Jeager, J. C., Conditions of heat in a solid with periodic boundary conditions with an application to the surface temperature of the moon, *Proc.- Cambr. Philosoph. Soc.*, 49, 355–359, 1953.

Jeffries, M. O., K. Morris, W. F. Weeks, and H. Wakabayashi, Structural and stratigraphic features and ERS-1 synthetic aperture radar backscatter characteristics of ice growing on shallow lakes in N.W. Alaska, winter 1991–1992, *J. Geophys. Res.*, 99(C11), 22459–22471, 1994.

Jeffries, M. O., K. Morris, and G. E. Liston, A method to determine lake depth and water availability on the north slope of Alaska with spaceborne imaging radar and numerical ice growth modeling, *Arctic*, 49(4), 367–374, 1996.

Kahle, A.B., A simple thermal model of the Earth's surface for geologic mapping by remote sensing, *J. Geophys. Res.*, 2(11), 1673–1680, 1977.

Kite, G., and A. Pietroniro, Remote sensing of surface water, in *Remote Sensing in Hydrology and Water Management*, edited by G. A. Schultz, and E. T. Engman, pp. 217–238, Springer, Berlin, 2000.

Kouraev, A.V., E.A. Zakharova, O. Samain, N.M. Mognard, and A. Cazanave, Ob' river discharge from TOPEX?Poseidon satellite altimetry (1992–2002), *Remote Sens. Environ.*, 93, 238–245, 2004.

Kuittinen, R., Remote sensing for hydrology progress and prospects, *Report No. 36*, World Meteorological Organization, Operational Hydrology, Secretariat of the World Meteorological Organization, Geneva, 1992.

Leconte, R., and P. D. Klassen, Lake and river ice investigations in northern Manitoba using airborne SAR imagery, *Arctic*, 44(Supp. 1), 153–163, 1991.

Leconte, R., F. Brissette, M. Galarneau, and T. J. Pultz, Monitoring snow cover in a watershed using RADARSAT data, in *Proceedings of the Workshop on Applications of Remote Sensing in Hydrology*, edited by A. Pietroniro, R. Granger, R., and T. J. Pultz, pp. 331–340, Santa Fe, New Mexico, 4–6 November, 1998, 2000.

Leconte, R., Brissette, F.P., Galarneau, M., and Rousselle, J., Mapping near surface soil moisture with Radarsat-1 SAR data, *Water Res. Res.*, 40, W01515, 2004.

Lewis, A. J., Geomorphic and hydrologic applications of active microwave remote sensing, in *Principles and Applications of Imaging Radar. Manual of Remote Sensing, Third Edition, Volume 2*, edited by F. M. Henderson, and A. J. Lewis, pp. 567–629, New York, John Wiley & Son, Inc., 1998.

MacDonald, H. C., W. P. Waite, and J. S. Demarcke, Use of seasat satellite radar imagery for the detection of standing water beneath forest vegetation, in *Proceedings of the Fall Technical Meeting of the American Society of Photogrammetry*, pp. RS-3-Bl to RS-3-B13, 1980.

Meade, N.G., L. D. Hinzman, and D. L. Kane, Spatial estimation of soil moisture using synthetic aperture radar in Alaska, *Adv. Space Res.*, 24(7), 935–940, 1999.

Melloh, R. A., C. H. Racine, S. W. Sprecher, N. H. Greeley, and P. B. Weyrick, Comparisons of digital terrain data for wetland inventory on two Alaskan army bases, *Special Report 99-15*, 21pp., US Army Corps of Engineers, Cold Regions Research and Engineering Laboratory (CRREL), 1999.

Mertes, L. A. K., Documentation and significance of the perirheic zone of inundated floodplains. *Water Resour. Res.*, 33(7), 1749–1762, 1997.

Morrissey, L. A., S. L. Durden, G. P. Livingston, J. A. Stearn, and L. S. Guild, Differentiating methane source areas in arctic

environments with multitemporal ERS-1 SAR data. *IEEE Trans. Geosci. Remote Sens.*, *34*(3), 667–673, 1996.

Mouchot, M.-C., T. Alfoldi, D. De Lisle, and G. McCullough, Monitoring the water bodies of the Mackenzie Delta by remote sensing methods, *Arctic*, *44*(Supp. 1), 21–28, 1991.

Mulders, M.A., *Remote Sensing in Soil Science*, 379 pp., Elsevier, Amsterdam, 1987.

Njoku, E.G., Jackson, T.J., Lakshmi, V., Chan, T.K., and Nghiem, S.V., Soil moisture retrieval from AMSR-E, *IEEE Trans. Geosci. Remote Sens.*, 41 (2), 215–229, 2003.

Obukhov, A. I., and D. S. Orlov, Spectral reflectivity of the major soil groups and possibility of using diffuse reflection in soil investigations, *Sov. Soil Sci.*, *1964*, 174–184, 1964.

Oh, Y.K., K. Sarabandi, and F. T. Ulaby, F.T. An empirical model and an inversion technique for radar scattering from bare soil surfaces, *IEEE Trans. Geosci. Remote Sens.*, *30*(2), 370–381, 1992.

Ormsby, J. P., B. J. Blanchard, and A. J. Blanchard, Detection of lowland flooding using active microwave systems, *Photogram. Eng. Remote Sens.*, *51*(3), 317–328, 1985.

Pietroniro, A., and R. Leconte, A review of Canadian remote sensing applications in hydrology, 1995–1999, *Hydrol. Processes*, *14*(9), 1641–1666, 2000.

Pietroniro, A., and R. Leconte, A review of Canadian remote sensing and hydrology—1999–2003, *Hydrol. Processes*, *19*, 285–301, 2005.

Pietroniro, A., E.D. Soulis, N. Kouwen, O. Rotunno, and D.W. Mullins, Using wide swath C-band SAR imagery for basin soil moisture mapping, *Can. J. Remote Sens., Special Issue, January*, 77–82, 1993.

Pietroniro, A., T. Prowse, and D. L. Peters, Hydrologic assessment of an inland freshwater delta using multi-temporal satellite remote sensing, *Hydrol. Processes*, *13*, 2483–2498, 1999.

Place, J. L., Mapping of forested wetland: use of Seasat radar images to complement conventional sources, 14pp., U.S. Geological Survey, Reston, Virginia, 1984.

Pratt, D. A., and C. D. Ellyett, The thermal inertia approach to mapping of soil moisture and geology, *Remote Sens .Environ.*, *8*, 151–168, 1979.

Price, J.C., Thermal inertia mapping: A new view of the Earth, *J. Geophys. Res.*, *82*, 2582–2590, 1977.

Price, J.C., The potential of remotely sensed thermal infrared data to infer surface soil moisture and evaporation, *Water Resour. Res.*, *16*, 787–795, 1980.

Pulliainen, J. T., P. J. Mikkelä, M. T. Hallikainen, and J.-P. Ikonen, Seasonal dynamics of C-band backscatter of boreal forests with applications to biomass and soil moisture estimation, *IEEE Trans. Geosci. Remote Sens.*, 34(3), 758–769, 1996.

Pultz, T. J., Y. Crevier, R. J. Brown, and J. B. Boisvert, Monitoring of local environment conditions with SIR-C/X-SAR, *Remote Sens. Environ.*, *59*(2), 248–255, 1997.

Pultz, T. J., D. I. Jobin, and J. Sokol, Temporal RADARSAT observations of pastures for applications in watershed management, in *Proceedings of the Workshop on Applications of Remote Sensing in Hydrology*, edited by A. Pietroniro, R. Granger, and

T. J. Pultz, pp. 361–362, Santa Fe, New Mexico, 4–6 November, 1998, 2000.

Rango, A. and V. V. Salomonson, Regional flood mapping from space. *Water Resour. Res.*, *10*, 473–484, 1974.

Richards, J. A., G.-Q. Sun, and D. S. Simonett, L-band radar backscatter modeling of forest stands. *IEEE Trans. Geosci. Remote Sens.*, *25*(4), 487–498, 1987a.

Richards, J. A., P. W. Woodgate, and A. K. Skidmore, An explanation of enhanced radar backscattering from flooded forests. *Int. J. Remote Sens.*, *8*(7):1093–1100, 1987b.

Roberts, A., K. Bach, C. Kirman, L. Lesack, and P. Marsh, Multitemporal classification of flood parameters in the Mackenzie Delta from airborne MSV and SAP imagery, in *Applications of Remote Sensing in Hydrology*, pp. 127–135, Proceedings of the Second International Workshop, NHRI Symposium No. 14, 1995.

Rosema A., J. H. Bijleveld, P. Reininger, G. Tassone, K. Blyth, and R. J. Gurney, A combined surface temperature, soil moisture and evaporation mapping approach, in *Proceeding of the 12th International Symposium on Remote Sensing of the Environment*, pp. 2267–2275, April 1978, Manilla, Philippines, 1978.

Rotunno Filho, O.C., E. D. Soulis, A. Abdeh-Kolahchi, N. Kouwen, T. J. Pultz, and Y. Crevier, Soil moisture in pasture fields using SAR data: preliminary result,. *Can. J. Remote Sens., 22*(1), 95–107, 1996.

Schmugge, T. J., Microwave approaches in hydrology. *Photogram. Eng. Remote Sens.*, *46*(4), 495–507, 1980.

Schmugge, T. J., Microwave remote sensing of soil moisture, *Recent Advances in Civil Space Remote Sensing, SPIE 481*, 249–257, 1984.

Schmugge, T. J., Remote sensing of soil moisture, in *Hydrological Forecasting*, edited by M. G. Anderson, and T. P. Burt, pp. 101–124, John Wiley and Sons, Chichester, 1985.

Seglenieks, F., E. D. Soulis, and N. Kouwen, Establishment of a relationship between RADARSAT backscatter and soil moisture at hydrologic modelling scales, in *Proceedings of the Workshop on Applications of Remote Sensing in Hydrology*, edited by A. Pietroniro, R. Granger, and T. J. Pultz, pp. 375–386, Santa Fe, New Mexico, 4–6 November, 1998, 2000.

Shi, J., J. V. Soares, L. Hess, E. T. Engman, and J. J. van Zyl, SAR-derived soil moisture measurements for bare fields, in *1991 International Geoscience and Remote Sensing Symposium (IGARSS'91), Vol. 2*, pp. 393–396, Espoo, Finland, 3–6 June, 1991, 1991.

Smith, L. C., Flood mapping from phase decorrelation of tandem ERS data: Ob' River, Siberia, in *Proceedings of the Third ERS Symposium on Space at the Service of our Environment. Vol. 1*, pp. 537–539, 1997a.

Smith, L. C., Satellite remote sensing of river inundation area, stage, and discharge: A review. *Hydrol. Processes*, *11*(10), 1427–1439, 1997b.

Smith, L. C., B. L. Isacks, R. R. Forster, A. L. Bloom, and I. Preuss, Estimation of discharge from braided glacial rivers using ERS 1 synthetic aperture radar: first results, *Water Resour. Res.*, *31*(5), 1325–1329, 1995.

Smith, L. C., B. L. Isacks, and A. L. Bloom, Estimation of discharge from three braided rivers using synthetic aperture radar satellite imagery: Potential application to ungaged basins, *Water Resour. Res.*, *32*(7), 2021–2034, 1996.

Soer, G. J. R. Estimation of regional evapotranspiration and soil moisture conditions using remotely sensed crop surface temperatures, *Remote Sens. Environ.*, *9*, 27–45, 1980.

Sokol, J., T. Pultz, and V. Bulzgis, Investigating Labrador fens and bogs using multi-temporal ERS-2 and RADARSAT data, in *22nd Canadian Symposium on Remote Sensing*, pp. 357–364, 2000.

Stratton, J. A., *Electromagnetic Theory*. McGraw–Hill, New York, 1941.

Swain, P. H., and S. M. Davis (Eds.), *Remote Sensing: The Quantitative Approach*, 396 pp., McGraw-Hill, New York, 1978.

Szekielda, K-H., *Satellite Monitoring of the Earth*, 326 pp., John Wiley and Sons, New York, 1988.

Topp, G.C., J. L. Davis, and A. P. Annan, Electromagnetic determination of soil water content: measurements in coxial transmission lines, *Water Resour. Res.*, *16*(3), 574–582, 1980.

Töyrä, J., A. Pietroniro, and L. W. Martz, Multisensor hydrologic assessment of a freshwater wetland, *Remote Sens. Environ.*, *75*(2), 162–173, 2001.

Ulaby, F.T., Radar measurements of soil moisture content, *IEEE Trans. Antennas. Propag.*, AP-22(2), 257–265, 1974.

Ulaby, F. T., Microwave remote sensing of hydrologic parameters, in *Proceedings of the Eleventh International Symposium of Remote Sensing of Environment, Volume 1*, pp. 67–86, 1977.

Ulaby, F.T., and P. P. Batlivala, Optimum radar parameters for mapping soil moisture". *IEEE Trans. Geosci. Electron.*, *GE-14*, 81–93, 1976.

Ulaby, F. T., R. K. Moore and A. K. Fung, *Microwave Remote Sensing—Active and Passive,* vol. 2, Addison - Wesley Publishing, Reading, Mass, 1982.

Ulaby, F.T., R. K. Moore, and A. K. Fung, *Microwave Remote Sensing: Active and Passive*, vol. 3, 2162 pp., Artech House, Dedham, 1986.

Van de Griend, A.A., and E. T. Engman, Partial area hydrology and remote sensing, *J. Hydrol.*, *81*, 211–251, 1985.

Vanderbilt, V. C., *et al.*, Discrimination of wetland and non-wetland community types with multi-spectral, multi-angle, polarized data, in *Proceedings of the Seventh International Symposium on Physical Measurements and Signatures in Remote Sensing. Vol. 2*, pp. 809–813, 1997.

Waite, W. P., H. C. MacDonald, V. H. Kaupp, and J. S. Demarcke, Wetland mapping with imaging radar, in *1981 International Geoscience and Remote Sensing Symposium (IGARSS '81). Vol. 2*, pp. 794–799, 1981.

Wang, Y., and M. L. Imhoff, Simulated and observed L-HH radar backscatter from tropical mangrove forests, *Int. J. Remote Sens.*, *14*(15), 2819–2828, 1993.

Wang, J.R., and T. J. Schmugge, An empirical model for the complex dielectric permittivity of soils as a function of water content, *IEEE Trans. Geosci. Remote Sens.*, *GE-18*, 288–295, 1980.

Wang, Y., J. L. Day, and G. Sun, Santa Barbara microwave backscattering model for woodlands, *Int. J. Remote Sens. 14*, 1477–1493, 1993.

Wang, Y., L. L. Hess, S. Filoso, and J. M. Melack, Understanding the radar backscattering from flooded and non-flooded Amazonian forests: Results from canopy backscatter modeling, *Remote Sens. Environ.*, *54*, 324–332, 1995.

Wang, Y., E. S. Kasischke, L. L. Bourgeau-Chavez, K. P. O'Neill, and N. H. F. French, Assessing the influence of vegetation cover on soil moisture signatures in fire-disturbed boreal forests in interior Alaska: modelled results, *Int. J. Remote Sens.*, *21*(4), 689–708, 2000.

Watson, K., Periodic heating of a layer over a semi-inflnite soil, *J. Geophys. Res.*, *78*, 5904–5910, 1973.

Wedler, E., and R. Kessler, Interpretation of vegetative cover in wetlands using four-channel SAR imagery, in *Proceedings of the Annual Meeting of the American Society of Photogrammetry*, pp. 111–124, 1981.

Weeks, W. F., P. V. Sellmann, and W. J. Campbell, Interesting features of radar imagery of ice-covered north slope lakes, *J. Glaciol.*, *18*(78), 129–136, 1977.

Weeks, W. F., A. G. Fountain, M. L. Bryan, and C. Elachi, Differences in radar returns from ice-covered north slope lakes, *J. Geophys. Res.*, *83*(C8), 4069–4073, 1978.

Wiesnet, D. R., D. F. McGinnis, and J. A. Pritchard, Mapping of the 1973 Mississippi River floods by the NOAA-2 satellite, *Water Resour. Bull.*, *10*(5), 1040–1049, 1974.

Work, E. A., and D. S. Gilmer, Utilization of satellite data for inventorying prairie ponds and lakes, *Photogram. Eng. Remote Sens.*, *42*(5), 685–694, 1976.

Xu, Q. P., J. B. Boisvert, I. Rubinstein, C. Hersom, N. Tremblay, R. Protz, and F. Bonn, Microwave, visible and infrared spectral properties as a function of water content in organic soils, *Can. J. Remote Sens.*, *24*(1), 3–16, 1998a.

Xu, Q. P., J. B. Boisvert, N. Tremblay, F. Bonn, R. J. Brown, Evaluation des hyperfrèquences pour le suivi de la teneur en eau des cultures dans les histosols, *Can. J. Remote Sens.*, *24*(1), 43–52, 1998b.

Yamagata, Y., and Y. Yasuoka, Classification of wetland vegetation by texture analysis methods using ERS-1 and JERS-1 images, in *1983 International Geoscience and Remote Sensing Symposium (IGARSS '93). Vol. 4*, pp. 1014–1016, 1993.

Geoff Kite, International Water Management Institute, IWMI, PO Box 2075, Colombo, Sri Lanka. (geoffkite@hydrologic-solutions.com)

Robert Leconte, Département de génie de la construction, École de technologie supérieure, 1100 rue Notre Dame Ouest, Montréal, Province Québec, H3C 1K3 Canada. (rleconte@ctn.etsmtl.ca)

Alain Pietroniro and Jessika Töyrä, National Water Research Institute, 11 Innovation Blvd., Saskatoon, Saskatchewan, S7N 3H5 Canada. (al.pietroniro@ec.gc.ca)

Evaporation/Evapotranspiration Estimates
With Remote Sensing

Raoul Granger

National Water Research Institute, Saskatoon, Saskatchewan, Canada

Normand Bussières

Meteorological Service of Canada, Downsview, Ontario, Canada

Evaporation is the transfer of water from a surface to the atmosphere. The evaporative process is intimately linked to the energy balance. In northern environments, the interactions between energy, land, and water can be different from those for more temperate regions. The application of any evapotranspiration model, with or without the use of remotely sensed data, to the northern environment requires that due consideration be given to those factors that become increasingly significant as one moves northward. For methods based on some reformulation of the energy balance, the inclusion and correct parameterization of the soil heat flux term is essential. The effect of the vegetation cover on the partitioning of energy to soil heat flux has been recognized and is demonstrated. Remote sensing of evaporation from water surfaces in northern regions suffers from two major deficiencies: (1) Relatively little is known about the evaporation regime of northern lakes; and (2) relatively little effort has been directed towards the development of remote sensing techniques for estimating evaporation from open water in general. For the estimation of lake evaporation, an improved understanding of the advective boundary layer over water is required. With respect to remote sensing of lake evaporation, although water surface temperatures are easily obtained in the absence of cloud cover, improved parameterization of ice formation and decay is required.

1. INTRODUCTION

Monitoring the Earth's water vapor cycle is crucial for improving the management of the planet's freshwater resources. Precipitation, runoff, stream flow, storage, evaporation from water surfaces, and transpiration from plants form the continental components of the water cycle. *Brutsaert* [1982], examining the water budget for the entire earth, indicated that the annual evaporation from

land surfaces is approximately 65% of annual precipitation; *Gray et al.* [1970] placed this figure near 75% for the North American continent. Using observed precipitation and runoff data from a 20-year study of water balance for the Mackenzie River basin, *Kite et al.* [1994] showed that for this northern basin, 57% of the precipitation was apportioned to evaporation. A significant portion of the water that is received at the surface through precipitation is thus returned to the atmosphere through evaporation. The correct determination of this flux is therefore important to the overall water balance of a region.

Knowing the spatial distribution and amount of evapotranspiration is important for a number of reasons: for the

water manager, to determine the balance within a river basin; for the agricultural manager, to determine potential yields and irrigation requirements; and for the meteorologist, to determine the location and intensity of cloud development. However, evapotranspiration is difficult and costly to measure, and accurate measurements of local water vapor flux are generally made only at a limited number of research sites. There is no direct method for measuring regional evapotranspiration, at the scale of a large hydrological basin, for example, but modeling and remote sensing techniques have been developed for this purpose. Approximate values can be computed locally with techniques that make use of standard meteorological network data, and regional values can be derived from interpolation of local values. In some regions, however, the data network is too sparse to allow for this. The remote, less densely populated and northern regions are typical of these. Remote sensing provides a means of obtaining information of a regional nature in regions where existing data networks are sparse.

1.1. Evaporation/Evapotranspiration Background

Evaporation is the transfer of water from a surface to the atmosphere. For the process of evaporation to proceed, the following three conditions must be satisfied: (1) There must be a source of water at the surface; (2) there must be a supply of energy to ensure the phase change from liquid to vapor; and (3) there must be a transport mechanism to carry the vapor from the surface.

The water vapor is carried from the surface to the overlying air along the water vapor gradient within the turbulent boundary layer. The evaporation rate can be determined by using aerodynamic, or flux-gradient, relationships:

$$E = f(U)\partial q/\partial z \qquad (1)$$

where $f(U)$ is a transfer coefficient (usually a function of the horizontal wind speed, U), q is the specific humidity, and z is the height above the surface.

The major source of energy for evaporation in the natural environment is the solar radiation reaching the surface; there can, of course, exist some situations where the advection of energy contributes to the evaporation process, but these tend to be of lesser importance than the radiation. There is also some competition at the surface for this energy; the radiant energy reaching a surface can also be partitioned to heat the soil and the overlying air. This partitioning of energy at a surface is controlled by the relative diffusivities, or effectiveness of the transport mechanisms, for the heat conduction into the soil, the turbulent heat transfer in the boundary layer, and the turbulent transport of water vapor.

The sources of water are varied. Open water surfaces obviously provide a direct, unrestricted supply of water for evaporation. Soil surfaces can provide water for evaporation when wetted by precipitation or irrigation, but these begin to dry as the evaporation process advances. Plants, on the other hand, have the capability through their vascular system of transporting water to their leaf surfaces and, through their stomata, of controlling the rate at which it is made available for evaporation. The process by which plants release water for evaporation is called transpiration. Since most of the Earth's land surface, with the exception of desert and polar regions, is covered by some form of vegetation, the land surface evaporative process, which includes both evaporation from the soil and transpiration by plants, is called evapotranspiration.

Evapotranspiration can thus be determined from the energy balance, expressed as the partitioning of the energy supply. This is written as

$$R_n = G + H + LE \qquad (2)$$

where R_n is the net radiation, G is the heat flux into the soil, H is the turbulent transfer of sensible heat in the atmosphere, and LE is the turbulent latent heat flux, with E being the evaporation rate and L the latent heat of vaporization. In equation (2), R_n directed towards the surface is taken as positive, while the other terms are taken as positive when directed away from the surface.

Evapotranspiration can also be determined from the water balance, expressed here as the partitioning of the water supply:

$$P = I + Q + \delta S + E \qquad (3)$$

where P is the precipitation, I is the infiltration into the soil, Q is the runoff, and δS is the change in water storage.

Evapotranspiration can also be determined from consideration of the turbulent boundary layer (flux-gradient relationships), which in its simplest form is expressed as:

$$E = K(q_s - q_a) \qquad (4)$$

where q is the humidity ratio; the subscripts s and a refer to the surface and the atmosphere, respectively; and K, the turbulent transfer coefficient, is a complex function of the wind field and the atmospheric stability.

Most of the practical schemes devised to estimate the evaporation/evapotranspiration rates take these three conditions into account in some manner. For example, *Penman* [1948] combined the energy balance and aerodynamic considerations for a wet surface to produce his well-known general equation for evaporation. The Penman equation, or

some form of extension of this equation to the nonsaturated case, now forms the basis for most evapotranspiration modeling approaches.

1.2. Evaporation/Evapotranspiration in Northern Environments

Relatively few studies have been directed specifically towards the determination of evaporation or evapotranspiration in northern environments; these have, nonetheless, demonstrated the importance of the evaporative component to the energy and water balances of these environments. *Rouse et al.* [1977] showed that the daily midsummer values of the evaporative fraction (ratio of latent heat to incoming radiant energy) can range from values near 0.3 for lichen heath and burned areas to near 0.5 for wet sedge tundra and a shallow tundra lake. *Kane et al.* [1990] provide values for the evaporative fraction ranging from 0.4 to 0.65 for a small Alaskan watershed; these represent from 35% to 65% of the annual precipitation. *Granger* [1999], in the Yukon Territory, Canada, and *Vourlitis and Oechel* [1999], in Alaska, USA, demonstrated that the seasonal variation of the evaporative component (Bowen ratio) decreased and evaporative fraction increased through the active growing season. Figure 1 compares the monthly Bowen ratios for the snow-free season over mature conifer stands in the southern (Prince Albert, Saskatchewan) and the northern (Whitehorse, Yukon) boreal forests. The data for these sites are taken from *Pomeroy et al.* [1997] and *Granger* [1999], respectively. The figure shows that although for the southern site, the Bowen ratio fluctuates between 0.7 and 0.9, for the northern site the Bowen ratio decreases continually from 0.95 after snowmelt to 0.5 at the end of the summer season. This suggests that the vegetation control on evapotranspiration in northern regions varies with the season in a manner that is quite different from that of southern vegetation [*Soegaard*, 1999; *Zhang et al.*, 2000].

Methods of estimating evapotranspiration developed in temperate climates—particularly those ignoring the effects of soil heat storage and employing plant physiological parameters such as stomatal controls—may not be directly transferable to northern areas. Measurements over Alaskan tundra [*Vourlitis and Oechel*, 1999] showed that 12–19% of net radiation is partitioned to soil heat flux. These results, similar to those of *Granger* [1996] for the Yukon Territory, indicate that for northern regions, ignoring the soil heat storage term can result in significant errors in evapotranspiration estimates. The reader is also referred to *Duguay et al.* [this volume] for a more complete discussion on the significance of frozen soils and permafrost in northern environments. Both these studies [*Granger*, 1996; *Vourlitis and Oechel*, 1999] also showed that controls exerted by vegetation may be quite
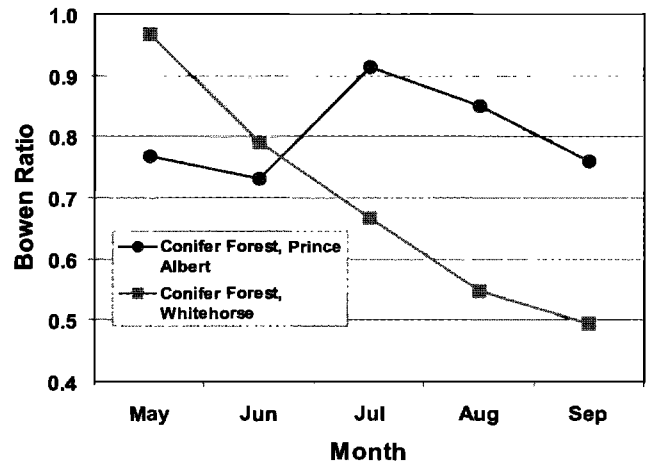
Figure 1. Monthly Bowen ratios over mature conifer stands in the southern (Prince Albert) and northern (Whitehorse) boreal forests. The values are averages for the three snow-free seasons from 1994 to 1996.

different in northern regions. *Granger* [1996] suggested that energy limitations are such that plants in northern regions have evolved to cope with the specific conditions. *Vourlitis and Oechel* [1999] showed that the Bowen ratio increased through the season, indicating that vegetation control varies with the season in a manner that is quite different from that of southern vegetation. The initially frozen or cold soils tend to limit the plants' capability to use water early in the season; the plants compensate for this by becoming increasingly active as the season progresses.

Fewer studies yet have been directed towards the remote sensing of evaporation or evapotranspiration in northern regions. *Gurney et al.* [1983] used HCMM and Landsat images to show the relationship between surface temperature and vegetation biomass in Alaska; *Duguay and Crevier* [1995] used remote sensing and field measurements to estimate surface energy balance components over alpine tundra surfaces. However, neither of these studies addressed evapotranspiration in a direct manner.

2. REMOTE SENSING OF EVAPOTRANSPIRATION FROM LAND SURFACES

Menenti [2000] presents a summary of the feasible observations and required model variables for the remote sensing of evaporation. However, the information obtained from remote sensing platforms is not always that which is most practical to, or directly applicable within, those algorithms available for estimating evapotranspiration. For example, within algorithms using an aerodynamic approach, the near-surface humidity gradient of the air determines the

evapotranspiration rate; however, the near-surface moisture content of the air is not detectable by remote sensing techniques. The near-surface wind speed, the major factor in the turbulent transfer coefficient, cannot be detected by using satellite remote sensing. Most of the terms of the water balance (equation 2) are not accessible through remote sensing. The surface soil moisture is detectable with radar or microwave sensors; however, the degree of accuracy of these measurements is generally insufficient for establishing the surface–air moisture gradient. The energy balance (equation 1), however, has been somewhat more accessible. *Royer et al.* [1997] discuss the parameterization of the energy balance terms using remote sensing. The net radiation, R_n, can be approximated by using remote sensing since the reflected radiance can provide a reasonable estimate of the surface albedo [*Gutman*, 1988; *Granger*, 1997], and the emitted radiance provides a means of estimating the surface temperature, which in turn provides the emitted portion of the long-wave exchange. The surface temperature is also the boundary condition for the soil heat term, G, as well as for the turbulent transfer of sensible heat, H.

The surface temperature is probably the most accessible remotely sensed parameter, whereas the vapor pressure deficit is not detectable remotely. It is not surprising then that most practical schemes devised to estimate evapotranspiration using remote sensing are based on some variation of the energy balance (equation 2). It is not our purpose here to provide a complete review of methods and results obtained, but to present only the general forms of the development of methods. *Bussières* [1990] provides a summary of the earlier versions of the simplified energy balance approaches. The earliest version [*Jackson et al.*, 1977] was a simplified form of equation (2), with the assumption of negligible soil heat flux and a linear relationship between the daily sensible heat flux, H, and the instantaneous (or one-time per day) temperature gradient in the air. These early energy balance methods all require the collection of concurrent ground data, usually air temperature, for their application.

Further refinements [*Seguin and Itier*, 1983; *Rambal et al.*, 1985] led to the following expression to estimate evapotranspiration by remote sensing:

$$LE^{24} \approx R_n^{24} + A - B(T_o - T_a)^n \qquad (5)$$

in which LE^{24} and R_n^{24} are the 24-h totals for latent heat and net radiation, respectively; T_o and T_a are the instantaneous surface and air temperatures, respectively; and A, B, and n are constants that require adjustment through calibration. Constant A can be seen as replacing the soil heat term, B the heat transfer coefficient, and n an additional calibration constant for use with a specific type of land cover condition.

The exercise quickly became one of finding the appropriate values for these coefficients. With a wide variety of surface cover types, wind regimes, and climatic conditions found in nature, there was, of course, an equally wide variety of coefficients to be found.

A second approach involves the addition of remotely sensed information to existing ecological, hydrological, and other engineering-type models. For example, remotely sensed radiances are converted through empirical relationships to surface temperature and leaf area index (LAI); evapotranspiration is then estimated by using a regression involving surface temperature (T_s) and the normalized difference vegetation index (*NDVI*) [*Running et al.*, 1989; *di Bella et al.*, 2000]:

$$LE = A + bT_s + cNDVI \qquad (6)$$

Relationships such as that represented by equation (6) have the advantage that no concurrent ground-based data are required; evapotranspiration is estimated only from remotely sensed data. *Liu et al.* [1997, 1999] used a combination of satellite-derived LAI estimates within the Boreal Ecosystems Productivity Simulator (BEPS), to produce a prototype yearly evapotranspiration map for the Canadian land surface for the 1994 water year. The BEPS model relies on a modified Penman–Monteith formulation in which the canopy resistance term is related to the vegetation index.

The approach proposed by *Granger* [1995, 1997] makes use of a feedback relationship between the surface and boundary layer, as described by *Bouchet* [1963] and *Morton* [1983]. Through regression, a relationship is established between the observed surface temperature and the vapor pressure deficit in the air.

Granger [1995] derived the following relationship between the mean daily vapor pressure deficit of the air, VP_{def}, and the saturation vapor pressure, VP^*_{Ts}, at the mean daily surface temperature:

$$VP_{def} = -0.278 - 0.015T_{ltm} + 0.668VP^*_{Ts} \qquad (7)$$

in which T_{ltm}, the long-term mean air temperature for the site, is used to account for seasonal effects in the relationship. *Granger* [1995] demonstrated that the advantage of this approach is that it provides the required input data (vapor pressure deficit) for the application of a conventional evapotranspiration model based on the extension of the *Penman* [1948] approach to nonsaturated conditions. Using the net radiation term estimated from the surface albedo obtained from the visible reflectance, this approach also allows for estimation of evapotranspiration by using only remotely sensed data.

Plate 1 is an evapotranspiration map [from *Granger*, 1995] of central Saskatchewan, Canada, generated for July 12, 1991. For the 5-day study period, the evapotranspiration obtained from the image (21.8 mm) compared very well with that obtained from ground-based data in conjunction with Morton's [1983] regional evapotranspiration model (23.7 mm).

Much more complex versions of the energy and water balances can also be used in conjunction with remotely sensed data to provide estimates of evapotranspiration. *Gellens-Meulenberghs et al.* [1994] were among the first to introduce a boundary layer treatment, including wind speed in flux parameterization for remotely sensed evapotranspiration estimates. *Friedl* [2002], reviewing most of the recent works associated with these more complex developments, illustrated the superiority of a two-layer ground-canopy model over the single-layer model given by equation (4). The most complex approaches that can be used are soil vegetation atmosphere transfer (SVAT) models. These models provide a more detailed and realistic representation of the land surface and boundary layer interactions. They can include parameterizations for soil moisture accounting, based on soil type and root extraction of moisture; they can account for the influence of vegetation type and state and of atmospheric stability on the turbulent transfer of heat and moisture; and they are usually coupled with planetary boundary layer models [e.g., *Bastiaanssen et al.*, 1998a,b].

Generally, the more complex the approach, the greater the number of required input parameters (e.g., air temperature, wind speed) and the greater the number of required parameterizations (e.g., soil physical parameters, vegetation physical parameters, roughness parameterizations, surface resistance parameterizations). With only very few of these being available through remote sensing, the law of diminishing returns quickly applies. For example, in a study over the Gediz basin in Turkey, the feedback approach [*Granger, 2000b*] and the surface energy balance model (SEBAL) [*Bastiaanssen*, 2000], despite a large difference in complexity, produced comparable results [*Kite and Droogers*, 2000].

2.1. Application to the Northern Environment

The application of any evapotranspiration model, with or without the use of remotely sensed data, to the northern environment requires that due consideration be given to those factors that become increasingly significant as one moves northward. For methods based on some reformulation of the energy balance, inclusion and correct parameterization of the soil heat flux term are essential. The effect of the vegetation cover (LAI) on the partitioning of energy to soil heat flux has been recognized and is becoming increasingly understood [*Kustas et al.*, 1993; *Duguay and Crevier*, 1995].

These authors showed a linear relationship between the daily soil heat flux ratio and the LAI. More recently, *Granger and Toth* [2001] have also demonstrated the added effects of season and latitude on the soil heat flux ratio. Using data from a number of nonpermafrost sites situated along a north–south transect from southern Saskatchewan to the Canadian arctic, they derived the following relationship:

$$Q_g/R_n = 0.00735\phi - 0.0043LAI - 0.266 \qquad (8)$$

where Q_g and R_n are the daily soil heat flux and net radiation, respectively, and ϕ is the solar angle in degrees. The regression coefficient for the relationship is 0.85. The presence of permafrost provides an added complication; the reader is referred to *Duguay et al.* [this volume] for a more complete discussion.

Those methods relying on the parameterization of canopy controls on evapotranspiration must also take into account the distinct manner in which these controls are exerted in the energy-limited northern environments [*Hall et al.*, 1992; *Granger*, 1996; *Vourlitis and Oechel*, 1999]. They must also consider the presence of wetlands, the sparse vegetation in some forested areas, and the manner in which nonvascular plants, such as lichens, exert controls on evapotranspiration.

The existing algorithms (equations 5 to 7) were designed for thermal remote sensing of the surface, which is limited to clear sky situations. Cloud cover can be very frequent in the warm season in northern environments. This represents a serious sampling drawback that was examined by *Bussières and Goita* [1997]. The International Satellite Cloud Climatology Project (ISCCP) [*Rossow et al.*, 1991] provides on their web site (http://isccp.giss.nasa.gov) global maps of the total cloud amount for 1983–1995. According to these maps, at latitudes north of 50°N, the 11-year mean spring, summer, and autumn cloud cover usually exceeds 60%, and over large areas it can exceed 80%. SVAT schemes coupled with earth–atmosphere models that can incorporate various types of data at discontinuous times and space scales (data assimilation) represent a potential solution to the sampling problems, if spatial scale issues can first be resolved [*Friedl*, 2002].

3. REMOTE SENSING OF EVAPORATION FROM WATER SURFACES

One need only look at any map of North America to note that open waters (lakes, rivers, and wetlands) account for a significant portion of the northern shield region of the continent. For instance, estimates from the 1-km resolution land cover classification indicates that the region covered by BOREAS (Boreal Ecosystem–Atmosphere Study) contains some 6,000 water bodies of 1 km² or greater in size; these
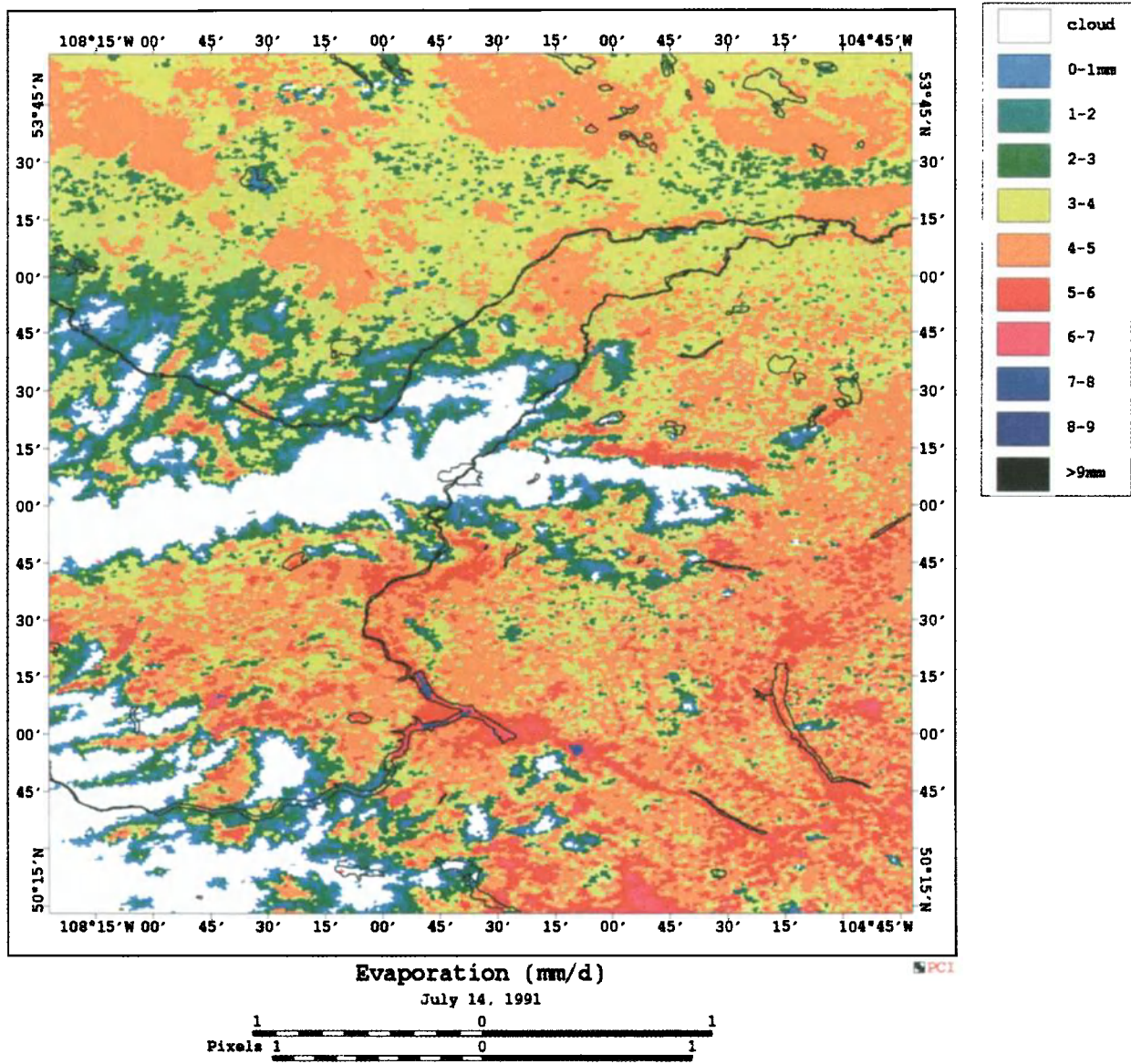
Plate 1. Evapotranspiration map of central Saskatchewan, Canada, generated from NOAA AVHRR imagery for July 14, 1991 [from *Granger*, 1995].

represent approximately 13% of the surface area of the region [*Bussières et al.*, 2002]. Evaporation from these wet surfaces must be an important consideration in the study of the water resources of the region.

Remote sensing of evaporation from water surfaces in northern regions suffers from two major deficiencies: (1) Relatively little is known about the evaporation regime of northern lakes—a few studies have been initiated as part of MAGS (Mackenzie GEWEX Sudy) [*Rouse et al.*, 2001; *Schertzer et al.*, 2000]; and (2) relatively little effort has been directed towards the development of remote sensing techniques for the estimation of evaporation from open water in general. For example, *Schultz and Engman* [2000], in their recent review of remote sensing for hydrology and water management, ignore the subject of evaporation from open water altogether.

The major deterrent to the development of appropriate and reliable techniques for estimating lake evaporation is the fact that the meteorological parameters required for the application of evaporation models and algorithms are rarely measured over water surfaces. Moreover, the thermal lag between the water and land surfaces renders the land-based measurements ineffective in the parameterization of open water evaporation. Lake evaporation estimates have been obtained from mass balance methods, from empirical formulae, and from models of open water evaporation. The empirical formulae, such as that of *Meyer* [1915], are based on simple regressions and, without significant recalibration efforts, are rarely transportable to basins other than that for which they were derived. Although lake evaporation models such as that of *Morton* [1983] are being used operationally, these rely totally on measurements obtained over land, incorporating the effects of the advection of energy between land and water surfaces in a very hypothetical manner. For example, *Morton* [1983] assumes that the lake evaporation, with adjustments for heat storage effects, is a manifestation of the "potential evaporation" as determined from adjacent land observations of temperature and humidity. *Granger* [2000a] points out that lake evaporation is largely uncoupled from the land surface evapotranspiration. The land surface processes follow closely the pattern of energy supply, so the partitioning of the net radiation is straightforward; the soil heat flux tends to be relatively small for most situations, and the turbulent fluxes of sensible and latent heat, for the most part, behave in a similar manner. The partitioning of energy at a lake surface, on the other hand, is more complex. This is demonstrated in Figure 2, which shows concurrent land surface and water surface evaporation from Quill Lake in central Saskatchewan. Whereas the land surface evapotranspiration follows the radiant energy supply, the lake surface evaporation does not
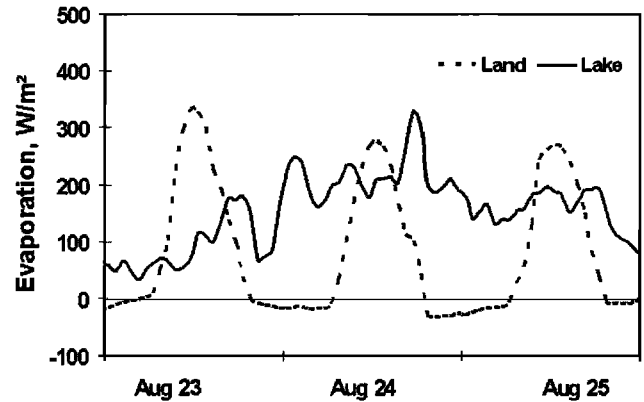
Figure 2. Water surface evaporation from Quill Lake, Saskatchewan, and evapotranspiration from adjacent land surface for three consecutive days in 1993 [from *Granger*, 2000a].

follow this diurnal cycle. The surface water temperature, which determines the vapor pressure gradient and thus the direction of the vapor flux, is affected by other factors, such as wind and the mixing of lake water. Because of radiation penetration, heat storage effects can be significant and may not immediately be reflected in the surface water temperature. The turbulent fluxes of sensible and latent heat are not necessarily in phase with the energy supply; rather, they are governed by the gradients of temperature and humidity in the boundary layer. These gradients are controlled both by water surface temperatures (affected by radiation and intermittent mixing of the water) and by the processes occurring at the upwind land surface (heating of the air and evapotranspiration). For these reasons, land surface data alone are insufficient to parameterize lake evaporation: Information about the lake surface is also required. For northern environments, the phase lag between seasonal land and water temperatures is increased.

The use of remotely sensed data provides a means of obtaining useful information about the evaporating water surface; airborne and spaceborne sensors can be used to measure land and water surface temperatures [*Wan and Dozier*, 1989; *Prata and Platt*, 1991; *Harris and Mason*, 1992]. For the northern region, *Bussières et al.* [2002] and *Bussières and Schertzer* [2003] observed the seasonal variation of water surface temperature for a series of lakes covering a broad range of locations and sizes.

Plate 2 shows the effect of latitude on the seasonal surface water temperatures for 52 Canadian lakes in the Mackenzie basin, determined from AVHRR images. A quadratic equation was fitted to temperature estimates for each lake, and results were grouped by 2° latitude bands from 50°N to 66°N. The figure illustrates that the more northerly lakes show a seasonal temperature curve with delayed thaw, lower amplitude, and delayed peak.
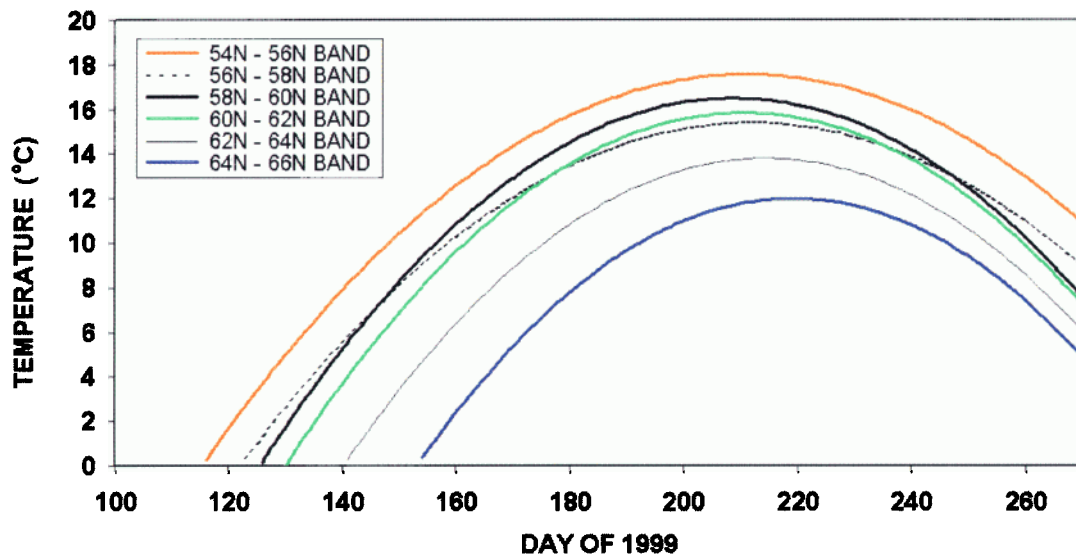
Plate 2. Derived seasonal water surface temperature curves for Canadian lakes, between 50° and 66°N, grouped in 2° bands [from *Bussières and Schertzer*, 2003].

However, water surface temperatures alone are insufficient to establish evaporation rates since, in an advective situation such as that represented by relatively dry air moving across a lake, the state of the boundary layer and the processes occurring over the adjacent land surfaces are also important. For remote sensing to be useful in the estimate of lake evaporation, the data must be applicable within an appropriate formulation of the transfer processes occurring in the advective boundary layer. A combined remote sensing and modelling approach is thus required. *Granger* [2000a] presented the potential of applying such an approach. He compared the numerical solution to the advection problem developed by *Weisman and Brutsaert* [1973] to the measured evaporation from a small lake in Saskatchewan.

Weisman and Brutsaert [1973] derived a numerical solution for the equations of conservation of mass, momentum, energy, and water vapor for the case of neutrally stratified air moving over a warm water surface. They expressed their results in terms of a dimensionless rate of evaporation:

$$E^* = \frac{(E_l - E_a)}{\rho \cdot u_* \cdot (q_s - q_{as})} \qquad (9)$$

where E_l is the mean evaporation from the water surface, E_a is the evapotranspiration from the upwind surface, ρ is the air density, u_* is the upwind friction velocity, and q_s and q_{as} are the specific humidity values at the water and upwind surfaces, respectively. The dimensionless rate of evaporation, E^*, was shown to be a simple power function of the dimensionless fetch, such that

$$E^* = a \left(\frac{X_f}{Z_o} \right)^{-b} \qquad (10)$$

where the fetch, X_f, is the distance from the shore, and Z_o is the roughness height of the upwind surface. For the purpose of their analysis, *Weisman and Brutsaert* [1973] assumed that the roughness heights of the land and water surfaces were similar. The coefficients, a and b, are constants for given values of the dimensionless parameters, A^* and B^*, which represent a measure of the discontinuity between the land and water surfaces. These parameters are defined as follows:

$$A^* = -\frac{(T_s - T_{as})}{T_{as}} \cdot \frac{kgZ_o}{u_*^2} \qquad (11)$$

and

$$B^* = -0.61 \cdot (q_s - q_{as}) \cdot \frac{kgZ_o}{u_*^2} \qquad (12)$$

where, k is the von Karman constant, g is the acceleration due to gravity, and T_s and T_{as} are the surface temperature values

at the water and upwind surfaces, respectively. *Weisman and Brutsaert* [1973] provide tables of values for the coefficients, a and b, for given values of the parameters A^* and B^*.

Combining equations (9) and (10) yields the following expression for the mean open water evaporation:

$$E_l = E_a + a\rho u_* \cdot (q_s - q_{as}) \cdot \left(\frac{X_f}{Z_o} \right)^{-b} \qquad (13)$$

Equation (13) relates the lake evaporation to the upwind evapotranspiration and to the discontinuity in surface values of specific humidity. From the point of view of developing a remote sensing–based approach, equation (13) is interesting in that most of the terms on the right-hand side can be obtained with the use of remotely sensed data; the only exception is the friction velocity, which can be estimated from ground-based observations of wind speed. There are practical methods for estimating the upwind evapotranspiration with remote sensing (see above). The remotely sensed water surface temperature yields the specific humidity, q_s, directly. The upwind surface humidity, q_{as}, can be estimated from the vapor transfer equation and the humidity gradient once E_a has been calculated. The coefficients, a and b, are also related to surface parameters that can be derived from remotely sensed data.

Granger [2000a], using observed lake evaporation data, demonstrated that this combined remote sensing–analytical approach works well. Unfortunately, the Weisman and Brutsaert analysis was limited to the case of an unstable boundary layer over the water; for this approach to be complete, the numerical solutions must be derived for the case of a stable boundary layer.

3.1. Application to the Northern Environment

In addition to those factors affecting land surface evapotranspiration, the application of schemes for the estimation of lake evaporation in northern environments must also take into account the influence of the lag in the storage of energy within the lakes and the seasonal presence of an ice cover.

In northern environments, the surface of most water bodies becomes completely frozen during the winter season. The ice-free period must then be determined for one to know when to compute evaporation from the free water surface to the atmosphere. The ice-free period varies depending on climate, latitude, and individual characteristics of each water body. The number of water bodies can be very large and in countries like Canada, for example, the ice conditions are monitored locally on just a small number of these water bodies [*Duguay et al.*, in press]. Remote sensing techniques have been developed to assist in obtaining the required information. A number of techniques involve either passive microwave data or satellite

radar data [*Goodison et al.*, 1999]. Approaches using these data as well as visible imagery are presented in *Jeffries et al.* [this volume]. Thermal infrared data can also serve for this purpose, while also allowing the determination of water temperature [*Bussières et al.*, 2002].

4. FUTURE RESEARCH NEEDS FOR NORTHERN ENVIRONMENTS

The improved representation of hydrological processes, including evaporation and evapotranspiration, in northern environments requires a better understanding of both the northern land covers and those factors affecting the key processes. The diversity of the northern landscape needs to be better understood along with the relative importance of shield areas, exposed rock, wetlands and their unique responses in northern environments, sparsely vegetated forests, and tundra vegetation. The effect of seasonally frozen soil, thawing soil, and permafrost on the partitioning of energy needs to be studied further. With respect to the application of remote sensing techniques for estimating evapotranspiration, the greatest potential lies in the development and/or improvement of combination approaches (remote sensing and modelling), such as SVAT models that use remotely sensed data. However, these methods must correctly parameterize those effects and processes, such as soil heat storage, that are significant in northern environments.

For estimation of lake evaporation, an improved understanding of the advective boundary layer over water is required, particularly for the case of the stable boundary layer. With respect to remote sensing of lake evaporation, improved parameterization of ice formation and decay is required. Improved techniques for obtaining surface parameters in the presence of cloud cover will also be necessary.

REFERENCES

Bastiaanssen W.G.M., SEBAL-based sensible and latent heat fluxes in the irrigated Gediz Basin, Turkey. In: Comparing actual evapotranspiration from satellite data, hydrological models and field data, *J. Hydrol.*, *229*(1–2), 87–100, 2000.

Bastiaanssen, W.G.M., M. Menenti, R.A. Feddes, A.A.M. Holtslag, A remote sensing surface energy balance algorithm for land (SEBAL). 1. Formulation. *J. Hydrol.*, 212/213(1/4), 198–212, 1998.

Bastiaanssen, W.G.M., H. Pelgrum, J. Wang, Y. Ma, J.F. Moreno, G.J. Roerink, T. van der Wal, A remote sensing surface energy balance algorithm for land (SEBAL). 2. Validation. *J. Hydrol.*, 212/213(1/4), 213–229, 1998.

Bouchet, R.J., Evapotranspiration réelle et potentielle, signification climatique. *Int. Assoc. Sci. Hydrol. Proc.* Berkeley, CA Symp. Publ. *62*, 134–142, 1963.

Brutsaert, W., *Evaporation Into the Atmosphere: Theory, History, and Application,* 299 pp., D. Reidel Publishing Co., Dordrecht, Holland, 1982.

Bussières, N., Developments in methods to estimate evapotranspiration using satellite and ground-based meteorological data, in *Proceedings of Eighth Conference on Hydrometeorology,* October 22-26, Kanakaskis Park, Alberta, Canada, pp. 204–206, 1990.

Bussières, N., and K. Goïta, Evaluation of strategies to deal with cloudy situations in satellite evapotranspiration algorithms, in *Third international workshop on the applications of remote sensing in hydrology,* NASA Goddard Space Centre, 16-18 October, 1996,Greenbelt, Maryland, pp. 33–44, 1997.

Bussières, N., and W.M. Schertzer, The evolution of AVHRR-derived water temperatures over lakes in the Mackenzie Basin and hydrometeorological applications, *J. Hydrometeorol.*, *4*(4), 660–672, 2003.

Bussières, N., D. Verseghy, and J.I. MacPherson, The evolution of AVHRR-derived water temperatures over boreal lakes. *Remote Sens. Environ.*, *80*(3), 373–384, 2002.

Di Bella, C.M., C.M. Rebella, J.M. Paruelo, Evapotranspiration estimates using NOAA AVHRR imagery in the Pampa region of Argentina, *Internat. J. Remote Sens.*, *21*(4), 791–797, 2000.

Duguay, C., and Y. Crevier, Use of remote sensing and field measurements to estimate surface energy balance components over alpine tundra surfaces, in *Proceedings of the 17th Canadian Symposium on Remote Sensing,* Saskatoon, June, 1995.

Duguay, C. R., T. D. Prowse, B. R. Bonsal, R. D. Brown, M. P. Lacroix, and P. Ménard, Recent trends in Canadian lake ice cover, *Hydrol. Proc.*, *19*, in press.

Friedl, M.A., Forward and inverse modeling of land surface energy balance using surface temperature measurements. *Remote Sens. Environ.*, *79*(2-3), 344–354, 2002.

Gellens-Meulenberghs, F., E. Roulin, P. Warnant, and Y. Govaerts, Integration of Meteosat, meteorological and vegetation data to assess evapotranspiration over Belgium, in: *Vegetation, Modelling and Climate Change Effects,* pp. 137–150, SPB Academic Publishing, The Hague, The Netherlands, 1994.

Goodison, B.E., R.D. Brown, M.M. Brugman, C.R. Duguay, G.M. Flato, E.F. LeDrew, and A.E. Walker, CRYSYS - Use of the cryospheric system to monitor global change in Canada: Overview and progress, *Can. J. Remote Sens.*, *25*(1): 3–11, 1999.

Granger, R.J., A feedback approach for the estimate of evapotranspiration using remotely-sensed data, in *Application of Remote Sensing in Hydrology, Proceedings of the Second International Workshop, NHRI Symposium No.14,* edited by G.W. Kite, A. Pietroniro, and T.J. Pultz, 18-19 October 1994, Saskatoon, pp. 211–222, 1995.

Granger, R.J., Summer energy balance at Wolf Creek research basin, Yukon, in *Hydro-ecolcogy workshop on the Arctic Environmental Strategy - Action on Water, NHRI Symposium No.16,* edited by D. Milburn, Canadian Geophysical Union - Hydrology Section Annual Meeting, 5–10 May, 1996, Banff, Canada, pp.325–342, 1996.

Granger, R.J., Comparison of surface and satellite-derived estimates of evapotranspiration using a feedback algorithm, in *Application of Remote Sensing in Hydrology, Proceedings of the Third International Workshop*, NHRI Symposium No.17, edited by G.W. Kite, A. Pietroniro and T.J. Pultz, October, 1996; NASA, Goddard Space Flight Center, Greenbelt, Maryland, pp. 71–81, 1997.

Granger, R.J., Partitioning of energy during the snow-free season at Wolf Creek Research Basin, in *Wolf Creek Research Basin - Hydrology, Ecology, Environment*, Proceedings of the Workshop, 5-7 March, 1998, Whitehorse, Yukon, pp. 33–43, 1999.

Granger, R.J., Potential for the use of remote sensing with the numerical analysis of advection in the estimate of lake evaporation, in *Applications of Remote Sensing in Hydrology, Proceedings of the 4th International Workshop*, edited by A. Pietroniro, R.J. Granger and T.J. Pultz, 4-7 November, Santa Fe, NM, pp. 105–112, 2000a.

Granger R.J., Satellite-derived estimates of evapotranspiration in the Gediz basin, *J. Hydrol., 229*(1-2), 70–76, 2000b.

Granger, R.J., Parameterization of evapotranspiration using remotely-sensed data, in *MAGS: Final Reports and Proceedings, 6th Scientific Workshop for MAGS*, G.S. Strong, 15-17 November, 2000, pp. 120–129, 2001.

Granger, R.J. and B. Toth, A simple technique for estimating soil heat flux over a range of latitudes and landcovers, Presented to the 27th Annual Scientific Meeting of the Canadian Geophysical Union. 14-17 May, 2001, Ottawa, Ontario, 2001.

Gray, D.M., G.A. McKay, and J.M. Wigham, Energy, evaporation and evapotranspiration, in *Handbook on the Principles of Hydrology*, edited by D.M. Gray, National Research Council of Canada, Ottawa, 1990.

Gurney, R.J., J.P. Ormsby, and D.K. Hall, A comparison of remotely sensed surface temperature and biomass estimates for aiding evapotranspiration determination in central Alaska, in *Permafrost; Fourth International Conference, Proceedings. International Conference on Permafrost, 4*, pp. 401–404, 1983.

Gutman, G., A simple method for estimating monthly mean albedo of land surfaces from AVHRR data, *J. Appl. Metoer., 27*, 973–988, 1988.

Hall, F.G., K.F. Huemmrich, S.J. Goetz, P.J. Sellers, and J.E. Nickeson, Satellite remote sensing of surface energy balance: successes, failures and unresolved issues in FIFE, *J. Geophys. Res., 97*, 19061–19089, 1992.

Harris, A.R., and I.M. Mason, An extension to the split-window technique giving improved atmospheric correction and total water vapour, *Int. J. Remote Sens. 13*(5), 881–892, 1992.

Jackson, R. D., R.J. Reginato, and S.B. Idso, Wheat canopy temperature: a practical tool for evaluating water requirements, *Water Res., 13*, 651–656, 1977.

Kane, D.L., R.E. Gieck, and L.D. Hinzman, Evapotranspiration from a small Alaskan arctic watershed, *Nordic Hydrol., 21*, 253–272, 1990.

Kite, G.W., and P. Droogers, Comparing evapotranspiration estimates from satellites, hydrological models and field data, *J. Hydrol., 229*(1/2), 3–18, 2000.

Kite, G.W., A. Dalton and K. Dion, Simulation of streamflow in a macroscale watershed using general circulation model data, *Water Resour.Res., 30*, 1547–1559, 1994.

Kustas, W.P., C.S.T. Daughtry, and P.J. Van Oeveln, Analytical treatment of the relationships between soil heat flux/net radiation ratio and vegetation indices, *Remote Sens. Env., 46*, 319–330, 1993.

Liu, J., J.M. Chen, J. Cihlar, and W.M. Park, A process-based boreal ecosystem productivity simulator using remote sensing inputs, *Remote Sens. Environ., 6*, 158–175, 1997.

Liu, J., J.M. Chen, J. Cihlar, W. Chen, and G. Pavlic, Quantifying the spatial distribution of evapotranspiration with satellite data, Proceedings published in CD format, Presented to the Fourth International Airborne Remote Sensing conference and Exibition/21st Canadian Symposium on Remote Sensing, June, 1999, Ottawa, 7pp., 1999.

Menenti, M., Evaporation, in Remote Sensing in Hydrology and Water Management, edited by G. A. Schultz and E.T. Engman, pp. 157–188, Springer Press, 2000.

Meyer, A. F., Computing runoff from rainfall and othter physical data, *Trans. Amer. Soc. Civil Engr., 79*, 1056–1155, 1915.

Morton, F.I., Operational estimates of areal evapotranspiration and their significance to the science and practice of hydrology, *J. Hydrol., 66*, 1–76, 1983.

Penman, H. L., Natural evaporation from open water, bare soil and grass, *Proc. R. Soc. London, Ser.A, 193*, 120–145, 1948.

Pomeroy, J.W., R.J. Granger, A. Pietroniro, J. E. Elliott, B. Toth, and N. Hedstrom, Hydrological Pathways in the Prince Albert Model Forest, Final report to the Prince Albert Model Forest Association. Environment Canada, NHRI Contribution Series No. CS-97004, 154 pp., 1997.

Prata, A.J., and C.M.R. Platt, Land surface temperature measurements from the AVHRR, in *Proceedings 5th AVHRR Data Users' Meeting*, 25–28 June, 1991, Tromso, Norway, pp. 433–438, 1991.

Rambal, S., B. Lacaze, H. Mazurek, and G. Debussche, Comparisons of hydrologically simulated and remotely sensed actual evapotranspiration from some Mediterranean vegetation formations, *Int. J. Remote Sens., 6*(8), 1475–1481, 1985.

Rossow, W.B., L.C. Garder, P.J. Lu, and A.W. Walker, International Satellite Cloud Climatology Project (ISCCP) Documentation of Cloud Data. WMO/TD-No. 266, World Meteorological Organization, 76 pp. plus appendices, 1991.

Rouse, W.R., P.F. Mills, and R.B. Stewart, Evaporation in high latitudes, *Water Resour. Res,. 13*(6), 909–914, 1977.

Rouse, W.R., P.D. Blanken, A.K. Eaton, R.M. Petrone, W.M. Schertzer, and C. Spence, Energy and water balanceee of high latitude surfaces, in *MAGS: Final Reports and Proceedings, 6th Scientific Workshop for MAGS*, edited by G.S. Strong, 15-17 November, 2000, pp. 81–98, 2001.

Royer, A., S.C.P. Traoré, N. O'Neil, K. Goïta, and N. Bussières, Paramétrisation globale du bilan d'energie à partir de la combinaison des paramètres satellitaires albédo, indice de végétation (NDVI) et température de surface, in *Physical Meaurements and Signatures in Remote Sensing, Proceedings of the Seventh International Symposium on Physical Measurements and Signatures in Remote Sensing*, edited by G. Guyot, and T. Phulpin, 7-11 April 1997, Courchevel France, Balkema, Rotterdam, pp. 773–777, 1997.

Running, S.W., R.R. Nemani, D.L. Peterson, L.E. Band, D.F. Potts, L.L. Pierce, and M.A. Spanner, Mapping regional forest evapotranspiration and photosynthesis by coupling satellite data with ecosystem simulation, *Ecol. Publ., 70* (4), 1090–1101, 1989.

Schertzer, W.M., W.R. Rouse, and P.D. Blanken, Cross-lake Variation of physical limnological and climatological processes of Great Slave Lake, *Phys. Geog., 21*(5), 385–406, 2000.

Schultz, G.A., and E.T. Engman (Eds.), *Remote Sensing in Hydrology and Water Management*, 483 pp., Springer Press, 2000.

Seguin, B., and B. Itier, Using midday surface temperature to estimate daily evaporation from satellite thermal IR data, *Int. J. Rem. Sens., 4*, 371–383, 1983.

Soegaard, H., Fluxes of carbon dioxide, water vapour and sensible heat in a boreal agricultural area of Sweden scaled from canopy to landscape level, *Agric Meteorol., 98/99*, 463–478, 1999.

Vourlitis, G.L., and W.C. Oechel, Eddy covariance measurements of CO_2 and energy fluxes of an Alaskan tussock tundra ecosystem, *Ecology, 80*(2), 686–701, 1999.

Wan, Z., and J. Dozier, Land-surface temperature measurement from space: Physical principles and inversion modeling, *IEEE Trans. Geosci. Remote Sens., 27*(3), 268–277, 1989.

Weisman, R. N., and W. Brutsaert, Evaporation and cooling of a lake under unstable atmospheric conditions, *Water Resour. Res., 9*, 1242–1257, 1973.

Zhang, Z., D.L. Kane, and L.D. Hinzman, Development and application of a spatially-distributed arctic hydrological and thermal process model (ARHYTHM), *Hydrol. Proc., 14*(6), 1017–1044, 2000.

Normand Bussières, Climate Processes and Earth Observation Division, Climate Research Branch, Meteorological Service of Canada, 4905 Dufferin St., Downsview, Ontario, M3H 5T4, Canada. (Normand.Bussieres@EC.GC.CA)

Raoul Granger, National Water Research Institute, 11 Innovation Blvd., Saskatoon, Saskatchewan, S7N 3H5, Canada. (Raoul.Granger@EC.GC.CA)

Appendix: Acronyms

Listed here are the names of satellites, instruments, physical parameters, agencies and other terms related to remote sensing in northern hydrology.

AATSR	Advanced Along Track Scanning Radiometer		DMSP	Defense Meteorological Satellite Program
			DMSP OLS	DMSP Operational Linescan System
ADEOS	Advanced Earth Observing System (Japanese)		DOC	Dissolved Organic Carbon
			DTFG	Depth To late-summer Frozen Ground
ALD	Active Layer Depth		ELA	Equilibrium Line Altitude
ALOS	Advanced Land Observing Satellite (Japanese)		ENVISAT	European Environment Satellite
			EO-1	Earth Observer 1
AMSR	Advanced Microwave Scanning Radiometer		EOS	Earth Observing System
			ERS	European Remote Sensing satellite
AMSR-E	Advanced Microwave Scanning Radiometer-E		ESA	European Space Agency
			ET	Equitemperature (metamorphism)
AMSU-B	Advanced Microwave Sounding Unit-B		ETM+	Enhanced Thematic Mapper Plus
ASAR	Advanced Synthetic Aperture Radar		FLA	Firn Line Altitude
ASTER	Advanced Spaceborne Thermal Emission and Reflection Radiometer		Geosat	Satellite name
			GISMO	Glaciers and Ice Sheets Mapping Orbiter
ATSR-2	Along Track Scanning Radiometer-2		GLAS	Geoscience Laser Altimeter System
AVHRR	Advanced Very High Resolution Radiometer		GLIMS	Global Land Ice Monitoring from Space
			GOES	Geostationary Operational Environmental Satellite
AVIRIS	Airborne Visible Infrared Imaging Spectrometer		GPS	Global Positioning System
BEPS	Boreal Ecosystems Productivity Simulator		GRACE	Gravity Recovery and Climate Experiment satellite mission
BOREAS	Boreal Ecosystem–Atmosphere Study		HBL	Hudson Bay Lowland
BRDF	Bidirectional Reflectance Distribution Functions		HCMM	Heat Capacity Mapping Mission
			HH	Horizontally polarized transmit and receive signal
C/X-SAR	C/X Band Synthetic Aperture Radar		HRV	High Resolution Visible
CLPP	Cold-Land Processes Pathfinder		HRVIR	High Resolution Visible Infrared
CMG	Climate-Modeling Grid		Hydros	Hydrosphere State Mission satellite
COST	European Cooperation in the Field of Scientific and Technical Research		HYPERION	Hyperspectral imaging instrument aboard the Earth Observer 1 satellite
CROCUS	One-dimensional numerical energy and mass evolution model of snow cover developed at Meteo France		ICESat	Ice Satellite
			IEM	Integral Equation Model
CRREL	Cold Regions Research and Engineering Laboratory		IFOV	Instantaneous Field-Of-View
			IHP	International Hydrological Programme
CryoSat	Cryosphere Satellite		IKONOS	Satellite name
CRYSYS	Cryospheric System to monitor global change in Canada		IMS	Interactive Multisensor Snow and Ice Mapping System
CSA	Canadian Space Agency		IR	Infrared
DAIS	Digital Airborne Imaging Spectrometer		IR/NrIR/TIR	Infrared/Near-Infrared/Thermal Infrared
DEM	Digital Elevation Model		ISCCP	International Satellite Cloud Climatology Project
D-InSAR	Differential SAR Interferometry			

JAXA	Japan Aerospace eXploration Agency
JERS-1	Japanese Earth Resources Satellite-1
kl	Normalised rms
ks	Normalised correlation length
LAI	Leaf Area Index
Landsat MSS	Land satellite Multispectral Scanner
Landsat TM	Land satellite Thematic Mapper
Landsat	Land satellite
LST	Land Surface Temperature
MAGS	Mackenzie GEWEX Study
MAP	Maximum A Posteriori
MAAT	Mean Annual Air Temperature
MEMLS	Microwave Emission Model of Layered Snowpacks
MERIS	Medium Resolution Imaging Spectrometer
MIR	Millimeter-wave Imaging Radiometer
MISR	Multiangle Imaging SpectroRadiometer
MODIS	Moderate Resolution Imaging Spectroradiometer
MORA	Multitemporal Optimal Resolution Approach
MSV	Multi-Spectral Video
NASA	National Aeronautics and Space Administration
NDSI	Normalized Difference Snow Index
NDVI	Normalized Difference Vegetation Index
NESDIS	National Environmental Satellite Data and Information Service
NIR/NrIR	Near infrared
NOAA	National Oceanic and Atmospheric Administration
NOHRSC	National Operational Hydrologic Remote Sensing Center
NRB	Northern Research Basins
NSCAT	NASA Scatterometer
NSIDC	National Snow and Ice Data Center
NSIDC EASE	NSIDC Equal Areal Scalable Earth
NSIDC FSA	NSIDC Frozen Soil Algorithm
NTB	Narrow-To-Broadband
NVE	Norges Vassdrags og Energiverk
NWI	National Wetland Inventory
NWS	National Weather Service
OrbView-2	Satellite also known as SeaStar
PALSAR	Phased Array type L-band Synthetic Aperture Radar
PDP	Portable Dielectric Probes
POLDER	POLarization and Directionality of the Earth Reflectance
PRISM	Panchromatic Remote sensing Instrument for Stereo Mapping
PRS^2	Plan of Research for Snowpack Properties Remote Sensing
Quickbird	Satellite name

QuikSCAT	Quick Scatterometer (NASA) Satellite
RADARSAT	Radar Satellite
RADARSAT-1	Radar Satellite-1
RADARSAT-2	Radar Satellite-2
RAR	Real Aperture Radar
rms	root-mean-square
RMSE	Root-Mean-Square-Error
S1 ice	congelation ice with vertical c-axis
S2 ice	congelation ice with horizontal c-axis
SAR	Synthetic Aperture Radar
SCA	Snow-Covered Area
ScanSAR	RADARSAT operation mode with a very large swath width (300 or 500 km), allowing gathering of regional data
Seasat	Satellite name
SeaWiFS	Sea-viewing Wide Field-of-view Sensor
SEBAL	Surface Energy BALance model
SIR	Shuttle Imaging Radar
SIRAL	Synthetic aperture radar Interferometric Radar Altimeter
SLC	Scan Line Corrector
SMA	Spectral Mixture Analysis
SMMR	Scanning Multichannel Microwave Radiometer
SMOS	Soil Moisture and Ocean Salinity (satellite mission)
SNTHERM	One-dimensional mass and energy balance model of snow physics
SPM	Small Perturbation Model
SPOT	Système Probatoire d'Observation de la Terre
SSC	Suspended Sediment Content
SSM/I	Special Sensor Microwave Imager
SVAT	Soil Vegetation Atmosphere Transfer Model
SWE	Snow Water Equivalent
SWIR	Short-Wave IR
TDR	Time Domain Reflectometry
TG	Temperature-Gradient (metamorphism)
THIR	Temperature Humidity Infrared Radiometer
TIR	Thermal InfraRed
TM4/TM5	Near-infrared to mid-infrared ratio of Landsat Thematic Mapper Bands 4 and 5
TOPEX/ POSEIDON	Satellite name
USGS	United States Geological Survey
VIR	Visible InfraRed sensor
VIS	VISible
VV	Vertically polarized transmit and receive signal
WatER	Water Elevation Recovery (satellite mission)

SUBJECT INDEX

157

SUBJECT INDEX

158

SUBJECT INDEX

SUBJECT INDEX

160